INFORMATION TO USERS

This manuscript has been reproduced from the microfilm master. UMI films the text directly from the original or copy submitted. Thus, some thesis and dissertation copies are in typewriter face, while others may be from any type of computer printer.

The quality of this reproduction is dependent upon the quality of the copy submitted. Broken or indistinct print, colored or poor quality illustrations and photographs, print bleedthrough, substandard margins, and improper alignment can adversely affect reproduction.

In the unlikely event that the author did not send UMI a complete manuscript and there are missing pages, these will be noted. Also, if unauthorized copyright material had to be removed, a note will indicate the deletion.

Oversize materials (e.g., maps, drawings, charts) are reproduced by sectioning the original, beginning at the upper left-hand corner and continuing from left to right in equal sections with small overlaps. Each original is also photographed in one exposure and is included in reduced form at the back of the book.

Photographs included in the original manuscript have been reproduced xerographically in this copy. Higher quality 6" x 9" black and white photographic prints are available for any photographs or illustrations appearing in this copy for an additional charge. Contact UMI directly to order.

UMI

A Bell & Howell Information Company
300 North Zeeb Road, Ann Arbor MI 48106-1346 USA
313/761-4700 800/521-0600

TIME-DOMAIN NUMERICAL TECHNIQUES FOR THE ANALYSIS AND DESIGN OF MICROWAVE CIRCUITS

by

Emmanouil M. Tentzeris

A dissertation submitted in partial fulfillment
of the requirements for the degree of
Doctor of Philosophy
(Electrical Engineering)
in The University of Michigan
1998

Doctoral Committee:
Professor Linda P.B.Katehi, Chair
Assoc. Professor Kamal Sarabandi
Professor John Volakis
Professor Andrew Yagle
Dr. James Harvey

"As you set out for Ithaka hope your road is a long one, full of adventure, full of discovery. Laistrygonians, Cyclops, angry Poseidon - don't be afraid of them: you'll never find things like that one on your way as long as you keep your thoughts raised high, as long as a rare sensation touches your spirit and your body.

Keep Ithaka always in your mind. Arriving there is what you're destined for. But don't hurry the journey at all. Better if it lasts for years, so you're old by the time you reach the island, wealthy with all you've gained on the way, not expecting Ithaka to make you rich. Ithaka gave you the marvelous journey. Without her you wouldn't have set out. She has nothing left to give you now. And if you find her poor, Ithaka won't have fooled you. Wise as you become, so full of experience, you will have understood by then what these Ithakas mean. "

K.Kavafis, "Ithaka" (1911)

To my parents; To my brother, John.

ACKNOWLEDGEMENTS

The completion of this dissertation and my entire doctoral study at the University of Michigan would not have been possible without the support of many people. I would like to take this opportunity to express my sincere gratitude to all those who helped me in one way or another during these prolific and memorable years.

My first sincere gratitude and deepest appreciation goes to my advisor, Professor Linda Katehi, since without her insight, expertise, encouragement and understanding, this research would have been a much more difficult and painful journey. Her enthusiasm and boundless energy for research and teaching is very infectious. I am also grateful for her continuous financial support and for providing me with the opportunity to attend numerous conferences to present my research. I would also like to thank my committee members for their time and consideration.

Many friends and colleagues at the Radiation Laboratory have contributed to this work through discussions. Special thanks go to Dr. Michael Krumpholz, from whom I have constantly benefited through a great deal of fruitful conversations. Also, I would like to mention Mr. Robert Robertson. My close work with him and the understanding that we have between us made our research better and our friendship stronger. Dr. Nihad Dib and Ms. Kavita Goverdhanam are deeply appreciated for their useful suggestions. In summary, all Rad Lab friends, too many to mention by name, created a very enjoyable environment

for work and study.

I should mention that the theoretical work on the FG-CPW has been done in cooperation with Dr. George Ponchak from the NASA Lewis Research Center. I thank him for his time and for supplying us with the results which validated the developed theoretical analysis. I specially thank Professor Andreas Cangellaris at the University of Illinois at Urbana-Champaign for his comments on the development of an efficient Time and Space Adaptive Gridding Algorithm.

The major party of my study and research at the University of Michigan was sponsored by the Army Research Office. The continuous enthusiasm of this office, and especially of Dr.Harvey, in my research work is cordially appreciated.

Dr.George Eleftheriades, Dr. Hristos Anastasiou, Dr. George Papageorgakis, Dr. Nikos Zacharopoulos, John Papapolymerou, Hristos Patonis, Costas Stathis, Penelope Papailias, Theodoros Paschos, Kostas Katsibas, Loucas Louca, Panos Thomas and Kostas Sarris with their dear friendship made difficult moments easier. In addition, my numerous friends from the Hellenic Students Association of the University of Michigan gave a nice flavor and broadened my outlook on life.

I would like to express my special thanks to Prof. Uzunoglu, as well as to Prof. Fikioris and Prof. Kottis from the National Technical University of Athens, Greece, who introduced me to the challenging field of Electromagnetics during my undergraduate years.

I also express my deepest gratitude to my parents Markos and Irene Tentzeris, who sowed in me from the early years the seeds of aspiration to ascend to the highest levels in every aspect of life, especially in education and knowledge. Finally, I wish to thank my younger brother John, who has always believed in me throughout my entire education.

TABLE OF CONTENTS

LIST OF TABLES

LIST OF FIGURES

CHAPTER 1

Introduction

1.1 What are the Microwaves?

More and more often, the term "Microwaves" is used in applications related to radar and communication systems. Radar systems are used for detecting and locating air, ground or sea-going targets, by airport traffic-control radars, missile tracking radars, fire-control radars and other weapon systems. Radar is also used for weather prediction and remote sensing applications. Microwave communication systems handle a large fraction of international and other long-haul telephone traffic (satellite and radio-link communcations), in addition to wireless cellular applications.

As a result, a naturally rising question is: What are the Microwaves? This term refers to alternating current signals with frequencies between 300 MHz and 300 GHz. The corresponding electrical wavelength ranges from $\lambda = c/f$=1 m to λ=1 mm where $c = 3x10^8 m/sec$ is the speed of light in a vacuum. Because of the high frequencies (and short wavelengths), standard circuit theory cannot be applied directly to solve microwave network problems. Microwave components usually are distributed elements, where the phase of voltage or current changes significantly over the physical length of the device because its physical di-

mensions are on the order of the microwave wavelength. At much lower frequencies, the wavelength is so large that there is a minor phase variation across the component (lumped approximations).

The small wavelengths of microwave energy provide unique advantages. Antenna gain is proportional to the electric size of the antenna. At higher frequencies, more antenna gain is possible for a given physical antenna size. More bandwidth (information-carrying capacity) can be realized at higher frequencies. Microwave signals travel by line-of-sight and are not bent by the ionosphere as are lower frequency signals. Terrestrial and satellite communication links with high capacities are thus possible. In addition, the radar cross-section of a radar target is usually proportional to the target's electrical size; this fact makes microwave frequencies the preferred band for radar applications. Nevertheless, one must begin with Maxwell's equations to analyze microwave topologies. In practical applications, high mathematical complexity arises, as Maxwell's equations involve vector differential or integral operations.

1.2 Time-Domain Techniques

With the advent of microwave circuits used in high-frequency communications, there is a compelling need to develop efficient and reliable full wave simulation techniques for the modeling process. Until 1990, the modeling of electromagnetic wave interactions was dominated by frequency-domain techniques. Apart from high-frequency asymptotic methods [1, 2], electromagnetic simulations involved setting up and solving frequency-domain integral equations [3, 4] for the phasor electric and magnetic currents induced on the surfaces of the geometries of interest. This Method of Moments (MoM) involves setting up and solving dense, full, complex-valued systems of tens of thousands of linear equations using

direct or iterative techniques. The use of MoM in EM has become popular since the work of Richmond [5] and Harrington [6] in 1967. The method has been successfully applied to a wide variety of EM problems of practical interest such as radiation due to thin-wire elements and arrays, scattering problems, analysis of microstrips and lossy structures, antenna beam pattern and many more. The procedure for applying MoM usually involves initially the derivation of the appropriate integral equation (IE). This IE is converted (discretized) into a matrix equation using basis (expansion) functions and weighting (testing) functions. After the matrix elements have been evaluated, the matrix equation is solved, thus deriving the parameters of interest. Though MoM has been proven to be a very robust technique, it is plagued by significant computational burdens, when it is used at very large geometries. In addition, modeling of a new structure requires the reformulation of the integral equation, a task that may require the very difficult derivation of a geometry-specific Green's function.

On the contrary, techniques based on the partial differential equation (PDE) solutions of the Maxwell's equations yield either sparse matrices (frequency-domain finite-element methods) or no matrices at all (time-domain finite-difference or finite-volume methods). It is well known [7] that classical (analytical) approaches may fail if the PDE is not linear and cannot be linearized without seriously affecting the result, the solution region is complex, the boundary conditions are of mixed types or time-dependent or if the medium is inhomogeneous or anisotropic. In these cases, it is preferable to use numerical solutions.

The Finite-difference method was first developed by A.Thom [8] in the 1920's under the title "method of squares" to solve nonlinear hydrodynamic equations. This technique divides the solution region into a grid of nodes and approximates the given differential equation by finite difference equivalents that relate the dependent variable at a point in the solution region to its values at the neighboring points. The new difference equations are

solved subject to the prescribed boundary and/or initial conditions.

The Finite-element analysis of any problem [9] involves the discretization of the solution region into finite number of subregions or elements and the derivation of the governing equations for a typical element. All elements are assembled in the solution region and finally the solution of the system of equations is obtained.

Generally, when using PDE approximation techniques, specifying a new geometry is reduced to a problem of mesh generation only. Thus, time-domain PDE solvers could provide a framework for a space/time microscope permitting the EM designer to visualize with submicron/subpicosecond resolution the dynamics of electromagnetic wave phenomena propagating at light speed within proposed geometries. EM Finite-Difference Time-Domain (FDTD) is a direct solution method for Maxwell's time dependent curl equations. It is based upon volumetric sampling of the unknown near-field distribution within and around the structure of interest over a period of time. No potentials are employed. The sampling is set below the Nyquist limit and typically more than 10 samples per wavelength are required. The time-step has to satisfy the stability condition. For simulations of open geometries, absorbing boundary conditions (ABC) are employed at the outer grid truncation planes in order to reduce spurious numerical reflection from the grid termination.

In 1966, Yee [10] introduced the first finite-difference time-domain technique (FDTD) for the solution of Maxwell's curl equations. Interleaved positioning of the electric and magnetic field components provided a second-order accuracy of the algorithm. Taflove and Boldwin [11] presented the numerical stability criterion for Yee's algorithm and Mur [12] published the first numerically stable second-order accurate absorbing boundary condition (ABC) for the Yee's mesh. The perfectly Matched Layer (PML) ABC, introduced in 2D by Berenger in 1994 [13] and extended to 3D by Katz et al. [14], provides numerical reflection

comparable to the reflection of anechoic chambers with values -40dB lower than the Mur ABC. The FDTD technique has been applied to various High-Frequency simulations with remarkable success. Taflove [15] and Umashankar [16] used FDTD to model scattering and compute near/far fields and RCS for 2D and 3D structures. Waveguide - Cavity structures and microstrips were analyzed with FDTD by Choi [17] and Zhang [18] respectively. Maloney [19] introduced the FDTD modeling of antennas and El-Ghazaly [20] applied this technique to picosecond optoelectronic switches. Toland et al. [21] published the first FDTD models of nonlinear devices (tunnel diodes and Gunn diodes) exciting cavities and antennas and Sui et al. [22]modeled lumped electronic circuit elements in 2D.

Despite the numerous applications of FDTD, many practical geometries, especially in microwave and millimeter-wave integrated circuits (MMIC), packaging, interconnects, subnanosecond digital electronic circuits (such as multichip modules (MCM)) and antennas used in wireless and microwave communication systems, have been left untreated due to their complexity and the inability of the existing techniques to deal with requirements for large size and high resolution. Multiresolution analysis based on the expansion in scaling and wavelet functions has demonstrated a capability to provide space and time adaptive gridding without the problems encountered by the conventional Finite Difference Time-Domain schemes. As a result, it could be used as a powerful foundation for the development of very efficient electromagnetic simulation techniques.

1.3 Wavelets-Multiresolution Analysis

The term "wavelets" has a very broad meaning, ranging from singular integral operators in harmonic analysis to subband coding algorithms in signal processing, from coherent states in quantum analysis to spline analysis in approximation theory, from multiresolution

transform in computer vision to a multilevel approach in the numerical solution of partial differential equations, and so on. Considering the characteristics of time-domain numerical techniques for the solution of Maxwells' equations, wavelets could be considered to be mathematical tools for waveform representations and segmentations, time-frequency analysis and fast and efficient algorithms for easy implementation in both time and frequency domains.

One of the most important characteristics of expansion to scaling and wavelet functions is the time-frequency localization. The standard approach in ideal lowpass ("scaling") and bandpass ("wavelet") filtering for separating an analog signal into different frequency bands emphasizes the importance of time localization. The Multiresolution Analysis (MRA), introduced by Mallat and Meyer [23, 24], provides a very powerful tool for the construction of wavelets and implementation of the wavelet decomposition/reconstruction algorithms. The sampling theorem can be used to formulate analog signal representations in terms of superpositions of certain uniform shifts of a single function called a scaling function. Stability of this signal representation is achieved by imposing the Riesz condition on the scaling function. Another important condition of an MRA is the nested sequence of subspaces as a result of using scales by integer powers of 2.

In the case of cardinal B-splines [25], an orthonormalization process is used to produce an orthonormal scaling function and, hence, its corresponding orthonormal wavelet by a suitable modification of the two-scale sequence. The orthonormalization process was introduced by Schweinler and Wigner [26] and the resulting wavelets are the Battle-Lemarie wavelets, obtained independently by Battle [27] and Lemarie [28] using different methods. The only orthonormal wavelet that is symmetric or antisymmetric and has compact support (to give finite decomposition and reconstruction series) is the Haar [29] wavelet [30]. Nev-

ertheless, these wavelets exhibit poor time-frequency localization. Throughout this Thesis, Battle-Lemarie and Haar scaling and wavelet functions will be used as an expansion basis for the E- and H- field components in space and time domain respectively, in order to derive an efficient and fast Multiresolution Time-Domain Scheme for the numerical approximation of Maxwell's equations in a way similar to [31].

1.4 Overview of the Dissertation - Achievements

Chapter 2 gives a general overview of the FDTD Technique. Excitation topics and ways of improving the algorithm performance are discussed separately. Next, FDTD is used in the analysis of various planar circuits and waveguide probe structures. A new waveguide absorber based on analytic modal Green's functions is developed; it is characterized by a better performance in memory requirements than the PML absorber, while maintaining similar accuracy. The scattering parameters of the probe structures are calculated and verified by comparison with FEM and experimental data. The effect of critical geometrical parameters on the probe performance are investigated and the probe behavior is optimized.

Chapter 3 starts with a discussion on the need of development of novel time-domain schemes which would alleviate the serious memory and execution time limitations of the existing techniques. The basic principles of the Multiresolution Analysis as well as the technique of the construction of wavelet functions are presented. Analytical spectral expressions for the linear and cubic cardinal splines are derived as an example. The 2D MRTD algorithm based on Battle-Lemarie expansion basis is developed for a grid similar to that of the FDTD. Hard Boundaries, such as Perfect Electric Conductors, and arbitrary excitations are implemented in an automatic way. The principles of the PML absorber are extended in split and nonsplit formulations providing a very efficient absorber. Notes on the total field

value calculation at every spatial point conclude this Chapter.

In Chapter 4, the MRTD scheme is applied to the numerical analysis of 2.5D shielded and open striplines and microstrips. The field patterns and the characteristic impedance are calculated and verified by comparison to reference data. Simulations display memory savings by a factor of 25 and execution time savings by a factor of 4-5. For structures where the edge effect is prominent, additional wavelet resolutions have to be introduced to maintain a satisfactory performance while using a coarse MRTD grid. The non-split PML algorithm is evaluated for different cells sizes and its performance is comparable to that of the conventional FDTD PML absorber.

Chapter 5 investigates the stability and the dispersion performance of MRTD for different stencil (number of summation terms) sizes and for 0-resolution of wavelets. Analytical expressions for the maximum stable time-step are derived for schemes containing only scaling functions or combination of scaling and wavelet functions. It is proved that larger stencils decrease the numerical phase error making it significantly lower than FDTD for low and medium discretizations. The addition of wavelets further improves the dispersion characteristics for discretizations close to the Nyquist limit, though it decreases the value of the maximum stable time-step.

A mathematically correct way of dielectric modeling is presented and evaluated in the first part of Chapter 6. A dynamically changing space- and time- adaptive meshing MRTD algorithm based on a combination of absolute and relative thresholding of the wavelet values is proposed. Different thresholding implementations are evaluated by the application of the dynamically changing grid to the numerical analysis of various nonhomogeneous 2D waveguide structures. This scheme offers memory savings by a factor of 5-6 per dimension in comparison to FDTD.

The direct application of the principles of the Multiresolution Analysis to the time domain is presented in Chapter 7. A Time Adaptive Time-Domain Technique based on Haar basis is proposed and applied to various types of circuits problems with active and passive lumped and distributed elements. The addition of the wavelets increases the resolution in time, something that is very important especially in circuits with nonlinear devices such as diodes and transistors. This scheme exhibits significant savings in execution time and memory requirements while maintaining a similar accuracy with conventional circuit simulators. The Thesis closes with ideas for future work described in Chapter 8.

CHAPTER 2

The Finite Difference Time Domain Technique (F.D.T.D.) and its Applications in the Analysis and Design of Microwave Circuits and Waveguide Probes

2.1 Foundations of the Finite Difference Time Domain (F.D.T.D.) Technique

Considering an area with no electric or magnetic current sources, the time-dependent Maxwell's equations are given in differential form by

Faraday's Law:

$$\frac{\partial B}{\partial t} = \nabla \times E - J_m$$

Ampere's Law:

$$\frac{\partial D}{\partial t} = \nabla \times H - J_e$$

Gauss's Law for the electric field:

$$\nabla \cdot D = 0$$

Gauss's Law for the magnetic field:

$$\nabla \cdot B = 0$$

Here, E is the electric field vector, D is the electric flux density vector, H is the magnetic field vector, B is the magnetic flux density vector, J_e is the electric conduction current density, J_m is the equivalent magnetic conduction current density. In linear, isotropic nondispersive materials, B and D can be related to H and E, respectively, using the constitutive equations:

$$\begin{aligned} B &= \mu H \\ D &= \epsilon E \end{aligned} \tag{2.1}$$

where μ is the magnetic permeability and ϵ is the electric permittivity. To account for the electric and magnetic loss mechanisms, an equivalent electric and magnetic current can be introduced

$$\begin{aligned} J_e &= \sigma E \\ J_m &= \rho' H \end{aligned} \tag{2.2}$$

with σ the electric conductivity and ρ' the equivalent magnetic resistivity. Combining Eqs.(2.1)–(2.2) with Maxwell's equations, we obtain

$$\frac{\partial H}{\partial t} = -\frac{1}{\mu}\nabla \times E - \frac{\rho'}{\mu}H \tag{2.3}$$

$$\frac{\partial E}{\partial t} = \frac{1}{\epsilon}\nabla \times H - \frac{\sigma}{\epsilon}E \tag{2.4}$$

The curl equations (2.3)–(2.4) yield the following system of six coupled scalar equations in the 3-D rectangular coordinate system (x, y, z):

$$\frac{\partial H_x}{\partial t} = \frac{1}{\mu}\left(\frac{\partial E_y}{\partial z} - \frac{\partial E_z}{\partial y} - \rho' H_x\right)$$

$$
\begin{aligned}
\frac{\partial H_y}{\partial t} &= \frac{1}{\mu}\left(\frac{\partial E_z}{\partial x} - \frac{\partial E_x}{\partial z} - \rho' H_y\right) \\
\frac{\partial H_z}{\partial t} &= \frac{1}{\mu}\left(\frac{\partial E_x}{\partial y} - \frac{\partial E_y}{\partial x} - \rho' H_z\right) \\
\frac{\partial E_x}{\partial t} &= \frac{1}{\epsilon}\left(\frac{\partial H_z}{\partial y} - \frac{\partial H_y}{\partial z} - \sigma E_x\right) \\
\frac{\partial E_y}{\partial t} &= \frac{1}{\epsilon}\left(\frac{\partial H_x}{\partial z} - \frac{\partial H_z}{\partial x} - \sigma E_y\right) \\
\frac{\partial E_z}{\partial t} &= \frac{1}{\epsilon}\left(\frac{\partial H_y}{\partial x} - \frac{\partial H_x}{\partial y} - \sigma E_z\right)
\end{aligned} \tag{2.5}
$$

Eq.(2.5) forms the basis of the FDTD numerical algorithm for general 3-D objects. The FDTD algorithm need not explicitly enforce the Gauss's Law relations. This occurs because they are theoretically a direct consequence of the curl equations. However, the FDTD space grid must be structured so that the Gauss's Law relations are implicit in the positions of the electric and magnetic field vector components in the grid and the numerical space derivative operations upon these vector components that model the action of the curl operator.

The above system of equations can be reduced to 2-D assuming no variation in the z-direction. That means that all partial derivatives with respect to z equal zero and that the analyzed structure extends to infinity in the z-direction with no change in the shape or position of its transverse cross section. Eq.(2.5) will give in rectangular coordinates:

$$\frac{\partial H_x}{\partial t} = \frac{1}{\mu}\left(-\frac{\partial E_z}{\partial y} - \rho' H_x\right) \tag{2.6}$$

$$\frac{\partial H_y}{\partial t} = \frac{1}{\mu}\left(\frac{\partial E_z}{\partial x} - \rho' H_y\right) \tag{2.7}$$

$$\frac{\partial H_z}{\partial t} = \frac{1}{\mu}\left(\frac{\partial E_x}{\partial y} - \frac{\partial E_y}{\partial x} - \rho' H_z\right) \tag{2.8}$$

$$\frac{\partial E_x}{\partial t} = \frac{1}{\epsilon}\left(\frac{\partial H_z}{\partial y} - \sigma E_x\right) \tag{2.9}$$

$$\frac{\partial E_y}{\partial t} = \frac{1}{\epsilon}\left(-\frac{\partial H_z}{\partial x} - \sigma E_y\right) \tag{2.10}$$

$$\frac{\partial E_z}{\partial t} = \frac{1}{\epsilon}\left(\frac{\partial H_y}{\partial x} - \frac{\partial H_x}{\partial y} - \sigma E_z\right) \tag{2.11}$$

Eqs.(2.6),(2.7),(2.11) constitute the transverse magnetic (TM^z) mode; the rest the trans-

verse electric (TE^z) mode 2-D equations. The TE^z and TM^z modes are decoupled since they contain no common field vector components. These modes are completely independent for structures composed of isotropic materials or anisotropic materials having no off-diagonal components in the constitutive tensors. That means that they can exist simultaneously with no mutual interactions.

Equations for 1-D cases can be derived in a similar way assuming no variation in the x- or y-direction in excess to no variation in the z-direction.

Yee [10] proposed a set of finite-difference equations for the time-dependent Maxwell's curl equations, solving for both electric and magnetic fields in time and space instead of solving for the electric field alone (or the magnetic field alone) with a wave equation. In this way, the solution is more robust and more accurate for a wider class of structures. In addition, both electric and magnetic material properties can be modeled in a straightforward manner. In Yee's discretization cell (Fig.2.1), E- and H- fields are interlaced by half space and time gridding steps. The spatial displacement is very useful in specifying field boundary conditions and singularities and creates finite-difference expressions for the space derivatives which are central in nature and second-order accurate. It has been proven that the Yee mesh is divergence-free with respect to its electric and magnetic fields, and thereby properly enforces the absence of free electric and magnetic charge in the source-free space being modeled. The time displacement (leapfrog) is fully explicit, completely avoiding the problems involved with simultaneous equations and matrix inversion. The resulting time-stepping algorithm is non-dissipative; numerical wave modes propagating in the mesh do not spuriously decay due to a nonphysical artifact of the time-stepping algorithm.

Denoting any function u of space and time evaluated at a discrete point in the grid and

at a discrete point in time as

$$u(i\Delta x, j\Delta y, k\Delta z, l\Delta t) = {}_l u_{i,j,k}$$

where Δt is the time step and $\Delta x, \Delta y, \Delta z$ the cell size to the x-, y- and z-direction, the first partial space derivative of u in the x-direction and the first time derivative of u are approximated with the following central differences respectively

$$\begin{aligned}
\frac{\partial u}{\partial x}(i\Delta x, j\Delta y, k\Delta z, l\Delta t) &= \frac{{}_l u_{i+1/2,j,k} - {}_l u_{i-1/2,j,k}}{\Delta x} + O[(\Delta x)^2] \\
\frac{\partial u}{\partial t}(i\Delta x, j\Delta y, k\Delta z, l\Delta t) &= \frac{{}_{l+1/2} u_{i,j,k} - {}_{l-1/2} u_{i,j,k}}{\Delta t} + O[(\Delta t)^2]
\end{aligned} \tag{2.12}$$

Applying the above notation, the following FDTD equations are derived for 3-D geometries

$$\begin{aligned}
{}_{l_{0.5}} H^x_{i,j-0.5,k-0.5} &= \left(\frac{1 - \frac{\rho'_{i,j,k}\Delta t}{2\mu_{i,j,k}}}{1 + \frac{\rho'_{i,j,k}\Delta t}{2\mu_{i,j,k}}} \right) {}_{l-0.5} H^x_{i,j-0.5,k-0.5} \\
&+ \left(\frac{\frac{\Delta t}{\mu_{i,j,k}}}{1 + \frac{\rho'_{i,j,k}\Delta t}{2\mu_{i,j,k}}} \right) \left(\frac{{}_l E^y_{i,j-0.5,k} - {}_l E^y_{i,j-0.5,k-1}}{\Delta z} - \frac{{}_l E^z_{i,j,k-0.5} - {}_l E^z_{i,j-1,k-0.5}}{\Delta y} \right)
\end{aligned} \tag{2.13}$$

$$\begin{aligned}
{}_{l_{0.5}} H^y_{i-0.5,j,k-0.5} &= \left(\frac{1 - \frac{\rho'_{i,j,k}\Delta t}{2\mu_{i,j,k}}}{1 + \frac{\rho'_{i,j,k}\Delta t}{2\mu_{i,j,k}}} \right) {}_{l-0.5} H^y_{i-0.5,j,k-0.5} \\
&+ \left(\frac{\frac{\Delta t}{\mu_{i,j,k}}}{1 + \frac{\rho'_{i,j,k}\Delta t}{2\mu_{i,j,k}}} \right) \left(\frac{{}_l E^z_{i,j,k-0.5} - {}_l E^z_{i-1,j,k-0.5}}{\Delta x} - \frac{{}_l E^x_{i-0.5,j,k} - {}_l E^x_{i-0.5,j,k-1}}{\Delta z} \right)
\end{aligned} \tag{2.14}$$

$$\begin{aligned}
{}_{l_{0.5}} H^z_{i-0.5,j-0.5,k} &= \left(\frac{1 - \frac{\rho'_{i,j,k}\Delta t}{2\mu_{i,j,k}}}{1 + \frac{\rho'_{i,j,k}\Delta t}{2\mu_{i,j,k}}} \right) {}_{l-0.5} H^z_{i-0.5,j-0.5,k} \\
&+ \left(\frac{\frac{\Delta t}{\mu_{i,j,k}}}{1 + \frac{\rho'_{i,j,k}\Delta t}{2\mu_{i,j,k}}} \right) \left(\frac{{}_l E^x_{i-0.5,j,k} - {}_l E^x_{i-0.5,j-1,k}}{\Delta y} - \frac{{}_l E^y_{i,j-0.5,k} - {}_l E^y_{i-1,j-0.5,k}}{\Delta x} \right)
\end{aligned} \tag{2.15}$$

$$\begin{aligned}
{}_{l_1} E^x_{i-0.5,j,k} &= \left(\frac{1 - \frac{\sigma_{i,j,k}\Delta t}{2\epsilon_{i,j,k}}}{1 + \frac{\sigma_{i,j,k}\Delta t}{2\epsilon_{i,j,k}}} \right) {}_l E^x_{i-0.5,j,k} + \left(\frac{\frac{\Delta t}{\epsilon_{i,j,k}}}{1 + \frac{\sigma_{i,j,k}\Delta t}{2\epsilon_{i,j,k}}} \right) \cdot \\
&\cdot \left(\frac{{}_{l_{0.5}} H^z_{i-0.5,j_{0.5},k} - {}_{l_{0.5}} H^z_{i-0.5,j-0.5,k}}{\Delta y} - \frac{{}_l H^y_{i-0.5,j,k_{0.5}} - {}_l H^y_{i-0.5,j,k-0.5}}{\Delta z} \right)
\end{aligned}$$

(2.16)

$$
\begin{aligned}
{}_{l_1}E^{y}_{i,j-0.5,k} &= \left(\frac{1-\frac{\sigma_{i,j,k}\Delta t}{2\epsilon_{i,j,k}}}{1+\frac{\sigma_{i,j,k}\Delta t}{2\epsilon_{i,j,k}}}\right) {}_{l}E^{y}_{i,j-0.5,k} + \left(\frac{\frac{\Delta t}{\epsilon_{i,j,k}}}{1+\frac{\sigma_{i,j,k}\Delta t}{2\epsilon_{i,j,k}}}\right) \cdot \\
&\cdot \left(\frac{{}_{l_{0.5}}H^{x}_{i,j_{0.5},k_{0.5}} - {}_{l_{0.5}}H^{x}_{i,j_{0.5},k-0.5}}{\Delta z} - \frac{{}_{l_{0.5}}H^{z}_{i_{0.5},j_{0.5},k} - {}_{l_{0.5}}H^{z}_{i-0.5,j_{0.5},k}}{\Delta x}\right)
\end{aligned}
$$

(2.17)

$$
\begin{aligned}
{}_{l_1}E^{z}_{i,j,k-0.5} &= \left(\frac{1-\frac{\sigma_{i,j,k}\Delta t}{2\epsilon_{i,j,k}}}{1+\frac{\sigma_{i,j,k}\Delta t}{2\epsilon_{i,j,k}}}\right) {}_{l}E^{z}_{i,j,k-0.5} + \left(\frac{\frac{\Delta t}{\epsilon_{i,j,k}}}{1+\frac{\sigma_{i,j,k}\Delta t}{2\epsilon_{i,j,k}}}\right) \cdot \\
&\cdot \left(\frac{{}_{l_{0.5}}H^{y}_{i_{0.5},j,k-0.5} - {}_{l_{0.5}}H^{y}_{i-0.5,j,k-0.5}}{\Delta x} - \frac{{}_{l_{0.5}}H^{x}_{i,j_{0.5},k-0.5} - {}_{l_{0.5}}H^{x}_{i,j-0.5,k-0.5}}{\Delta y}\right)
\end{aligned}
$$

(2.18)

where $\sigma_{i,j,k}$ and $\rho'_{i,j,k}$ are the electric and magnetic loss coefficients for the $(i,j,k)-$cell. The notation

$$ {}_{l_a}u_{i_b,j_c,k_d} = {}_{l-a}u_{i-b,j-c,k-d} $$

is used for compactness.It can be observed that a new value of a field vector component at any space lattice point depends only on its previous value and the previous values of the components of the other field vectors at adjacent points. Therefore, at any given time step, the value of a field vector component at p different lattice points can be calculated simultaneously if p parallel processors are employed, something that demonstrates the fact that the FDTD algorithm is highly parallelizable.

The exponential decay of propagating waves in certain highly lossy media is so rapid that the standard Yee time-stepping algorithm fails to describe. Holland [32] has proposed an exponential time-stepping. For example, for large values of σ, the field component E_x is given by

$$
\begin{aligned}
{}_{l_1}E^{x}_{i-0.5,j,k} &= e^{-\sigma_{i,j,k}\Delta t/\epsilon_{i,j,k}} {}_{l}E^{x}_{i-0.5,j,k} - \frac{1}{\sigma_{i,j,k}}(e^{-\sigma_{i,j,k}\Delta t/\epsilon_{i,j,k}} - 1) \cdot \\
&\cdot \left(\frac{{}_{l_{0.5}}H^{z}_{i-0.5,j_{0.5},k} - {}_{l_{0.5}}H^{z}_{i-0.5,j-0.5,k}}{\Delta y} - \frac{{}_{l}H^{y}_{i-0.5,j,k_{0.5}} - {}_{l}H^{y}_{i-0.5,j,k-0.5}}{\Delta z}\right)
\end{aligned}
\tag{2.19}
$$

instead of Eq.(2.16).

Stability analysis [62] has shown that the upper bound for the FDTD time step for a homogeneous region of space (ϵ_r, μ_r) is given by

$$\Delta t \leq \frac{\sqrt{\epsilon_r \mu_r}}{c\sqrt{\frac{1}{(\Delta x)^2} + \frac{1}{(\Delta y)^2} + \frac{1}{(\Delta z)^2}}}$$

for 3-D simulations and

$$\Delta t \leq \frac{\sqrt{\epsilon_r \mu_r}}{c\sqrt{\frac{1}{(\Delta x)^2} + \frac{1}{(\Delta y)^2}}}$$

for 2-D simulations. Lower values of upper bounds are used in case a highly lossy material or a variable grid is employed. Discretization with at least 10-20 cells/wavelength almost guarantee that the FDTD algorithm will have satisfactory dispersion characteristics (phase error smaller than $5^o/\lambda$ for time step close to the upper bound value).

2.1.1 Overview of Numerical Absorbing Boundary Conditions

It is very common for the geometries of interest to be defined in "open" regions where the spatial domain of the computed EM fields is unbounded in one or more coordinate directions. Since no computer can store an unlimited amount of data, the field computation domain must be limited in size. The computation domain must be large enough to enclose the structure of interest, and a suitable absorbing boundary condition (ABC) on the outer perimeter of the domain must be used to simulate its extension to infinity. ABC's cannot be directly obtained from the numerical algorithms for Maxwells' curl equations defined by the Yee's finite-difference systems. This is due to the fact that these systems employ a central spatial difference scheme that requires knowledge of the field one-half cell to each side of an observation point. Central differences cannot be implemented at the outermost lattice planes, since by definition there exists no information concerning the fields at points one-half space cell outside of these planes. Backward finite differences are generally of lower accuracy

for a given space discretization, so they cannot be used as a reliable solution. Several approximate ABC's have been proposed [33, 34, 35, 36]. In our FDTD simulations, 1st and 2nd order Mur ABC [12], coupled with Mei-Fang Superabsorption [37] for complicated structures, have been used to terminate open domains due to their simplicity and versatility . Reflection coefficients close to $-60dB$ have been achieved for a wide range of incidence angles and frequencies. For waveguide structures a new ABC based on Green's functions has been developed. Reflection coefficients obtained by the recently developed PML [13] have been used as a reference for the validation of the novel ABC.

2.1.2 Excitation Topics

The first source to be modeled in FDTD was a plane wave incoming from infinity [10]. The plane wave source is very useful in modeling radar scattering problems, since in most cases of this type the target of interest is in the near field of the radiating antenna, and the incident illumination can be considered to be a plane wave.

The hard source [38] is another common FDTD source implementation. It is set up simply by assigning a desired time function to specific electric or magnetic field components in the FDTD space lattice. In this way, it radiates a numerical wave having a time waveform corresponding to the source function. This numerical wave propagates symmetrically in both directions from the source point. However, this way of excitation has some drawbacks. As time-stepping is continued to obtain either the sinusoidal steady state or the late-time impulse response, the reflected - from the discontinuities - numerical wave eventually returns to the source grid location. Since the total electric field is specified at the excitation point without regard to any possible reflected waves, the hard source causes a spurious, nonphysical retroreflection of these waves toward the structure of interest, failing

to simulate the propagation of the reflected wave energy. A simple way to avoid this problem is to remove the source from the algorithm after the pulse has decayed essentially to zero and apply instead the regular Yee update. However, this approach cannot be used for continuous source waveforms where the source remains active even after reflections propagate back to it. It has been observed that much less error occurs for hard sources in 2-D and 3-D than in 1-D because the hard sources in 2-D and 3-D intercept and retroreflect much smaller fractions of the total energy in the FDTD grid. Collinear arrays of hard-source field vector components in 3D can be useful for exciting waveguides and strip lines.

The total field excitation eliminates the retroreflection problems of the hard source. A proper field component is simply added to the field values given by the regular FDTD equations. Let's consider for example Eq.(2.16) for $\sigma_{i,j,k} = 0$ and no field variation to the z-direction

$$ {}_{l_1}E^x_{i-0.5,j,k} = {}_lE^x_{i-0.5,j,k} + \frac{\Delta t}{\epsilon_{i,j,k}} \left(\frac{{}_{l_{0.5}}H^z_{i-0.5,j_{0.5},k} - {}_{l_{0.5}}H^z_{i-0.5,j-0.5,k}}{\Delta y} \right) $$

In the total field implementation of the source, one time dependent term is added to the field component of interest. Calling for simplicity this term Δs, E_x component at the excitation cell is updated by

$$ {}_{l_1}E^x_{i-0.5,j,k} = {}_lE^x_{i-0.5,j,k} + \frac{\Delta t}{\epsilon_{i,j,k}} \left(\frac{{}_{l_{0.5}}H^z_{i-0.5,j_{0.5},k} - {}_{l_{0.5}}H^z_{i-0.5,j-0.5,k}}{\Delta y} \right) + \Delta s $$

If the circuit and the position where the source is applied allow a conductance current to flow, this term actually can be seen as an impressed conductance current density given by

$$ \Delta s = \frac{\Delta t}{\epsilon} J^{n+1/2}_{cz} $$

On the other side, if a conductance current cannot flow, and thus only a displacement current can exist (e.g. the excitation of an empty cavity by applying a point source in

the middle), it actually works as if an additional term added to the E_x component. The modified discretized Maxwell equation can be written as:

$$_{l_1}E^x_{i-0.5,j,k} - {}_{l}E^x_{i-0.5,j,k} - \Delta s = \frac{\Delta t}{\epsilon_{i,j,k}} \left(\frac{{}_{l_{0.5}}H^z_{i-0.5,j_{0.5},k} - {}_{l_{0.5}}H^z_{i-0.5,j-0.5,k}}{\Delta y} \right)$$

That corresponds to the following analytical expression

$$\epsilon \frac{\partial E_x}{\partial t} - \frac{ds(t)}{dt} = \frac{\partial H_z}{\partial y}$$

Thus, the term added to the field component is the derivative of the waveform we want to obtain. As a conclusion, if the circuit allows a conductive current density to be supported, the desired waveform must be simply added to the field component at the location of the source; if only a displacement current can be supported by the structure, the derivative of the desired waveform must be added instead. In the FDTD simulations reported in this Chapter, a Gaussian pulse (nonzero DC content) was used as the excitation of the microstrip and stripline structures.The Gabor function

$$s(t) = e^{-((t-t_o)/(pw))^2} \sin(wt) \tag{2.20}$$

where $pw = 2 \cdot \frac{\sqrt{6}}{\pi(f_{max}-f_{min})}$, $t_o = 2pw$, $w = \pi(f_{min} + f_{max})$, was used as the excitation of the waveguide structures, since it has zero DC content. By modifying the parameters pw and w, the frequency spectrum of the Gabor function can be practically restricted to the interval $[f_{min}, f_{max}]$. As a result, the envelope of the Gabor function represents a Gaussian function in both time and frequency domain.

2.1.3 Linear Predictors

It is very common, especially for high-speed circuit structures, to use a cell size Δ that is dictated by the very fine dimensions of the circuit and is almost always much finer than

needed to resolve the smallest spectral wavelength propagating in the circuit. As a result, with the time step Δt bound to Δ by numerical stability considerations, FDTD simulations have to run for tens of thousands of time steps in order to fully evolve the impulse responses needed for calculating impedances, S-parameters or resonant frequencies. One popular way to avoid virtually prohibitive execution time has been to apply contemporary analysis techniques from the discipline of digital signal processing and spectrum estimation. The strategy is to extrapolate the electromagnetic field time waveform by 10:1 or more beyond the actual FDTD time window, allowing a very good estimate of the complete system response with 90% or greater reduction in computation time.

The class of linear predictors or autoregressive models (AR) is the most popular time series modeling approach due to the fact that an accurate estimate of the AR parameters can be derived by solving a set of linear equations. Though Prony's method [39] uses a sum of deterministic exponential functions to fit the data, the AR approach constructs a random model to fit a statistical data base to the second-order. Let's consider the FDTD impulse response $p+1$ equally spaced time samples after at time-step n

$$f|^{n}_{i,j,k}, f|^{n+1}_{i,j,k}, ..., f|^{n+p}_{i,j,k}$$

This time series is said to represent the realization of an AR process of order p if it satisfies the following relationship

$$f|^{n}_{i,j,k} = -a_1 f|^{n+1}_{i,j,k} - ... - a_p|f^{n+p}_{i,j,k} + q(n)$$

where the constants $a_1, ..., a_p$ are the AR parameters to be determined from the previous values of f and $q(n)$ is a white noise process whose variance has to be calculated before carrying out the extrapolation of f. Once the AR coefficients have been determined, the above equation permits the prediction of a new value of the time series from p known

previous values. Numerous different approaches for the evaluation of a_i have been proposed. Three of them of the most widely used: the covariance method, the forward-backward method and the nonlinear predictor. The covariance method involves setting up and solving a $p \times p$ linear system of equations

$$\begin{pmatrix} c_{ff}(1,1) & c_{ff}(1,2) & \dots & c_{ff}(1,p) \\ c_{ff}(2,1) & c_{ff}(2,2) & \dots & c_{ff}(2,p) \\ \vdots & \vdots & \ddots & \vdots \\ c_{ff}(p,1) & c_{ff}(p,2) & \dots & c_{ff}(p,p) \end{pmatrix} \begin{pmatrix} a_1 \\ a_2 \\ \vdots \\ a_p \end{pmatrix} = - \begin{pmatrix} c_{ff}(1,0) \\ c_{ff}(2,0) \\ \vdots \\ c_{ff}(p,0) \end{pmatrix}$$

where c_{ff} are the covariances defined by

$$c_{ff}(a,b) = \frac{1}{N-p} \sum_{n=p}^{N-1} (f|_{i,j,k}^{M+n-a} + f|_{i,j,k}^{M+n-b})$$

The above matrix can be solved with Cholesky decomposition. The order p of the model is very critical. The use of low order AR model causes the extrapolated waveform to attenuate quickly in a nonphysical manner. However, a high-order model can cause divergence problems in some cases because of statistical instabilities introduced by the large order. A common way to estimate p is the use of the Akaike Information criterion [39].

Forward and backward prediction methods avoid these problems by working directly with the time-domain data, rather than calculating the covariance functions of the data. It solves the following $(p+1) \times (p+1)$ linear system

$$\begin{pmatrix} r(0,0) & \dots & r(0,p) \\ r(1,0) & \dots & r(1,p) \\ \vdots & \ddots & \vdots \\ r(p,0) & \dots & r(p,p) \end{pmatrix} \begin{pmatrix} 1 \\ a_1 \\ \vdots \\ a_p \end{pmatrix} = - \begin{pmatrix} e_p \\ 0 \\ \vdots \\ 0 \end{pmatrix}$$

where for $0 \le a, b \le p$,

$$r(a,b) = \sum_{l=1}^{N-p} (f|_{i,j,k}^{M+p+l-b} f|_{i,j,k}^{M+p+l-a} + f|_{i,j,k}^{M+l+b} f|_{i,j,k}^{M+l+a})$$

$$e_p = \sum_{l=0}^{p} a_l r(0,l)$$

Marple [40] reported favorable results for the forward-backward method versus existing popular AR approaches such as the Burg and the Yule-Walker algorithms. It provided more accurate spectra and its order was much lower (close to 10% – 15% of the order of the other approaches). In addition, the forward-backward method is sufficiently robust and fast, though it's slightly less stable than the covariance methods.

2.2 Applications of F.D.T.D. to Planar Circuits

2.2.1 Open Circuit Design

The F.D.T.D. is initially applied in the design of a patch to be used as an open for the frequency range from 0-6 GHz (Fig.2.2). The dielectric constant of the substrate is $\epsilon_r = 5.46$ and the dielectric thickness is 0.5 mm. The feeding microstrip line (104.86875 mm) is excited by applying horizontally the Gaussian pulse $e^{-(\frac{t\Delta t - t_0}{pw})^2}$ with $pw = 8.333 \cdot 10^{-11}$, $dt = 2.9 \cdot 10^{-13} sec$, $t_0 = 3pw$. The excitation is on for $t = 0, .., t_{ab}$ time-steps with $t_{ab} = 6pw/\Delta t$. During this period, a PEC (perfect electric conductor) is placed behind the source at the vertical to the propagation plane. After t becomes larger than t_{ab}, this PEC is replaced with a 1st order Mur's absorber and the results converge after 30,000 time steps. After numerical experimentation, it is observed that the smallest vertical distance the top-plane 1st order Mur absorber can work efficiently equals to 30 times the substrate thickness. The front and the side absorbers are placed at a distance 49.35 mm and 7.7425 mm away from the patch respectively. In addition, the resonant frequency of the patch antenna should be such that it would not cause any problems for the operating frequency range. As a result, the almost square shape of the patch is maintained, but the dimensions

have to be appropriately modified. After using a mesh with cell size $dx = 0.1mm, dy = 0.20375mm, dz = 1.23375mm$, the optimum performance patch dimensions are found to be: 7.4025 mm (length) x 7.335 mm (width). (Fig. 2.3) demonstrates that the performance of the open is almost perfect since the reflection coefficient is larger than 0.97 for the whole frequency range.

2.2.2 Viahole Analysis

The viahole transition between two bended microstrips (Fig.2.4) is another geometry analyzed with F.D.T.D. The two microstrip lines are sandwiched on a dielectric substrate with $\epsilon_r = 7$ and the ground plane is placed in the middle of their distance. The top stripline is excited by applying horizontally a Gaussian pulse 0-20GHz. The discretization cell has dimensions $10\mu m \times 50\mu m \times 50\mu m$ and the time step is 31ps. A forward-backward predictor based on the first 4,300 steps with order $p = 27$ is employed to shorten the computation time of the 18,000 steps. The S-parameters are calculated (Fig.2.5). (Fig.2.6-2.7) showing the total E-field distribution along the top and bottom microstrip planes as well as along the ground plane at frequency 10 GHz, demonstrate the capability of the F.D.T.D. technique for an accurate spatial mapping of EM energy. Knowledge of the electric field intensity over a microwave circuit is extremely useful in directly identifying microwave circuit problems such as the existence of substrate modes, circuit radiation, device to device coupling. With tighter control over line lengths and losses that may be derived from electric field intensity (and phase), it may be possible to reduce the number of iterations during the design of MMIC's. Also, with a map of the electric field intensity above the substrate it would be possible to define low electric field regions around a device that could be used for placement of more circuitry, thus saving valuable chip real-estate.

2.2.3 Filter Design

(Fig.2.8) displays the geometry of a three stage coupled line filter fabricated on Duroid (ϵ_r=10.8, h=635 μm). All dimensions are in μm. The bandpass filter has a measured insertion loss of 2.0 dB in the passband from 8.0GHz to 10.5GHz and provides better than -25dB rejection at 12GHz. (Fig.2.9) shows that good agreement is achieved between measurements and FDTD calculations. The FDTD cell was chosen to be 52.9 μm for the vertical direction, 100 μm for the propagation direction and 25 μm for the direction normal to propagation. The time step is chosen to be 73 fsec to satisfy the stability criterion. These choices result in a grid with 140x234x448 cells. The 1st-order Mur's ABC is applied to the boundaries of the computational domain and superabsorber is enhanced at the input and output planes.

For wideband S-parameter extraction, a Gaussian pulse of 100 psec is used as the vertical microstrip excitation. The source is applied 5 cells inside the feedline in the propagation direction. Two simulations of pulse propagation along the microstrip line are made: one simulation for the filter and one for a 50 Ω microstrip through-line. The filter simulation gives the sum of the incident and the reflected waveforms and the through-line simulation gives only the incident waveform. By subtracting the incident from the total waveform, the reflected waveform at the input port is derived, which permits the calculation of the reflection coefficient S_{11}. The transmission coefficient S_{21} is given by the ratio of the Fourier transforms of the transmitted and the incident waveforms. The field probes are located at distances far enough from the filter discontinuities to eliminate evanescent waves.

2.2.4 Finite-Ground CPW Line Analysis

Coplanar waveguide with finite width ground planes (F.G.C.) (Fig.2.10) is characterized through measurements and F.D.T.D. to determine the optimum ground plane width. It is found that the characteristics (attenuation, effective permittivity) of the Finite Ground Coplanar Line are not dependent on the ground plane width if it is greater than twice the center conductor width, but less than $\lambda_d/8$ to keep the radiation losses and dispersion small. Also, the field distribution plots show that the power that propagates along the F.G.C. is concentrated on the surface of the substrate and the magnitude of this power is inversely dependent on the ground plane width. For small finite ground plane, there exists a significant amount of power on the surface of the substrate outside of the ground planes.This is demonstrated by the distribution of the normal-to-strip magnetic field H_y for lines with ground plane widths of B=25 and B=100 μm (Fig.2.11) and $S = W = 25\mu m$ on Si wafers of ϵ_r=11.9 and of thickness of 400 μm. The field is approximately twice as strong for the narrower ground plane, and decays away from the outer edge of the ground plane. As a conclusion, coplanar waveguide with a finite ground plane width as small as twice the center strip width may be used without adversely affecting the attenuation and permittivity of the lines.

The 2.5-D FDTD algorithm is used in the simulations. The dimensions of the Yee's cell are chosen to be 2.5μm for the direction parallel to the coplanar line and 25μm for the normal direction. The time step is 7.45 ps and the 1st-order Mur's ABC is applied to the top, left and right boundaries of the computational domain. The top absorber is placed at a distance equal to 15 times the dielectric thickness and the side absorbers at a distance equal to 7 times the gap of the coplanar line. A delta function with even (odd) symmetry is used for the excitation of the horizontal electric field across the gaps. The propagation

constant used in the simulations has the value 100.

2.3 Application of FDTD to Waveguide Structures

2.3.1 FDTD and Waveguide Probe Structures

Significant attention is being devoted now-a-days to the analysis and design of waveguide-probes [41] – [58]. Many different configurations of waveguide probes are used either to sense the modal propagation inside the waveguides or to mount active elements inside cavities. The common design objective is to maximize the coupling between the probe and the waveguide over the widest possible frequency range. The characterization of waveguide-probes demands an accurate calculation of the scattering parameters over a wide band of frequencies. In this Section, FDTD is used in the RF characterization of diode mounting and waveguide probe structures. The waveguide probe geometry analyzed in this section is shown in (Fig.2.12). The probe is fed by a shielded coplanar line and has the shape of a patch. It is inserted into the waveguide through a slot and it is supported by a dielectric substrate which is not connected to any waveguide wall. The dimensions of the probe as well as the thickness and the dielectric constant of the substrate are of critical importance to achieve broadband coupling and low reflection loss.

Usually more than one mode are excited inside the rectangular waveguide, making the numerical simulation tedious when using the conventional absorbing boundary conditions (ABC's) [12], [37]. These ABC's specify the tangential electric field components at the boundary of the mesh in such a way that waves are not reflected. For TEM structures the waves will be normally incident to the boundaries of the mesh, thus requiring a simple approximate absorbing boundary condition, Mur's first order absorbing boundary condition

[12]. The assumption of normal incidence is not valid for the fringing fields propagating tangential to the walls. For this reason, for non-TEM structures the superabsorption boundary condition [37] is used in conjunction with Mur's absorber for better accuracy. This combination results in an improvement with respect to the reflection coefficient. However, despite the use of superabsorber, when the frequency range of interest becomes large, significant reflections occur, even if there is only one propagating mode. To overcome this difficulty, numerous approaches have been proposed. The technique of diakoptics [45], initially developed for TLM [46] and later for FDTD [47], used in conjunction with the modal Green's function has been successfully applied to TLM [48], [49], [50]. In the analogous FDTD approach [51], the fields are decomposed into incident and reflected wave amplitudes ("TLM" approach) and the characteristic impedance is used for the calculation of the reflected wave amplitudes. A similar absorber based on a circuit (voltage-current) approach has been proposed by F. Moglie et al. [52]. Due to the field decomposition, both of these approaches are characterized by higher memory and execution time requirements than the conventional FDTD absorbers.

In contrast to these approaches, the Diakoptics technique is derived directly from Maxwell's equations following an approach similar to [53] and only total field values are used. The absorber proposed is based on the analytic Green's functions of the waveguide modes. These Green's functions are used to calculate the tangential electric (for TE modes) and magnetic (for TM modes) field components located at the boundary of the mesh. The tangential fields one cell away from the boundary are decomposed into modes and for each mode the tangential field at the boundary is calculated by taking the convolution of the mode amplitude and the Green's function for this mode with respect to time. For simplicity, we consider only TE propagating modes, while the approach for the TM propagating modes

is dual and straightforward. A similar approach based on numerical Green's functions has been presented in [54]. This approach requires the numerical evaluation of each mode's Green's function that is obtained by running an FDTD simulation for each mode and/or the application of the FD^2 principles. On the contrary, the proposed absorber evaluates analytically the Green's functions by applying the Inverse Fourier transform to the well-known expressions in frequency domain. Thus, similar accuracy is obtained without a significant computational overhead.

2.3.2 Novel Absorber Description

For the sake of simplicity in the presentation, we consider only $TE^z_{m,n}$ modes, propagating in the z-direction, and assume that the waveguide cross-section is located on the xy-plane. For the tangential magnetic field adjacent to the boundary of the mesh at $k = n_z - 0.5$, eqs.(2.13),(2.14) for non-lossy material are simplified to

$$ {}^{l+1/2}H^x_{i,j+1/2,n_z-0.5} - {}^{l-1/2}H^x_{i,j+1/2,n_z-0.5} = \frac{\Delta t}{\mu_o}\left(\frac{{}^{l}E^y_{i,j+1/2,n_z} - {}^{l}E^y_{i,j+1/2,n_z-1}}{\Delta z}\right) \qquad (2.21) $$

$$ {}^{l+1/2}H^y_{i+1/2,j,n_z-0.5} - {}^{l-1/2}H^y_{i+1/2,j,n_z-0.5} = \frac{\Delta t}{\mu_o}\left(\frac{{}^{l}E^x_{i+1/2,j,n_z-1} - {}^{l}E^x_{i+1/2,j,n_z}}{\Delta z}\right) \quad . \qquad (2.22) $$

The absorber is used to calculate the tangential electric field components at the boundary of the mesh ($k = n_z$) from the tangential electric field components one cell away from the boundary plane ($k = n_z - 1$). The tangential magnetic field components $H^x_{i,j,n_z-0.5}$ and $H^y_{i,j,n_z-0.5}$ are updated using eqs.(2.21)–(2.22) and depend both on the values of the electric field components calculated by Yee's FDTD scheme and on the values of the electric field components calculated by the absorber. Using eq.(2.15), the normal magnetic field components at $k = n_z$, $H^z_{i+1/2,j+1/2,n_z}$, may be calculated from $E^x_{i+1/2,j,n_z}$ and $E^y_{i,j+1/2,n_z}$. Thus, for the $TE^z_{m,n}$ modes, the normal magnetic field components are also determined so

that the reflection from the boundary is minimized. A similar argument can be used for the position of the absorber for the $TM^z_{m,n}$ modes.

In order to derive the absorber based on the analytic Green's functions, we start with the wave equation in cartesian coordinates

$$\nabla^2 F - \frac{1}{c^2}\frac{\partial^2 F}{\partial t^2} = (\frac{\partial^2}{\partial x^2} + \frac{\partial^2}{\partial y^2} + \frac{\partial^2}{\partial z^2} - \frac{1}{c^2}\frac{\partial^2}{\partial t^2})F = 0 \tag{2.23}$$

where F indicates the tangential electric field components $E^x(x,y,z,t)$, $E^y(x,y,z,t)$ and c represents the velocity of light. The tangential electric field components in the waveguide can be written as

$$E^x(x,y,z,t) = \sum_{m=0}^{\infty}\sum_{n=1}^{\infty} E^x_{m,n}(z,t)\cos(\beta_{x,m}x)\sin(\beta_{y,n}y) \tag{2.24}$$

$$E^y(x,y,z,t) = \sum_{m=1}^{\infty}\sum_{n=0}^{\infty} E^y_{m,n}(z,t)\sin(\beta_{x,m}x)\cos(\beta_{y,n}y) \tag{2.25}$$

where

$$\beta_{x,m} = \frac{m\pi}{a},\ \beta_{y,n} = \frac{n\pi}{b} \quad , \tag{2.26}$$

$m,\ n \in$ N, a×b are the waveguide cross section area and $E^x_{m,n}(z,t)$ and $E^y_{m,n}(z,t)$ are the modal coefficients given by

$$E^x_{m,n}(z,t) = \frac{2(2-\delta_{m,0})}{a\,b}\int_0^a\int_0^b E^x(x,y,z,t)\cos(\frac{m\pi}{a}x)\sin(\frac{n\pi}{b}y)\,dxdy \tag{2.27}$$

$$E^y_{m,n}(z,t) = \frac{2(2-\delta_{n,0})}{a\,b}\int_0^a\int_0^b E^y(x,y,z,t)\sin(\frac{m\pi}{a}x)\cos(\frac{n\pi}{b}y)\,dxdy \quad . \tag{2.28}$$

In eqs. (2.27) and (2.28), $\delta_{m,0}$ is the Kroenecker delta given by

$$\delta_{m,0} = \begin{cases} 1 & \text{for } m = 0 \\ 0 & \text{for } m \neq 0 \end{cases} \quad .$$

In view of the above, eq.(2.23) yields

$$\frac{\partial^2 F_{m,n}(z,t)}{\partial z^2} - \left(\beta_{x,m}^2 + \beta_{y,n}^2 + \frac{1}{c^2}\frac{\partial^2}{\partial t^2}\right) F_{m,n}(z,t) = 0 \quad , \tag{2.29}$$

where $F_{m,n}(z,t) = E_{m,n}^{x,y}(z,t)$.

Applying the Fourier transformation ($\bar{F}_{m,n}(z,\omega) = \mathcal{F}\{F_{m,n}(z,t)\}$) with the angular frequency ω=2πf, the wave equation is transformed into frequency domain, and eq.(2.29) yields

$$\frac{\partial^2 \bar{F}_{m,n}(z,\omega)}{\partial z^2} - \left(\beta_{x,m}^2 + \beta_{y,n}^2 - \frac{\omega^2}{c^2}\right) \bar{F}_{m,n}(z,\omega) = 0 \quad . \tag{2.30}$$

Following a procedure analogous to [53] and assuming a given amplitude $\bar{F}_{m,n}((n_z-1)\Delta z,\omega)$ of the $TE_{m,n}^z$ mode at $k = n_z - 1$, we obtain

$$\begin{aligned}\bar{F}_{m,n}(z,\omega) \;=\; & \frac{e^{j\beta_{z,mn}(z-(n_z-1)\Delta z)}}{2}\left(\bar{F}_{m,n}((n_z-1)\Delta z,\omega) - \frac{j}{\beta_{z,mn}}\left.\frac{\partial \bar{F}_{m,n}(z,\omega)}{\partial z}\right|_{z=(n_z-1)\Delta z}\right) \\ & + \frac{e^{-j\beta_{z,mn}(z-(n_z-1)\Delta z)}}{2}\left(\bar{F}_{m,n}((n_z-1)\Delta z,\omega) + \frac{j}{\beta_{z,mn}}\left.\frac{\partial \bar{F}_{m,n}(z,\omega)}{\partial z}\right|_{z=(n_z-1)\Delta z}\right)\end{aligned} \tag{2.31}$$

with

$$\beta_{z,mn} = \begin{cases} \frac{1}{c}\sqrt{\omega^2 - \omega_{c,mn}^2} & \text{for } \omega \geq \omega_{c,mn} \\ -j\frac{1}{c}\sqrt{\omega_{c,mn}^2 - \omega^2} & \text{for } \omega \leq \omega_{c,mn} \end{cases} \quad , \tag{2.32}$$

where $\omega_{c,mn} = c\sqrt{(\beta_{x,m})^2 + (\beta_{y,n})^2}$ is the cutoff frequency of the $TE_{m,n}^z$ mode. The function $\bar{F}_{m,n}(z,\omega)$ has exponentially increasing and decreasing solutions with respect to z for $\omega \leq \omega_{c,mn}$. The exponentially increasing solutions have to vanish for $z \to \infty$ for $\omega \leq \omega_{c,mn}$, thus eq.(2.31) yields

$$\bar{F}_{m,n}((n_z-1)\Delta z,\omega) = \frac{j}{\beta_{z,mn}}\left.\frac{\partial \bar{F}_{m,n}(z,\omega)}{\partial z}\right|_{z=(n_z-1)\Delta z} \tag{2.33}$$

and

$$\bar{F}_{m,n}(z,\omega) \;=\; \bar{G}_{TE^z_{m,n}}(z-(n_z-1)\Delta z,\omega)\;\bar{F}_{m,n}((n_z-1)\Delta z,\omega) \qquad , \qquad (2.34)$$

where $\bar{G}_{TE^z_{m,n}}(z,\omega) = e^{-\jmath\beta_{z,mn}z}$ is the Green's function for the $TE^z_{m,n}$ modes. By satisfying eq.(2.33), $\bar{F}_{m,n}((n_z-1)\Delta z,\omega)$ results in an outward propagating solution with respect to z for $\omega \geq \omega_{c,mn}$ only. Thus, computation of $\bar{F}_{m,n}(z,\omega)$ according to eq.(2.34) requires no backward propagating solution.

Applying the convolution theorem [55], eq.(2.34) in time-domain reduces to

$$F_{m,n}(z,t) \;=\; \int_{-\infty}^{+\infty} G_{TE^z_{m,n}}(z-(n_z-1)\Delta z, t-t')\;F_{m,n}((n_z-1)\Delta z,t')\;dt' \qquad (2.35)$$

where $G_{TE^z_{m,n}}(z,t) = \mathcal{F}^{-1}\{\bar{G}_{TE^z_{m,n}}(z,\omega)\}$. As a result, the tangential electric field components at the boundary of the mesh at k=n_z are expressed in the form:

$$F_{m,n}(n_z\Delta z,t) \;=\; \int_{-\infty}^{+\infty} G_{TE^z_{m,n}}(\Delta z, t-t')\;F_{m,n}((n_z-1)\Delta z,t')\;dt' \qquad . \qquad (2.36)$$

Following a procedure similar to [68], $F_{m,n}((n_z-1)\Delta z,t')$ can be expanded in a series of triangle basis functions in time-domain. Inserting this expansion in eq.(2.36) and sampling $F_{m,n}(n_z\Delta z,t)$ using delta functions with respect to time, we obtain

$$F_{m,n}(n_z\Delta z, l\Delta t) \;=\; \sum_{l'=-\infty}^{\infty} {}_{l-l'}G_{TE^z_{m,n}}\;F_{m,n}((n_z-1)\Delta z, l'\Delta t) \qquad , \qquad (2.37)$$

where the discrete FDTD Green's function ${}_lG_{TE^z_{m,n}}$ may be calculated analytically by

$${}_lG_{TE^z_{m,n}} = \int_{-\infty}^{+\infty} G_{TE^z_{m,n}}(\Delta z, l\Delta t - x)\;g(x)\;dx = \frac{1}{2\pi}\int_{-\infty}^{+\infty} \bar{G}_{TE^z_{m,n}}(\Delta z,\omega)\;\bar{g}(\omega)\;e^{j\omega l\Delta t}\;d\omega \quad (2.38)$$

and $x = t' - l'\Delta t$. The triangle basis function is given by:

$$g(x) = \begin{cases} 1-|\frac{x}{\Delta t}| & \text{for } |x| \leq \Delta t \\ \\ 0 & \text{for } |x| \geq \Delta t \end{cases} \qquad .$$

and its Fourier transform is:

$$\bar{g}(\omega) = \mathcal{F}\{g(t)\} = \Delta t \left[\frac{\sin(\frac{\omega \Delta t}{2})}{\frac{\omega \Delta t}{2}} \right]^2 \quad . \tag{2.39}$$

Due to causality, we have

$${}_lG_{TE^z_{m,n}} = 0 \qquad \text{for } l < 0 \tag{2.40}$$

and as a result,

$$F_{m,n}(n_z \Delta z, l\Delta t) \;=\; \sum_{l'=-\infty}^{l} {}_{l-l'}G_{TE^z_{m,n}} \; F_{m,n}((n_z - 1)\Delta z, l'\Delta t) \quad , \tag{2.41}$$

which represents the mathematical formulation of the Diakoptics technique.

As an example, let's consider the $TE^z_{1,0}$ mode. For the y-component ${}_lE^y_{i,j,n_z}$ of the tangential electric field at $k = n_z$, eqs.(2.25) and (2.41) yield

$${}_lE^y_{i,j,n_z} = \sum_{l'=-\infty}^{l} {}_{l-l'}G_{TE^z_{1,0}} \; E^y_{1,0}((n_z - 1)\Delta z, l'\Delta t) \; \sin(\pi i \Delta x/a) \quad , \tag{2.42}$$

where $E^y_{1,0}((n_z - 1)\Delta z, l'\Delta t)$ may be calculated from eq.(2.28) . The discrete FDTD Green's function ${}_{l-l'}G_{TE^z_{1,0}}$ is given by

$${}_{l-l'}G_{TE^z_{1,0}} = \frac{1}{2\pi} \int_{-\infty}^{+\infty} \bar{G}_{TE^z_{1,0}}(\Delta z, \omega) \; g(\omega) \; e^{j\omega(l-l')\Delta t} d\omega \tag{2.43}$$

with $g(\omega)$ given by eq.(2.39) and

$$\bar{G}_{TE^z_{1,0}}(\Delta z, \omega) = e^{-j\beta_{z,10}\Delta z} \quad , \tag{2.44}$$

where $\beta_{z,10}$ is calculated by eq.(2.32) for $m = 1, n = 0$.

Absorber Evaluation

To validate the absorber presented herein, we calculate the magnitude of the reflection coefficient in frequency domain for the waveguide structure shown in (Fig.2.13). The xy-plane of the waveguide at $z = 0$ is short-circuited and the ABC is utilized to calculate the

electric field components in the xy-plane at $z = 2880\Delta z$. The waveguide cross-section is $47.6mm \times 22mm$ and the cell size is given by $\Delta x = 4.76mm$, $\Delta y = 1.1mm$ and $\Delta z = 0.4mm$. We use a mesh of the size $10 \times 20 \times 2880$ and run the simulation for 25000 time-steps. All conductors are assumed to be perfect electric conductors.

We simulate the wave propagation for frequencies between $3.1GHz$ and $7.4GHz$ so that three different modes are excited, $TE^z_{1,0}, TE^z_{2,0}$ and $TE^z_{0,1}$. To accommodate the presence of these three modes, we use a superposition of three Gaussian pulses multiplied with the corresponding mode patterns at $z = 2840\Delta z$ to provide the correct excitation. For the calculation of the reflection coefficient ρ, we use the formula

$$\rho = \frac{E_t - E_{ref}}{E_{ref}} \quad , \tag{2.45}$$

where E_t is the tangential electric field probed at $z = 2860\Delta z$ and E_{ref} is the tangential electric field probed at the same position of a semi-infinitely long waveguide (no effect from reflections from the ABC) with the same cross section. The semi-infinite length of the waveguide is approximated by $6700\Delta z$ and the tangential electric field is probed again at $z = 2860\Delta z$. The evaluated ABC is replaced by a PEC. The length of this reference waveguide is chosen such as no reflections from the PEC plane return to the probe position for the 25000 steps of simulation. The absorber based on the analytic Green's function is compared to the 1st-order Mur's ABC coupled with the superabsorption condition. The effective dielectric constant [37] for the superabsorber is chosen to 0.407.

For practical applications, the infinite summation in eq.(2.41) has to be approximated by a finite number of terms T. This approximation corresponds to a truncation of the discrete FDTD Green's function according to

$${}_lG_{TE^z_{m,n}} = 0 \qquad \text{for } l > T \quad , \tag{2.46}$$

where T represents the length of the discrete FDTD Green's function with respect to time. We obtain

$$F_{m,n}(n_z,t) = \sum_{l'=l-T}^{l} {}_{l-l'}G_{TE^z_{m,n}}\, F_{m,n}(n_z-1,l') \quad . \tag{2.47}$$

and eq.(2.42) can be written as

$${}_{l}E^{y}_{i,j,n_z} = \sum_{l'=l-T}^{l} {}_{l-l'}G_{TE^z_{1,0}}\, E^{y}_{1,0}(n_z-1,l')\, \sin(\pi i \Delta x/a) \quad . \tag{2.48}$$

The reflection coefficient is minimized if we truncate the discrete FDTD Green's function at its zeros. In (Fig.2.14), results for the reflection coefficient for the $TE^z_{1,0}$ mode are shown for three different values of T, 616, 1127 and 2646. The graph for the 1st-order Mur ABC with the Superabsorption condition is symbolized with (sup). The larger the length T of the discrete FDTD Green's function, the more effective the absorber becomes. For $T = 2646$, the amplitude of the reflection coefficient is less than -40dB for almost the whole frequency range. Thus, the ABC based on the analytic Green's function is effective in a much wider frequency range than the super-absorbing 1st-order Mur ABC. This is true even when we improve the performance of the superabsorbing 1st-order Mur ABC by applying it to each waveguide mode separately. Similar results were observed for the reflection coefficient for the $TE^z_{2,0}$ and $TE^z_{0,1}$ modes.

The PML absorber [13] achieves a comparable behavior for a wide frequency range. For example, the length $T = 2646$ of the discrete $TE^z_{1,0}$ Green's function offers a reflection coefficient very close to that of a PML layer of 4 cells with $R = 10^{-5}$ (Fig.2.15) and $T = 4161$ has similar performance with a PML layer of 8 cells with $R = 10^{-5}$. Generally, considering larger values of the length T is equivalent to increasing the number of the PML cells. Nevertheless, the memory requirements of the proposed absorber are much lower than the memory requirements for the PML absorber. For each mode, the convolution of eq.(2.42)

requires the storage of the T terms of the modal Green's function and of the T previous values of the mode amplitude at the $z = (n_z - 1)\Delta z$. Thus, the extra memory requirement of the Green's function absorber is $2 \times T$ real numbers per mode. A PML layer of N cells to the z-direction requires $M = 6 \times N \times n_x \times n_y$ new variables, where $n_x \times n_y$ is the grid size for the waveguide cross-section. Generally $M \gg 2 \times T$, especially for large grids. Due to the details of the waveguide probe structure analyzed in the next section, the waveguide cross-section grid has a size of 477×220 cells. That means that even a PML layer of 4 cells to the z-direction requires the storage of $M = 2,518,560$ new variables !! Using an absorber based on Green's functions with length $T = 2646$ for the $TE^z_{1,0}$, $T = 2238$ for the $TE^z_{2,0}$ and $T = 2412$ for the $TE^z_{0,1}$, only 14,592 new variables have to be stored (0.58% of the PML memory requirements). As a result, the Green's function-based ABC offers a significant economy in memory while maintaining similar accuracy with the PML absorber.

Waveguide Probe Structure Characterization

The FDTD technique coupled with the proposed waveguide absorber is used in the RF characterization of the waveguide probe geometry shown in (Fig.2.12). The probe in the shape of a rectangular patch is fed by a shielded 50Ω coplanar line and is inserted into the waveguide through a slot. The dielectric substrate carrying the probe is not connected to any waveguide wall. This type of probe can be used as a coupler to a rectangular waveguide or as a diode mounting structure. The dimensions of the probe as well as the substrate thickness and the dielectric constant of the substrate are of critical importance in optimizing coupling to the waveguide.

In our simulations, we try to optimize the thickness of the dielectric substrate carrying a probe which is 3.6mm wide. The dielectric constant of the substrate is assumed to be

ϵ_r=12 (GaAs). The width of the dielectric substrate entering the waveguide is 5.8mm and its thickness is limited to less than 2mm. The probe is designed to feed a WR-187 rectangular waveguide and for this reason, excitation is provided on the coplanar feedline by a Gabor function which covers the frequency range of 3.1 GHz to 7.4 GHz. For the simulated frequency range, three different modes are excited inside the waveguide, $TE^z_{1,0}$, $TE^z_{2,0}$ and $TE^z_{0,1}$, with the cutoff frequencies 3.15 GHz, 6.30 GHz and 6.82 GHz respectively. The mesh used in the FDTD simulation consists of 480x477x52 cells with a time step of $\Delta t = 0.31425ps$. The simulation runs for 20,000 time steps to achieve converging results. The absorber discussed previously is used to absorb simultaneously all propagating modes of the waveguide for the simulated frequency range.

To characterize the probe performance for different dielectric thicknesses, the magnitude of the reflection coefficient $|S_{11}|$ for the dominant $TE^z_{1,0}$ mode is calculated. For validation purposes, the calculated results are compared to data derived by the FEM (Finite Element Method) assuming a probe width of 3.6mm and a dielectric thickness of 2.0 mm (See (Fig.2.16)). For the FDTD simulation, the waveguide absorber based on the Green's functions for the three propagating waveguide modes is used at the terminal plane. For the FEM simulation, an artificial absorber depending on frequency and angle of incidence is applied to terminate the waveguide. For the whole operating frequency range (3.1-7.5 GHz) the performance of both absorbers is comparable and the results show very good agreement.

The dimensions of the shield of the coplanar feedline are chosen to be 5.8mm x 3.8mm, such as only the CPW dominant mode can propagate and the field patterns are not disturbed by the side walls in the frequency range of the simulation. In this way, the superabsorption condition can be applied effectively at the input plane of the feedline.

The performance of the probe has been evaluated for three different dielectric thicknesses

2.0mm, 1.2mm and 0.0 mm, with the last value corresponding to a microwave probe printed on a dielectric membrane [57]. Results in terms of the reflection coefficient are shown in (Fig.2.17). As it can be observed from this figure, the value of the reflection coefficient reduces over a large frequency range and shows symmetrical behavior round the center design frequency as the dielectric thickness approaches zero. The electric field (E) and magnetic field (H) distributions for zero dielectric thickness are plotted for t = 6,000 time steps across the probe structure symmetry plane (Fig.2.18) and across the coplanar feedline plane (Fig.2.19) and represent the transmitted and the reflected energy respectively.

The reflection coefficient of the Si-membrane printed probe has been calculated for four different patch widths 3.6mm, 9.8mm, 11.4mm and 13.0mm and the results are shown in (Fig.2.20). From this figure, it can be concluded that the width of 9.8mm offers the most symmetrical behavior for the frequency of operation. The reflection coefficient for widths larger than 9.8mm is much smaller than that of 3.6mm for most of the simulated frequencies except a small region round 4.6 GHz. Nevertheless, the widths of 11.4mm and 13.0mm offer no significant improvement over the width of 9.8mm.

Another geometry parameter of the Si-membrane printed probe that has been investigated is the distance of the probe patch from the short circuit of the waveguide. Lengths of 8.8mm, 10.4mm, 12.0mm and 13.6mm have been used and the results are plotted in (Fig.2.21) it can be noticed that the value of 12.0mm offers the best performance in terms of the value and the bandwidth of the reflection coefficient.

The FDTD results derived by using the absorber presented in Section III.2 have been validated by comparing to experimental data. The probe has dimensions 13.2mm x 4.3mm on a dielectric substrate with thickness 2.1mm, width 28.7mm and ϵ_r=13. The probe has been inserted in a WR229 waveguide and is located at a distance of 14.7mm from the top

surface short circuit. For the FDTD absorber there have been used T=2871 time steps. The performance of the probe has been evaluated for the frequency range of 3.3-4.6GHz and the results are shown in (Figs.2.22–2.23). The agreement between the FDTD and the experimental results is good especially in the frequency range of the optimum performance of the probe. The abrupt variation in S_{21} observed for the higher frequencies in the experiment is maybe due to calibration or other reasons related to the experimental setup.

2.4 Conclusion

The finite-difference time-domain method has been used to analyze planar circuits and waveguide probe structures. For the analysis, a waveguide absorber based on analytic Green's functions has been developed. This absorber is characterized by a better performance in accuracy and computational efficiency than the super-absorbing 1st-order Mur ABC and by a better performance in memory requirements than the PML absorber. The scattering parameters of the probe structures have been calculated and the results have been verified by comparison with FEM and experimental data. The influence of critical geometrical parameters on the probe performance has been investigated and optimized.

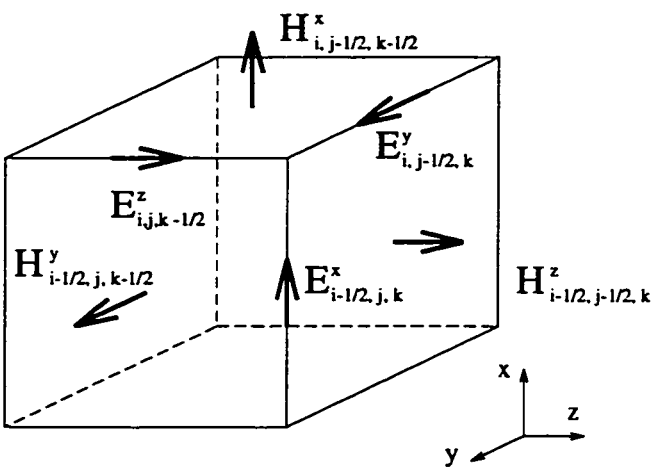

Figure 2.1: Yee's FDTD cell.

Figure 2.2: Patch Geometry to be used as Open.

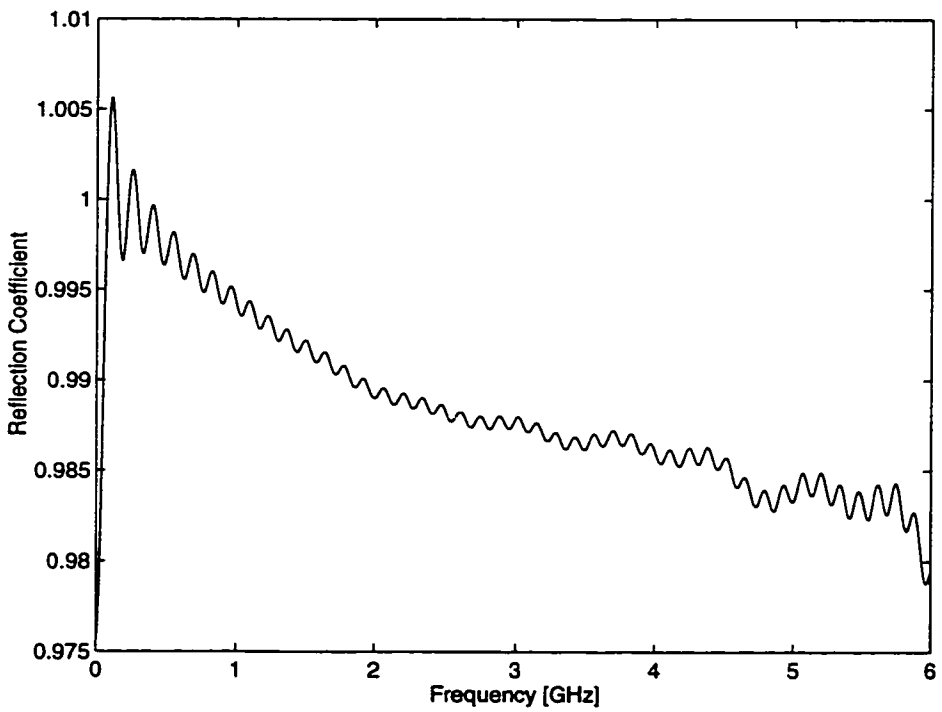

Figure 2.3: Reflection Coefficient of the Open.

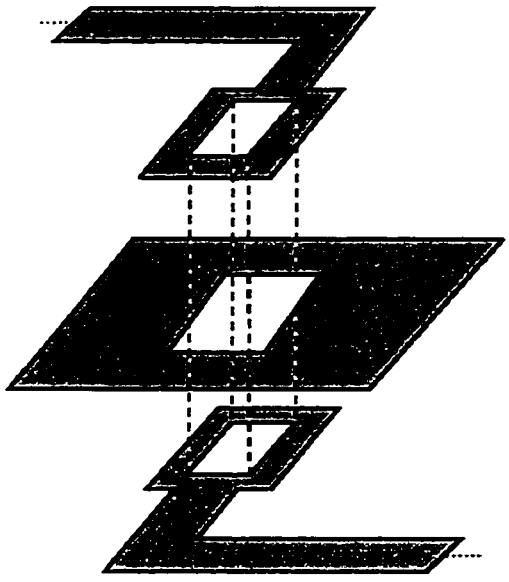

Figure 2.4: Viahole Structure.

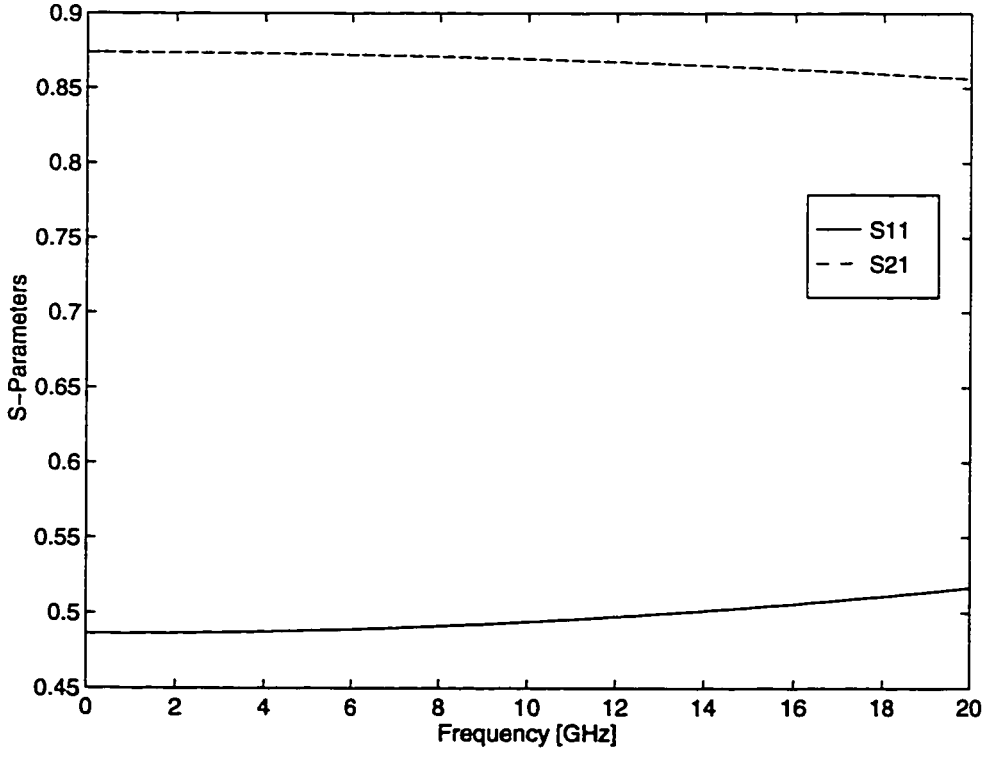

Figure 2.5: S-Parameters of the Viahole.

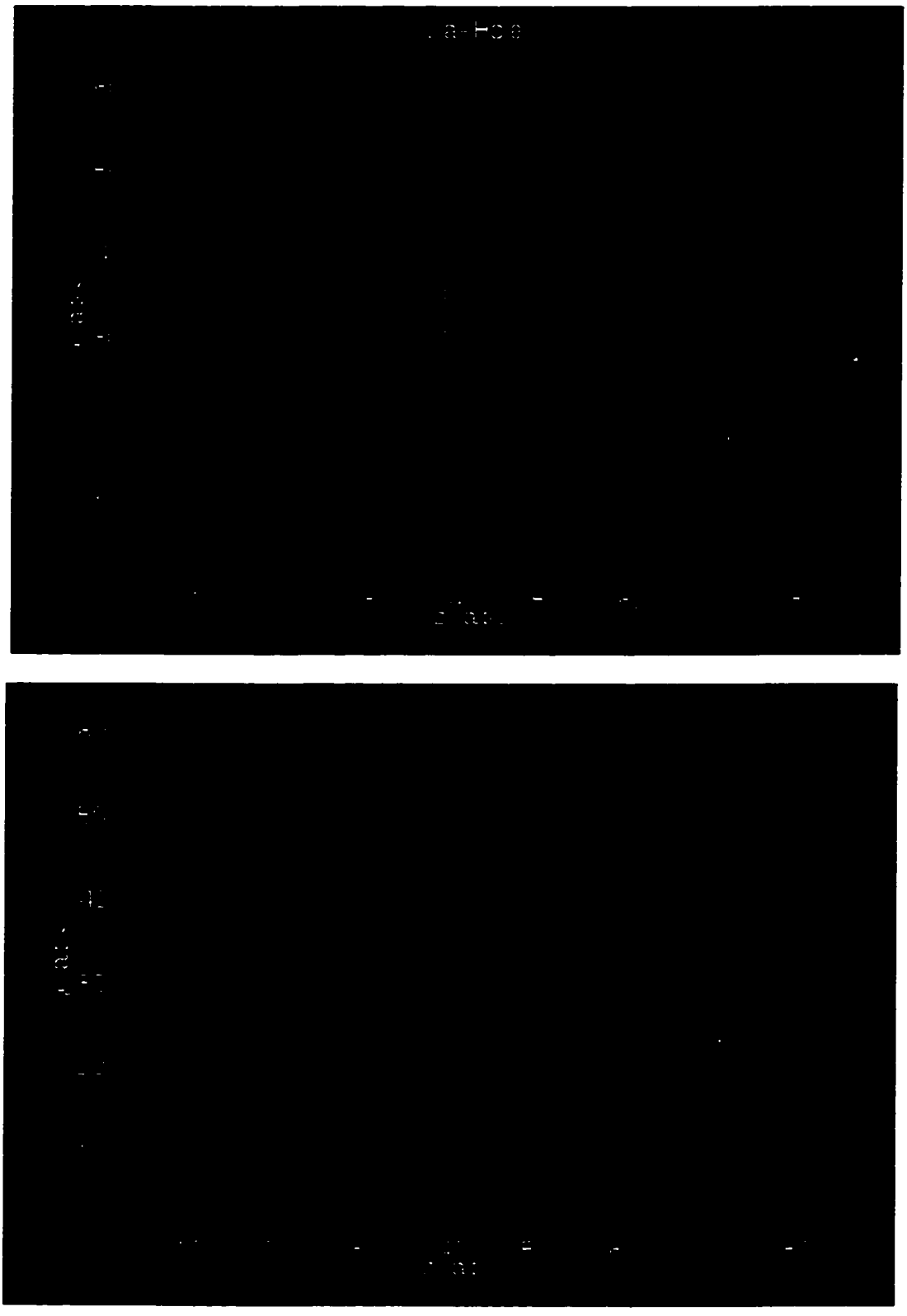

Figure 2.6: E-Distribution across Top Viahole (Top), Middle Ground Plane (Bottom).

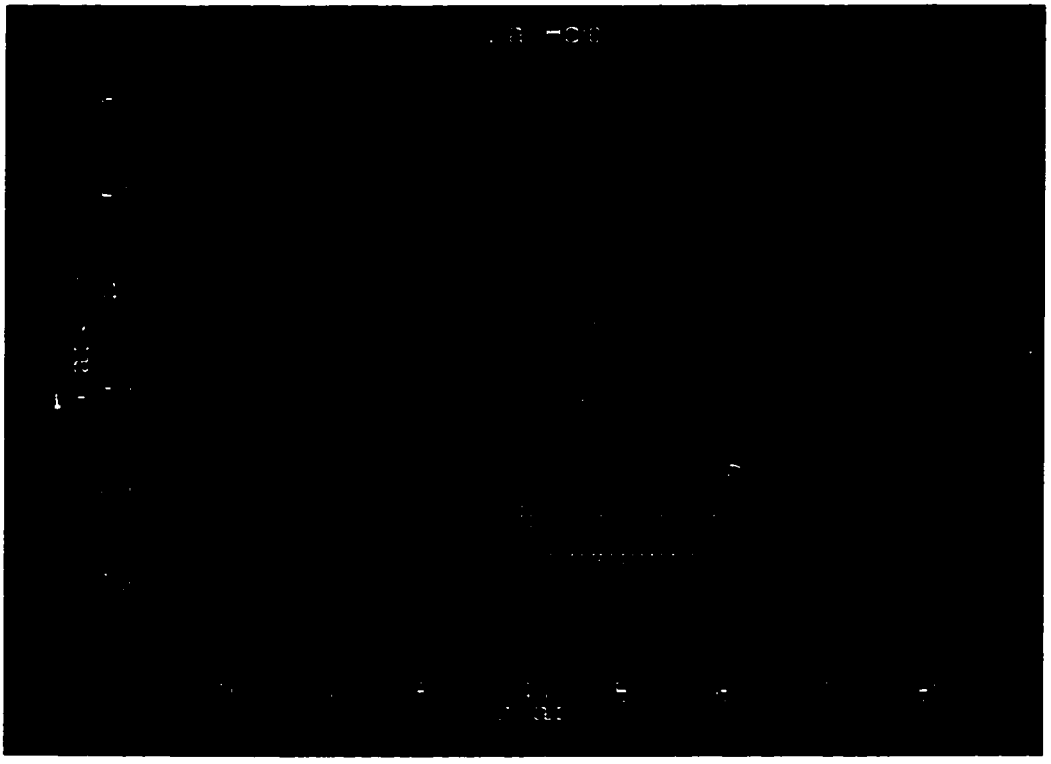

Figure 2.7: E-Distribution across Bottom Viahole.

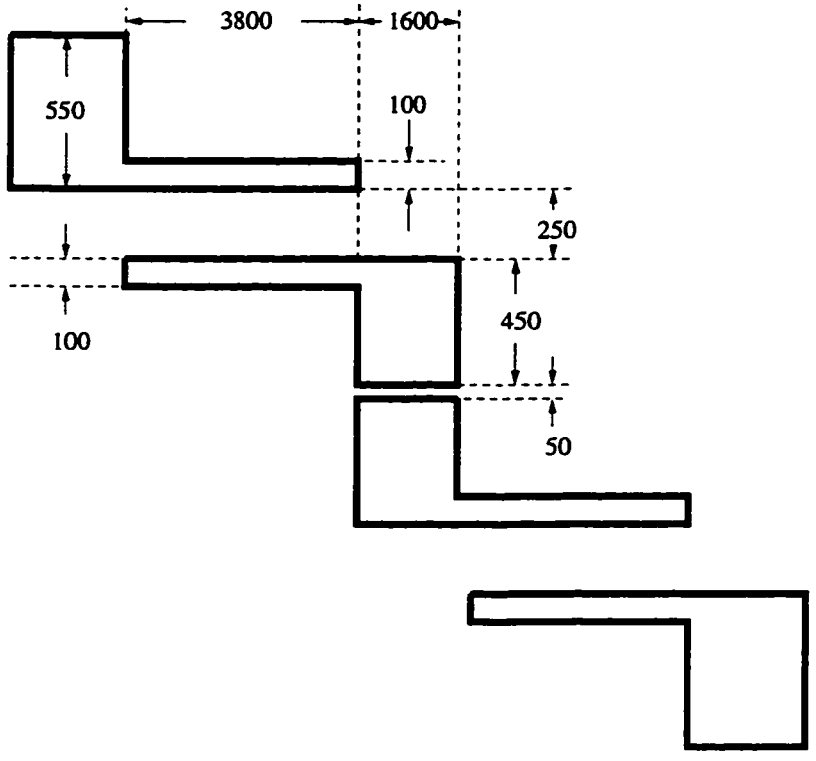

Figure 2.8: Coupled Line Filter Geometry.

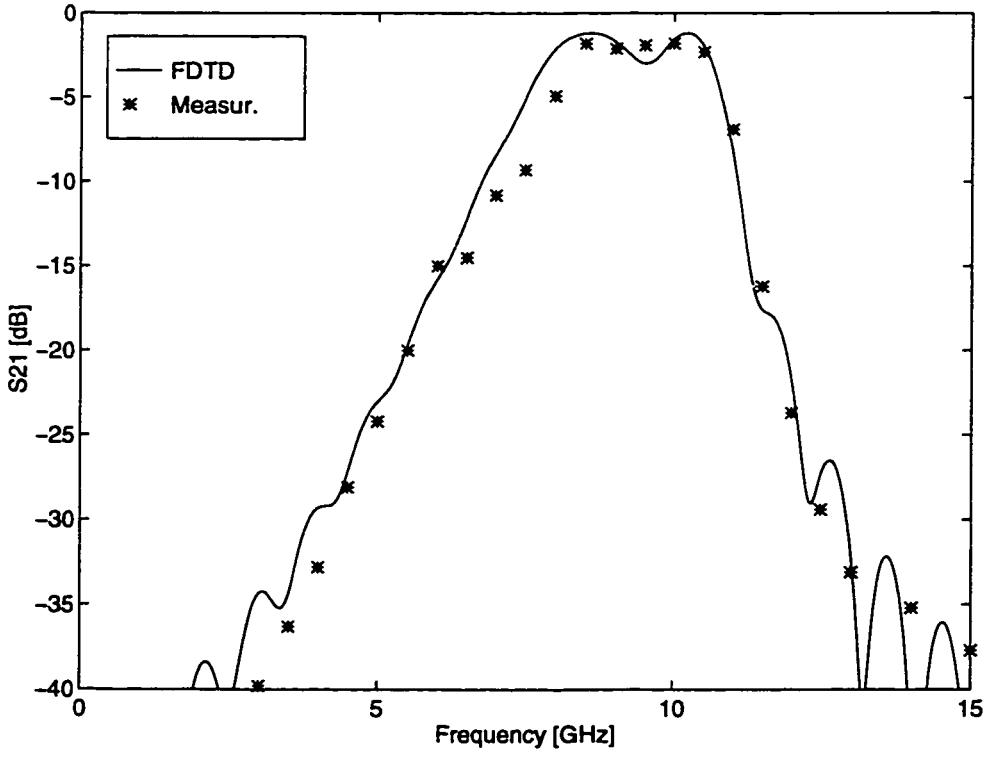

Figure 2.9: Coupled Line Filter S_{21}.

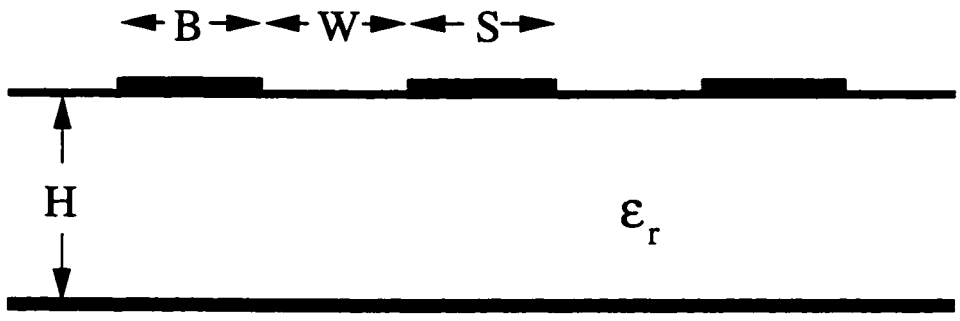

Figure 2.10: Coplanar waveguide with finite width ground planes (F.G.C.).

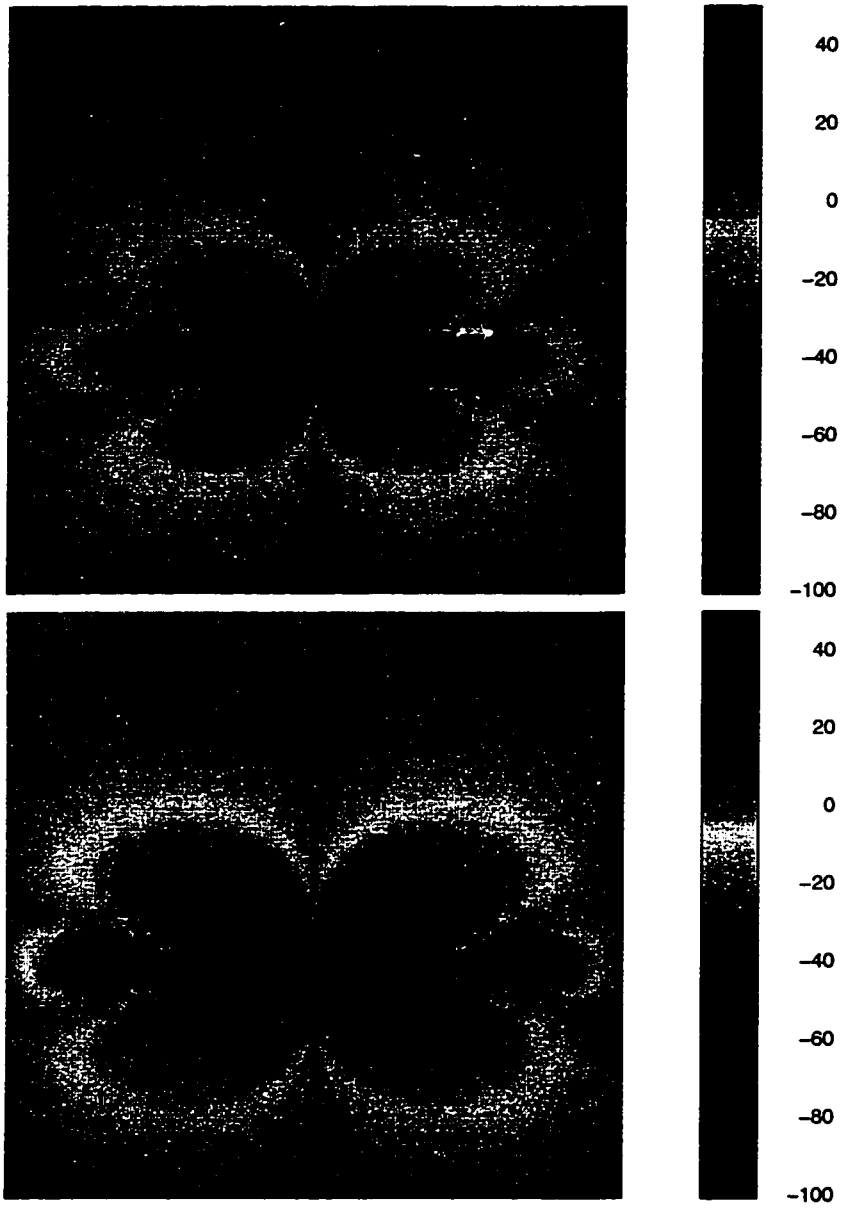

Figure 2.11: Normal H-Distribution (Log) for B=25 μm (up), 100 μm (bottom).

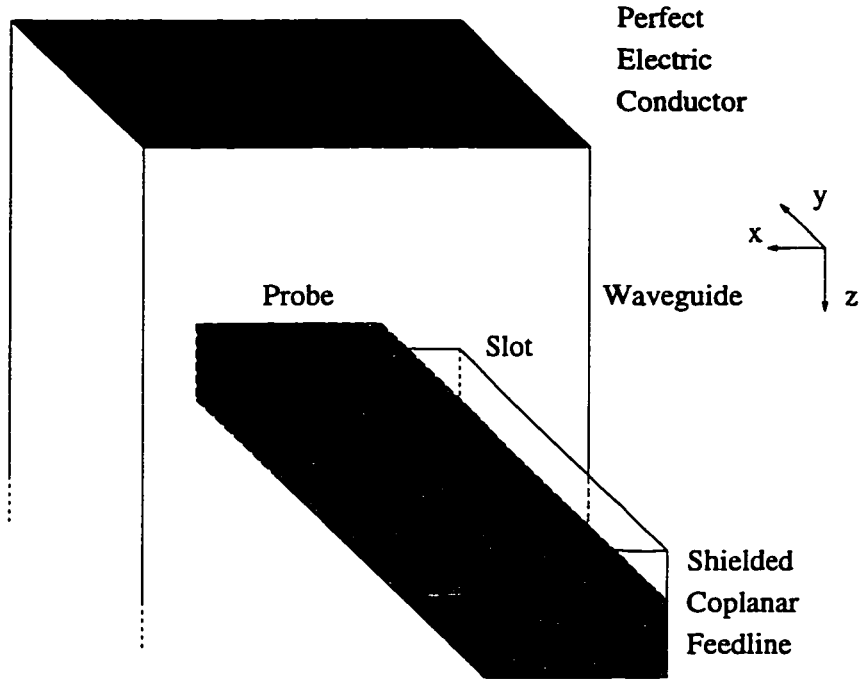

Figure 2.12: Waveguide probe structure.

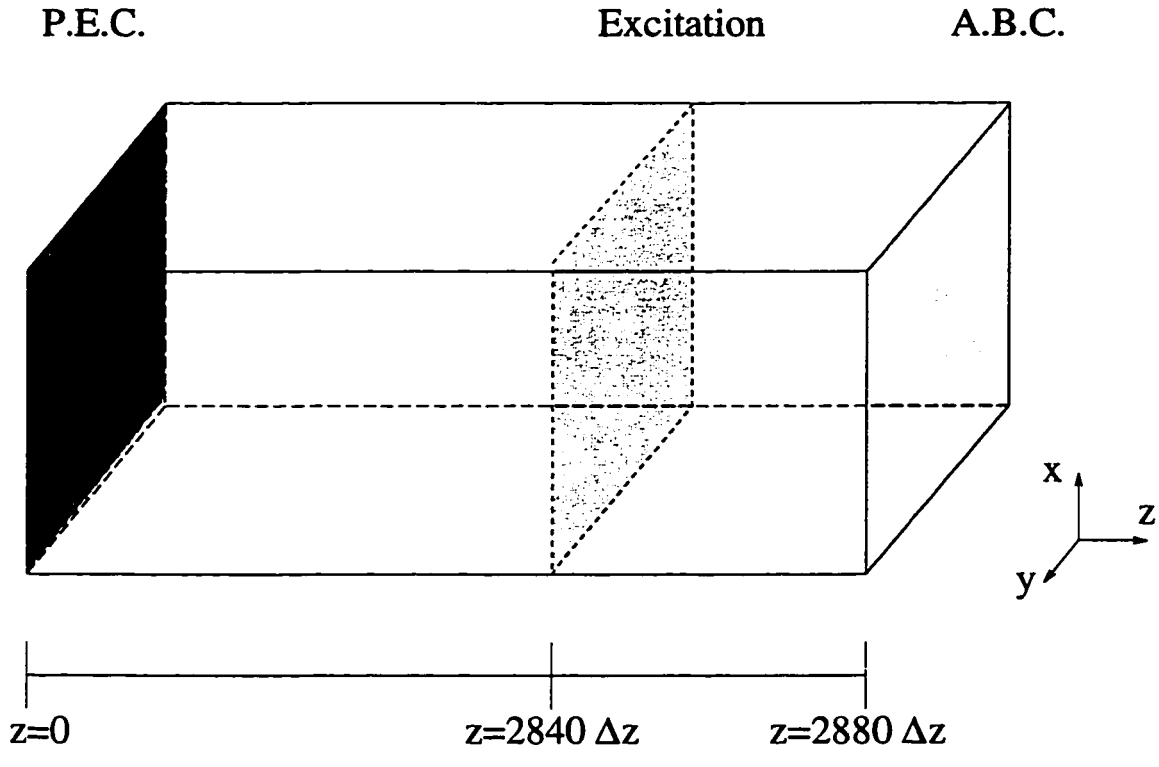

Figure 2.13: Waveguide Test Structure.

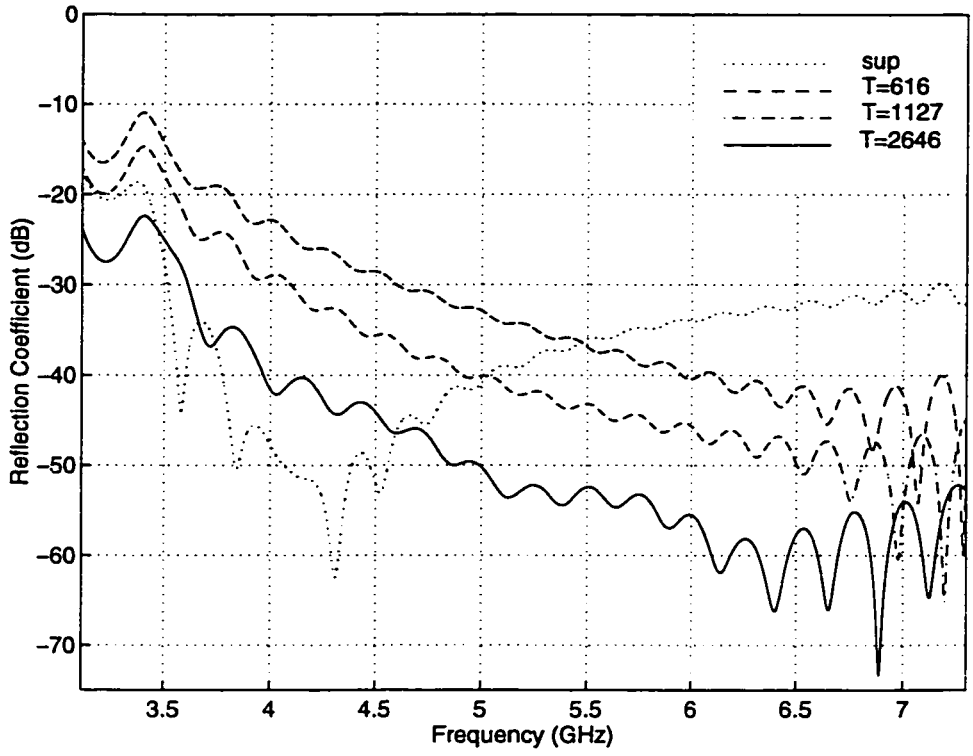

Figure 2.14: Reflection coefficient for the $TE^z_{1,0}$ mode.

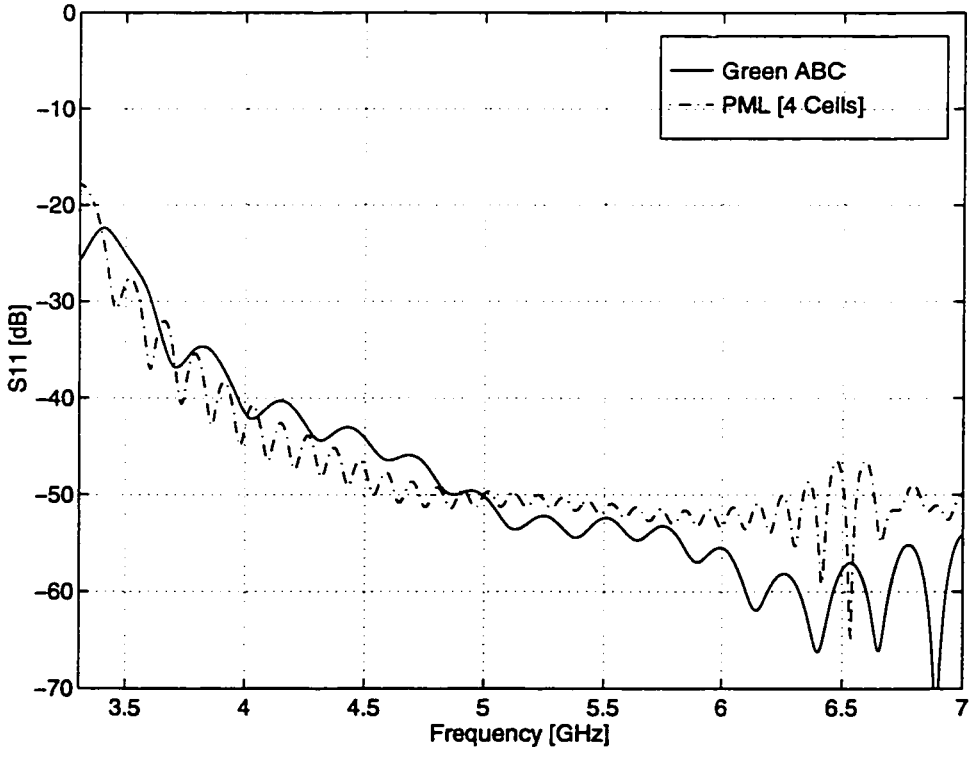

Figure 2.15: Comparison of Green's Function ABC and PML.

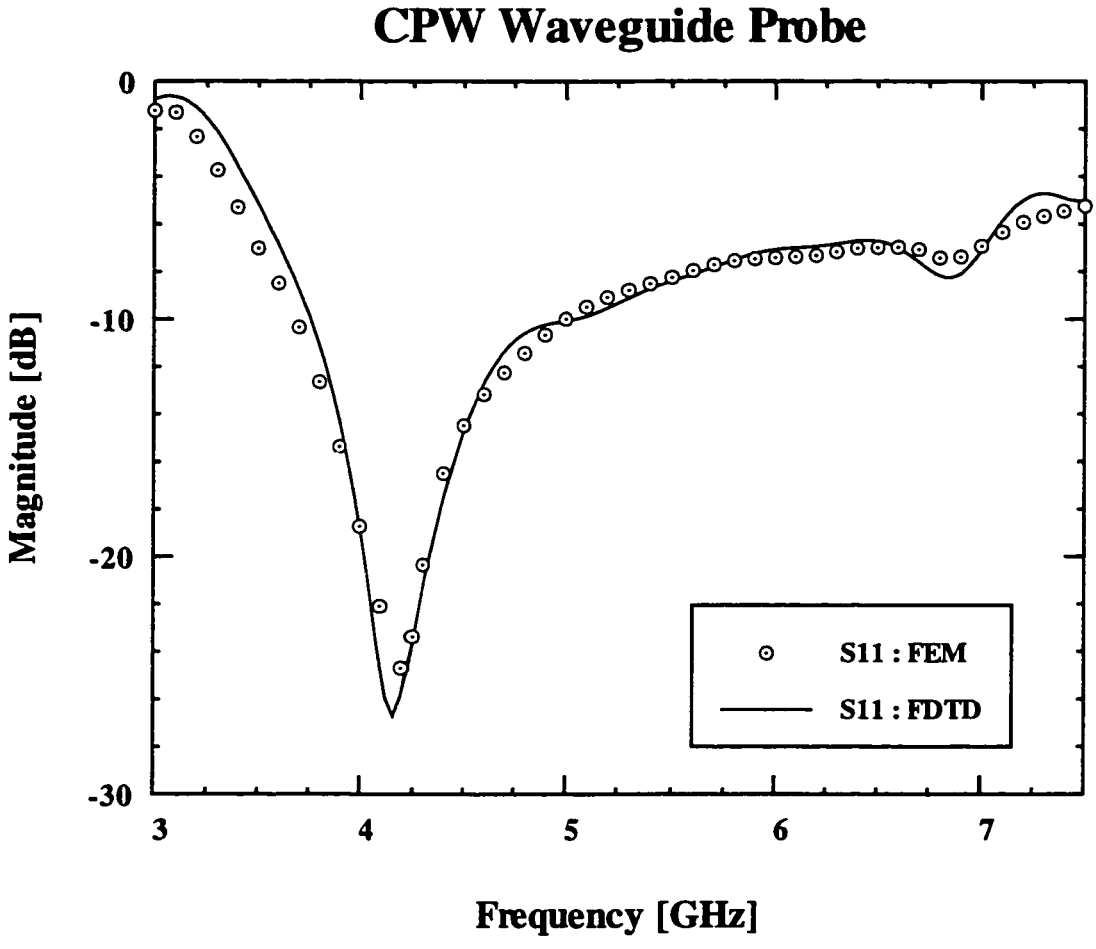

Figure 2.16: Validation Data for the Reflection Coefficient.

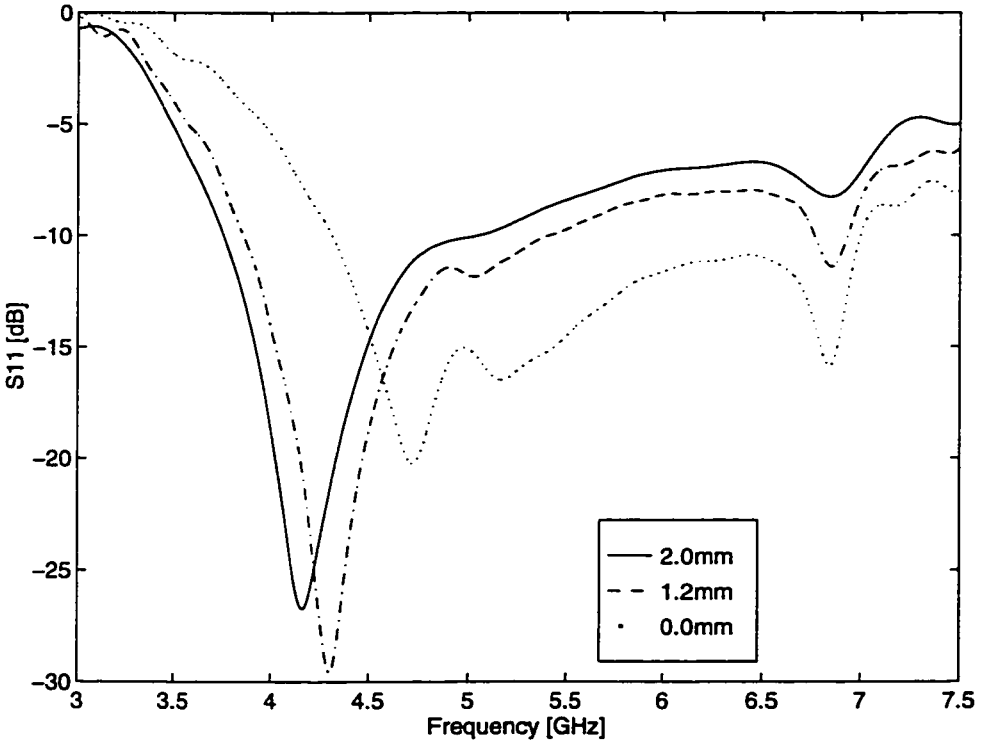

Figure 2.17: Reflection Coefficient for different Dielectric Thicknesses.

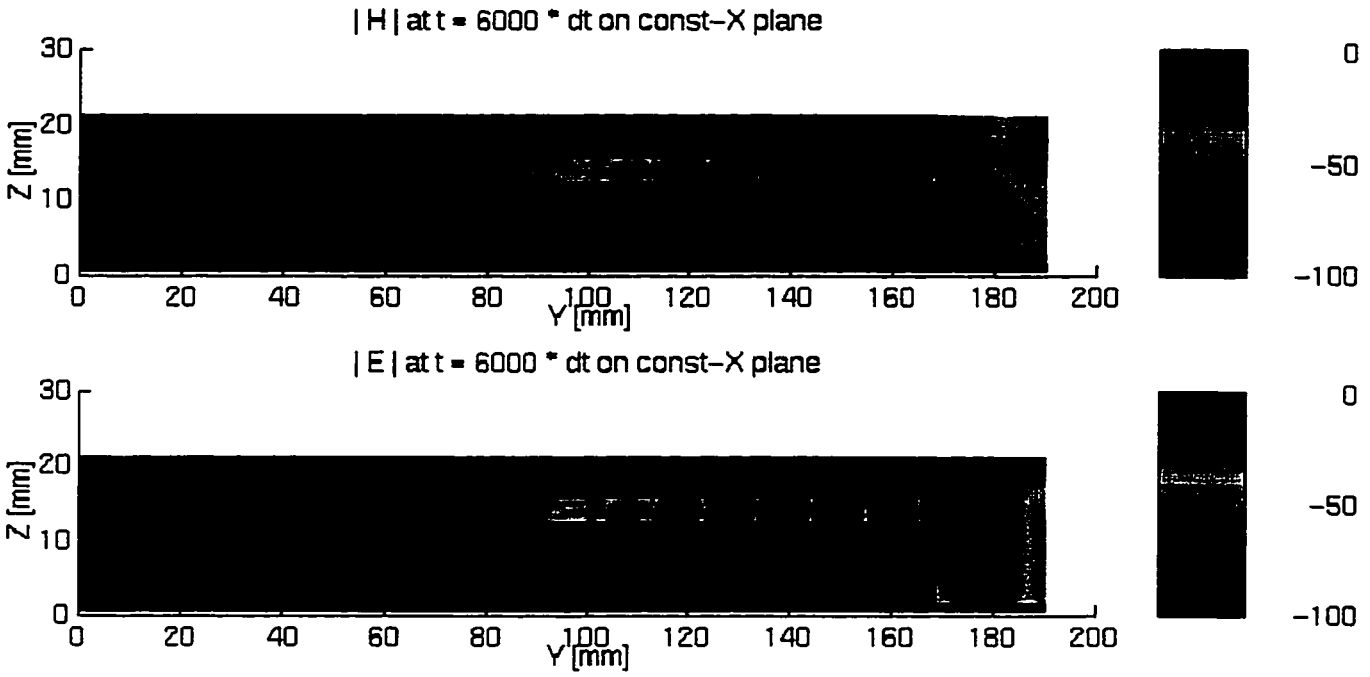

Figure 2.18: E- and H-field Distributions across the Probe Structure Symmetry Plane.

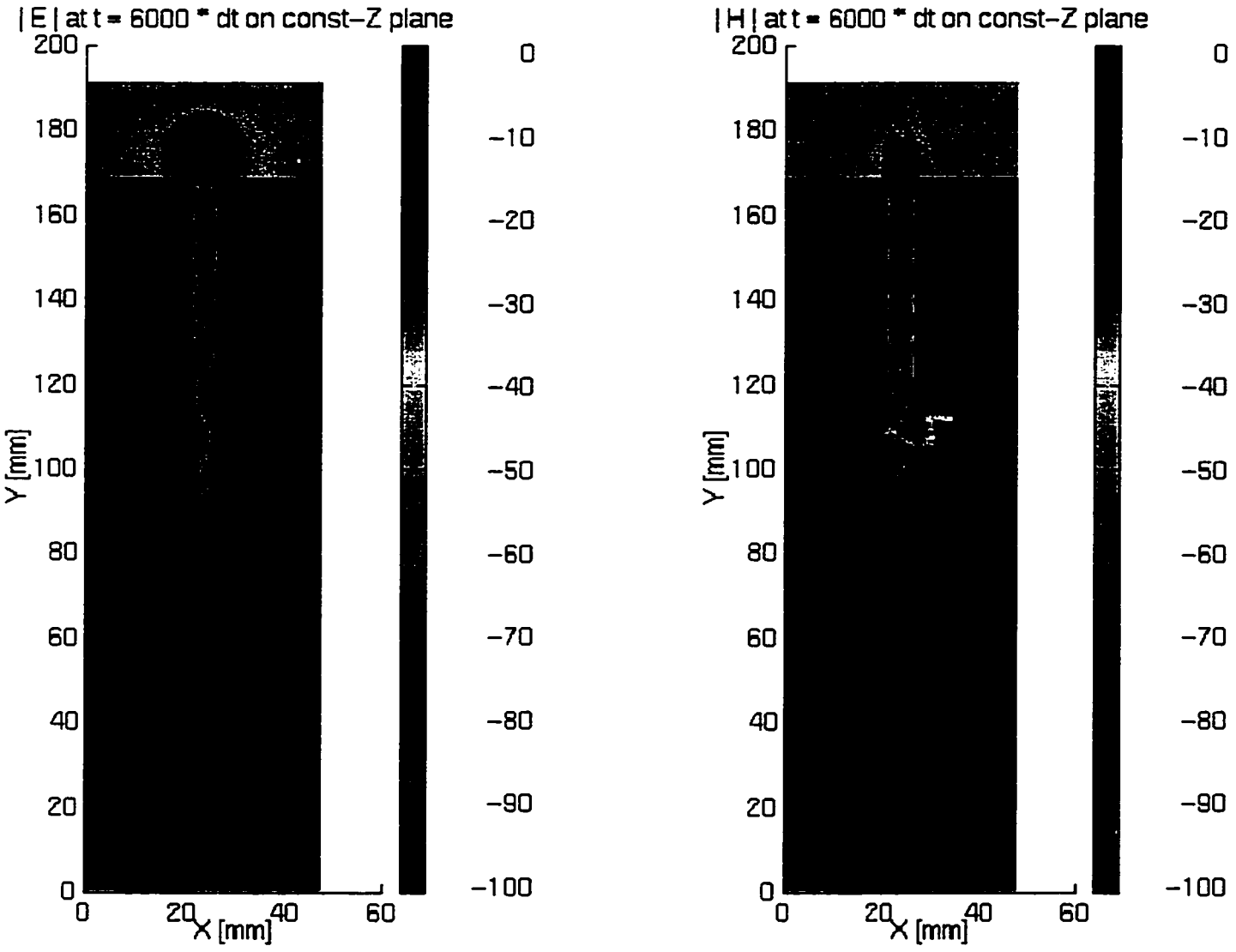

Figure 2.19: E- and H-field Distributions across the Coplanar Feedline Plane.

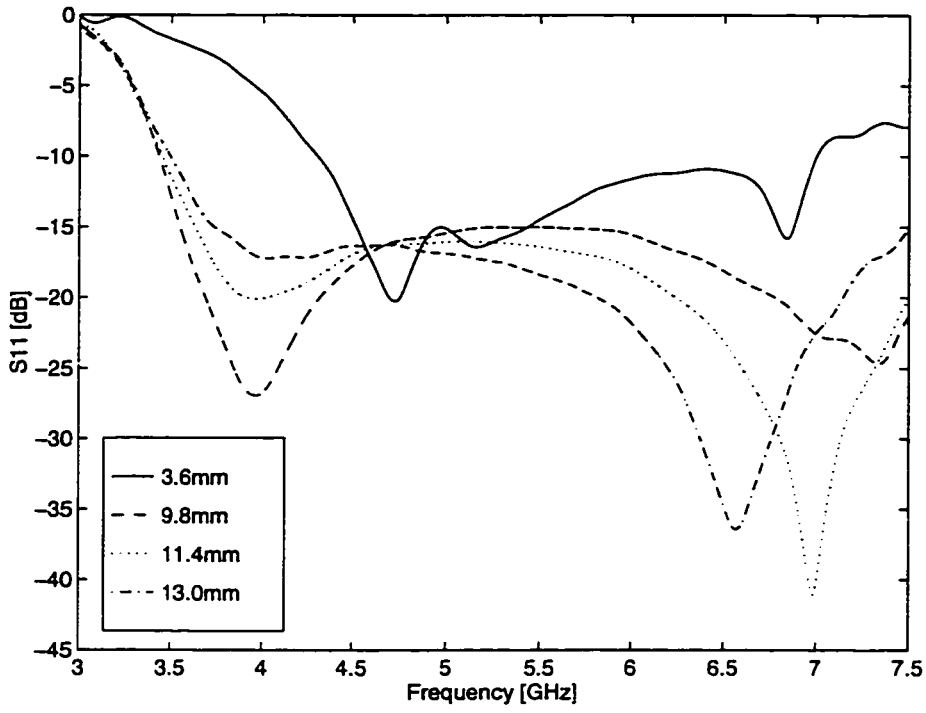

Figure 2.20: Reflection Coefficient for different Patch Widths.

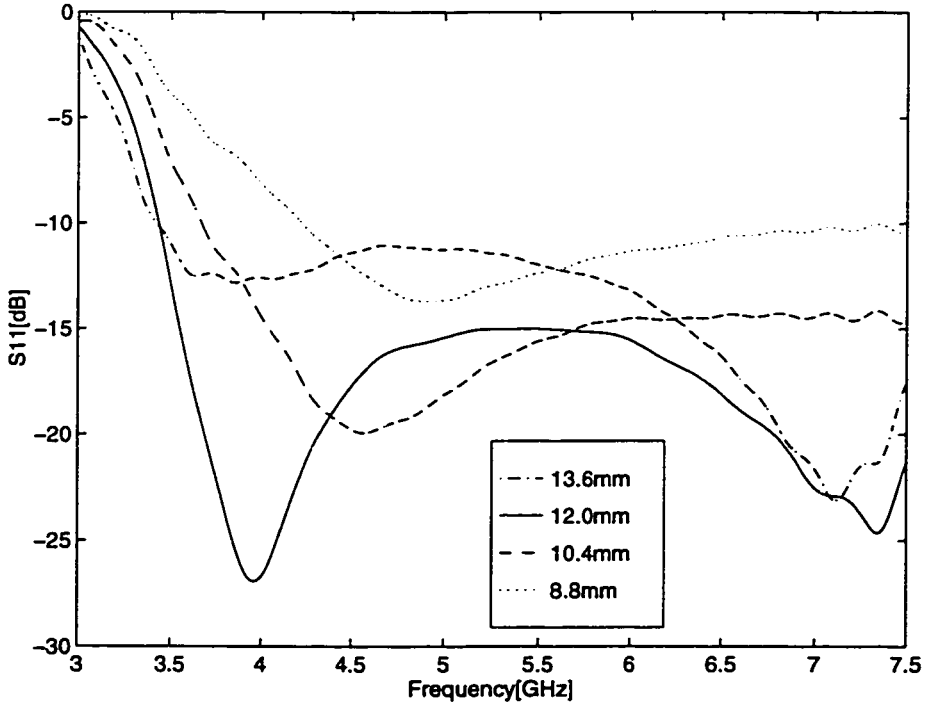

Figure 2.21: Reflection Coefficient for different Distances from the Top Surface Short-Circuit.

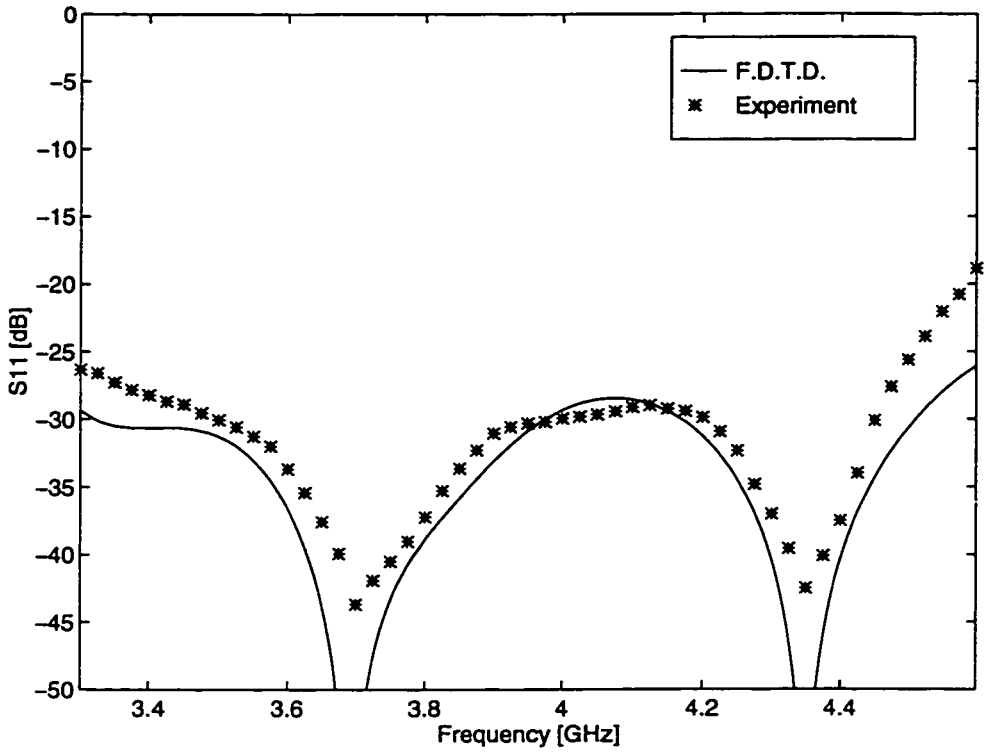

Figure 2.22: Experimental Validation for S_{11}.

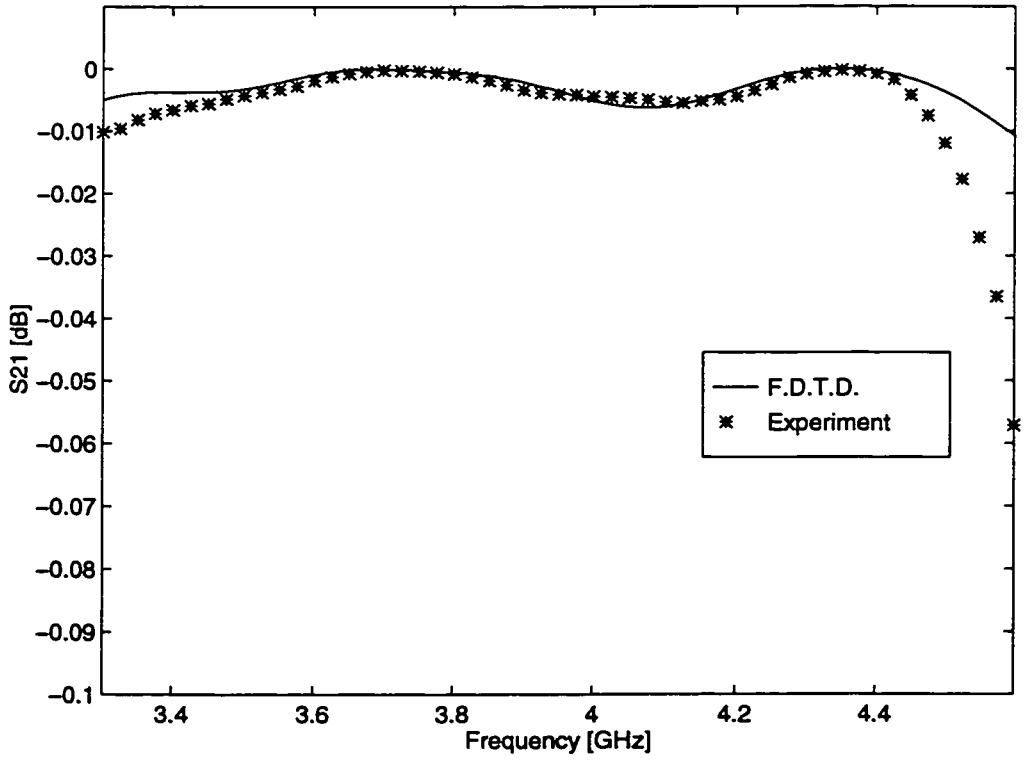

Figure 2.23: Experimental Validation for S_{21}.

CHAPTER 3

Development of New Time-Domain Schemes with Higher Order Basis Functions

3.1 Introduction

Significant attention is being devoted now-a-days to the analysis and design of various types of printed components for microwave applications. To understand high-frequency effects and incorporate them into the design process, there is a compelling need to implement full-wave solutions during the modeling process. There has been a variety of full wave techniques developed for this purpose, with many of them available commercially. Despite the wealth of available codes, many problems in electromagnetics and specifically in circuit and antenna problems have been left untreated due to the complexity of the geometries and the inability of the existing techniques to deal with the requirements for large size and high resolution due to the fine but electrically important geometrical details. The straightforward use of existing discretization methods suffers from serious limitations due to the required substantial computer resources and unrealistically long computation times. As a result, during the past thirty years the available techniques are almost incapable of dealing with the needs of technology leading into a quest for fundamentally different

modeling approaches.

The use of multiresolution analysis in time domain has shown that Yee's FDTD scheme can be derived by applying the method of moments for the discretization of Maxwell's equations [56] using pulse basis functions for the expansion of the unknown fields. The use of scaling and wavelet functions as a complete set of basis functions is called multiresolution analysis and demonstrates that Multiresolution Time-Domain (MRTD) schemes are generalization s to Yee's FDTD and can extend the capabilities of the conventional FDTD by improving computational efficiency and substantially reducing computer resources.

3.2 Fundamentals on Multiresolution Analysis

A multiresolution analysis consists of a sequence of successive approximation spaces V_j. More precisely, the closed subspaces V_j satisfy

$$\ldots V_2 \subset V_1 \subset V_0 \subset V_{-1} \subset V_{-2} \subset \ldots \tag{3.1}$$

with

$$\overline{\bigcup_{j \in Z} V_j} = L^2(R) \ (density) \tag{3.2}$$

$$\bigcap_{j \in Z} Vj = \{0\} \ (separation) \tag{3.3}$$

There exist many ladders of spaces satisfying the above conditions that have nothing to do with "multiresolution"; the multiresolution aspect is a consequence of the additional requirement

$$f(x) \in V_j \leftrightarrow f(2^j x) \in V_0 \ (scaling) \tag{3.4}$$

That is, all the spaces are scaled versions of the central space V_0. Another feature that we

require from multiresolution analysis is the invariance of V_0 under integer translations

$$f(x) \in V_0 \leftrightarrow f(x-n) \in V_0, \forall n \in \mathbf{Z} \tag{3.5}$$

Because of Eq.(3.4), this implies that if $f(x) \in V_j$, then $f(x-2^j n) \in V_j$ for all $n \in \mathbf{Z}$. Finally, we require that there exists $\phi \in V_0$ such that $\{\phi_{0,n}, n \in \mathbf{Z}\}$ is an orthonormal basis in V_0, where for all $j, n \in Z, \phi_{j,n}(x) = 2^{-j/2}\phi(2^{-j}x - n)$. As a result, $\{\phi_{j,n}, n \in \mathbf{Z}\}$ is an orthonormal basis for V_j for all $j \in \mathbf{Z}$; that is,

$$< \phi_{j,m}, \phi_{j,n} >= \delta_{m,n}, \;\; m, n \in Z \tag{3.6}$$

where δ notates the Kronecker symbol

$$\delta_{m,n} = \begin{cases} 1 & m = n \\ 0 & elsewhere \end{cases}$$

Throughout this Chapter, there will be used the following notations for the *inner product* and *norm* for the space $L^2(R)$:

$$< f, g >= \int_{-\infty}^{\infty} f(x)\overline{g(x)}dx$$

$$||f|| = ||f||_2 =< f, f >^{1/2}$$

The basic idea of the multiresolution analysis is that whenever a collection of closed subspaces satisfy Eqs.(3.1)–(3.5), then there exists an orthonormal wavelet basis $\{\psi_{j,n}, n \in \mathbf{Z}\}$ of $L^2(\mathbf{R})$, $\psi_{j,n}(x) = 2^{-j/2}\psi(2^{-j}x - n)$, such that for all f in $L^2(\mathbf{R})$,

$$P_{j-1}f = P_j f + \sum_{k \in Z} < f, \psi_{j,k} > \psi_{j,k} \qquad , \tag{3.7}$$

where P_j is the orthogonal projection onto V_j. For every $j \in Z$, define W_j to be the orthogonal complement of V_j in V_{j-1}. We have

$$V_{j-1} = V_j \oplus W_j \tag{3.8}$$

and

$$W_j \perp W_{j'}, j \neq j' \tag{3.9}$$

It follows that, for $j < J$,

$$V_j = V_J \oplus (\oplus_{k=0}^{J-j-1} W_{J-k}) \tag{3.10}$$

where all these subspaces are orthogonal. Eq.(3.8) is the foundation of Multiresolution. Supposing that scaling functions of J-order approximation are used, the enhancement of wavelets of orders J to j+1 create an approximation with much better accuracy (j-order approximation). In other words, the scaling functions describe accurately the smooth features of a function and the wavelets the finer details for which a more accurate approximation has to be used. In this way, Multiresolution Analysis operates as a "mathematical microscope". Wherever needed, a finite linear combination of wavelets can offer an arbitrarily small precision of the approximation.

It has to be noted that the W_j spaces inherit the scaling property from the V_j:

$$f(x) \in W_j \leftrightarrow f(2^j x) \in W_0 \tag{3.11}$$

3.3 How to construct a Wavelet Function

Before describing the construction procedure of the wavelets, it would be worthy to write out some interesting properties of the scaling functions. Each $\phi \in V_0 \subset V_{-1}$ can be written as a linear combination of the $\phi_{-1,n}$ which are an orthonormal basis of V_{-1}:

$$\phi = \sum_n h_n \phi_{-1,n} \tag{3.12}$$

with

$$h_n = < \phi, \phi_{-1,n} >, \sum_{n \in Z} |h_n|^2 = 1 \tag{3.13}$$

Eq.(3.11) can be rewritten as

$$\phi(x) = \sqrt{2}\sum_n h_n \phi(2x - n) \tag{3.14}$$

Defining $\hat{f}$ to be the Fourier transform of a function f

$$\hat{f} = \frac{1}{\sqrt{2\pi}} \int_{-\infty}^{\infty} f(x) e^{-ix\xi} dx \tag{3.15}$$

eq.(3.14) is written as

$$\hat{\phi}(\xi) = \frac{1}{\sqrt{2}} \sum_n h_n e^{-in\xi/2} \hat{\phi}(\xi/2) = m_0(\xi/2)\hat{\phi}(\xi/2) \tag{3.16}$$

where

$$m_0(\xi) = \frac{1}{\sqrt{2}} \sum_n h_n e^{-in\xi} \tag{3.17}$$

The function $m_0(\xi)$ is a 2π periodic function in $L^2([0, 2\pi])$.

Daubechies has proven the following Theorem:

If a ladder of closed subspaces $(V_j)_{j\in Z}$ in $L^2(R)$ satisfies Eqs. (3.1)–(3.6), then there exists an associated orthonormal wavelet basis $\{\psi_{j,k}; j, k \in Z\}$ for $L^2(R)$ such that

$$P_{j-1} = P_j + \sum_k < ., \psi_{j,k} > \psi_{j,k} \tag{3.18}$$

One possibility for the construction of the wavelet ψ is

$$\hat{\psi}(\xi) = e^{i\xi/2} \overline{m_0(\xi/2 + \pi)} \hat{\phi}(\xi/2) \tag{3.19}$$

or equivalently

$$\psi = \sum_n (-1)^{n-1} h_{-n-1} \phi_{-1,n} \tag{3.20}$$

$$\psi(x) = \sqrt{(2)} \sum_n (-1)^{n-1} h_{-n-1} \phi(2x - n) \tag{3.21}$$

It has to be noted that ψ is not determined uniquely by the multiresolution analysis ladder and Eq.(3.19): if ψ satisfies Eq.(3.19), then so will any $\psi^\dagger$ of the type

$$\hat{\psi}^\dagger(\xi) = \rho(\xi)\hat{\psi}(\xi) \tag{3.22}$$

with ρ 2π-periodic and $|\rho(\xi)|$=1. In particular, we can choose $\rho(\xi) = \rho_0 e^{imp}$ with $m \in Z, |\rho_0| = 1$, which corresponds to a phase change and a shift by m for ψ. We will use this freedom to define

$$\psi = \sum_n g_n \phi_{-1,n}, \;\; g_n = (-1)^n h_{-n+1} \tag{3.23}$$

The orthonormality condition of Eq.(3.6) can be relaxed. It is sufficient to require that the $\phi(x-k)$ constitute a Riesz basis of V_0; that means that they span V_0 and for all $(c_k)_{k\in Z} \in L^2(Z)$ with $\sum_k |c_k|^2 < \infty$ it holds

$$A \sum_k |c_k|^2 \leq || \sum_k c_k \phi(x-k)||^2 \leq B \sum_k |c_k|^2 \tag{3.24}$$

or equivalently

$$0 < (2\pi)^{-1} A \leq \sum_l |\hat{\phi}(\xi + 2\pi l)|^2 \leq (2\pi)^{-1} B < \infty \tag{3.25}$$

where $A > 0, B < \infty$ are independent of the c_n. Supposing that $\phi \in L^2(R)$ satisfies Eq.(3.25) and defining $V_j = \overline{Span\{\phi_{j,k}; k \in Z\}}$, then $\bigcap_{j\in Z} V_j = 0$. Also, if $\hat{\phi}(\xi)$ is bounded for all ξ and continuous near $\xi = 0$, with $\hat{\phi}(0) \neq 0$, then $\overline{\bigcup_{j\in Z} V_j} = L^2(R)$. One Riesz basis which satisfies these criteria, satisfies the density and separation qualities of the multiresolution analysis.

Chui [?] has proven that $\{\phi(x-k) : k \in Z\}$ is an orthonormal family if and only if $2\pi \sum_{k=-\infty}^{\infty} |\hat{\phi}(\xi + 2\pi l)|^2 = 1, \forall x \in R$. This is a very useful criterion for the orthonormality of a specific scaling family.

We can therefore construct an orthonormal basis $\phi^{\perp}$ for V_0 by defining

$$\hat{\phi}^{\perp} = (2\pi)^{-1/2} [\sum_l |\hat{\phi}(\xi + 2\pi l)|^2]^{-1/2} \;\; \hat{\phi}(\xi) \tag{3.26}$$

Clearly, $\sum_l |\hat{\phi}^{\perp}(\xi + 2\pi l)|^2 = (2\pi)^{-1}$, which means that the $\phi^{\perp}(x-k)$ are orthonormal. Finally,

$$\hat{\psi}(\xi) = e^{i\xi/2} \; \overline{m_0^{\perp}(\xi/2 + \pi)} \; \hat{\phi}^{\perp}(\xi/2) \tag{3.27}$$

with

$$m_0^{\perp}(\xi) = m_0(\xi)[\sum_l |\hat{\phi}(\xi + 2\pi l)|^2]^{1/2} \, [\sum_l |\hat{\phi}(2\xi + 2\pi l)|^2]^{-1/2} \tag{3.28}$$

or equivalently

$$\psi(x) = \sum_n (-1)^n \, h_{-n+1}^{\perp} \phi^{\perp}(x - n) \tag{3.29}$$

with $m_0^{\perp}(\xi) = \frac{1}{\sqrt{2}} \sum_n h_n^{\perp} \, e^{-in\xi}$.

The Battle-Lemarié wavelets [27, 28] are associated with multiresolution analysis ladders consisting of spline function spaces. A B-spline with knots at the integers is considered the original scaling function. The zero order cardinal B-spline N_0 is the characteristic function of the unit interval [0,1)

$$N_0(x) = \begin{cases} 1 & 0 \leq x \leq 1 \\ 0 & elsewhere \end{cases}$$

For $m \geq 1$, the m-th order cardinal B-spline N_m is defined recursively by the following convolution:

$$\begin{aligned} N_m(x) &= \int_{-\infty}^{\infty} N_{m-1}(x - t) N_0(t) dt \\ &= \int_0^1 N_{m-1}(x - t) dt \end{aligned} \tag{3.30}$$

with the Fourier transform

$$\hat{N}_m(\omega) = (2\pi)^{-1/2} e^{-i\varrho\xi/2} \left(\frac{sin(\xi/2)}{\xi/2} \right)^{m+1}$$

where $\varrho = 0$ if m is odd and $\varrho = 1$ if m is even. For even m, $\phi = N_m$ is symmetric around $x = 1/2$, for odd m, around $x = 0$. Except for $m = 0$ the scaling functions constitute a Riesz basis, but they are not orthonormal. To apply the orthonormalization of Eq.(3.26), Daubechies [30] has shown that

$$2\pi \sum_{k=-\infty}^{\infty} |\hat{N}_m(2x + 2\pi k)|^2 = -\frac{sin^{2m+2}(x)}{(2m+1)!} \frac{d^{2m+1}}{dx^{2m+1}} \, cot(x)$$

The result of the orthonormalization is that support of the $\phi^{\perp}$ = R = support of the ψ for all the Battle-Lemarie wavelets. The "orthonormalized" $\phi^{\perp}$ has the same symmetry axis as ϕ. The symmetry axis of ψ always lies at $x = 1/2$. (For m even, ψ is antisymmetric around this axis, for m odd, ψ is symmetric). Even though the supports of $\phi^{\perp}$ and ψ equal the whole R, $\phi^{\perp}$ and ψ still have very good (exponential) decay

$$|\phi^{\perp}, \psi(x)| \leq Ce^{-\gamma|x|}, x \in R$$

The Battle-Lemarie wavelets based on the m-th order cardinal B-splines belong to C^k with $k \leq m-1$ and have m vanishing moments: $\int dx\ x^l\ \psi(x) = 0$ for l=0,1,..,m for $\psi^{(l)}$ bounded for $l \leq m$. It is impossible for orthonormal ψ, to have exponential decay and to belong to C^{∞}, with all derivatives bounded, unless $\psi \equiv 0$. As a result, to achieve fast (exponential) decay, only a finite number k of derivatives can be continuous. The decay rate decreases as k increases. On the contrary, the Meyer wavelet, which is C^{∞}, decays faster than any inverse polynomial, but not exponentially fast.

In the general case, $\phi = N_m$, the ϕ satisfies $\int dx \phi(x) = 1$ and

$$\phi(x) = \begin{cases} 2^{-2n} \sum_{j=0}^{2n+1} \begin{pmatrix} 2n+1 \\ j \end{pmatrix} \phi(2x - n - 1 + j), \ \ m = 2n = even \\ 2^{-2n-1} \sum_{j=0}^{2n+2} \begin{pmatrix} 2n+2 \\ j \end{pmatrix} \phi(2x - n - 1 + j), \ \ m = 2n+1 = odd \end{cases}$$

If we choose ϕ to be the 0-th order cardinal spline,

$$\phi(x) = \begin{cases} 1 & 0 \leq x \leq 1 \\ 0 & elsewhere \end{cases}$$

and we follow the previous steps, we end up with the Haar basis

$$\psi(x) = \begin{cases} 1 & 0 \le x \le 1/2 \\ -1 & -1/2 \le x \le 1/2 \\ 0 & elsewhere \end{cases}$$

No orthonormalization is needed since ϕ is orthogonal to its translations.

Choosing the piecewise linear spline (m=1) as the scaling function,

$$\phi(x) = \begin{cases} 1 - |x| & 0 \le |x| \le 1 \\ 0 & elsewhere \end{cases}$$

it satisfies

$$\phi(x) = 0.5\phi(2x+1) + \phi(2x) + 0.5\phi(2x-1) \tag{3.31}$$

and its Fourier transform is

$$\hat{\phi}(\xi) = (2\pi)^{-1/2} e^{-i\xi/2} (\frac{sin\xi/2}{\xi/2})^2$$

It can be observed that

$$2\pi \sum_{l \in Z} |\hat{\phi}(\xi + 2\pi l)|^2 = \frac{2}{3} + \frac{1}{3} cos\xi = \frac{1}{3}(1 + 2cos^2(\xi/2))$$

Since ϕ is not orthogonal to its translates, it is needed to apply the orthogonalization trick described above. The orthonormalized scaling function is given by

$$\hat{\phi}^{\perp}(\xi) = \sqrt{3}(2\pi)^{-1/2} \frac{4sin^2(\xi/2)}{\xi^2[1 + 2cos^2(\xi/2)]^{1/2}}$$

The $\phi^{\perp}$ is not compactly supported unlike ϕ itself. The corresponding $m_0^{\perp}$ is

$$\hat{m_0}^{\perp}(\xi) = cos^2(\xi/2) \left[\frac{1 + 2cos^2(\xi/2)}{1 + 2cos^2(\xi)} \right]^{1/2}$$

and the wavelet ψ is given by

$$\hat{\psi}(\xi) = e^{i\xi/2} sin^2(\xi/4) \left[\frac{1 + 2sin^2(\xi/4)}{1 + 2cos^2(\xi/2)} \right]^{1/2} \hat{\phi}^{\perp}(\xi/2) \tag{3.32}$$

$$= \sqrt{3} e^{i\xi/2} sin^2(\xi/4) \left[\frac{1 + 2sin^2(\xi/4)}{(1 + 2cos^2(\xi/2))(1 + 2cos^2(\xi/4))} \right]^{1/2} \hat{\phi}(\xi/2) \tag{3.33}$$

The choice of the scaling function for the development of the new Time-Domain MRTD scheme is the cubic cardinal spline ($m = 3$). After orthonormalization, the spectral expressions of the scaling and the wavelet functions are

$$\hat{\phi}^{\perp}(\xi) = (2\pi)^{-1/2}\left(\frac{\sin(\frac{\xi}{2})}{\frac{\xi}{2}}\right)^4 \frac{1}{\sqrt{1 - \frac{4}{3}\sin^2(\frac{\xi}{2}) + \frac{2}{5}\sin^4(\frac{\xi}{2}) - \frac{4}{315}\sin^6(\frac{\xi}{2})}} \quad . \tag{3.34}$$

and

$$\hat{\psi}^{\perp}(\xi) = e^{i\xi/2}\frac{\hat{\phi}^{\perp}(\xi + 2\pi)}{\hat{\phi}^{\perp}(\xi/2 + \pi)}\hat{\phi}^{\perp}(\xi/2) = \hat{\psi}_0(\xi) \tag{3.35}$$

The Cubic Spline Battle-Lemarie Scaling and Wavelet functions are plotted in (Figs.3.1–3.2) in Spatial Domain and in (Figs.3.3–3.4) in Spectral Domain.

3.4 The 2D MRTD scheme

For simplicity, the 2D MRTD scheme is analyzed for a homogeneous lossless medium with the permittivity ϵ and the permeability μ. Assuming no variation along the y-direction, the Maxwell's equations for the two-dimensional TM^z mode [67] can be written as:

$$\frac{\partial E_x}{\partial t} = -\frac{1}{\epsilon}\frac{\partial H_y}{\partial z} \tag{3.36}$$

$$\frac{\partial H_y}{\partial t} = \frac{1}{\mu}\left(\frac{\partial E_z}{\partial x} - \frac{\partial E_x}{\partial z}\right) \tag{3.37}$$

$$\frac{\partial E_z}{\partial t} = \frac{1}{\epsilon}\frac{\partial H_y}{\partial x} \tag{3.38}$$

To derive the 2D MRTD Scheme, the electric and magnetic field components incorporated in these equations are expanded in a series of Battle-Lemarie scaling and wavelet functions in both x- and z-directions and in pulse functions in time.

$$E_x(x,z,t) = \sum_{k,l,m=-\infty}^{+\infty} {}_kE^{x,\phi\phi}_{l-1/2,m}\, h_k(t)\, \phi_{l-1/2}(x)\, \phi_m(z)$$

$$
\begin{aligned}
&+ \sum_{k,l,m=-\infty}^{+\infty} \sum_{r_z=0}^{+\infty} \sum_{p_z=0}^{2^{r_z}-1} {}_kE^{x,\phi\psi_{r_z,p_z}}_{l-1/2,m}\; h_k(t)\; \phi_{l-1/2}(x)\; \psi^{r_z}_{m,p_z}(z) \\
&+ \sum_{k,l,m=-\infty}^{+\infty} \sum_{r_x=0}^{+\infty} \sum_{p_x=0}^{2^{r_x}-1} {}_kE^{x,\psi_{r_x,p_x}\phi}_{l-1/2,m}\; h_k(t)\; \psi^{r_x}_{l-1/2,p_x}(x)\; \phi_m(z) \\
&+ \sum_{k,l,m=-\infty}^{+\infty} \sum_{r_x,r_z=0}^{+\infty} \sum_{p_x,p_z=0}^{2^{r_x,r_z}-1} {}_kE^{x,\psi_{r_x,p_x}\psi_{r_z,p_z}}_{l-1/2,m}\; h_k(t)\; \psi^{r_x}_{l-1/2,p_x}(x)\; \psi^{r_z}_{m,p_z}(z) \\
E_z(x,z,t) \;&=\; \sum_{k,l,m=-\infty}^{+\infty} {}_kE^{z,\phi\phi}_{l,m-1/2}\; h_k(t)\; \phi_l(x)\; \phi_{m-1/2}(z) \\
&+ \sum_{k,l,m=-\infty}^{+\infty} \sum_{r_z=0}^{+\infty} \sum_{p_z=0}^{2^{r_z}-1} {}_kE^{z,\phi\psi_{r_z,p_z}}_{l,m-1/2}\; h_k(t)\; \phi_l(x)\; \psi^{r_z}_{m-1/2,p_z}(z) \\
&+ \sum_{k,l,m=-\infty}^{+\infty} \sum_{r_x=0}^{+\infty} \sum_{p_x=0}^{2^{r_x}-1} {}_kE^{z,\psi_{r_x,p_x}\phi}_{l,m-1/2}\; h_k(t)\; \psi^{r_x}_{l,p_x}(x)\; \phi_{m-1/2}(z) \\
&+ \sum_{k,l,m=-\infty}^{+\infty} \sum_{r_x,r_z=0}^{+\infty} \sum_{p_x,p_z=0}^{2^{r_x,r_z}-1} {}_kE^{z,\psi_{r_x,p_x}\psi_{r_z,p_z}}_{l,m-1/2}\; h_k(t)\; \psi^{r_x}_{l,p_x}(x)\; \psi^{r_z}_{m-1/2,p_z}(z) \\
H_y(x,z,t) \;&=\; \sum_{k,l,m=-\infty}^{+\infty} {}_{k+1/2}H^{y,\phi\phi}_{l-1/2,m-1/2}\; h_{k+1/2}(t)\; \phi_{l-1/2}(x)\; \phi_{m-1/2}(z) \\
&+ \sum_{k,l,m=-\infty}^{+\infty} \sum_{r_z=0}^{+\infty} \sum_{p_z=0}^{2^{r_z}-1} {}_{k+1/2}H^{y,\phi\psi_{r_z,p_z}}_{l-1/2,m-1/2}\; h_{k+1/2}(t)\; \phi_{l-1/2}(x)\; \psi^{r_z}_{m-1/2,p_z}(z) \\
&+ \sum_{k,l,m=-\infty}^{+\infty} \sum_{r_x=0}^{+\infty} \sum_{p_x=0}^{2^{r_x}-1} {}_{k+1/2}H^{y,\psi_{r_x,p_x}\phi}_{l-1/2,m-1/2}\; h_{k+1/2}(t)\; \psi^{r_x}_{l-1/2,p_x}(x)\; \phi_{m-1/2}(z) \\
&+ \sum_{k,l,m=-\infty}^{+\infty} \sum_{r_x,r_z=0}^{+\infty} \sum_{p_x,p_z=0}^{2^{r_x,r_z}-1} {}_{k+1/2}H^{y,\psi_{r_x,p_x}\psi_{r_z,p_z}}_{l-1/2,m-1/2}\; h_{k+1/2}(t)\; \psi^{r_x}_{l-1/2,p_x}(x)\; \psi^{r_z}_{m-1/2,p_z}(z) \quad ,
\end{aligned}
\tag{3.39}
$$

where $\phi_n(x) = \phi(\frac{x}{\Delta x} - n)$ and $\psi^r_{n,p}(x) = 2^{r/2}\,\psi_0(2^r[\frac{x}{\Delta x} - n] - p)$ represent the Battle-Lemarie scaling and r-resolution wavelet function respectively. The expressions of the scaling and the 0-resolution wavelet in the spectral domain are given in Eqs.(3.34)–(3.35).Since higher resolutions of wavelets are shifted and dilated versions of the 0-resolution, their domain will be a fraction of that of the 0-resolution wavelet; thus there are going to be more than one higher resolution wavelet coefficients for each MRTD cell. Specifically, for the the arbitrary r-resolution and for the n-cell to the x-direction, there exist 2^r wavelet

coefficients located at $\frac{x}{\Delta x} = n + \frac{p}{2^{r+1}}$, $p = 0, .., 2^r - 1$. This is the reason for the summation of the p terms for each resolution r in the expansion of Eq.(39). ${}_kE_{l,m}^{\kappa,\mu\nu}$ and ${}_{k+1/2}H_{l,m}^{\kappa,\mu\nu}$ with $\kappa = x, y, z$ and $\mu, \nu = \phi, \psi$ are the coefficients for the field expansions in terms of scaling and wavelet functions. The indices l, m and k are the discrete space and time indices related to the space and time coordinates via $x = l\Delta x$,$z = m\Delta z$ and $t = k\Delta t$, where Δx,Δz are the space discretization intervals in x- and z-direction and Δt is the time discretization interval. For an accuracy of 0.1% the above summations are truncated to a finite number of terms determined by the dispersion and stability requirements (typically between 22-26). The time-domain expansion function $h_k(t)$ is defined as

$$h_k(t) = h(\frac{t}{\Delta t} - k) \tag{3.40}$$

with the rectangular pulse function

$$h(t) = \begin{cases} 1 & \text{for } |t| < 1/2 \\ 1/2 & \text{for } |t| = 1/2 \\ 0 & \text{for } |t| > 1/2 \end{cases} .$$

The magnetic field components are shifted by half a discretization interval in space and time-domain with respect to the electric field components (leap-frog).

Upon inserting the field expansions, Maxwell's equations are sampled using pulse functions as time-domain test functions and scaling/wavelet functions as space-domain test-functions. For the sampling in time-domain, the following integrals are utilized

$$\int_{-\infty}^{+\infty} h_k(t) h_{k'}(t) dt = \delta_{k,k'} \Delta t \tag{3.41}$$

and

$$\int_{-\infty}^{+\infty} h_k(t) \frac{\partial h_{k'+1/2}(t)}{\partial t} dt = \delta_{k,k'} - \delta_{k,k'+1} \tag{3.42}$$

where $\delta_{k,k'}$ is the Kroenecker symbol,

$$\delta_{k,k'} = \begin{cases} 1 & \text{for } k = k' \\ 0 & \text{for } k \neq k' \end{cases} .$$

Sampling in space-domain is obtained by use of the orthogonality relationships f or the scaling and for the wavelet functions [30]

$$\int_{-\infty}^{+\infty} \phi_m(x)\phi_{m'}(x)dx = \delta_{m,m'}\Delta x, \tag{3.43}$$

$$\int_{-\infty}^{+\infty} \phi_m(x)\psi^r_{m',p'}(x)dx = 0, \quad \forall\ r,p \tag{3.44}$$

and

$$\int_{-\infty}^{+\infty} \psi^r_{m,p}(x)\psi^{r'}_{m',p'}(x)dx = \delta_{r,r'}\ \delta_{m,m'}\ \delta_{p,p'}\ \Delta x \tag{3.45}$$

The integrals containing derivatives can be approximated by the following expressions:

$$\int_{-\infty}^{+\infty} \phi_m(x) \frac{\partial \phi_{m'+1/2}(x)}{\partial x} dx \approx \sum_{i=-n_a}^{n_a-1} a(i)\delta_{m+i,m'} \tag{3.46}$$

with

$$a(i) = \frac{1}{\pi}\int_0^{\infty} |\hat{\phi}(\xi)|^2\, \xi\, sin[\xi\,(i+1/2)]d\xi \quad , \tag{3.47}$$

$$\int_{-\infty}^{+\infty} \phi_m(x) \frac{\partial \psi^r_{m'+1/2,p}(x)}{\partial x} dx \approx \sum_{i=-n_{d,r,1}}^{n_{d,r,2}} d_r(i,p)\delta_{m+i,m'} \tag{3.48}$$

with

$$d_r(i,p) = \frac{1}{\pi}\int_0^{\infty} 2^{-r/2}\hat{\phi}_m(\xi)\,|\hat{\psi}_0(\xi/2^r)|\;\xi\;sin[\xi\,(i+0.5+p/2^r+1/2^{r+1})]\;d\xi \quad , \quad (3.49)$$

$$\int_{-\infty}^{+\infty} \psi^r_{m,p}(x)\frac{\partial\phi_{m'+1/2}(x)}{\partial x}dx \approx \sum_{i=-n_{c,r,1}}^{n_{c,r,2}} c_r(i,p)\delta_{m+i,m'} \quad (3.50)$$

with

$$c_r(i,p) = \frac{1}{\pi}\int_0^{\infty} 2^{-r/2}\hat{\phi}_m(\xi)\,|\hat{\psi}_0(\xi/2^r)|\;\xi\;sin[\xi\,(i+0.5-p/2^r-1/2^{r+1})]\;d\xi \quad , \quad (3.51)$$

$$\int_{-\infty}^{+\infty} \psi^{r_1}_{m,p_1}(x)\frac{\partial\psi^{r_2}_{m'+1/2,p_2}(x)}{\partial x}dx \approx \sum_{i=-n_{b,r_1,r_2,1}}^{n_{b,r_1,r_2,2}} b_{r_1,r_2}(i,p_1,p_2)\delta_{m+i,m'} \quad (3.52)$$

with

$$b_{r_1,r_2}(i,p_1,p_2) = \int_0^{\infty} |\hat{\psi}_0(\xi/2^{r_1})|\,|\hat{\psi}_0(\xi/2^{r_2})|\,\xi\,sin[\xi\,(i+1/2+p_2/2^{r_2}-p_1/2^{r_1}+1/2^{r_2+1}-1/2^{r_1+1})]d\xi \quad (3.53)$$

For the rest of the MRTD Technique description, an expansion only in a series of scaling and 0-resolution wavelet functions will be considered. Hints for the enhancement of additional wavelet resolutions will be presented where needed. Since for the 0-resolution ($r = 0$) there is only one wavelet coefficient per cell ($p = 0$), the p symbols will be omitted from the definition of the b, c, d coefficients, which will be given by

$$\int_{-\infty}^{+\infty} \psi^0_m(x)\frac{\partial\phi_{m'+1/2}(x)}{\partial x}dx \approx \sum_{i=-n_{c,0,1}}^{n_{c,0,2}} c_0(i)\delta_{m+i,m'} \quad (3.54)$$

with

$$c_0(i) = \frac{1}{\pi}\int_0^{\infty} \hat{\phi}_m(\xi)\,|\hat{\psi}_0(\xi)|\;\xi\;sin[\xi\,i]\;d\xi \quad , \quad (3.55)$$

$$\int_{-\infty}^{+\infty} \phi_m(x)\frac{\partial\psi^0_{m'+1/2}(x)}{\partial x}dx \approx \sum_{i=-n_{d,0,1}}^{n_{d,0,2}} d_0(i)\delta_{m+i,m'} \quad (3.56)$$

with

$$d_0(i) = \int_0^{\infty} \hat{\phi}_m(\xi)\, |\hat{\psi}_0(\xi)|\, \xi\, sin(\xi\, i + 1)\, d\xi = c_0(i+1) \tag{3.57}$$

Thus, eq.(3.56) can be written as

$$\int_{-\infty}^{+\infty} \phi_m(x) \frac{\partial \psi_{0,m'+1/2}(x)}{\partial x} dx \approx \sum_{i=-n_{c,0,1}-1}^{n_{c,0,2}-1} c_0(i+1)\delta_{m+i,m'} \tag{3.58}$$

$$\int_{-\infty}^{+\infty} \psi_m^0(x) \frac{\partial \psi^0_{m'+1/2}(x)}{\partial x} dx \approx \sum_{i=-n_{b,0,0,1}}^{n_{b,0,0,2}} b_0(i)\delta_{m+i,m'} \tag{3.59}$$

with

$$b_0(i) = b_{0,0}(i) = \int_0^{\infty} |\hat{\psi}_0(\xi)|^2\, \xi\, sin[\xi\,(i+1/2)] d\xi \tag{3.60}$$

with $a(i), b_0(i), c_0(i)$ given in Table (3.1) [31]. Due to symmetries in the integrals for the 0-resolution, the coefficients satisfy the conditions: $a(-1-i) = -a(i)$, $b_0(-1-i) = -b_0(i)$ and $c_0(-i) = -c_0(i)$ for $i < 0$. Hence, the stencil lengths have to be: $n_{b,0,0,1} = n_{b,0,0,2} + 1 = n_b$ and $n_{c,0,1} = n_{c,0,2} = n_c$. These conditions are not general and do not hold for any other arbitrary resolution. The stencil size is determined by the dispersion requirements. It has to be noted that the Battle-Lemarie scaling function has exponential decay; thus, the coefficients $a(i)$ for $i > 12$ are not zero, but their value is negligible ($\leq 10^{-4}$).

After applying the Galerkin technique to Eqs.(3.36)–(3.38), the following MRTD equations are derived:

$$\begin{aligned}
\frac{{}_{k+1}E^{x,\phi\phi}_{i-1/2,j} - {}_{k}E^{x,\phi\phi}_{i-1/2,j}}{\Delta t} = & - \frac{1}{\epsilon \Delta z}\Big(\sum_{j'=-n_a}^{n_a-1} a(j')_{k+1/2} H^{y,\phi\phi}_{i-1/2,j+j'+1-1/2} \\
& + \sum_{j'=-n_c}^{n_c} c_0(j')_{k+1/2} H^{y,\phi\psi_0}_{i-1/2,j+j'-1/2} \Big) \\
\frac{{}_{k+1}E^{x,\psi_0\phi}_{i-1/2,j} - {}_{k}E^{x,\psi_0\phi}_{i-1/2,j}}{\Delta t} = & - \frac{1}{\epsilon \Delta z}\Big(\sum_{j'=-n_a}^{n_a-1} a(j')_{k+1/2} H^{y,\psi_0\phi}_{i-1/2,j+j'+1-1/2}
\end{aligned}$$

i	$a(i)$	$b_0(i)$	$c_0(i)$
0	1.29161604157839	2.47253977327429	0.
1	-0.155978843323672	0.9562282774123074	-4.659725793402785E-02
2	5.960603303246872 90E-02	0.1660591600788887	5.453939813583327E-02
3	-2.929157759806890E-02	9.392437777679437E-02	-3.699957746974982E-02
4	1.536239945742678 0E-02	3.141444475216036E-03	2.057449098775452E-02
5	-8.184462325283712E-03	1.349356908709108E-02	-1.115303180864957E-02
6	4.375758555235483 0E-03	-2.858941810094752E-03	5.976877725279031E-03
7	-2.342365356649461E-03	2.778680514115529E-03	-3.202621363952005E-03
8	1.252877717042020E-03	-1.129446167303586E-03	1.714086849566890E-03
9	-6.716635068590737E-04	7.071507309377701E-04	-9.176508438494196E-04
10	3.583506907489797E-04	-3.491267305845643E-04	4.911754748072018E-04
11	-1.931321684715780E-04	1.952711419194906E-04	-2.629253013538502E-04
12	1.019327767057869E-04	-1.021304423384722E-04	1.407386855875626E-04
13	-5.613943183518454E-05	5.531259273864269E-05	-7.533840689573666E-05
14	2.834596805928539E-05	-2.947330468694831E-05	4.033146235099674E-05
15	-1.700348604873522E-05	1.572110653438641E-05	-2.159462850665844E-05

Table 3.1: Coefficients $a(i)$, $b_0(i)$, $c_0(i)$

$$+ \sum_{j'=-n_c}^{n_c} c_0(j')_{k+1/2} H^{y,\psi_0\psi_0}_{i-1/2,j+j'-1/2})$$

$$\frac{{}_{k+1}E^{x,\phi\psi_0}_{i-1/2,j} - {}_{k}E^{x,\phi\psi_0}_{i-1/2,j}}{\Delta t} = -\frac{1}{\epsilon\Delta z}\Big(\sum_{j'=-n_c}^{n_c} c_0(j')_{k+1/2} H^{y,\phi\phi}_{i-1/2,j+j'+1-1/2}$$

$$+ \sum_{j'=-n_b}^{n_b-1} b_0(j')_{k+1/2} H^{y,\phi\psi_0}_{i-1/2,j+j'+1-1/2}\Big)$$

$$\frac{{}_{k+1}E^{x,\psi_0\psi_0}_{i-1/2,j} - {}_{k}E^{x,\psi_0\psi_0}_{i-1/2,j}}{\Delta t} = -\frac{1}{\epsilon\Delta z}\Big(\sum_{j'=-n_c}^{n_c} c_0(j')_{k+1/2} H^{y,\psi_0\phi}_{i-1/2,j+j'+1-1/2}$$

$$+ \sum_{j'=-n_b}^{n_b-1} b_0(j')_{k+1/2} H^{y,\psi_0\psi_0}_{i-1/2,j+j'+1-1/2}\Big)$$

$$\frac{{}_{k+1}E^{z,\phi\phi}_{i,j-1/2} - {}_{k}E^{z,\phi\phi}_{i,j-1/2}}{\Delta t} = \frac{1}{\epsilon\Delta x}\Big(\sum_{i'=-n_a}^{n_a-1} a(i')_{k+1/2} H^{y,\phi\phi}_{i+i'+1-1/2,j-1/2}$$

$$+ \sum_{i'=-n_c}^{n_c} c_0(i')_{k+1/2} H^{y,\psi_0\phi}_{i+i'-1/2,j-1/2}\Big)$$

$$\frac{{}_{k+1}E^{z,\phi\psi_0}_{i,j-1/2} - {}_{k}E^{z,\phi\psi_0}_{i,j-1/2}}{\Delta t} = \frac{1}{\epsilon\Delta x}\Big(\sum_{i'=-n_a}^{n_a-1} a(i')_{k+1/2} H^{y,\phi\psi_0}_{i+i'+1-1/2,j-1/2}$$

$$+ \sum_{i'=-n_c}^{n_c} c_0(i')_{k+1/2} H^{y,\psi_0\psi_0}_{i+i'-1/2,j-1/2}\Big)$$

$$\frac{{}_{k+1}E^{z,\psi_0\phi}_{i,j-1/2} - {}_{k}E^{z,\psi_0\phi}_{i,j-1/2}}{\Delta t} = \frac{1}{\epsilon\Delta x}\Big(\sum_{i'=-n_c}^{n_c} c_0(i')_{k+1/2} H^{y,\phi\phi}_{i+i'+1-1/2,j-1/2}$$

$$+ \sum_{i'=-n_b}^{n_b-1} b_0(i')_{k+1/2} H^{y,\psi_0\phi}_{i+i'+1-1/2,j-1/2}\Big)$$

$$\frac{{}_{k+1}E^{z,\psi_0\psi_0}_{i,j-1/2} - {}_{k}E^{z,\psi_0\psi_0}_{i,j-1/2}}{\Delta t} = \frac{1}{\epsilon\Delta x}\Big(\sum_{i'=-n_c}^{n_c} c_0(i')_{k+1/2} H^{y,\phi\psi_0}_{i+i'+1-1/2,j-1/2}$$

$$+ \sum_{i'=-n_b}^{n_b-1} b_0(i')_{k+1/2} H^{y,\psi_0\psi_0}_{i+i'+1-1/2,j-1/2}\Big) \qquad (3.61)$$

$$\frac{{}_{k+1/2}H^{y,\phi\phi}_{i-1/2,j-1/2} - {}_{k-1/2}H^{y,\phi\phi}_{i-1/2,j-1/2}}{\Delta t} = \frac{1}{\mu}\Big[\frac{1}{\Delta x}\Big(\sum_{i'=-n_a}^{n_a-1} a(i')_k E^{z,\phi\phi}_{i+i',j-1/2}$$

$$+ \sum_{i'=-n_c}^{n_c} c_0(i')_k E^{z,\psi_0\phi}_{i+i'-1,j-1/2}\Big) - \frac{1}{\Delta z}\Big(\sum_{j'=-n_a}^{n_a-1} a(j')\ {}_k E^{x,\phi\phi}_{i-1/2,j+j'} + \sum_{j'=-n_c}^{n_c} c_0(j')_k E^{x,\phi\psi_0}_{i-1/2,j+j'-1}$$

$$\frac{{}_{k+1/2}H^{y,\psi_0\phi}_{i-1/2,j-1/2} - {}_{k-1/2}H^{y,\psi_0\phi}_{i-1/2,j-1/2}}{\Delta t} = \frac{1}{\mu}\Big[\frac{1}{\Delta x}\Big(\sum_{i'=-n_c}^{n_c} c_0(i')_k E^{z,\phi\phi}_{i+i',j-1/2}$$

$$+ \sum_{i'=-n_b}^{n_b-1} b_0(i')_k E^{z,\psi_0\phi}_{i+i',j-1/2}\Big) - \frac{1}{\Delta z}\Big(\sum_{j'=-n_a}^{n_a-1} a(j')\ {}_k E^{x,\psi_0\phi}_{i-1/2,j+j'} + \sum_{j'=-n_c}^{n_c} c_0(j')_k E^{x,\psi_0\psi_0}_{i-1/2,j+j'-1}$$

$$\frac{{}_{k+1/2}H^{y,\phi\psi_0}_{i-1/2,j-1/2} - {}_{k-1/2}H^{y,\phi\psi_0}_{i-1/2,j-1/2}}{\Delta t} = \frac{1}{\mu}[\frac{1}{\Delta x}(\sum_{i'=-n_a}^{n_a-1} a(i')_k E^{z,\phi\psi_0}_{i+i',j-1/2} + \sum_{i'=-n_c}^{n_c} c_0(i')_k E^{z,\psi_0\psi_0}_{i+i'-1,j-1/2}) - \frac{1}{\Delta z}(\sum_{j'=-n_c}^{n_c} c_0(j')\ {}_k E^{x,\phi\phi}_{i-1/2,j+j'} + \sum_{j'=-n_b}^{n_b-1} b_0(j')_k E^{x,\phi\psi_0}_{i-1/2,j+j'})]$$

$$\frac{{}_{k+1/2}H^{y,\psi_0\psi_0}_{i-1/2,j-1/2} - {}_{k-1/2}H^{y,\psi_0\psi_0}_{i-1/2,j-1/2}}{\Delta t} = \frac{1}{\mu}[\frac{1}{\Delta x}(\sum_{i'=-n_c}^{n_c} c_0(i')_k E^{z,\phi\psi_0}_{i+i',j-1/2} + \sum_{i'=-n_b}^{n_b-1} b_0(i')_k E^{z,\psi_0\psi_0}_{i+i',j-1/2}) - \frac{1}{\Delta z}(\sum_{j'=-n_c}^{n_c} c_0(j')\ {}_k E^{x,\psi_0\phi}_{i-1/2,j+j'} + \sum_{j'=-n_b}^{n_b-1} b_0(j')_k E^{x,\psi_0\psi_0}_{i-1/2,j+j'})] \quad (3.62)$$

The indices i, j and k are the discrete space and time indices related to the space and time coordinates via $x = i\Delta x$,$z = j\Delta z$ and $t = k\Delta t$, where Δx,Δz are the space discretization intervals in x- and z-direction and Δt is the time discretization interval. The values of the stencil lengths n_a, n_b, n_c depend on the accuracy and dispersion requirements.

3.4.1 Modeling of Hard Boundaries

Unlike the FDTD where the consistency with the image theory is implicit in the application of the boundary conditions, for MRTD schemes based on entire-domain functions this theory must be applied explicitly in the locations of Perfect Electric (PEC) or Magnetic Conductors (PMC). The total value of a field component at a specific cell is affected by a theoretically infinite - practically finite - number of neighboring cells due to the fact that the basis functions extend from -∞ to ∞. Some of these neighbors may be located on the other side of the conductor. This effect is taken into consideration by applying the image theory (Fig.3.5). In this way, the physical boundary condition of zeroing-out the E-field tangential to the PEC is automatically satisfied. For example, even symmetry is applied for the normal-to-PEC electric field components and odd symmetry for the parallel-to-PEC. Image Theory can be implemented automatically for an arbitrary number of hard boundaries.

The time-domain numerical techniques are modeling the real space by creating a discrete numerical grid. Sometimes, this mesh does not coincide with the electrical one and MRTD is one example. The enhancement of wavelets on MRTD requires a special treatment of the wavelet components of the normal-to-PEC electric field. Assuming a vertical PEC in (Fig.3.6), the electrical domains (I) and (II) are isolated from each other. That means that one wavelet component value of the normal electric field EXACTLY ON the PEC would create a non-physical electrical coupling. Thus, TWO wavelet components, one located infinitesimally left of the PEC and the other infinitesimally right of the PEC, have to be defined in order to satisfy the electrical isolation condition. The H-field component that is parallel to the PEC has to be treated in a similar way. The rest components of the E- and H-field have to be zeroed-out on both sides of the PEC, so one value is sufficient. In FDTD the interleaved positioning of the field components on the Yee's cell (which are the same with the scaling functions components on the MRTD's cell) requires that the normal-to-PEC E-field component is located half cell size away from the conductor. In this way, the definition of only one field component per cell is sufficient.

3.4.2 Modeling of Excitation

Without loss of generality, the modeling of the excitation for the 2D and 2.5D MRTD is presented. The 3D algorithm is a direct extension of the 2D. For simplicity, only 0-resolution wavelets are used.

In order to apply a point (pulse) excitation $P(x_o, z_o)$ for $x_o = m\Delta x, z_o = n\Delta z$, the pulse has to be decomposed in terms of scaling and wavelet functions

$$P(x_o, z_o) = \sum_{l_{x,\phi}=-\infty}^{\infty} \sum_{l_{z,\phi}=-\infty}^{\infty} c_{\phi\phi}(l_{x,\phi}, l_{z,\phi})\ \phi(m + l_{x,\phi})\ \phi(n + l_{z,\phi})$$

$$+ \sum_{l_{x,\phi}=-\infty}^{\infty} \sum_{l_{z,\psi}=-\infty}^{\infty} c_{\phi\psi}(l_{x,\phi}, l_{z,\psi})\ \phi(m+l_{x,\phi})\ \psi(n+l_{z,\psi})$$

$$+ \sum_{l_{x,\psi}=-\infty}^{\infty} \sum_{l_{z,\phi}=-\infty}^{\infty} c_{\psi\phi}(l_{x,\psi}, l_{z,\phi})\ \psi(m+l_{x,\psi})\ \phi(n+l_{z,\phi})$$

$$+ \sum_{l_{x,\psi}=-\infty}^{\infty} \sum_{l_{z,\psi}=-\infty}^{\infty} c_{\psi\psi}(l_{x,\psi}, l_{z,\psi})\ \psi(m+l_{x,\psi})\ \psi(n+l_{z,\psi}) \quad . \quad (3.63)$$

with

$$\begin{aligned}
c_{\phi\phi}(l_{x,\phi}, l_{z,\phi}) &= \int_{m-0.5}^{m+0.5} \int_{n-0.5}^{n+0.5} \phi(m+l_{x,\phi})\ \phi(n+l_{z,\phi})\, dz\, dx \\
c_{\phi\psi}(l_{x,\phi}, l_{z,\psi}) &= \int_{m-0.5}^{m+0.5} \int_{n-0.5}^{n+0.5} \phi(m+l_{x,\phi})\ \phi(n+l_{z,\psi})\, dz\, dx \\
c_{\psi\phi}(l_{x,\psi}, l_{z,\phi}) &= \int_{m-0.5}^{m+0.5} \int_{n-0.5}^{n+0.5} \phi(m+l_{x,\psi})\ \phi(n+l_{z,\phi})\, dz\, dx \\
c_{\psi\psi}(l_{x,\psi}, l_{z,\psi}) &= \int_{m-0.5}^{m+0.5} \int_{n-0.5}^{n+0.5} \phi(m+l_{x,\psi})\ \phi(n+l_{z,\psi})\, dz\, dx \quad . \quad (3.64)
\end{aligned}$$

Practically, the summations of Eq.(3.63) can be truncated to a finite number of terms. Usually 6-8 terms on each side of the excitation point per direction can offer an accuracy of representation close to 0.1%. In case the neighboring scaling or wavelet functions are located outside the computational domain (e.g. $m + l_{x,\phi} > n_x$ or $m + l_{x,\phi} < 0$ for a domain $[0, n_x]$ to the x-direction), image theory has to be applied for their translation inside the computational grid.

If there is no discontinuity (hard boundary or dielectric interface) in the summation interval of Eq.(3.63), the double integrals of Eq.(3.64) can be split in two single integrals

$$\begin{aligned}
c_{\phi\phi}(l_{x,\phi}, l_{z,\phi}) &= \int_{m-0.5}^{m+0.5} \phi(m+l_{x,\phi})\, dx \int_{n-0.5}^{n+0.5} \phi(n+l_{z,\phi})\, dz = c_{\phi}(l_{x,\phi})\ c_{\phi}(l_{z,\phi}) \\
c_{\phi\psi}(l_{x,\phi}, l_{z,\psi}) &= \int_{m-0.5}^{m+0.5} \phi(m+l_{x,\phi})\, dx \int_{n-0.5}^{n+0.5} \psi(n+l_{z,\psi})\, dz = c_{\phi}(l_{x,\phi})\ c_{\psi}(l_{z,\psi}) \\
c_{\psi\phi}(l_{x,\psi}, l_{z,\phi}) &= \int_{m-0.5}^{m+0.5} \psi(m+l_{x,\psi})\, dx \int_{n-0.5}^{n+0.5} \phi(n+l_{z,\phi})\, dz = c_{\psi}(l_{x,\psi})\ c_{\phi}(l_{z,\phi}) \\
c_{\psi\psi}(l_{x,\psi}, l_{z,\psi}) &= \int_{m-0.5}^{m+0.5} \psi(m+l_{x,\psi})\, dx \int_{n-0.5}^{n+0.5} \psi(n+l_{z,\psi})\, dz = c_{\psi}(l_{x,\psi})\ c_{\psi}(l_{z,\psi}) \quad ,
\end{aligned}$$

with c_{ϕ}, c_{ψ} given in Tables (3.2)–(3.3).

Due to the symmetries of the Battle-Lemarie scaling and wavelet functions, the decomposition coefficients have to satisfy the following conditions

$$c_\phi(l_\phi) = c_\phi(-l_\phi), \qquad l_\phi = -1, -2, ..$$

$$c_\psi(l_\psi) = c_\psi(1 - l_\psi), \qquad l_\psi = 0, -1, -2, ..$$

For each time-step, the excitation scaling and wavelet components have to be superimposed to the respective field values obtained by the MRTD algorithm in order to provide a transparent source similar to that described in Section 2.1.2.

$$\begin{aligned}
{}_kE^{\phi\phi,total}_{m+l_{x,\phi},n+l_{z,\phi}} &= {}_kE^{\phi\phi}_{m+l_{x,\phi},n+l_{z,\phi}} + c_{\phi\phi}(l_{x,\phi}, l_{z,\phi}) \\
{}_kE^{\phi\psi,total}_{m+l_{x,\phi},n+l_{z,\psi}} &= {}_kE^{\phi\psi}_{m+l_{x,\phi},n+l_{z,\psi}} + c_{\phi\psi}(l_{x,\phi}, l_{z,\psi}) \\
{}_kE^{\psi\phi,total}_{m+l_{x,\psi},n+l_{z,\phi}} &= {}_kE^{\phi\psi}_{m+l_{x,\psi},n+l_{z,\phi}} + c_{\psi\phi}(l_{x,\psi}, l_{z,\phi}) \\
{}_kE^{\psi\psi,total}_{m+l_{x,\psi},n+l_{z,\psi}} &= {}_kE^{\psi\psi}_{m+l_{x,\psi},n+l_{z,\psi}} + c_{\psi\psi}(l_{x,\psi}, l_{z,\psi}) \quad .
\end{aligned}$$

For the 2.5D-MRTD algorithm that requires impulse excitation in time-domain, the above superposition takes place only for the first time step (t=0). Nevertheless, for the 2D-MRTD it has to be repeated throughout the number of time-steps that the excitation is on. The

l_ϕ	0	1	2	3	4	5	6
$c_\phi(l_\phi)$	0.91507	0.03820	0.00963	-0.00863	0.00502	-0.00268	0.00141

Table 3.2: Excitation Scaling Decomposition Coefficients

l_ψ	1	2	3	4	5	6	7
$c_\psi(l_\psi)$	-0.10250	0.12115	-0.02975	0.01501	-0.00598	0.00298	-0.00139

Table 3.3: Excitation Wavelet Decomposition Coefficients

appropriate number of the time-steps will depend on the time dependence of the excitation (Gaussian, Gabor, ...).

Arbitrary excitation spatial distributions $f(x,z)$ for an area $[x_1 = m_1\Delta x, x_2 = m_2\Delta x] \times [z_1 = n_1\Delta z, z_2 = n_2\Delta z]$ can be modeled in a similar way. The spatial distribution has to be sampled with scaling and wavelet functions, giving the new decomposition coefficients

$$
\begin{aligned}
c_{\phi\phi}(l_{x,\phi}, l_{z,\phi}) &= \int_{m_1-0.5}^{m_2+0.5}\int_{n_1-0.5}^{n_2+0.5} f(x,z)\ \phi(m_1 + l_{x,\phi})\ \phi(n_1 + l_{z,\phi})\ dz\ dx \\
c_{\phi\psi}(l_{x,\phi}, l_{z,\psi}) &= \int_{m_1-0.5}^{m_2+0.5}\int_{n_1-0.5}^{n_2+0.5} f(x,z)\ \phi(m_1 + l_{x,\phi})\ \psi(n_1 + l_{z,\psi})\ dz\ dx \\
c_{\psi\phi}(l_{x,\psi}, l_{z,\phi}) &= \int_{m_1-0.5}^{m_2+0.5}\int_{n_1-0.5}^{n_2+0.5} f(x,z)\ \psi(m_1 + l_{x,\psi})\ \phi(n_1 + l_{z,\phi})\ dz\ dx \\
c_{\psi\psi}(l_{x,\psi}, l_{z,\psi}) &= \int_{m_1-0.5}^{m_2+0.5}\int_{n_1-0.5}^{n_2+0.5} f(x,z)\ \psi(m_1 + l_{x,\psi})\ \psi(n_1 + l_{z,\psi})\ dz\ dx \quad .
\end{aligned}
$$

For most simulations the choice of $-8 \leq l_{x,\phi}, l_{x,\psi} \leq (m_2 - m_1) + 8$ and $-8 \leq l_{z,\phi}, l_{z,\psi} \leq (n_2 - n_1) + 8$ offer an accuracy close to 0.1%.

3.4.3 Treatment of Open Boundaries - PML Absorber

As it was discussed in Ch.2, for all discrete-space full wave techniques a special treatment should be given to geometries of interest defined in "open" regions where the computational grid is unbounded in one or more directions. Since the computational domain is limited in space by storage limitations, an appropriate boundary condition should be implemented to effectively simulate open space and satisfy the radiation condition. Berenger [13] proposed the Perfect Matched Layer (PML) Absorber, which is based upon splitting the E- and H- field components in the ABC area and assigning artificial electric and magnetic loss coefficients. On the condition that these loss coefficients satisfy the PML relationship for each point of the absorber area, this nonphysical absorbing medium has a wave impedance less sensitive to the angle of incidence and frequency of outgoing waves than the preexisting

absorbers.In this Subsection, the non-split and split extensions of the PML absorber for the 2D-TM^z Battle-Lemarie MRTD are discussed. Their performance is going to be validated in Ch.4. Assuming that the PML area is characterized by (ϵ_o, μ_o) and electric and magnetic conductivities (σ_E, σ_H), the TM^z equations can be written by adding an extra term to Eqs.(3.36)–(3.38)

$$\epsilon_o \frac{\partial E_x}{\partial t} + \sigma_E E_x = -\frac{\partial H_y}{\partial z} \tag{3.65}$$

$$\epsilon_o \frac{\partial E_z}{\partial t} + \sigma_E E_z = \frac{\partial H_y}{\partial x} \tag{3.66}$$

$$\mu_o \frac{\partial H_y}{\partial t} + \sigma_H H_y = \frac{\partial E_z}{\partial x} - \frac{\partial E_x}{\partial z} \quad . \tag{3.67}$$

Without loss of generality, PML cells only along the z-direction are considered. The extension to the x- and y- directions is straightforward. For each point z of the PML area, the magnetic conductivity σ_H needs to be chosen as [13]:

$$\frac{\sigma_E(z)}{\epsilon_o} = \frac{\sigma_H(z)}{\mu_o} \quad , \tag{3.68}$$

for a perfect absorption of the outgoing waves. A parabolic spatial distribution of $\sigma_{E,H}$,

$$\sigma_{E,H}(z) = \sigma_{E,H}^{max}(1 - \frac{z}{\delta})^p \quad \text{, with p=2} \quad \text{for } 0 \leq z \leq \delta \tag{3.69}$$

is used in the simulations, though higher order distributions (e.g.Cubic p=3) can give similar results. The PML area is terminated with a PEC and usually has a thickness varying between 4-32 cells. The maximum value σ_E^{max} is determined by the designated reflection coefficient R at normal incidence, which is given by the relationship

$$R = e^{-\frac{2}{\epsilon_o c}\int_o^\delta \sigma_E(z)dz} = e^{-\frac{2\sigma_E^{max}\delta}{\epsilon_o c(p+1)}} \quad . \tag{3.70}$$

In MRTD, the PML area can be modeled by discretizing the above equations in a similar way to the non-conductive area described in the beginning of Section 3.4 and split and non-split formulations can be derived.

Similarly, the PML equations for the TE^z can be written as,

$$\mu_o \frac{\partial H_x}{\partial t} + \sigma_H H_x = \frac{\partial E_y}{\partial z} \tag{3.71}$$

$$\mu_o \frac{\partial H_z}{\partial t} + \sigma_H H_z = -\frac{\partial E_y}{\partial x} \tag{3.72}$$

$$\epsilon_o \frac{\partial E_y}{\partial t} + \sigma_E E_y = -\frac{\partial H_z}{\partial x} + \frac{\partial H_x}{\partial z} \quad . \tag{3.73}$$

Split Formulation

Following the approach of [13], H_y is split in two subcomponents, H_{yx}, H_{yz} and Eqs.(3.65)–(3.67) are written as,

$$\epsilon_o \frac{\partial E_x}{\partial t} + \sigma_E(z) E_x = -\frac{\partial H_{yx} + H_{yz}}{\partial z} \tag{3.74}$$

$$\epsilon_o \frac{\partial E_z}{\partial t} = \frac{\partial H_{yx} + H_{yz}}{\partial x} \tag{3.75}$$

$$\mu_o \frac{\partial H_{yx}}{\partial t} = \frac{\partial E_z}{\partial x} \tag{3.76}$$

$$\mu_o \frac{\partial H_{yz}}{\partial t} + \sigma_H(z) H_{yz} = -\frac{\partial E_x}{\partial z} \quad . \tag{3.77}$$

For the sake of simplicity in the presentation and without loss of generality, the fields E_x, E_z, H_{yx}, H_{yz} are expanded in terms of scaling functions only in space domain and pulse functions in time domain. By applying Galerkin's technique [31, 58], the following split PML equations are obtained

$$\begin{aligned}
{}_{k+1}E^{x,\phi\phi}_{i-1/2,j} &= e^{-\sigma^j_E \Delta t/\epsilon_o}\, {}_{k}E^{x,\phi\phi}_{i-1/2,j} \\
&+ \frac{1}{\Delta z\, \sigma^j_E}(e^{-\sigma^j_E \Delta t/\epsilon_o} - 1) \\
&\sum_{i'=-n_a}^{n_a-1} a(i')({}_{k+1/2}H^{yx,\phi\phi}_{i-1/2,j+j'+1-1/2} + {}_{k+1/2}H^{yz,\phi\phi}_{i-1/2,j+j'+1-1/2}) \\
{}_{k+1}E^{z,\phi\phi}_{i,j-1/2} &= {}_{k}E^{z,\phi\phi}_{i,j-1/2} \\
&+ \frac{\Delta t}{\epsilon_o \Delta x} \sum_{i'=-n_a}^{n_a-1} a(i')({}_{k+1/2}H^{yx,\phi\phi}_{i+i'+1-1/2,j-1/2} + {}_{k+1/2}H^{yz,\phi\phi}_{i+i'+1-1/2,j-1/2}) \\
{}_{k+1/2}H^{yx,\phi\phi}_{i-1/2,j-1/2} &= {}_{k-1/2}H^{yx,\phi\phi}_{i-1/2,j-1/2}
\end{aligned}$$

$$
\begin{aligned}
&+ \frac{\Delta t}{\mu_o \Delta x}\Big(\sum_{i'=-n_a}^{n_a-1} a(i')_k E^{z,\phi\phi}_{i+i',j-1/2}\Big) \\
{}_{k+1/2}H^{yz,\phi\phi}_{i-1/2,j-1/2} &= e^{-\sigma_H^{j-1/2}\Delta t/\mu_o}\,{}_{k-1/2}H^{yz,\phi\phi}_{i-1/2,j-1/2} \\
&+ \frac{1}{\Delta z\ \sigma_H^{j-1/2}}(e^{-\sigma_H^{j-1/2}\Delta t/\mu_o}-1)\sum_{j'=-n_a}^{n_a-1} a(j')_k E^{x,\phi\phi}_{i-1/2,j+j'} \quad . \qquad (3.78)
\end{aligned}
$$

Exponential time-stepping is being used for the field components affected by the PML conductivities σ_E, σ_H. Due to the entire-domain nature of the Battle-Lemarie scaling functions, the PML conductivity must be sampled by them over at least 12 cells (6 cells per side),

$$
\sigma^j_{E,H} = \int_{j-6}^{j+6} \sigma_{E,H}(z)\phi_j(z)dz \quad . \qquad (3.79)
$$

Image theory is applied to extend the conductivity layer outside the terminating PEC's. The presented formulation follows the idea introduced by Berenger for the FDTD. Nevertheless, an efficient non-split form of the PML equations does not demand extra memory for the storage of two H_y subcomponents per cell.

Non-split Formulation

Substituting in Eqs.(3.65)–(3.67) [59]:

$$
E_i(x,z,t) = \tilde{E}_i(x,z,t)e^{-\sigma_E(z)t/\epsilon_o} \qquad (3.80)
$$

and

$$
H_j(x,z,t) = \tilde{H}_j(x,z,t)e^{-\sigma_H(z)t/\mu_o} \qquad (3.81)
$$

for i=x,z and j=y leads to the following system of equations:

$$
\epsilon_o \frac{\partial \tilde{E}_x}{\partial t} = -\frac{\partial \tilde{H}_y}{\partial z} \qquad (3.82)
$$

$$
\epsilon_o \frac{\partial \tilde{E}_z}{\partial t} = \frac{\partial \tilde{H}_y}{\partial x} \qquad (3.83)
$$

$$\mu_o \frac{\partial \tilde{H}_y}{\partial t} = \frac{\partial \tilde{E}_z}{\partial x} - \frac{\partial \tilde{E}_x}{\partial z} \quad . \tag{3.84}$$

Discretizing Eqs.(3.82)–(3.84) and inserting Eqs.(3.80)–(3.81) yields the unsplit formulation of the fields for the PML region:

$$\begin{aligned}
{}_{k+1}E^{x,\phi\phi}_{i-1/2,j} &= e^{-\sigma_E^j \Delta t/\epsilon_o}\, {}_kE^{x,\phi\phi}_{i-1/2,j} \\
&- e^{-0.5\sigma_E^j \Delta t/\epsilon_o}\, \frac{\Delta t}{\epsilon_o} \left(\frac{1}{\Delta z} \sum_{j'=-n_a}^{n_a-1} a(i')_{k+1/2} H^{y,\phi\phi}_{i-1/2,j+j'+1-1/2}\right) \\
{}_{k+1}E^{z,\phi\phi}_{i,j-1/2} &= e^{-\sigma_E^{j-1/2} \Delta t/\epsilon_o}\, {}_kE^{z,\phi\phi}_{i,j-1/2} \\
&+ e^{-0.5\sigma_E^{j-1/2} \Delta t/\epsilon_o}\, \frac{\Delta t}{\epsilon_o} \left(\frac{1}{\Delta x} \sum_{i'=-n_a}^{n_a-1} a(i')_{k+1/2} H^{y,\phi\phi}_{i+i'+1-1/2,j-1/2}\right) \\
{}_{k+1/2}H^{y,\phi\phi}_{i-1/2,j-1/2} &= e^{-\sigma_H^{j-1/2} \Delta t/\ mu_o}\, {}_{k-1/2}H^{y,\phi\phi}_{i-1/2,j-1/2} \\
&+ e^{-0.5\sigma_H^{j-1/2} \Delta t/\mu_o}\, \frac{\Delta t}{\mu_o} \\
&\left(\frac{1}{\Delta x} \sum_{i'=-n_a}^{n_a-1} a(i')_k E^{z,\phi\phi}_{i+i',j-1/2} - \frac{1}{\Delta z} \sum_{j'=-n_a}^{n_a-1} a(j')_k E^{x,\phi\phi}_{i-1/2,j+j'}\right) \quad ,
\end{aligned} \tag{3.85}$$

where the terms $\sigma^j_{E,H}$ are given by Eq.(3.79).

3.4.4 Total Field Calculation

Due to the nature of the Battle-Lemarie expansion functions, the total field is a summation of the contributions from the non-localized scaling and wavelet functions. For example, the total electric field $E_x(x_o, z_o, t_o)$ with $(k - 1/2)\,\Delta t < t_o < (k + 1/2)\,\Delta t$, $(i - 1)\,\Delta x < x_o < i\,\Delta x$ and $(j - 1/2)\,\Delta z < z_o < (j + 1/2)\,\Delta z$ is calculated in the same way with [31, 58] by

$$\begin{aligned}
E_x(x_o, z_o, t_o) &= \sum_{i',j'=-l_1}^{l_1} {}_kE^{x,\phi\phi}_{i+i'-1/2,j+j'}\, \phi_{i+i'-1/2}(x_o)\, \phi_{j+j'}(z_o) \\
&+ \sum_{r_x=0}^{r_{max}} \sum_{i',j'=-l_{2,r}}^{l_{2,r}} \sum_{p_x=0}^{2^{r_x}-1} {}_kE^{x,\phi\psi_{r_x,p_x}}_{i+i'-1/2,j+j'}\, \phi_{i+i'-1/2}(x_o)\, \psi^{r_x}_{j+j',p_x}(z_o)
\end{aligned}$$

$$+ \sum_{r_x=0}^{r_{max}} \sum_{i',j'=-l_{3,r}}^{l_{3,r}} \sum_{p_x=0}^{2^{r_x}-1} {}_k E^{x,\psi_{r_x,p_x}\phi}_{i+i'-1/2,j+j'} \; \psi^{r_x}_{i+i'-1/2,p_x}(x_o) \; \phi_{j+j'}(z_o)$$

$$+ \sum_{r_x,r_z=0}^{r_{max}} \sum_{i',j'=-l_{4,r}}^{l_{4,r}} \sum_{p_x,p_z=0}^{2^{r_x,r_z}-1} {}_k E^{x,\psi_{r_x,p_x}\psi_{r_z,p_z}}_{i+i'-1/2,j+j'} \; \psi^{r_x}_{i+i'-1/2,p_x}(x_o) \; \psi^{r_z}_{j+j',p_z}(z_o) \tag{3.86}$$

where $\phi_n(x) = \phi(\frac{x}{\Delta x} - n)$ and $\psi^r_{n,p}(x) = 2^{r/2} \; \psi_0(2^r[\frac{x}{\Delta x} - n] - p)$ represent the Battle-Lemarie scaling and r-resolution wavelet function respectively and r_{max} is the maximum wavelet resolution used in this area of the computational domain. It has been observed that the values $l_1 = l_{2,0} = l_{3,0} = l_{4,0} = 10$ and $l_{2,1} = l_{3,1} = l_{4,1} = 6$ offer accuracy close to 0.5% for most simulations incorporating the first two wavelet resolutions. For the cases of narrow strips with very sharp field discontinuities, the summation limits must increase up to 15-20 terms per direction.

The fact that the MRTD is based on entire-domain basis functions with varying values along each cell offers the unique opportunity of a multi-point field representation per cell. The neighboring scaling and wavelet coefficients can be combined in an appropriate way to calculate the total field value for more than one interior cell points. In this way, MRTD creates a mesh with much larger density than that offered by the nominal number of the cells without increasing the memory requirements. This additional density is very useful in the calculation of the characteristic impedance of planar lines, where even a small field variation can cause a perturbation of the impedance value by $5 - 10\Omega$. On the contrary, FDTD is based on pulse basis functions that have a constant value for each cell, offering a single-point field representation.

3.5 Conclusions

After reviewing the general principles of Multiresolution Analysis, novel time-domain schemes based on expansions in scaling and wavelet functions (MRTD) have been derived. FDTD implementation schemes (excitation, hard/open boundary and dielectric interfaces) have been extended to Multiresolution schemes based on entire-domain expansion basis, while maintaining similar performance characteristics. These schemes offer the unique opportunity of a multi-point field representation per cell. Battle-Lemarie functions are used throughout the dissertation due to their special qualities.

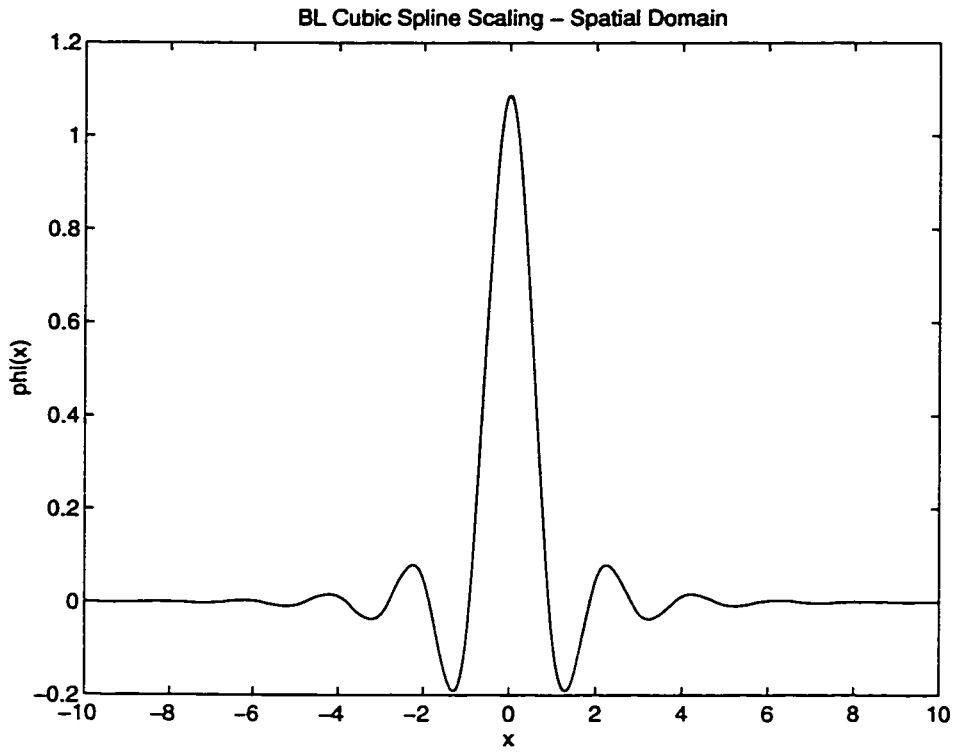

Figure 3.1: BL Cubic Spline Scaling - Spatial Domain.

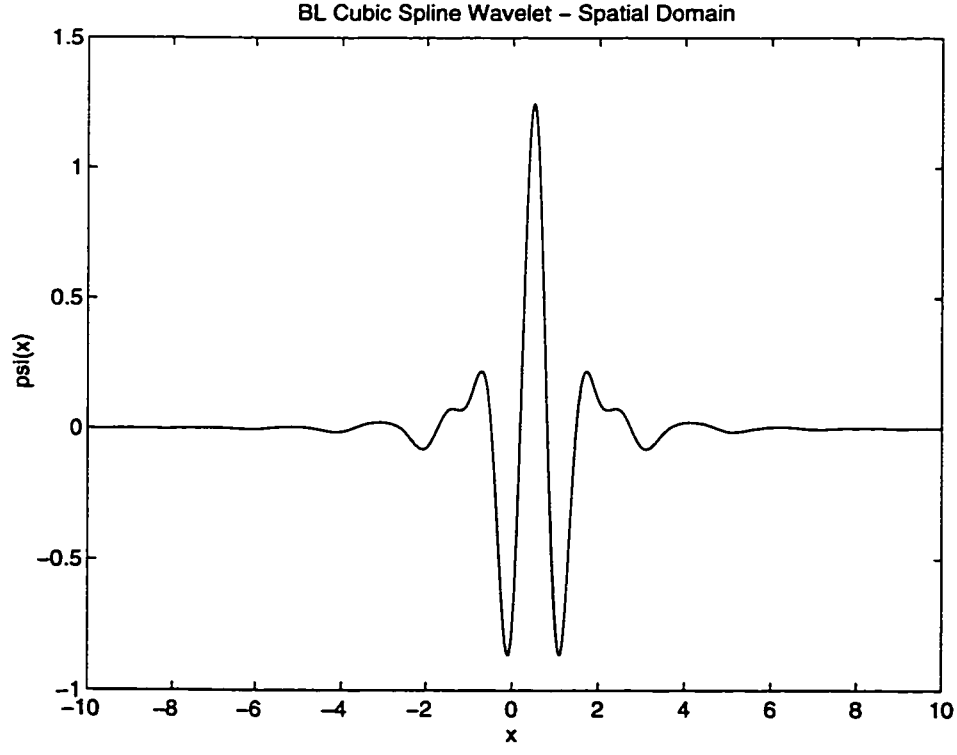

Figure 3.2: BL Cubic Spline Wavelet - Spatial Domain.

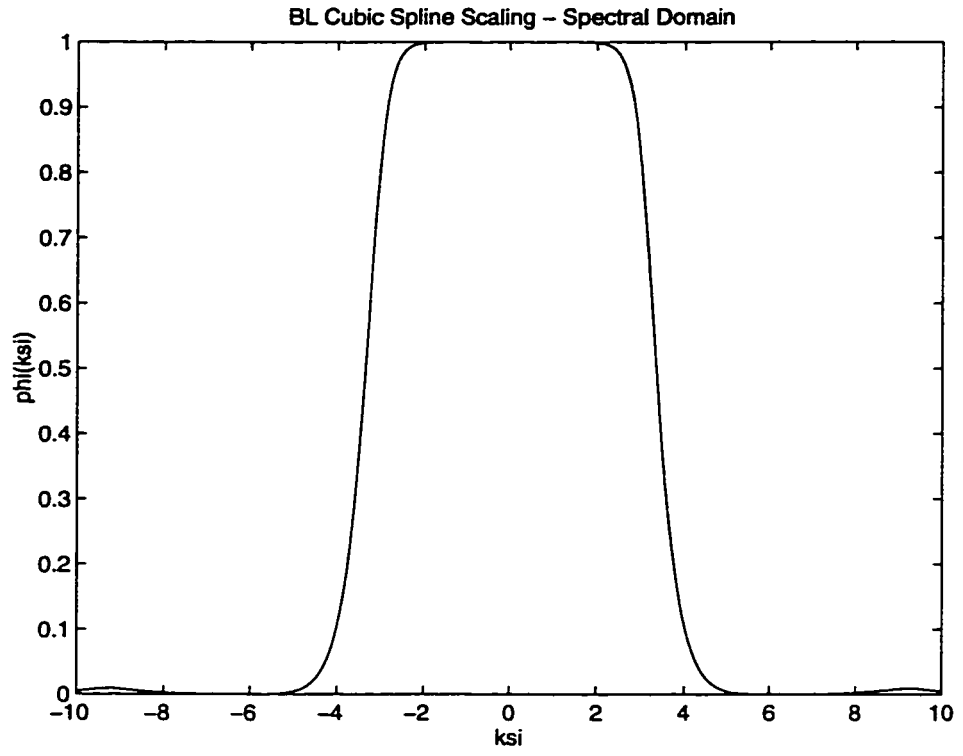

Figure 3.3: BL Cubic Spline Scaling - Spectral Domain.

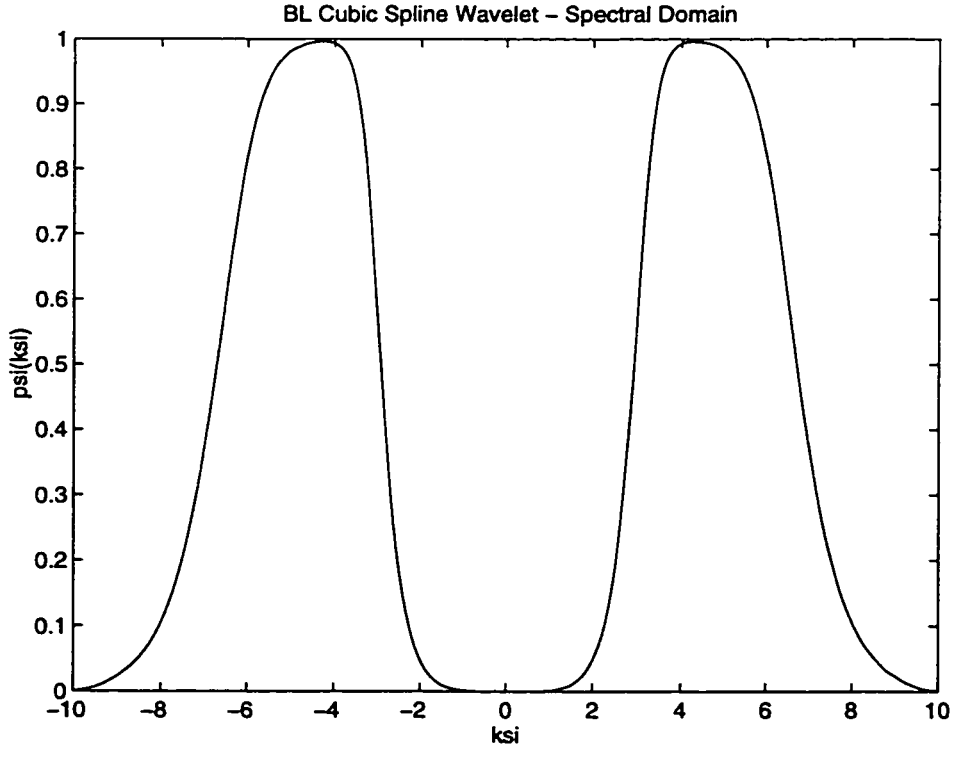

Figure 3.4: BL Cubic Spline Wavelet - Spectral Domain.

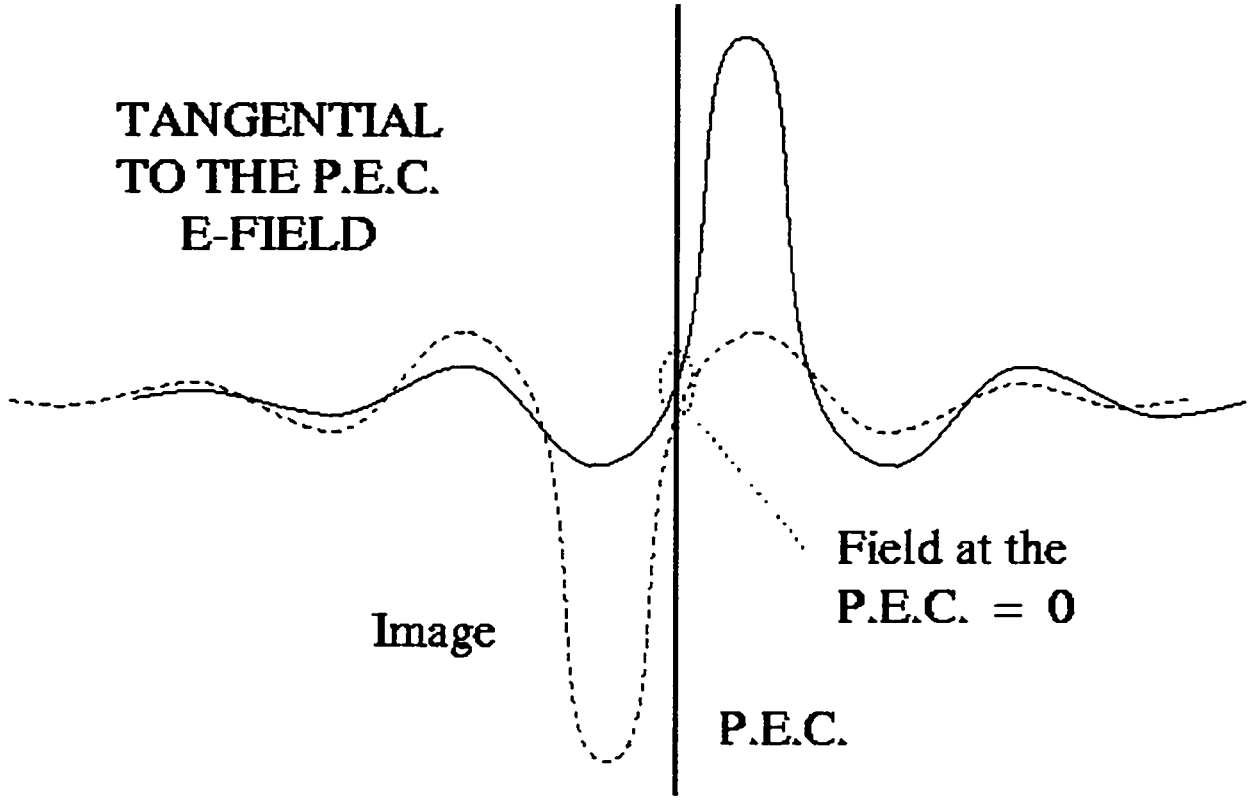

Figure 3.5: Image Theory Application for tangential-to-PEC E-field.

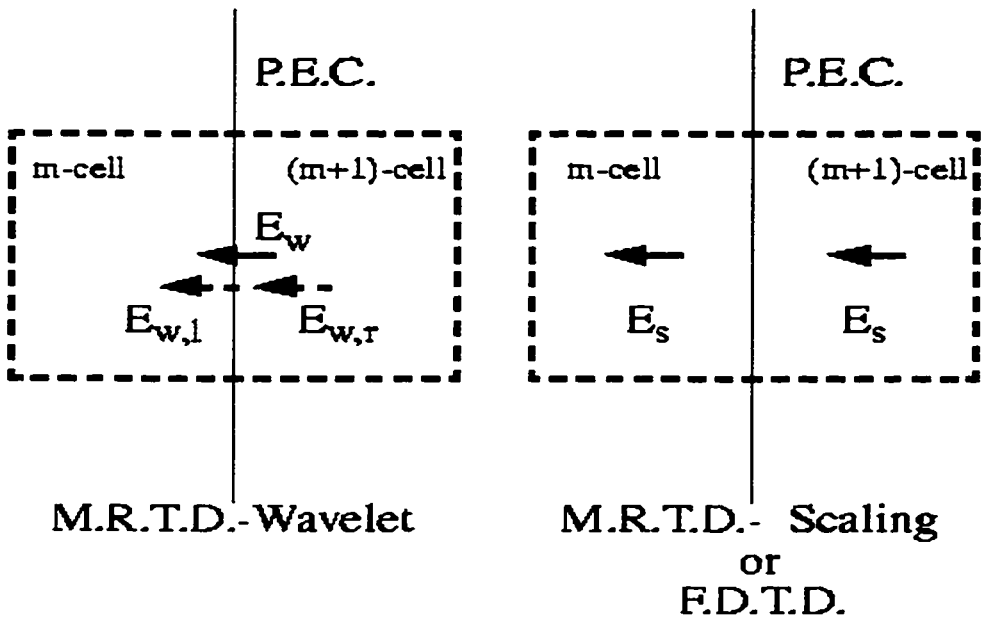

Figure 3.6: Treatment of Wavelet Components of normal-to-PEC E-field.

CHAPTER 4

Characterization of Microwave Circuit Components Using the Multiresolution Time Domain Method (MRTD)

4.1 Introduction

Recently, the Battle-Lemarie based MRTD technique has been successfully applied [31, 58, 59] to a variety of microwave problems and has demonstrated unparalleled properties. When applied to linear as well as nonlinear propagation problems, it has exhibited MRTD schemes based on other entire-domain expansion basis can be developed in a similar way by calculating the appropriate summation coefficients. The use of Battle-Lemarie basis allows for a more simplified evaluation of the moment method integrals is simplified due to the existence of closed form expressions in spectral domain and simple representations in terms of cubic spline functions in space domain. The use of non-localized basis functions cannot accommodate localized boundary conditions. To overcome this difficulty, the image principle is used to model perfect electric and magnetic boundary conditions. Pulse functions are used as expansion and test functions in time-domain. In this Chapter, a 2.5D MRTD scheme is developed and applied to a variety of shielded and open of transmission line problems. Specifically, propagation constant, characteristic impedance and field patterns are derived

for shielded and open transmission line structures and compared to FDTD results. For the treatment of open boundaries, Berenger's PML principles [13] have been extended in split and non-split form, so as they can be used for entire-domain basis MRTD schemes.

4.2 The 2.5D-MRTD scheme

For simplicity, an overview of the 2.5D-MRTD scheme is presented for a homogeneous medium. The derivation is similar to that of the 2D-MRTD scheme in CH.3, which uses the method of moments with pulse functions as expansion and test functions. The magnetic field components are shifted by half a discretization interval in space and time-domain with respect to the electric field components.

Using the approach of [60], Maxwell's curl equations for a homogeneous medium with the permittivity ϵ and the permeability μ can be written in the following form

$$\epsilon \frac{\partial E_x}{\partial t} = \frac{\partial H_z}{\partial y} + \beta H_y \tag{4.1}$$

$$\epsilon \frac{\partial E_y}{\partial t} = -\beta H_x - \frac{\partial H_z}{\partial x} \tag{4.2}$$

$$\epsilon \frac{\partial E_z}{\partial t} = \frac{\partial H_y}{\partial x} - \frac{\partial H_x}{\partial y} \quad , \tag{4.3}$$

where β is the propagation constant and $j = \sqrt{-1}$. The electric and magnetic field components incorporated in these equations are expanded in a series of Battle-Lemarie scaling and wavelet functions in both x- and y-directions. For example, E_x can be represented as:

$$\begin{aligned} E_x(x,y,t) = & \sum_{k,l,m=-\infty}^{+\infty} {}_kE^{x,\phi\phi}_{l-1/2,m}\, h_k(t)\, \phi_{l-1/2}(x)\, \phi_m(y) \\ & + \sum_{k,l,m=-\infty}^{+\infty} \sum_{r_y=0}^{+\infty} \sum_{p_y=0}^{2^{r_y}-1} {}_kE^{x,\phi\psi_{r_y,p_y}}_{l-1/2,m}\, h_k(t)\, \phi_{l-1/2}(x)\, \psi^{r_y}_{m,p_y}(y) \\ & + \sum_{k,l,m=-\infty}^{+\infty} \sum_{r_x=0}^{+\infty} sum_{p_x=0}^{2^{r_x}-1}\, {}_kE^{x,\psi_{r_x,p_x}\phi}_{l-1/2,m}\, h_k(t)\, \psi^{r_x}_{l-1/2,p_x}(x)\, \phi_m(y) \end{aligned}$$

$$+ \sum_{k,l,m=-\infty}^{+\infty} \sum_{r_x,r_y=0}^{+\infty} \sum_{p_x,p_y=0}^{2^{r_x,r_y}-1} {}_kE^{x,\psi_{r_x,p_x}\psi_{r_y,p_y}}_{l-1/2,m}\ h_k(t)\ \psi^{r_x}_{l-1/2,p_x}(x)\ \psi^{r_y}_{m,p_y}(y) \tag{4.4}$$

where $\phi_n(x) = \phi(\frac{x}{\Delta x} - n)$ and $\psi^r_{n,p}(x) = 2^{r/2}\ \psi_0(2^r[\frac{x}{\Delta x} - n] - p)$ represent the Battle-Lemarie scaling and r-resolution wavelet function respectively in space and $h_k(t)$ represent rectangular pulses in time. ${}_kE^{\kappa,\mu\nu}_{i,j}$ and ${}_{k+1/2}H^{\kappa,\mu\nu}_{i,j}$ with $\kappa = x, y, z$ and $\mu, \nu = \phi, \psi$ are the coefficients for the field expansions in terms of scaling and wavelet functions. The indices i, j and k are the discrete space and time indices related to the space and time coordinates via $x = i\Delta x$, $y = j\Delta y$ and $t = k\Delta t$, where Δx,Δy are the space discretization intervals in x- and y-direction and Δt is the time discretization interval. Upon inserting the field expansions, Maxwell's equations are sampled using pulse functions as time-domain test functions and scaling and wavelet functions as space-domain test-functions. Following the procedure of Section 3.4, the 2.5D MRTD scheme is derived. As an example, let's consider the discretization of eq.(4.1). For simplicity, it is assumed that the fields have been expanded only in scaling functions summations. Wavelets can be added in a straightforward way yielding equations similar to (3.61). Applying the Galerkin's technique, the following difference equation is obtained for a homogeneous medium with the permittivity ϵ,

$$\frac{\epsilon}{\Delta t}({}_{k+1}E^{x,\phi\phi}_{i-1/2,j} - {}_kE^{x,\phi\phi}_{i-1/2,j}) = \frac{1}{\Delta y}(\sum_{j'=-n_a}^{n_a-1} a(j')\,{}_{k+1/2}H^{z,\phi\phi}_{i-1/2,j+j'+1-1/2}) + \beta\ {}_{k+1/2}H^{y,\phi\phi}_{i-1/2,j}\ , \tag{4.5}$$

with the coefficients $a(j')$ being defined in Table (3.1) The unit cell of the 2.5D-MRTD scheme is identical to the unit cell of the conventional Yee's FDTD scheme. To calculate the total field at a space point, the field expansions are sampled with delta test functions in space and time domain. For example, the total electric field $E_x(x_o, y_o, t_o)$ with $(k-1/2)\,\Delta t <$

$t_o < (k+1/2)\,\Delta t$, $\Delta x < x_o < i\,\Delta x$ and $(j-1/2)\,\Delta y < y_o < (j+1/2)\,\Delta y$ is calculated by

$$\begin{aligned} E_x(x_o, y_o, t_o) &= \int\int\int E_x(x,y,t)\,\delta(x-x_o)\,\delta(y-y_o)\,\delta(t-t_o)\,dx\,dy\,dt \\ &= \sum_{i',j'=-\infty}^{\infty} {}_k E^{x,\phi\phi}_{i+i'-1/2,j+j'}\,\phi_{i+i'-1/2}(x_o)\,\phi_{j+j'}(y_o) \\ &\approx \sum_{i',j'=-l_1}^{l_1} {}_k E^{x,\phi\phi}_{i+i'-1/2,j+j'}\,\phi_{i+i'-1/2}(x_o)\,\phi_{j+j'}(y_o) \quad . \end{aligned} \tag{4.6}$$

Extending the dispersion analysis from 2D to 2.5D space, the stability condition for the 2.5D S-MRTD scheme results in

$$\Delta t \leq \frac{1}{c\sqrt{((\frac{1}{\Delta x})^2 + (\frac{1}{\Delta y})^2)\sum_{i=0}^{n_a-1}|a(i')|^2 + (\frac{\beta}{2})^2}} \tag{4.7}$$

with the wave propagation velocity c. It is preferable to choose Δt at least 1.2-2.5 time less than the stability limit. In this way, much more linearity of the dispersion characteristics is achieved.

4.3 Applications of the 2.5D-MRTD scheme to Shielded Transmission Lines

First, the 2.5D-MRTD scheme is applied to the analysis of shielded stripline and microstrip lines to investigate propagation and coupling effects. Results for these shielded structures are presented and discussed separately below.

A shielded stripline is a simplified version of a membrane microstrip shown in (Fig.4.1a). The metallic shield has dimensions $47.6mm \times 22.0mm$ and the central strip has length $11.9mm$. The stripline is filled with air ($\epsilon_r = 1.$). The analysis for the higher order propagating modes is straightforward. For the analysis using Yee's FDTD scheme, a 40×10 mesh was used resulting in a total number of 400 grid points. When the structure was analyzed with the 2.5D-MRTD scheme , a mesh 8×4 (32 grid points) was chosen reducing

Mode	TEM	Shield TE_{10}
Analytic values	1.4324 GHz	3.4615 GHz
8x2 MRTD	1.4325 GHz	3.4648 GHz
Rel.Error	0.007%	0.095%
8x4 MRTD	1.4325 GHz	3.4641 GHz
Rel.Error	0.007%	0.075%
16x4 MRTD	1.4325 GHz	3.4633 GHz
Rel.Error	0.007%	0.052%
40x10 FDTD	1.4322 GHz	3.4585 GHz
Rel.Error	-0.014%	-0.087%

Table 4.1: Mode frequencies for $\beta = 30$

the total number of grid points by a factor of 12.5. In addition, the execution time for the analysis was reduced by a factor of 3 to 4. The time discretization interval was chosen to be identical for both schemes and equal to the 0.8 of the 2.5D-MRTD maximum Δt. For the analysis $\beta = 30$ was used and 5,000 time-steps were considered.

From (Table 4.1) it can observed that the calculated frequencies of the two first propagating modes for $\beta = 30$ by use of 2.5D-MRTD scheme are very close to the theoretical values, since the largest error is less than 0.1%. The relative error of the 2.5D-MRTD calculated frequencies is always positive, which corresponds to an overestimation of the resonant frequencies. This is exactly what has to be expected from the dispersion behavior of the MRTD schemes.

The non-localized character of the basis functions offers the opportunity to calculate the field values in any point of the discretization cells. The field values at the neighboring cells

can be combined appropriately by adjusting the scaling functions' values and by applying the image principle. For example, the total electric field $E_x(x_o, y_o, t_o)$ with $(k - 1/2)\,\Delta t < t_o < (k + 1/2)\,\Delta t$ is calculated by Eq.(4.6) by simply truncating the i', j' summation from $l_1 = -12, .., 12$ for each index. That means that the summation based only at the 12 neighboring cells from each side gives the total field component values with good accuracy. In (Fig.4.2-4.4), the value of the E_y field has been calculated and plotted for the 4 cells exactly below the strip by use of the 2.5D-MRTD scheme. The relative position of the strip is from 15 to 25 . For the TEM mode the pattern obtained by use of the conventional FDTD scheme is plotted for comparison. For the shield TE_{10} mode, the analytically calculated pattern has been added for reference. All results are normalized to the peak value. It can observed that the agreement of the MRTD calculated field pattern with the reference data is very good for the shield TE_{10} mode, where the values are changing slowly (sinusoidally) (Fig.4.2). On the contrary, for the TEM mode where the edge effect is more prominent, the agreement is not good. In this case, wavelets of 0-Resolution are added in both directions to describe the higher spatial frequencies. It can be observed from (Fig.4.3) that the wavelet coefficients for the 8x4 grid have a significant contribution (> 10%) close to the stripline. Increasing the grid size from 8 to 16 to the strip direction and/or from 4 to 8 to the normal to the strip direction improves more the accuracy of the field representation (Fig.4.4). It has been observed that 0-Resolution MRTD Schemes converge faster if the wavelet excitation coefficients are 3-4 times higher than the respective scaling coefficients.

The characteristic impedance Z_o for the TEM mode of the stripline is computed from the equation:

$$Z_o = \frac{V}{I} = \frac{\int_{C_v} E_y dy}{\oint_{C_c} H dl} \quad , \tag{4.8}$$

Subpoints/cell	Z_o^{sc} (Ω)	Relative error	Z_o^{wa} (Ω)	Relative error
3	80.56	-15.71 %	84.04	-12.07 %
5	94.46	-1.17 %	92.55	-3.17 %
7	99.06	+3.64 %	94.59	-1.04 %
9	101.44	+6.13 %	94.96	-0.65 %
11	97.56	+2.07 %	95.01	-0.60 %

Table 4.2: Z_o for different number of subpoints/cell (8x4 Grid).

where the integration paths C_v and C_c are shown in (Fig.4.1a). Since both of the schemes used in the analysis are discrete in space-domain, the above integrals are transformed to summations. For the FDTD summations, only one field value per cell is needed, due to the fact that pulse expansion functions which are constant for each cell are utilized. On the contrary, for the 2.5D-MRTD summation the field values for a number of subpoints along the integration path have to be calculated, since the expansion functions are not constant for each cell. It can be observed from (Table 4.2) that the accuracy of the calculation of the characteristic impedance is improved by increasing the number of subpoints per cell, at which the field values are calculated. An accuracy better than 1% is achieved if the field values are computed for more than 9 subpoints per cell along the integration path for the scheme including wavelets of 0-resolution to both directions. On the contrary, the value of Z_o that is calculated from the scheme based only on scaling functions is oscillating, thus indicating that a denser mesh is required. The analytical value of the Z_o is 95.58 Ω [61].

The modification of the dimensions of the MRTD mesh (Table 4.3) shows that the accuracy of the calculation of the Z_o by use of the MRTD is much better than that of the Yee's FDTD scheme with a 40x10 mesh (relative error -3.28%).

	Z_o (Ω)	Relative error
Analyt. Value	95.58	0.0%
8x4 MRTD	95.01	-0.60%
8x8 MRTD	95.19	-0.41%
16x4 MRTD	95.71	0.14%
40x10 FDTD	92.44	-3.28%

Table 4.3: Z_o for different mesh sizes (11 subpoints/cell).

A similar procedure is used for the analysis of the shielded coupled-stripline geometry of (Fig.4.1b) for the first even and odd mode. Both strips have a length of $11.9mm$, the distances between them is $11.9mm$, from the top and bottom PEC's are $11.0mm$ and from the left and right PEC's are $11.9mm$. The structure is filled with air ($\epsilon_r = 1.$). For the analysis with the conventional FDTD scheme, a 70×20 mesh resulted in a total number of 1400 grid pints. The same accuracy is achieved by an MRTD mesh 14×4 (56 grid points) resulting in an economy of memory by a factor of 25. The space distribution of the tangential-to-stripline E is plotted in logarithmic scale in (Fig.4.5) for the even mode.

The 2-D MRTD technique is also used for the analysis of a shielded microstrip (Fig.4.1c) with width $9.9mm$ on a dielectric substrate with $\epsilon_r = 10.65$ and thickness $11mm$. The microstrip is placed in the center of a rectangular shield $69.3mm$ x $44mm$. The same accuracy for the characteristic impedance calculation (Theoretical $Z_o = 50$ Ohms) is achieved by an FDTD mesh 140×80 and an MRTD mesh 28×20resulting in an economy in memory by a factor of 20.

4.4 Validation of the MRTD-PML Split and Non-split Algorithms

The extension of the popular PML absorber [13] principles for MRTD applications has been presented in CH.3. In this Section, the numerical performance of this absorber is investigated for 4-32 cells and for different cell sizes ($\lambda/10$-$\lambda/2.5$). Specifically, propagation constant, characteristic impedance and field patterns are derived for open transmission lines and compared to 2D results.

A parallel-plate waveguide of width d=48 mm, terminated at both ends by PML, is used to validate the described algorithm. A TM^z line source with a Gabor time variation is excited close to the one side of the waveguide. The benchmark MRTD solution with no reflections is obtained by simulating the case of a much longer parallel-plate waveguide of the same width to provide a reflection-free observation area for the time interval of interest. A quadratic variation in PML conductivity is assumed for all cases, with maximum theoretical reflection coefficient of 10^{-5} at normal incidence. Two frequency ranges are investigated,$[0, 0.9 f_c^{TM_1}]$ (TEM propagation) and $[0, 0.9 f_c^{TM_2}]$ ($TEM + TM_1$ propagation), where $f_c^{TM_n} = \frac{nc}{2d} = 3.125\ n\ (GHz)$ is the cutoff frequency of the TM_n mode. The time-step is chosen to be 0.637 of the Courant limit according to the stability analysis of Ch.5.

For the TEM propagation frequency range, it can be seen from Figs.(4.6)–(4.8) that for dense grids (Cell Size = $\lambda_{max}/10$) even 8 PML cells offer a numerical reflection close to -80 dB. Different values of theoretical maximum reflection ranging from 10^{-5} to 10^{-8} don't change significantly the numerical performance of the absorber (variation of 4-5 dB's). When 16 PML cells are used, the spurious reflection is below -100 dB for the whole frequency range. Similar conclusions can be drawn for the multimodal propagation ($TEM + TM_1$) in

Fig.(4.9). It can be observed that 8 and 16 PML cells cause a numerical reflection close to -70 dB and below -100 dB respectively. For coarse grids with cell sizes close to the Nyquist limit (Cell Size = $\lambda_{max}/2.5$), the behavior of the PML layer changes. The Large cell size causes retrospective reflections between the lossy cells and the numerical reflections from the absorber increase. Thus, a larger number of cells is required to obtain an acceptable reflection coefficient. Fig.(4.10)–(4.11) show that at least 32 cells are needed for reflection around -50 dB for the high frequencies. Again, the reflection at lower frequencies is negligible (below -100 dB's). It should be emphasized that the loss coefficients assigned to each cell must be given by Eq.(3.79); that implies that the conductivity profile must be sampled with the scaling and wavelet functions that have a significant value in the PML layer. For all simulations, scaling (and wavelet) functions located up to 6 cells away from the PML layer are used for the sampling. When this procedure is not applied and the loss coefficients get the point value of the loss distribution at each cell (FDTD approach), the PML performance gets worse as it is displayed at Fig.(4.12). It should be noted that the performances of the split and the non-split formulations are almost identical as it is displayed in Fig.(4.13).

4.5 Application of PML to the Analysis of Open Stripline Geometries

The PML non-split algorithm presented in Section 3.3.2 can be easily extended for the 2.5D and the 3D MRTD algorithms incorporating scaling and wavelet functions maintaining the same performance characteristics. For each resolution added to the scheme, the conductivity must be sampled with an appropriately positioned wavelet function. It was observed that S_{11} changes only by 1-1.6 dB after the enhancement of multiple resolutions.

In this section, the 2.5D MRTD scheme is applied to the analysis of open single and coupled striplines to investigate propagation and coupling effects. In all simulations only wavelets of the 0-resolution are used for both directions, since the value of the higher resolution fields is negligible (smaller than 1%).

First, the 2.5D MRTD scheme is applied to the analysis of the open stripline for the first (quasi-TEM) propagating mode. The analysis for the higher order propagating modes is straightforward. The central strip has a length of $23.8mm$ and the distances from the top and bottom are $5.5mm$ and $16.5mm$ respectively. The structure is filled with air ($\epsilon_r = 1.$). The PML absorber is applied for 4 cells to the left and the right sides of the structure and the maximum theoretical reflection is R_{max}=1e-7. For the analysis using Yee's FDTD scheme, a 42×28 mesh is used resulting in a total number of 1176 grid points. Analyzing the structure with the 2D-MRTD scheme, a mesh 12×4 (48 grid points) is chosen to reduce the total number of grid points by a factor of 24.5 . In addition, the execution time for the analysis is reduced by a factor of 4 to 5. The time discretization interval is chosen to be identical for both schemes and equal to 1/10 of the 2D-MRTD maximum Δt. For the analysis $\beta = 30$ is used and 20,000 time-steps are considered. From (Table 4.4) it can observed that the calculated frequencies of the dominant propagating mode for $\beta = 30$ by use of 2D-MRTD scheme is very close to the theoretical values, since the largest error is less than 0.1%, for mesh sizes much smaller than those used for the conventional FDTD simulations.

In (Fig.4.14), the pattern of the E_y field just below the strip has been calculated and plotted by use of the 2D-MRTD scheme. The pattern obtained by use of the conventional FDTD scheme is plotted for comparison. Since the edge effect is prominent, a mesh 12×8 (96 grid points) with scaling functions and wavelets of 0-resolution is used for the MRTD

Mode	TEM	Rel.Error
Analytic values	1.4324 GHz	0.000%
12x4 MRTD	1.4329 GHz	0.035%
12x8 MRTD	1.4325 GHz	0.007%
42x28 FDTD	1.4321 GHZ	-0.021%

Table 4.4: Dominant mode frequency for $\beta = 30$

simulation. The characteristic impedance Z_o for the quasi-TEM mode of the stripline is computed from Eq.(4.8).

For the FDTD summations, only one field value per cell is needed, due to the fact that pulse expansion functions which are constant for each cell are utilized. On the contrary, for the 2D-MRTD summation the field values for a number of subpoints along the integration path have to be calculated, since the expansion functions are not constant for each cell. (Table 4.5) shows that the accuracy of the calculation of the characteristic impedance is improved by increasing the number of subpoints per cell, at which the field values are calculated. An accuracy better than 1% is achieved if the field values are computed for more than 9 subpoints per cell along the integration path. (Table 4.5) shows the calculated values of the characteristic impedance Z_o.

A similar procedure was used for the analysis of the open coupled-stripline geometry of (Fig.4.15) for the dominant even and odd modes. Both strips have a length of $23.8mm$, the distances between them is $23.8mm$, from the top PEC $16.5mm$ and from the bottom PEC $5.5mm$. The MRTD-PML layer has a thickness of 4 cells ($23.8mm$) with maximum reflection R_{max}=1e-7 and starts *exactly* at the edge of the striplines. The structure is filled with air ($\epsilon_r = 1.$). For the analysis with the conventional FDTD scheme, a 65×20 mesh

	Z_o (Ω)	Relative error
Analyt. Value	56.83	0.0%
12x4 MRTD	57.24	+0.72%
12x8 MRTD	57.09	+0.46%
42x28 FDTD	54.96	-3.29%

Table 4.5: Z_o for different mesh sizes.

resulted in a total number of 1300 grid points. The same accuracy is achieved by an MRTD mesh 20×4 (80 grid points) resulting in an economy of memory by a factor of 16.25. The space distribution of the tangential-to-stripline E is plotted in logarithmic scale in (Fig.4.16) for the even mode and in (Fig.4.17) for the odd mode.

4.6 Conclusion

A multiresolution time-domain scheme in 2D has been applied to the numerical analysis of shielded and open striplines and microstrips. The field patterns and the characteristic impedance have been calculated and verified by comparison to reference data. In comparison to Yee's conventional FDTD scheme, the proposed 2.5D-MRTD scheme offer memory savings by a factor of 25 and execution time savings by a factor of about 4-5 maintaining a better accuracy for characteristic impedance calculations. This indicates memory savings of a factor 5 per dimension leading to two orders of memory savings in three dimensions. Compared to 2.5D-FDTD, 25 times less cells in MRTD require about 5 times less running time, thus the computation time per cell is increased by a factor of 5. This leads to computation time savings of more than one order for 3 dimensional structures. For structures, where the edge effect is prominent, additional wavelets have to be introduced to improve the accuracy

when using a coarse MRTD mesh. A non-split PML absorber has been evaluated and its performance is similar to that of the conventional FDTD Split PML absorber (reflections close to -100 dB).

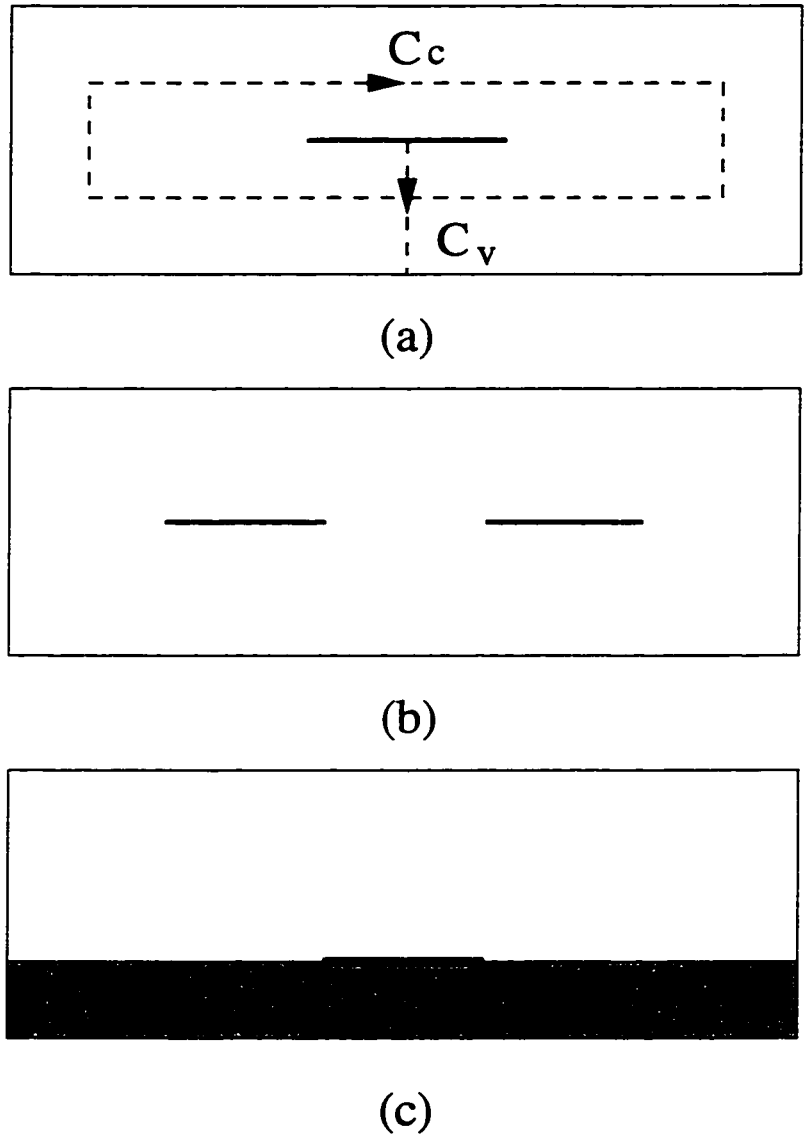

Figure 4.1: Printed Lines Geometries.

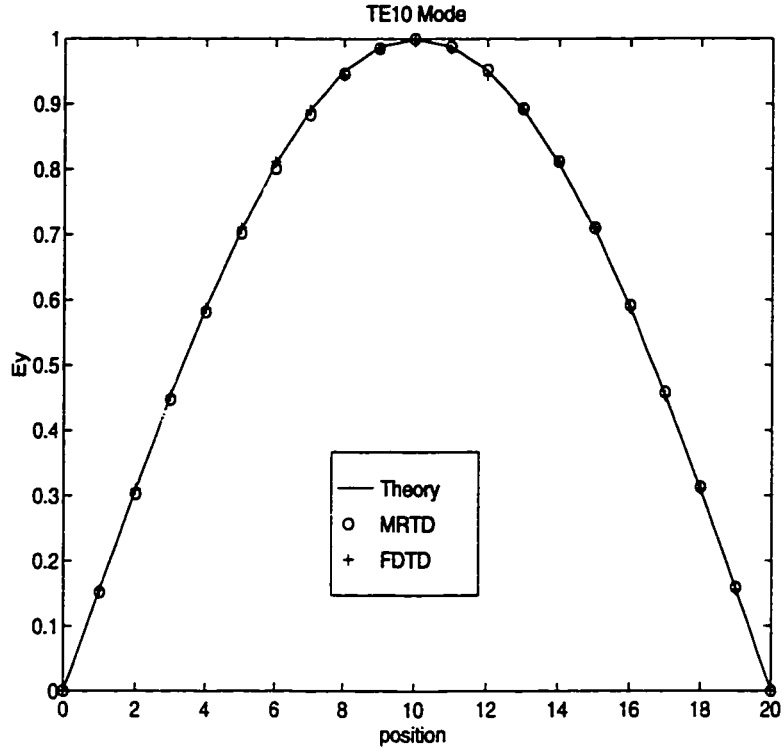

Figure 4.2: Shield TE_{10} E_y pattern.

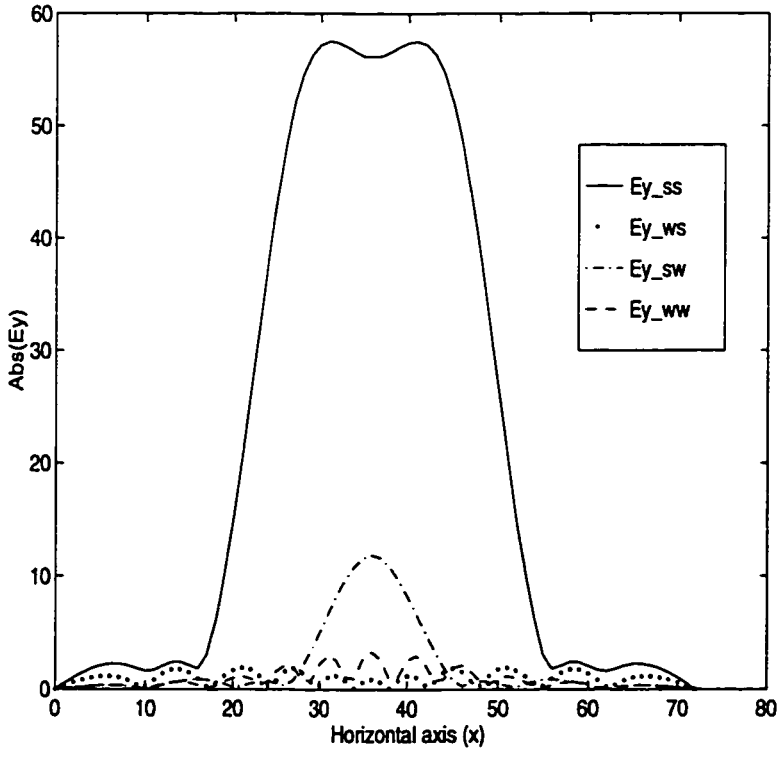

Figure 4.3: TEM E_y Pattern Components (8x8 Grid).

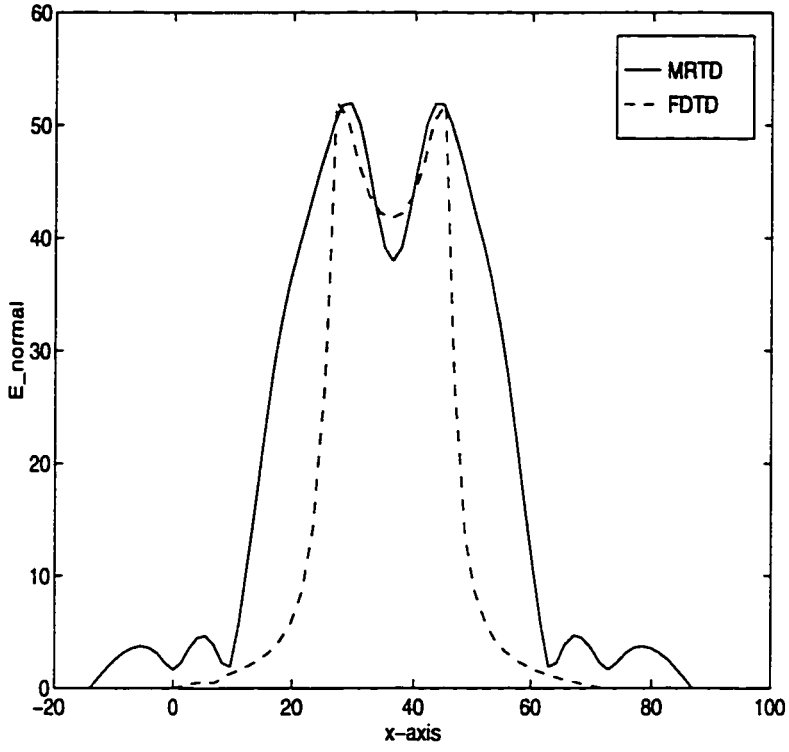

Figure 4.4: TEM E_y Pattern Comparison (8x8 Grid).

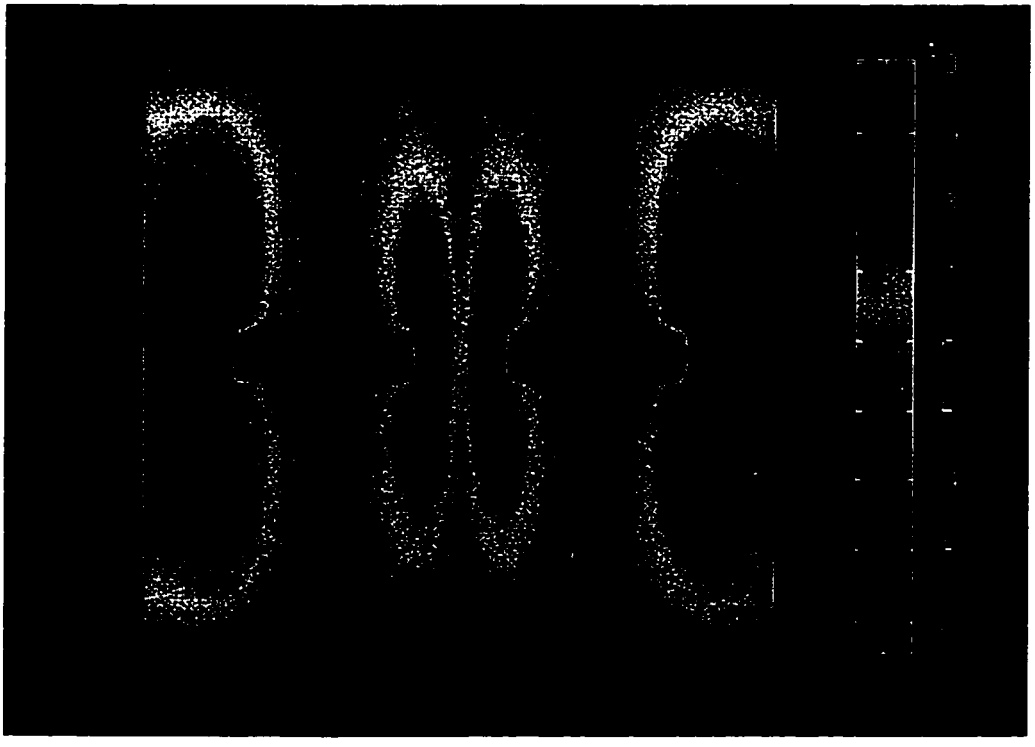

Figure 4.5: Tangential E-field Distribution (Shielded - Even Mode).

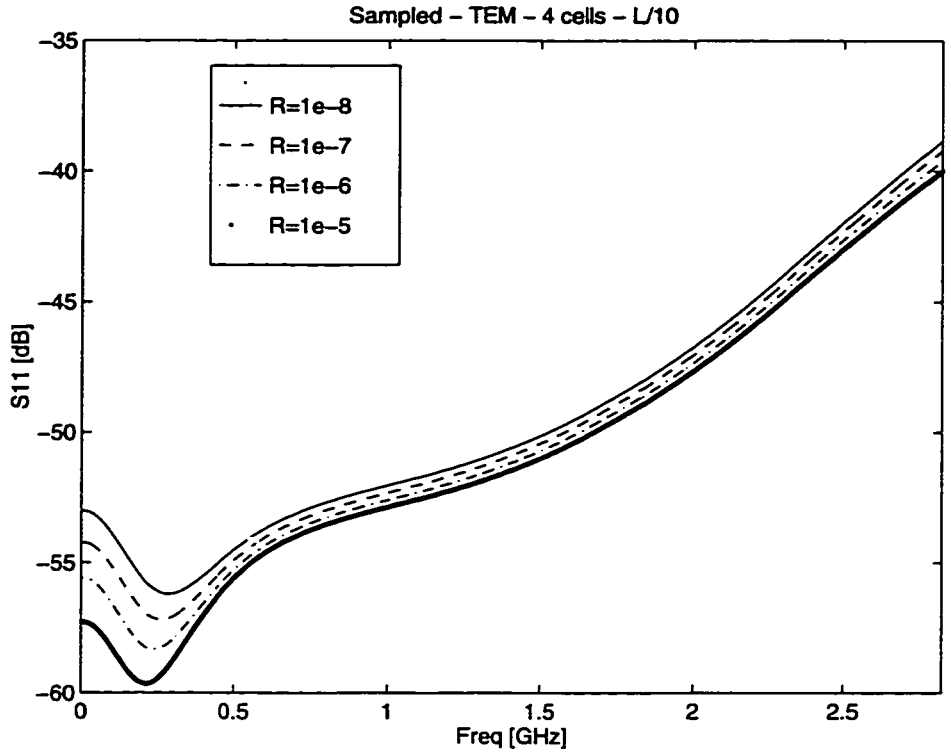

Figure 4.6: 4 PML cells - Non-split formulation - Dense Grid.

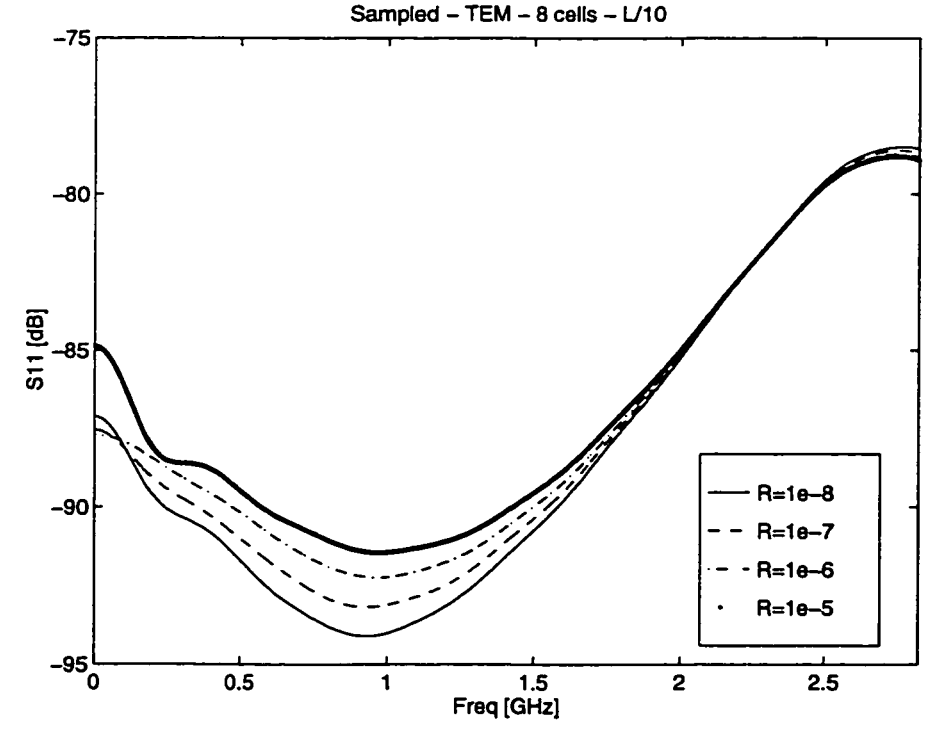

Figure 4.7: 8 PML cells - Non-split formulation - Dense Grid.

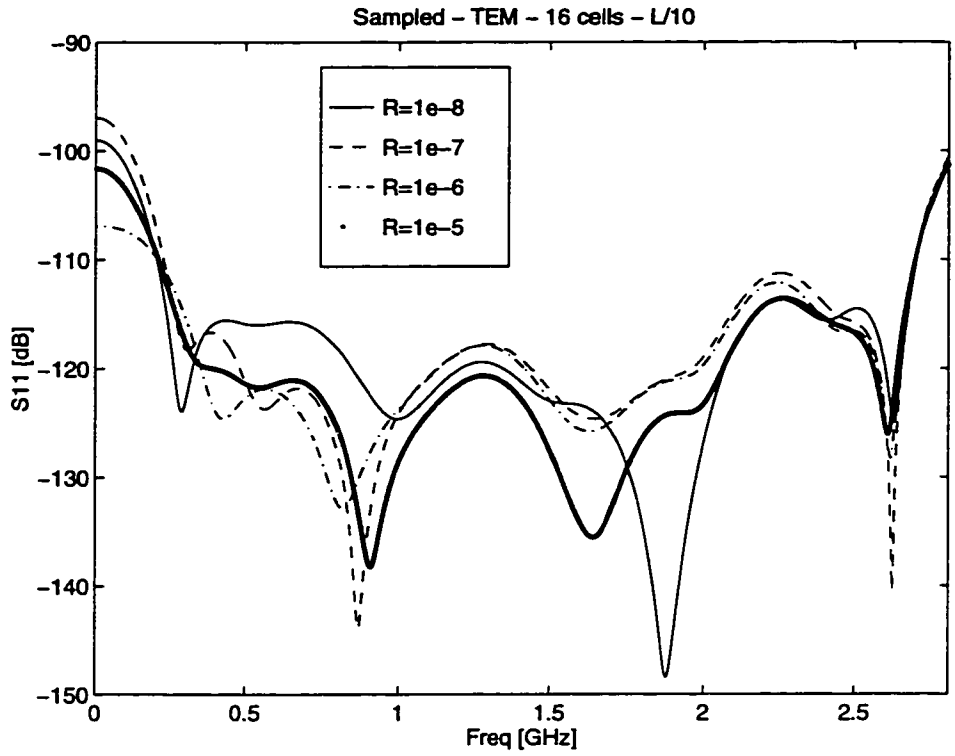

Figure 4.8: 16 PML cells - Non-split formulation - Dense Grid.

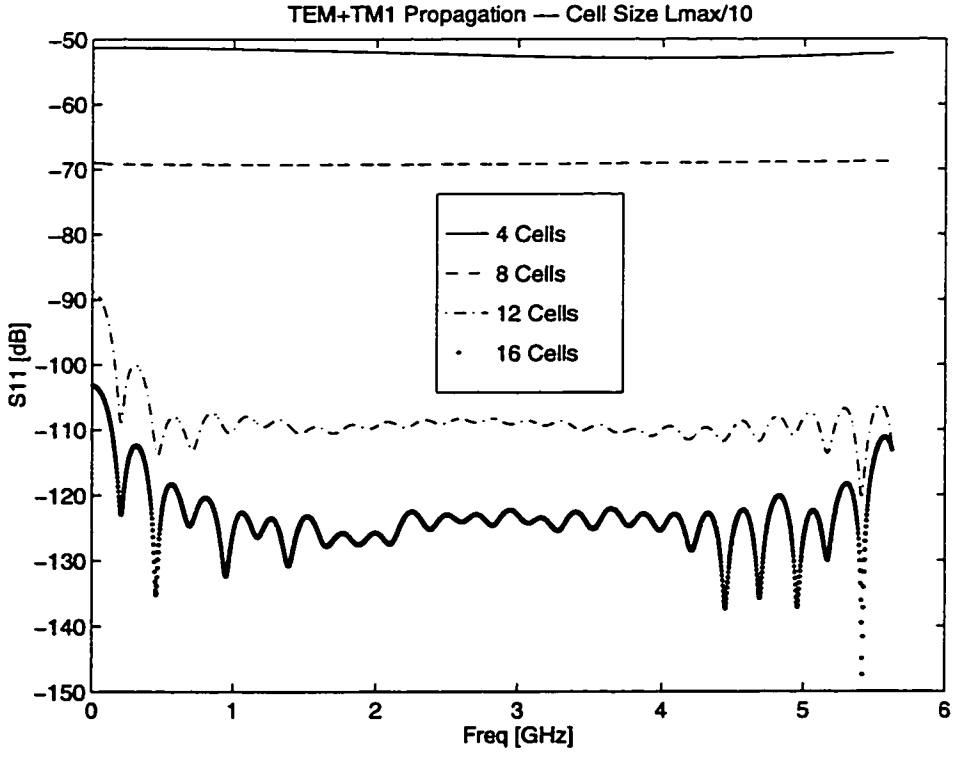

Figure 4.9: Multimodal Propagation - Dense Grid.

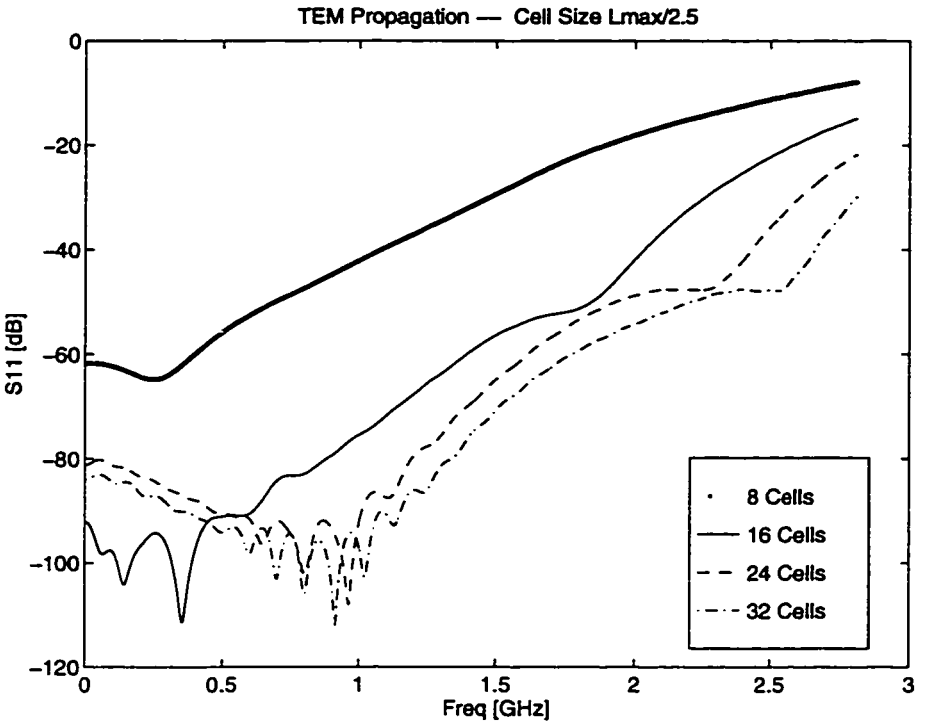

Figure 4.10: TEM Propagation - Coarse Grid.

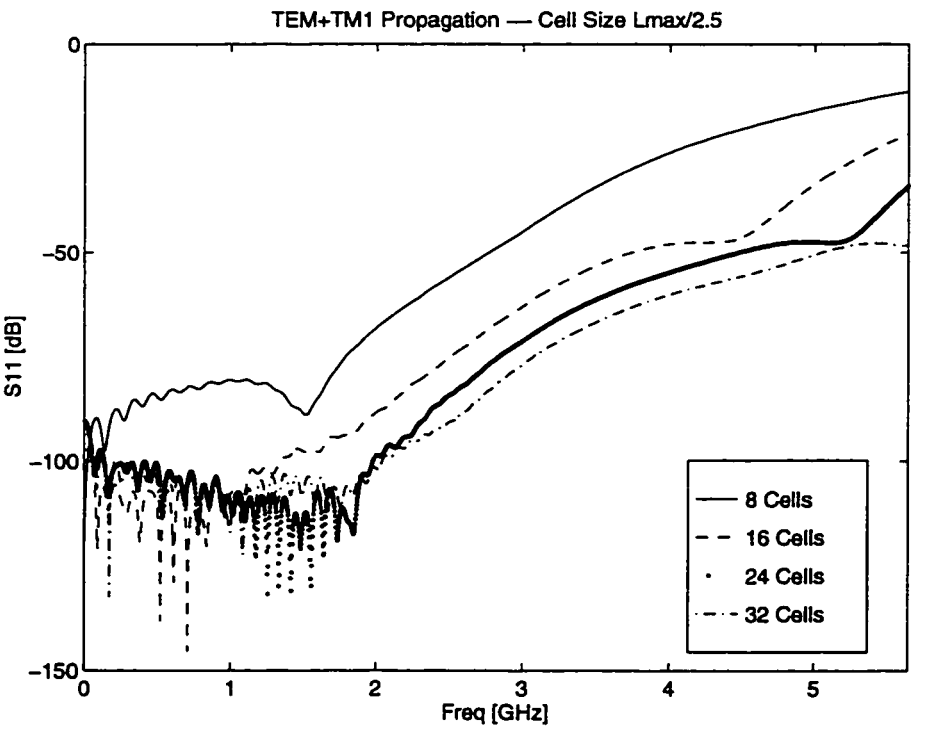

Figure 4.11: Multimodal Propagation - Coarse Grid.

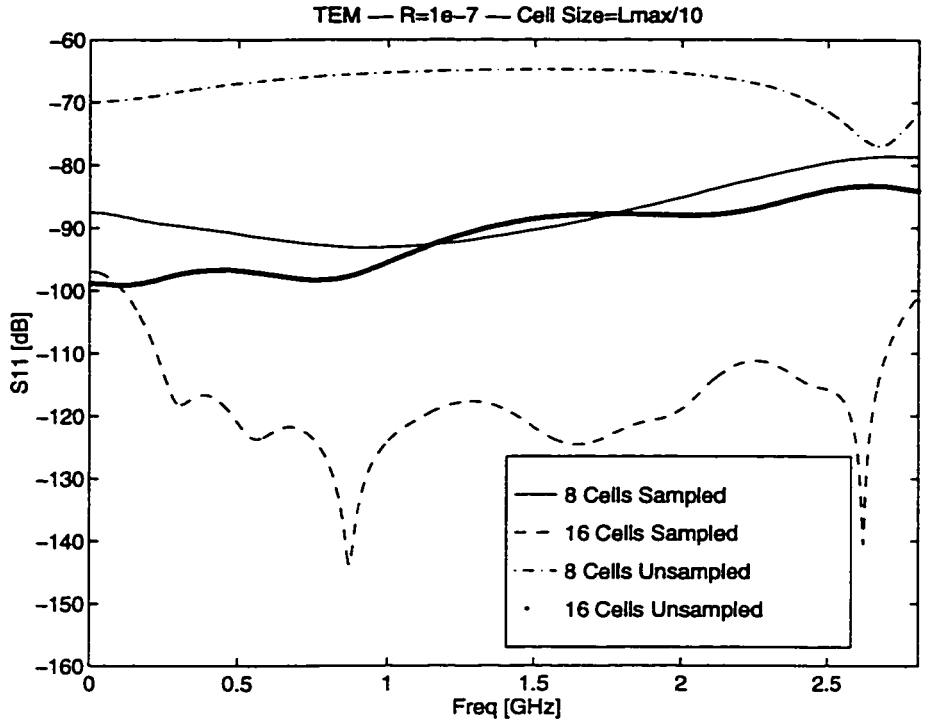

Figure 4.12: Comparison of Sampled vs. Non-sampled PML.

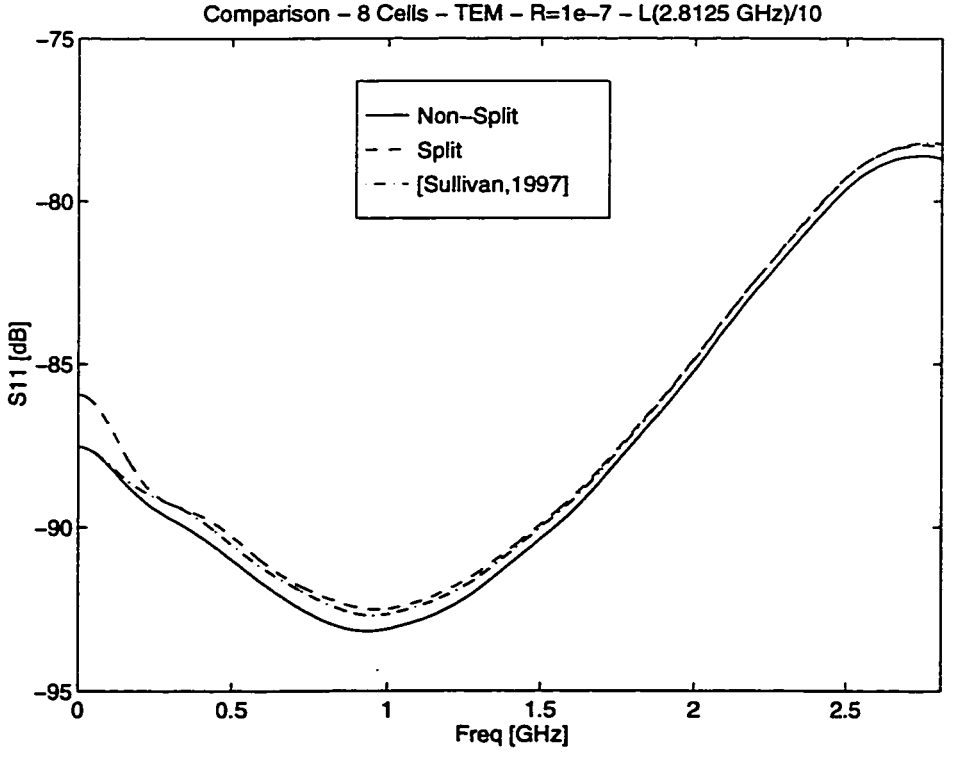

Figure 4.13: Comparison of the Split and Non-split Formulations.

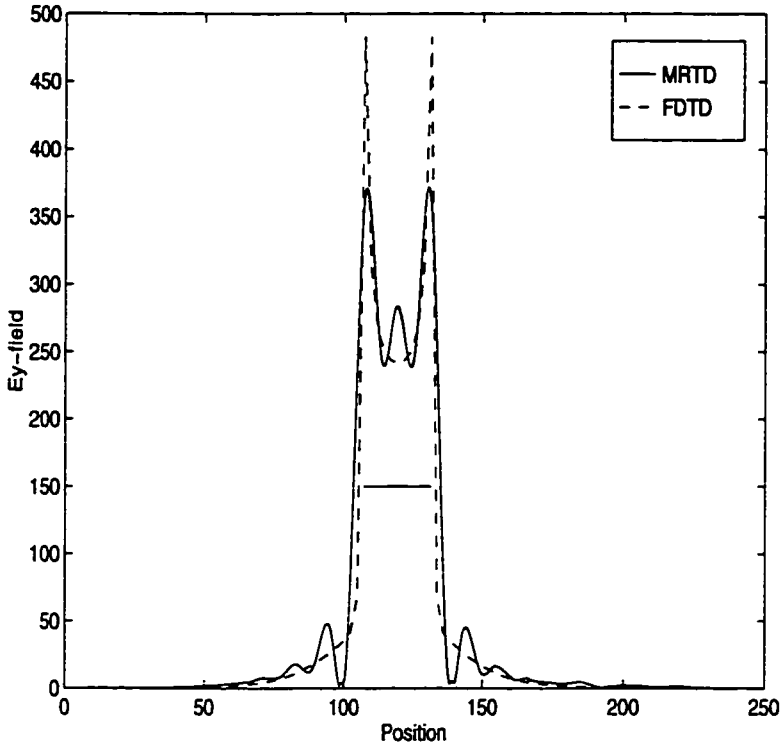

Figure 4.14: Open Single Stripline - E_y TEM Distribution.

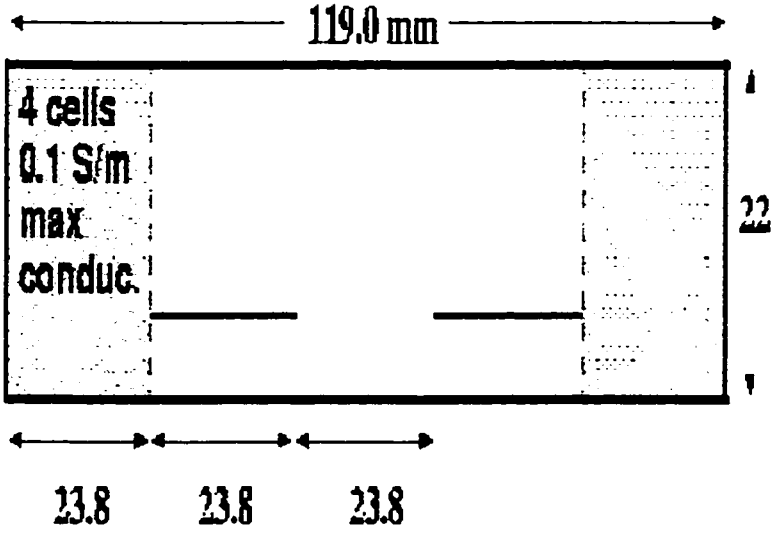

Figure 4.15: Open Coupled Stripline Geometry.

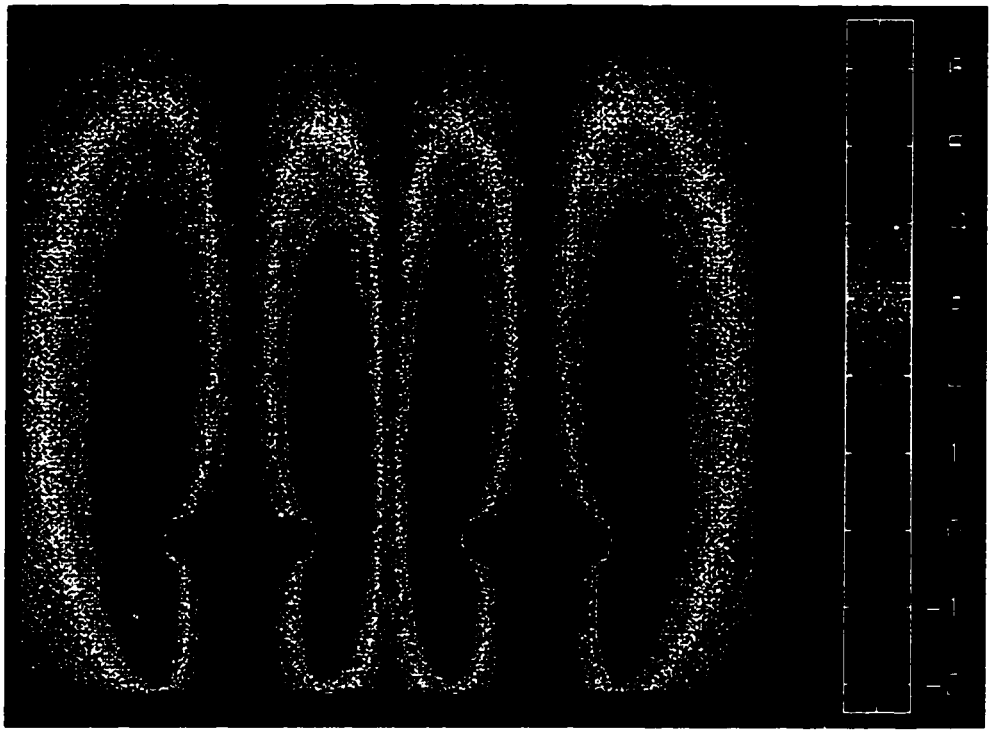

Figure 4.16: Tangential E-field Distribution (Open - Even Mode).

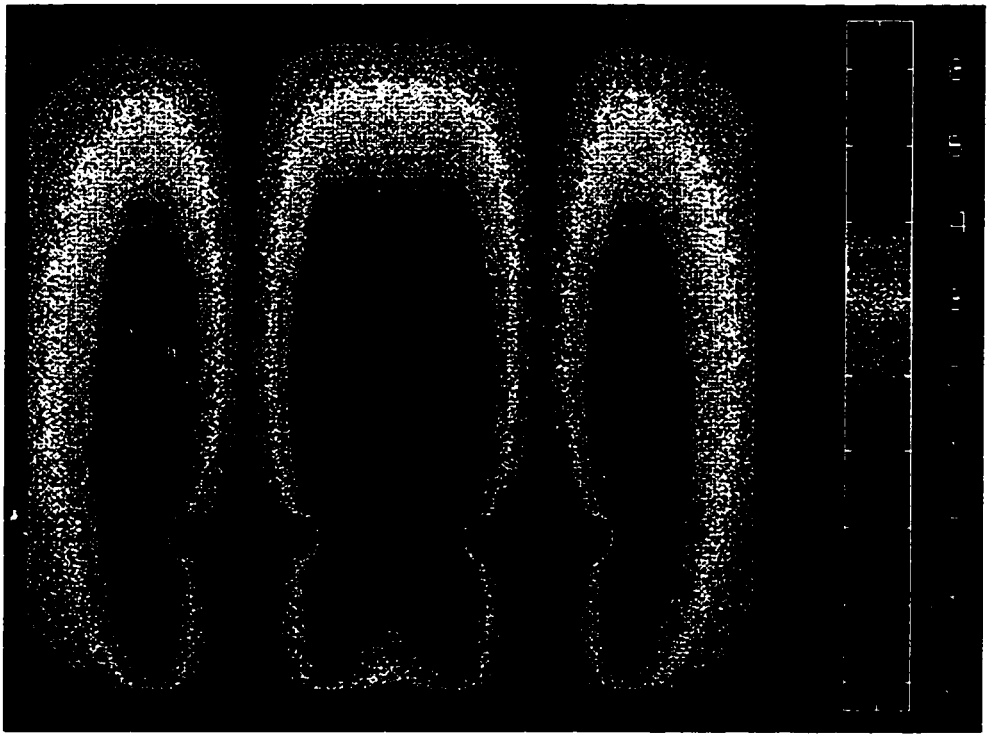

Figure 4.17: Tangential E-field Distribution (Open - Odd Mode).

CHAPTER 5

Stability and Dispersion Analysis of Multiresolution Time-Domain Schemes

5.1 Introduction

Discretized Time-Domain numerical techniques are very popular in the analysis of various microwave geometries and for the modeling of EM wave propagation. Though many of them are very simple to implement and can be easily applied to different topologies with remarkable accuracy, they cause a numerical phase error during the propagation along the discretized grid [62]. For example, the numerical phase velocity in the FDTD can be different than the velocity of light, depending on the cell size as a fraction of the smallest propagating wavelength and the direction of the grid propagation. Thus, a non-physical dispersion is introduced and affects the accuracy limits of FDTD simulations, especially of large structures.

In addition, it is well-known that the finite-difference schemes in time and space domain require that the used time step should take values within an interval that is a function of the cell size. If the time-step takes a value outside the bounds of this interval, the algorithm will be numerically unstable, leading to a spurious increase of the field values without limit

as the time increases.

Though the stability and the dispersion analysis for the conventional Yee's FDTD algorithm has been thoroughly investigated, only a few results have been presented concerning MRTD schemes based on cubic spline Battle-Lemarie scaling and wavelet functions [31]. The functions of this family do not have compact support, thus the finite approximations of the derivatives are finite-stencil summations instead of finite differences. In this paper, the effect of these stencils' size as well as of the enhancement of wavelets is investigated and a comparison with 2nd-order and higher-order FDTD schemes exhibits the differences in their respective behaviors.

5.2 Stability Analysis

Following the stability analysis described in [62], the MRTD [31] equations are decomposed into separate time and space eigenvalue problems. Assuming a 2D expansion only to scaling functions (S-MRTD) similar to Eqs.(3.36)-(3.38) of CH.3, the left-hand side time-differentiation parts can be written as an eigenvalue problem

$$\frac{{}_{k+1/2}H^x_{i,j-1/2} - {}_{k-1/2}H^x_{i,j-1/2}}{\Delta t} = \Lambda \; {}_kH^x_{i,j-1/2} \tag{5.1}$$

$$\frac{{}_{k+1/2}H^y_{i-1/2,j} - {}_{k-1/2}H^y_{i-1/2,j}}{\Delta t} = \Lambda \; {}_kH^y_{i-1/2,j} \tag{5.2}$$

$$\frac{{}_{k+1}E^z_{i,j} - {}_kE^z_{i,j}}{\Delta t} = \Lambda \; {}_{k+1/2}E^z_{i,j} \quad . \tag{5.3}$$

In order to avoid having any spatial mode increasing without limit during normal time-stepping, the imaginary part of Λ, $Imag(\Lambda)$, must satisfy the equation

$$-\frac{2}{\Delta t} \leq Imag(\Lambda) \leq \frac{2}{\Delta t} \quad . \tag{5.4}$$

For each time step k, the instantaneous values of the electric and magnetic fields distributed in space across the grid can be Fourier-transformed with respect to the i- and j- coordinates

to provide a spectrum of sinusoidal modes (plane wave eigenmodes of the grid). Assuming an eigenmode of the spatial-frequency domain with k_x and k_y being the x- and y- components of the numerical eigenvector, the field components can be written

$$\begin{aligned} E^z_{I,J} &= E_{z_o} e^{j(k_x I\Delta x + k_y J\Delta y} \\ H^x_{I,J-1/2} &= H_{x_o} e^{j(k_x I\Delta x + k_y (J-1/2)\Delta y} \\ H^y_{I-1/2,J} &= H_{y_o} e^{j(k_x (I-1/2)\Delta x + k_y J\Delta y} \end{aligned} \quad .$$

Substituting these expressions to (5.1)–(5.3) and applying Euler's identity, we get

$$\Lambda^2 = -\frac{4}{\mu\epsilon}[\frac{1}{(\Delta x)^2}(\sum_{i'=0}^{n_a-1} a(i') sin(k_x(i+1/2)\Delta x))^2 + \frac{1}{(\Delta y)^2}(\sum_{j'=0}^{n_a-1} a(j') sin(k_y(j+1/2)\Delta y))^2] \quad .$$

Thus, Λ is a pure imaginary, which can be bounded for any wavevector $k = (k_x, k_y)$:

$$\begin{aligned} -\ 2c\ (\sum_{i'=0}^{n_a-1} |a(i')|) \sqrt{\frac{1}{(\Delta x)^2} + \frac{1}{(\Delta y)^2}} &\leq Imag(\Lambda) \\ \leq\ 2c\ (\sum_{i'=0}^{n_a-1} |a(i')|) \sqrt{\frac{1}{(\Delta x)^2} + \frac{1}{(\Delta y)^2}} &\quad , \end{aligned} \tag{5.5}$$

where $c = \frac{1}{\sqrt{\mu\epsilon}}$ is the velocity of the light in the modeled medium.

Numerical stability is maintained for every spatial mode only when the range of eigenvalues given by (5.5) is contained entirely within the stable range of time-differentiation eigenvalues given by (5.4). Since both ranges are symmetrical around zero, it is adequate to set the upper bound of (5.5) to be smaller or equal to (5.4), giving:

$$\Delta t \leq \frac{1}{c\ (\sum_{i'=0}^{n_a-1} |a(i')|) \sqrt{\frac{1}{(\Delta x)^2} + \frac{1}{(\Delta y)^2}}} \quad . \tag{5.6}$$

For $\Delta x = \Delta y = \Delta$, the above stability criterion gives

$$\Delta t_{S-MRTD} \leq \frac{\Delta}{c\sqrt{2}\sum_{i'=0}^{n_a-1} |a(i')|} = s_{SS}\frac{\Delta}{c\sqrt{2}} \quad . \tag{5.7}$$

It is known [10] that

$$\Delta t_{FDTD} \leq \frac{1}{c\sqrt{\frac{1}{(\Delta x)^2} + \frac{1}{(\Delta y)^2}}} \quad , \tag{5.8}$$

which gives for $\Delta x = \Delta y = \Delta$

$$\Delta t_{FDTD} \leq \frac{\Delta}{c\sqrt{2}} \quad . \tag{5.9}$$

Equations (5.7)–(5.9) show that for same discretization size, the upper bounds of the time-steps of FDTD and S-MRTD are comparable and related through the factor s. The stability analysis can be generalized easily to 3D. The new stability criteria can be derived by the equations (5.7) and (5.9) by substituting the term $\sqrt{2}$ with $\sqrt{3}$.

More complicated expressions can be derived for the maximum allowable time-step for schemes containing scaling and wavelet functions. For simplicity and without loss of generality, it is assumed that the stencil size is equal for all three summations ($n_a = n_b = n_c = n$). The upper bound of the time-step for the 2D MRTD scheme with 0-resolution wavelets to the one (x-direction) or two directions (x- and y-directions) for Δx=Δy=Δ is given by

$$\Delta t_{W_0S-MRTD,max} \approx s_{W_0S}\frac{\Delta}{c\sqrt{2}}$$

with

$$s_{W_0S} = \frac{2}{\sqrt{3(\sum_{i'}|a|)^2 + (\sum_{i'}|b_0|)^2 + 2(\sum_{i'}|c_0|)^2 + (\sum_{i'}|a+b_0|)\sqrt{(\sum_{i'}|a-b_0|)^2 + 4(\sum_{i'}|c_0|)^2}}}$$

and

$$\Delta t_{W_0W_0-MRTD,max} \approx s_{W_0W_0}\frac{\Delta}{c\sqrt{2}}$$

with

$$s_{W_0W_0} = \frac{2}{\sqrt{2(\sum_{i'}|a|)^2 + 2(\sum_{i'}|b_0|)^2 + 4(\sum_{i'}|c_0|)^2 + 2(\sum_{i'}|a+b_0|)\sqrt{(\sum_{i'}|a-b_0|)^2 + 4(\sum_{i'}|c_0|)^2}}}$$

where the notation

$$\sum_{k'}|x| = \sum_{k'=0}^{n-1}|x(k')|$$

has been used.

It can be observed that the upper bound of the time step depends on the stencil size n_a, n_b, n_c. This dependence is expressed through the coefficients $s_{SS}, s_{W_0S}, s_{W_0W_0}$, which decrease as the stencil size increases . (Figure 5.1) shows that s_{SS} practically converges to the value 0.6371 after $n_a \geq 10$ and $s_{W_0S} \approx 0.3433$ and $s_{W_0W_0} \approx 0.2625$ for $n_a = n_b = n_c \geq 10$. The expression of s_{SS} can be easily derived by the expressions of s_{W_0S} and $s_{W_0W_0}$ by zeroing out the effect of b_0,c_0.

5.3 Dispersion Analysis

To calculate the numerical dispersion of the S-MRTD scheme, plane monochromatic traveling-wave trial solutions are substituted in the discretized Maxwell's equations. For example, the E_z component for the TM^z mode has the form

$$ {}_kE^z_{I,J} = E_{z_o} e^{j(k_x I\Delta x + k_y J\Delta y - \omega k\Delta t)} \quad , $$

where k_x and k_y are the x- and y- components of the numerical wavevector and ω is the wave angular frequency. Substituting the above expressions into Eqs.(3.36)-(3.38), the following numerical dispersion relation is obtained for the TM^z mode for the S-MRTD Scheme after algebraic manipulation

$$ \begin{aligned} [\frac{1}{c\Delta t} sin(\frac{\omega\Delta t}{2})]^2 &= [\frac{1}{\Delta x}(\sum_{i'=0}^{n_a-1} a(i') sin(k_x(i+1/2)\Delta x))]^2 \\ &+ [\frac{1}{\Delta y}(\sum_{j'=0}^{n_a-1} a(j') sin(k_y(j+1/2)\Delta y))]^2 \end{aligned} \qquad (5.10) $$

For square unit cells (Δx=Δy=Δ) and wave propagating at an angle ϕ with respect to x-axis ($k_x = k\ cos\phi$ and $k_y = k\ sin\phi$), the above expression is simplified to

$$[\frac{\Delta}{c\Delta t}\ sin(\frac{\omega\ \Delta t}{2})]^2 \ = \ (\sum_{i'=0}^{n_a-1} a(i')\ sin(k\ cos\phi\ (i'+1/2)\ \Delta))^2$$
$$+ \ (\sum_{j'=0}^{n_a-1} a(j')\ sin(k\ sin\phi\ (j'+1/2)\ \Delta))^2 \qquad (5.11)$$

This equation relates the numerical wavevector, the wave frequency, the cell size and the time-step. Solving this numerically for different angles, time-step sizes and frequencies, the dispersion characteristics can be quantified.

Defining the Courant number $q = (c\Delta t)/\Delta$ and the number of cells per wavelength $n_l = \lambda_{REAL}/\Delta$ and using the definition of the wavevector $k = (2\pi)/\lambda_{NUM}$ the dispersion relationship can be written as

$$[\frac{1}{q}\ sin(\pi\ q\ /n_l)]^2 \ = \ [\sum_{i'=0}^{n_a-1} a(i')\ sin(\pi\ u\ (2i'+1)\ cos\phi\ /n_l)]^2$$
$$+ \ [\sum_{j'=0}^{n_a-1} a(j')\ sin(\pi\ u\ (2j'+1)\ sin\phi\ /n_l)]^2 \qquad (5.12)$$

where $u = \lambda_{REAL}/\lambda_{NUM}$ is the ratio of the theoretically given to the numerical value of the propagating wavelength and expresses the phase error introduced by the S-MRTD algorithm. To satisfy the stability requirements, q has to be smaller than 0.45 ($= 0.6371/\sqrt{2}$) for the 2D simulations.

The above analysis can be extended to cover the expansion in scaling and 0-resolution wavelet functions in x-, y- or both directions.

The general dispersion relationship is

$$\frac{\mu}{\epsilon}(C_1C_1 + C_2C_2 + C_4C_4 + C_5C_5) + (\frac{\mu}{\epsilon})^2[\frac{(C_4C_5 + C_5C_6)^2}{A} \ + \ \frac{(C_1C_2 + C_2C_3)^2}{B}]$$
$$+(\frac{\mu}{\epsilon})^4(C_1C_2 + C_2C_3)^2(C_4C_5 + C_5C_6)^2(\frac{1}{A} + \frac{1}{B})^2\frac{1}{F} \ = \ 1 \qquad (5.13)$$

with

$$F = 1 \ - \ [\frac{\mu}{\epsilon}(C_1C_2 + C_2C_3)]^2\frac{1}{A} - [\frac{\mu}{\epsilon}(C_4C_5 + C_5C_6)]^2\frac{1}{B}$$

Scheme	C_1	C_2	C_3	C_4	C_5	C_6
SS	$\neq 0$	0	0	$\neq 0$	0	0
W_0S	$\neq 0$	0	0	$\neq 0$	$\neq 0$	$\neq 0$
SW_0	$\neq 0$	$\neq 0$	$\neq 0$	$\neq 0$	0	0
W_0W_0	$\neq 0$	$\neq 0$	$\neq 0$	$\neq 0$	$\neq 0$	$\neq 0$

Table 5.1: Coefficients C_i for Different MRTD Schemes

$$- \ [\frac{\mu}{\epsilon}(C_2C_2 + C_3C_3 + C_5C_5 + C_6C_6] \tag{5.14}$$

$$\begin{aligned} A &= 1 - \frac{\mu}{\epsilon}(C_1C_1 + C_2C_2 + C_5C_5 + C_6C_6) \\ B &= 1 - \frac{\mu}{\epsilon}(C_2C_2 + C_3C_3 + C_4C_4 + C_5C_5) \end{aligned} \tag{5.15}$$

. The C_i are defined by

$$\begin{aligned} C_1 &= -\frac{\Delta t}{\mu\Delta sin(\omega\Delta t/2)} \sum_{j'=0}^{n_a} a(j')sin(k_y(j'+1/2)\Delta) \\ C_2 &= -\frac{\Delta t}{\mu\Delta sin(\omega\Delta t/2)} \sum_{j'=0}^{n_c} c_0(j')sin(k_y j'\Delta) \\ C_3 &= -\frac{\Delta t}{\mu\Delta sin(\omega\Delta t/2)} \sum_{j'=0}^{n_b} b_0(j')sin(k_y(j'+1/2)\Delta) \\ C_4 &= -\frac{\Delta t}{\mu\Delta sin(\omega\Delta t/2)} \sum_{i'=0}^{n_a} a(i')sin(k_x(i'+1/2)\Delta) \\ C_2 &= -\frac{\Delta t}{\mu\Delta sin(\omega\Delta t/2)} \sum_{i'=0}^{n_c} c_0(i')sin(k_x i'\Delta) \\ C_3 &= -\frac{\Delta t}{\mu\Delta sin(\omega\Delta t/2)} \sum_{i'=0}^{n_b} b_0(i')sin(k_x(i'+1/2)\Delta) \end{aligned} \tag{5.16}$$

Eq.(5.13) can be applied to the dispersion analysis of SS (only scaling functions), W_0S (0-resolution wavelets only to x-direction), SW_0 (0-resolution wavelets only to y-direction) and W_0W_0 (0-resolution wavelets to both x - and y- directions) following Table (5.1). In case the $C_i \neq 0$, it can be calculated by Eq.(5.16).

The above equation is solved numerically by use of Bisection-Newton-Raphson Hybrid

Technique for different values of n_a, n_b, n_c n_l, ϕ and q. (Figs.5.2–5.5) show the variation of the numerical phase velocity as a function of the inverse of the Courant number 1/s=1/q for stencil sizes $n_a = n_b = n_c = 8, 10, 12, 14$. For each figure, three different discretization sizes are used: 10 cells/wavelength (coarse), 20 cells/wavelength (normal) and 40 cells/wavelength (dense). The results are compared to the respective values of conventional FDTD. It can be observed that the phase error for F.D.T.D. decreases quadratically. The variation of the phase error in M.R.T.D. exhibits some unique features. Though for any stencil size the numerical phase error for M.R.T.D. discretization of $10 cells/\lambda$ is smaller than that of the F.D.T.D. discretization of $40 cells/\lambda$, the M.R.T.D. error doesn't behave monotonically [63]. It decreases up to a certain discretization value and then it starts increasing. This value depends on the stencil size and takes larger values for larger stencils. For example, this value is between 10 and 20 $cells/\lambda$ for stencil equal to 10, between 20 and 40 $cells/\lambda$ for stencil=12 and very close to 40 $cells/\lambda$ for stencil=14 and can be used as a criterion to characterize the discretization range that the M.R.T.D. offers significantly better numerical phase performance than the F.D.T.D.

The phase error caused by the dispersion is cumulative and it represents a limitation of the conventional FDTD Yee algorithm for the simulation of electrically large structures. It can be observed that the error of S-MRTD is significantly lower, allowing the modeling of larger structures. FDTD is derived be expanding the fields in pulse basis. As it is well known the Fourier transform of the pulse is a highly oscillating Si(x). On the contrary, the Fourier transform of the Battle-Lemarie Cubic spline is similar to a low-pass filter. That "smooth" spectral characteristic offers a much lower phase error even for very coarse (close to 3-4 cells/λ) cells.

By using a larger stencil n_a, the entire-domain oscillating nature of the scaling functions

is better represented. Thus, smoother performance for low discretizations (Fig.5.6) and lower phase error for higher discretizations (Fig.5.7) is achieved as n_a increases from 8 to 12. Wavelets contribute to the improvement of the dispersion characteristics for even coarser cells (close to 2.2-2.4 cells/λ) as it is demonstrated in (Figs.5.8–5.13). For discretizations above 4 cells/λ the effect of the wavelets is negligible. (Fig.5.11) and (Fig.5.13) show clearly that the phase error has a minimum for a specific discretization (17 for $n_a = 10$ and 25 for $n_a = 12$).

(Figs.5.14-5.17) show that for discretizations smaller than $30 cells/\lambda$ the choice of the Courant number affects significantly the dispersion performance which starts converging to the minimum numerical phase error (0.8 deg/λ for $n_a = n_b = n_c = 10$ and 0.2 deg/λ for $n_a = n_b = n_c = 12$) for 1/q close to 10. On the contrary, the F.D.T.D. dispersion is almost independent of the Courant number (Figs.5.18–5.19).

It has been claimed in [64] that the S-MRTD Scheme is slightly oscillating and its performance is only comparable with the 14^{th} order accuracy Yee's scheme. Though this is true for the S-MRTD schemes with stencil size of 8, the comparison of the dispersion diagrams of Yee's FDTD scheme, Yee's 16th order (H.F.D.-16) and 22th order (H.F.D.-22) and S-MRTD and Wo-MRTD schemes with different stencils leads to interesting results.For comparison purposes, the values of $\Delta t = \Delta t_{max}/5$ and $\Delta t_{max} = 0.368112\Delta l/c$ have been used and all the dispersion curves are subtracted by the linear dispersion relation for 1D simulations. (Fig.5.20) shows that the S-MRTD scheme with stencil 10 has a comparable performance to the 16th order Yee's scheme. The enhancement of the wavelets for the same stencil improves significantly the dispersion characteristics of the MRTD scheme increasing the dynamic range of ω by approximately 90% and comparing favorable even to the 22th order Yee's scheme. This is expected due to the fact that the scaling+wavelet basis spans

a larger ("more complete") subspace of R than the scaling functions alone. Both S-MRTD and Wo-MRTD schemes have identical numerical phase errors up to the point that the S-MRTD scheme starts diverging (Fig.5.21). As the stencil size of the Wo-MRTD scheme is increasing from 6 to 12 (Figs.5.22–5.23), the oscillatory variation of the phase error is diminishing to a negligible level generating an almost flat algorithm similar to the higher order Yee's ones.

As a conclusion, due to the poor dispersion performance of the FDTD technique even for 10 cells/wavelength a normal to coarse grid is always required to avoid significant pulse distortions especially for the higher-spatial-frequency components. MRTD offers low dispersion even for sparse grids very close to the Nyquist limit.

5.4 Conclusion

The stability and the dispersion performance of the recently developed Battle-Lemarie MRTD schemes has been investigated for different stencil sizes and for 0-resolution wavelets. Analytical expressions for the maximum stable time-step have been derived. Larger stencils decrease the numerical phase error making it significantly lower than FDTD for low and medium discretizations. Stencil sizes greater than 10 offer a smaller phase error than FDTD even for discretizations close to 40 cells/λ. The enhancement of wavelets further improves the dispersion performance for discretizations close to the Nyquist limit (2-3 cells/wavelength) making it comparable to that of much denser grids, though it decreases the value of the maximum time-step guaranteeing the stability of the scheme.

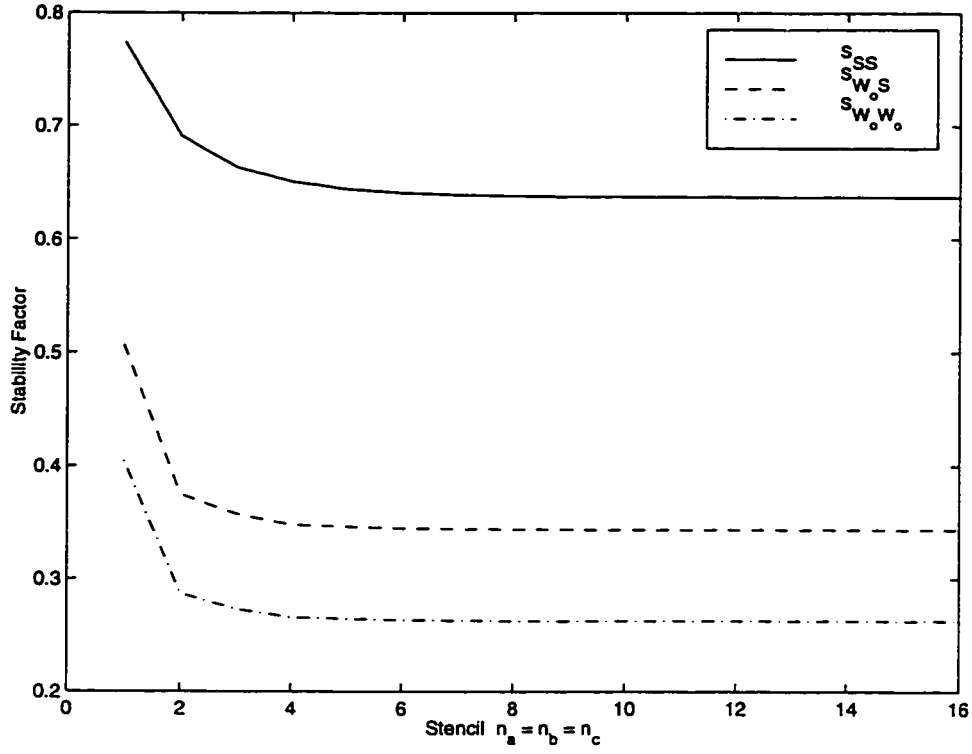

Figure 5.1: Stability Parameter s for MRTD.

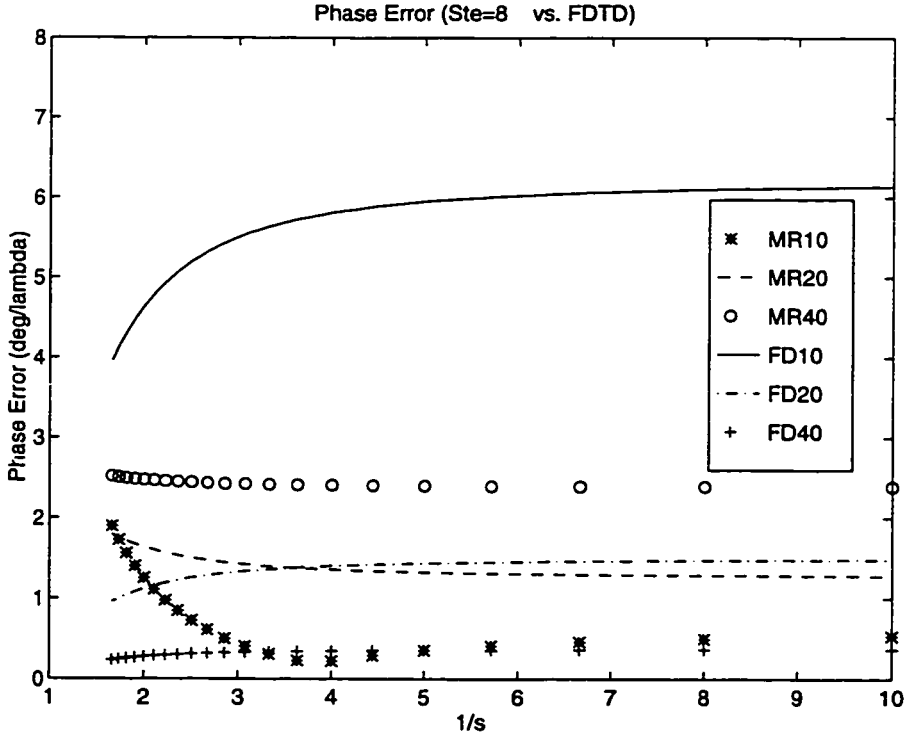

Figure 5.2: Dispersion Characteristics of S-MRTD for n_a=8.

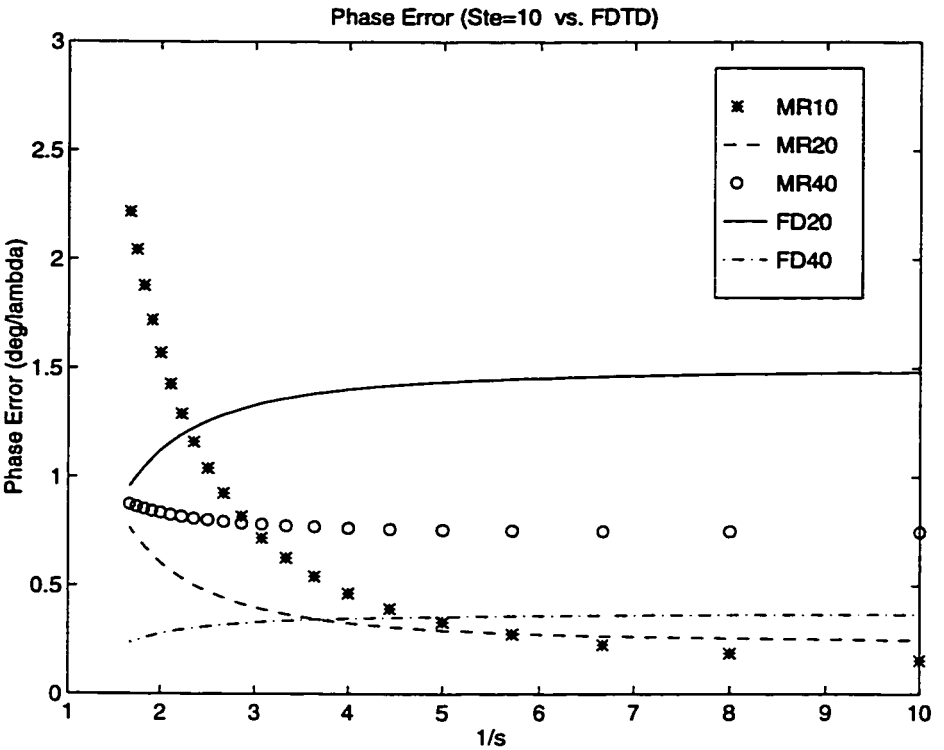

Figure 5.3: Dispersion Characteristics of S-MRTD for n_a=10.

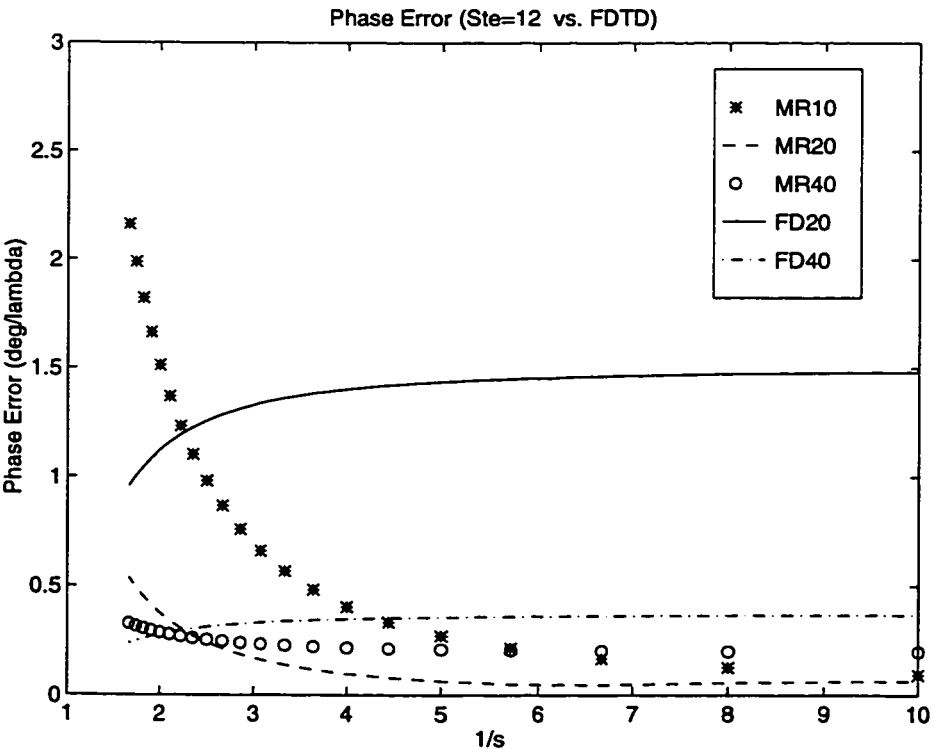

Figure 5.4: Dispersion Characteristics of S-MRTD for n_a=12.

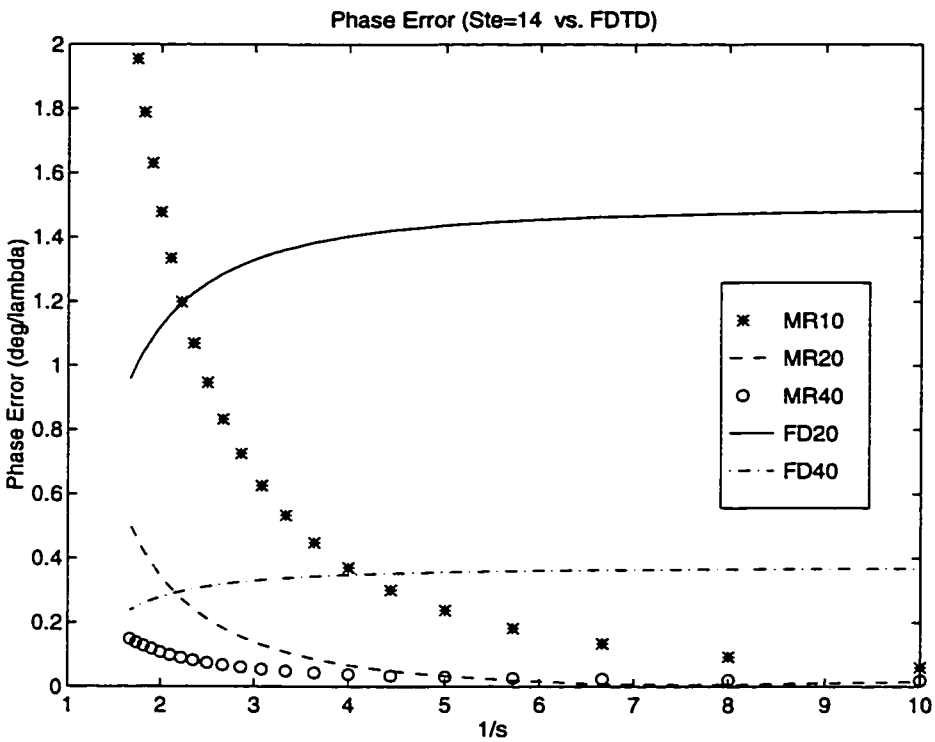

Figure 5.5: Dispersion Characteristics of S-MRTD for n_a=14.

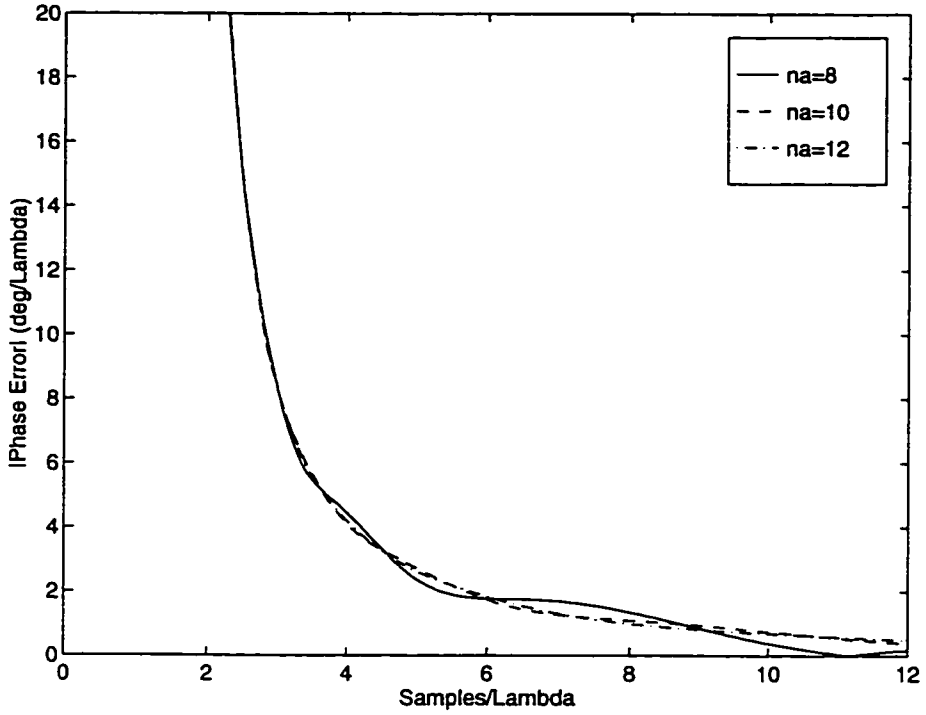

Figure 5.6: Stencil Effect on the Dispersion Characteristics of S-MRTD (Sparse Grid).

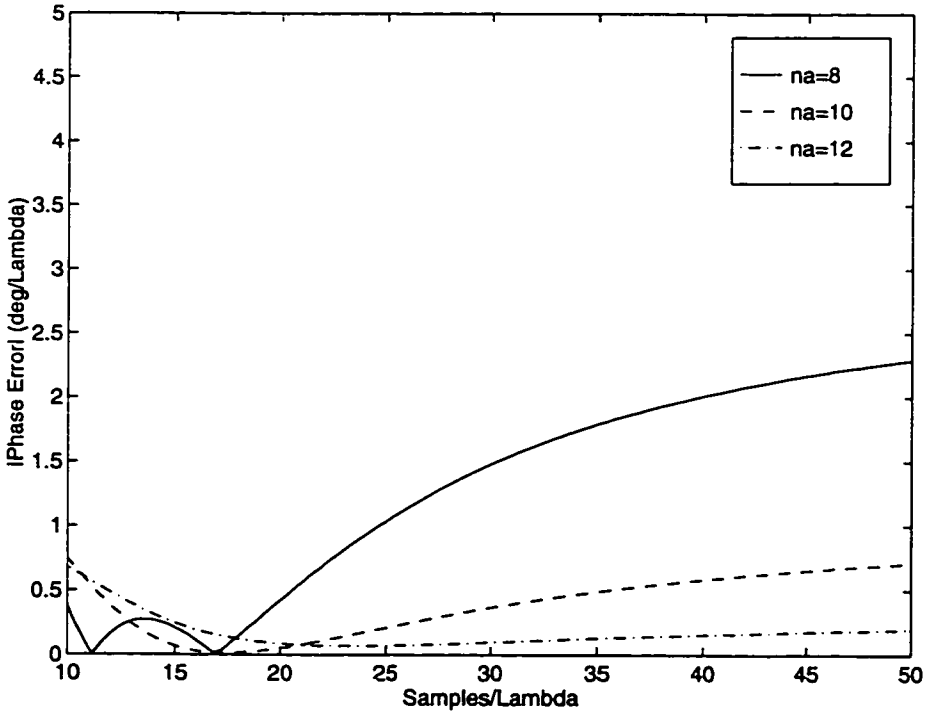

Figure 5.7: Stencil Effect on the Dispersion Characteristics of S-MRTD (Dense Grid).

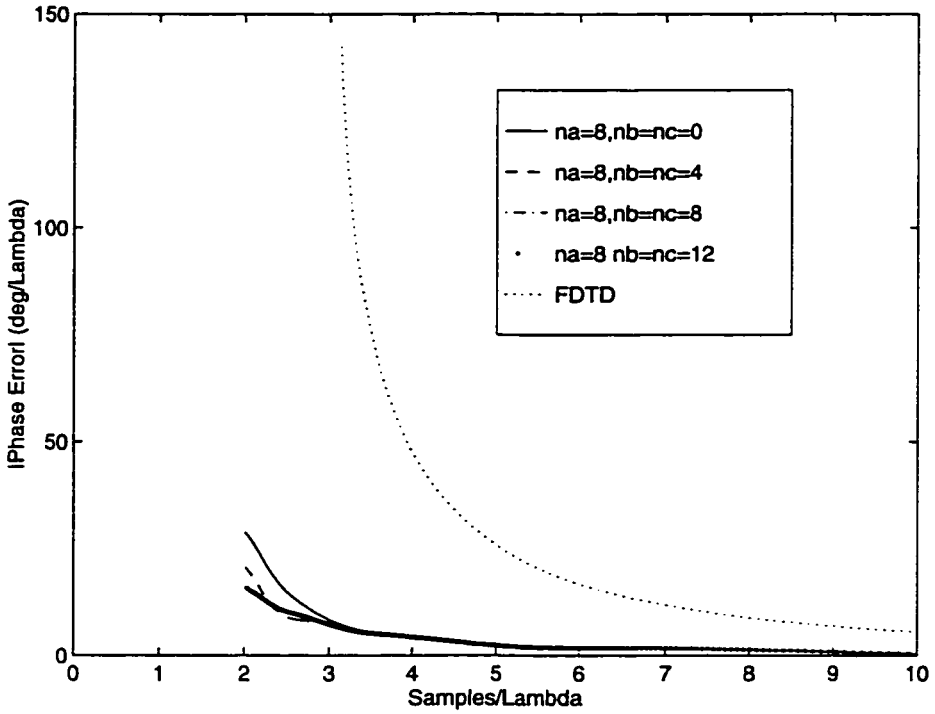

Figure 5.8: Wavelets Effect on the Dispersion Characteristics of MRTD for n_a=8 (Coarse Grid).

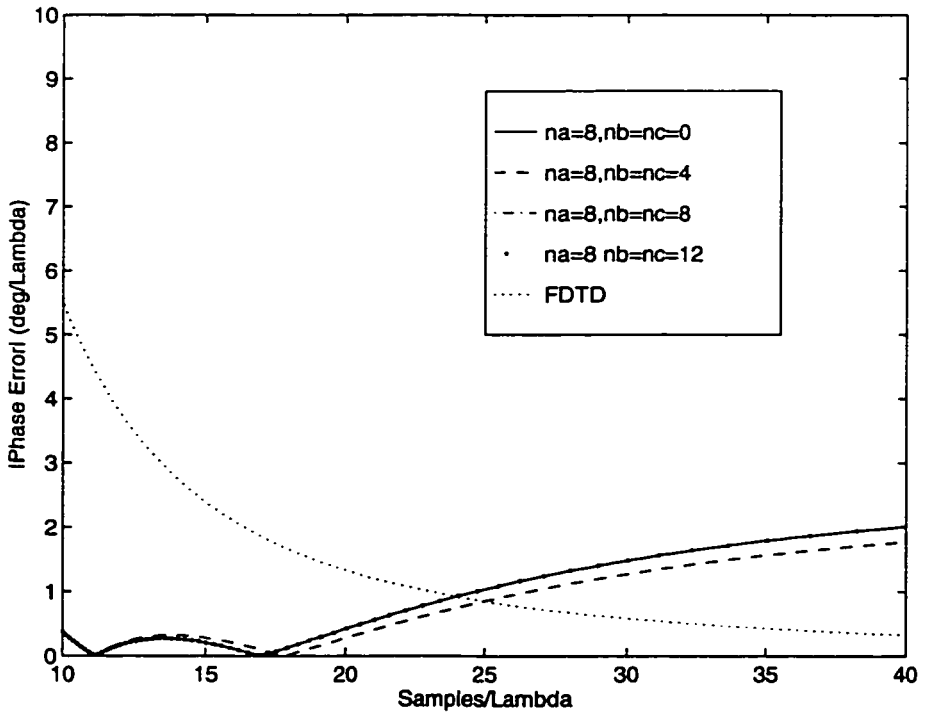

Figure 5.9: Wavelets Effect on the Dispersion Characteristics of MRTD for n_a=8 (Denser Grid).

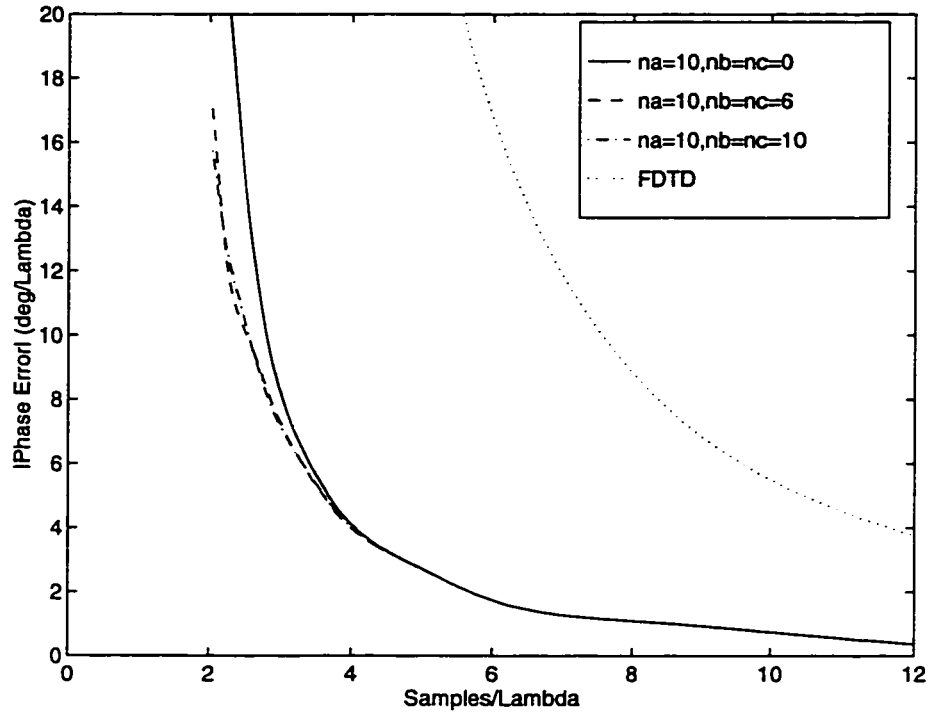

Figure 5.10: Wavelets Effect on the Dispersion Characteristics of MRTD for n_a=10 (Coarse Grid).

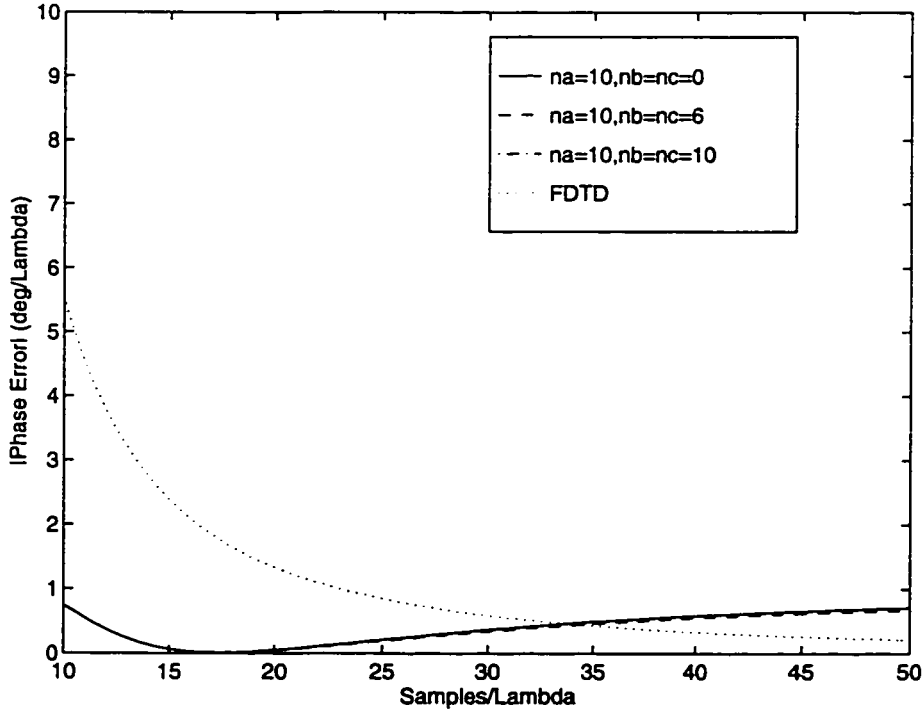

Figure 5.11: Wavelets Effect on the Dispersion Characteristics of MRTD for n_a=10 (Denser Grid).

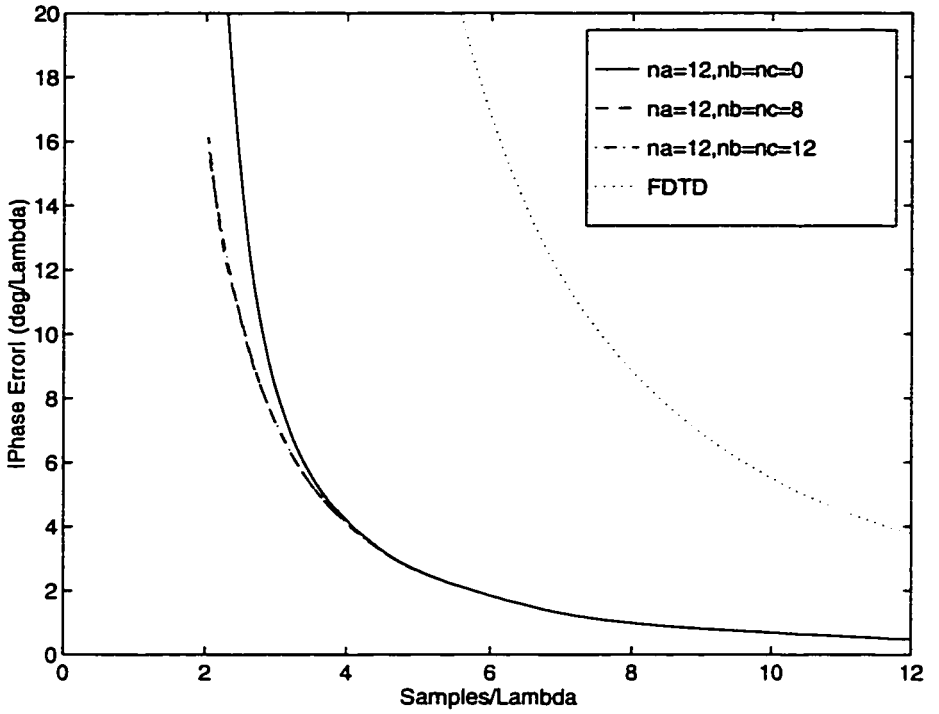

Figure 5.12: Wavelets Effect on the Dispersion Characteristics of MRTD for n_a=12 (Coarse Grid).

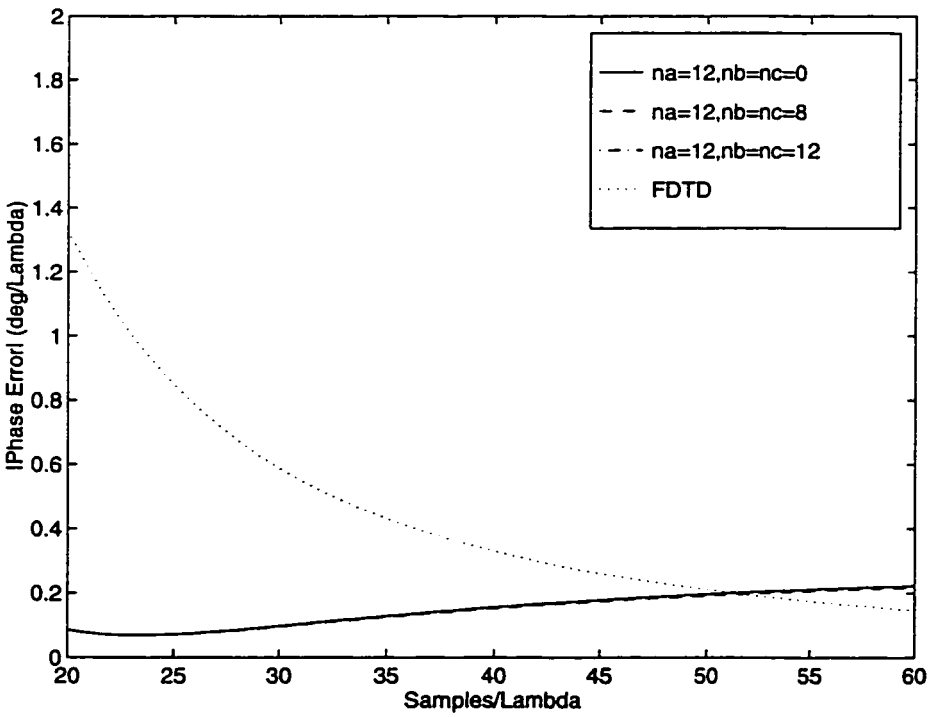

Figure 5.13: Wavelets Effect on the Dispersion Characteristics of MRTD for n_a=12 (Denser Grid).

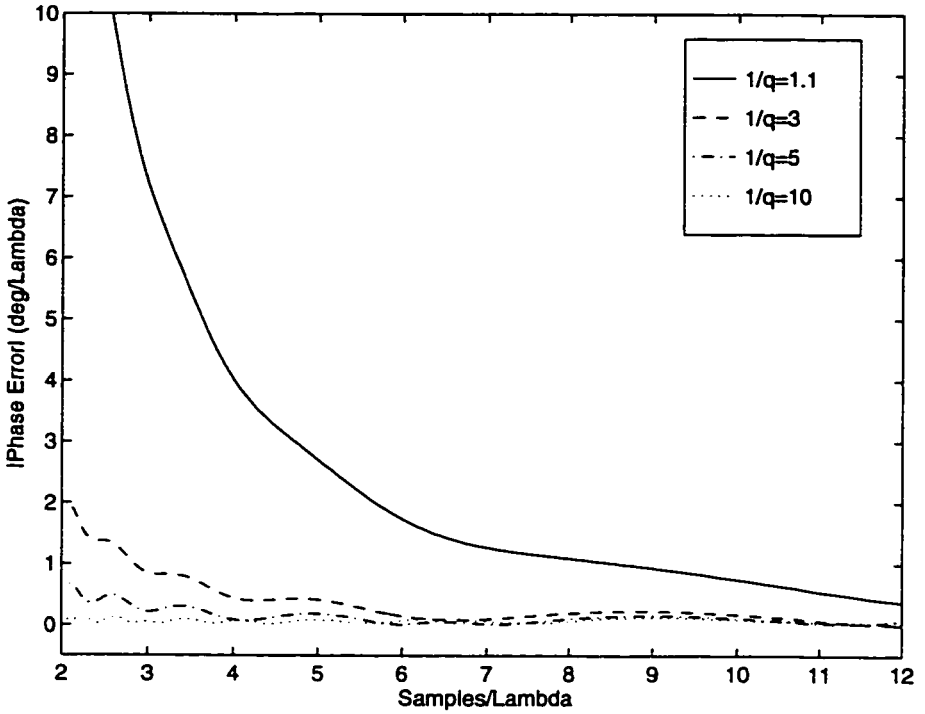

Figure 5.14: Effect of the Courant Number on the Dispersion Characteristics of $W_0 - MRTD$ for $n_a = n_b = n_c$=10 (Coarse Grid).

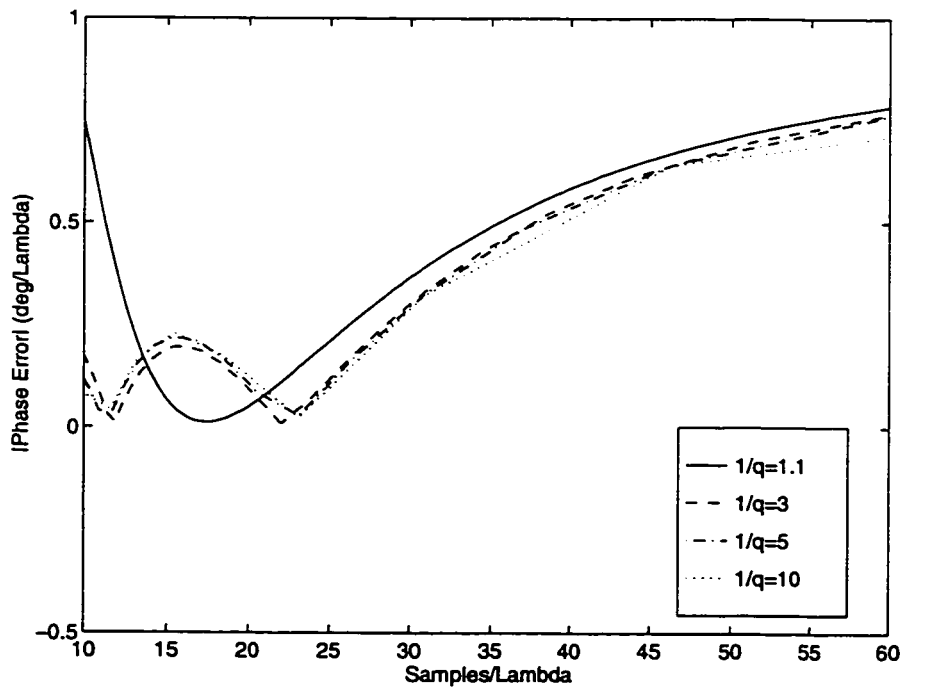

Figure 5.15: Effect of the Courant Number on the Dispersion Characteristics of $W_0 - MRTD$ for $n_a = n_b = n_c$=10 (Denser Grid).

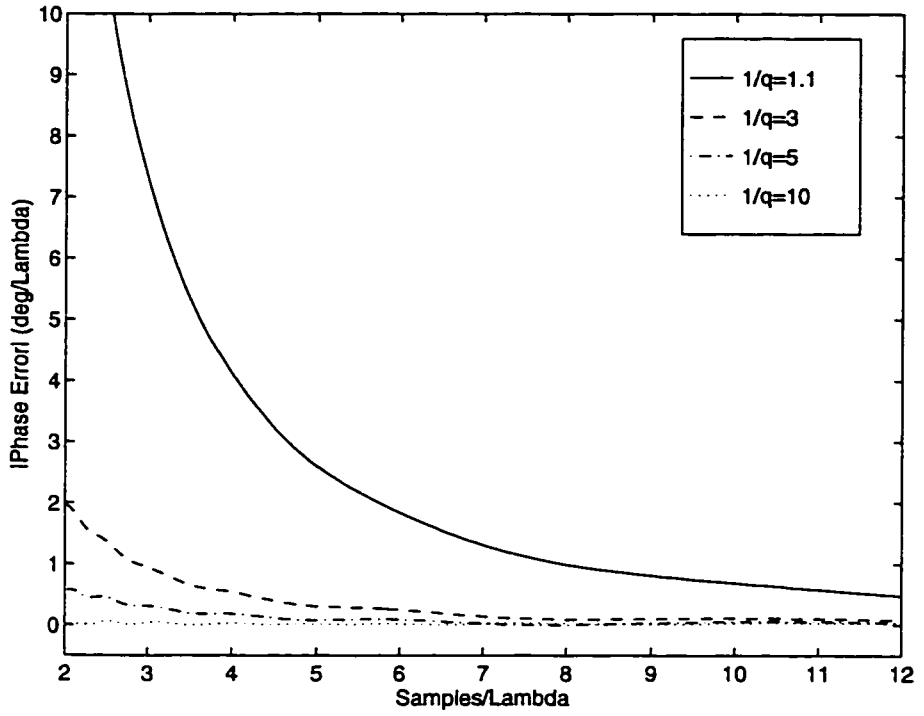

Figure 5.16: Effect of the Courant Number on the Dispersion Characteristics of $W_0 - MRTD$ for $n_a = n_b = n_c$=12 (Coarse Grid).

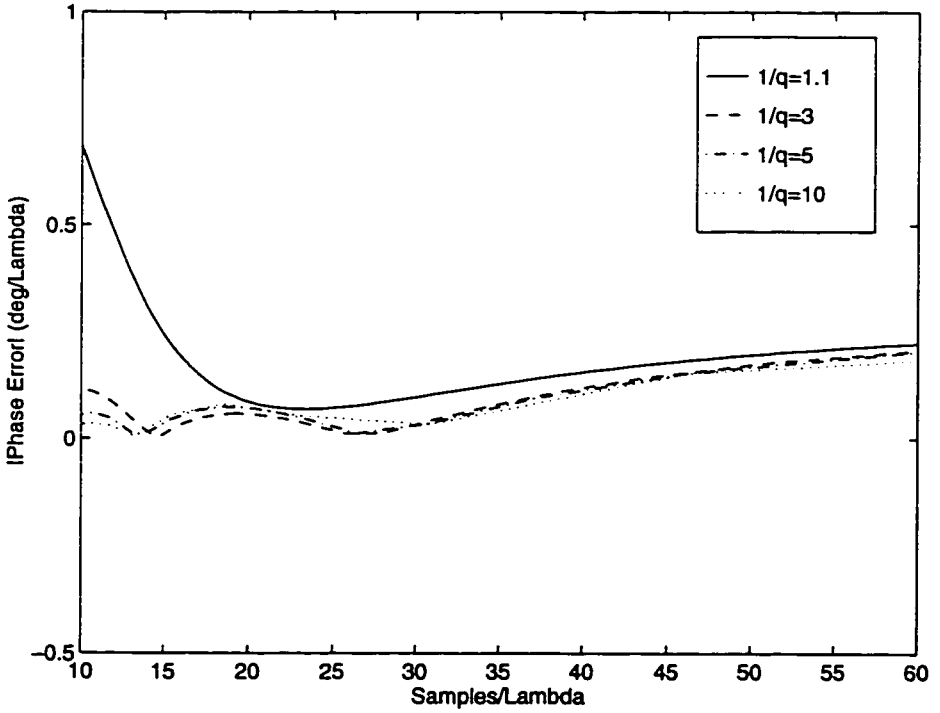

Figure 5.17: Effect of the Courant Number on the Dispersion Characteristics of $W_0 - MRTD$ for $n_a = n_b = n_c$=12 (Denser Grid).

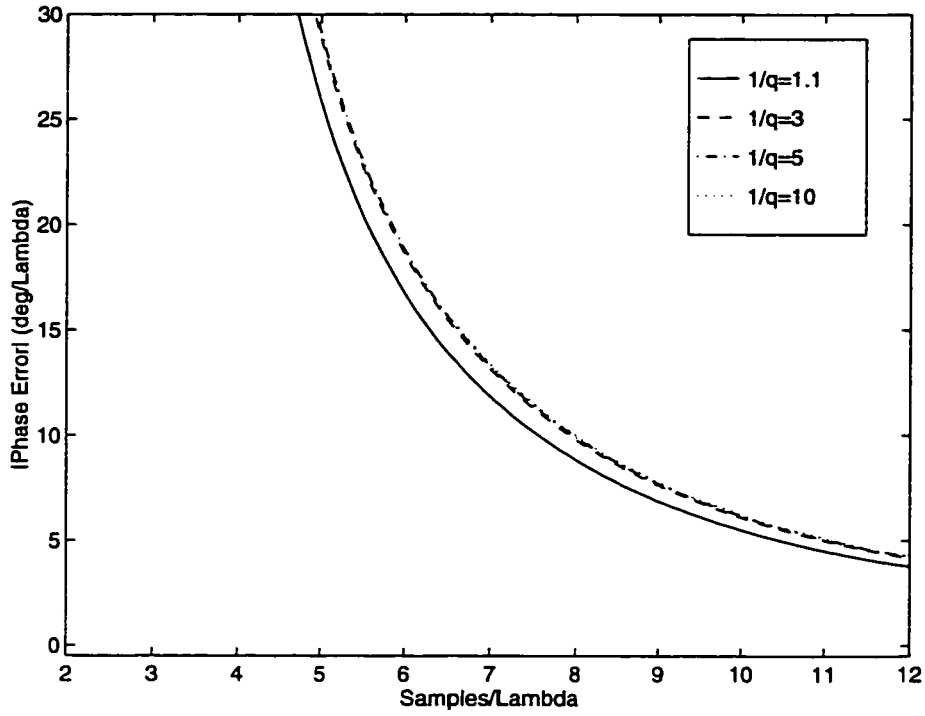

Figure 5.18: Effect of the Courant Number on the Dispersion Characteristics of FDTD (Coarse Grid).

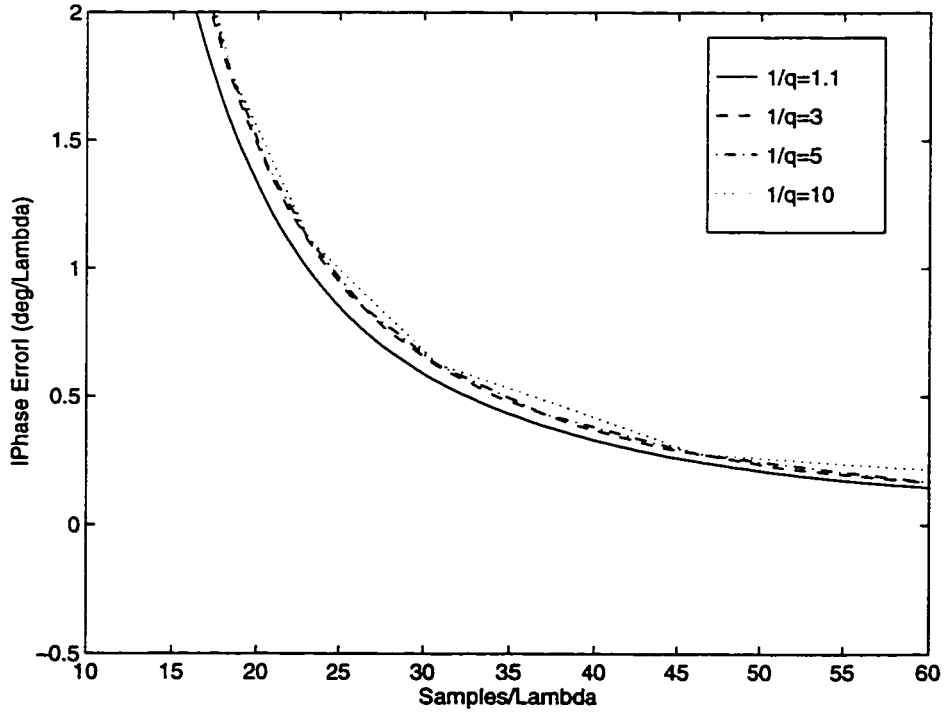

Figure 5.19: Effect of the Courant Number on the Dispersion Characteristics of FDTD (Denser Grid).

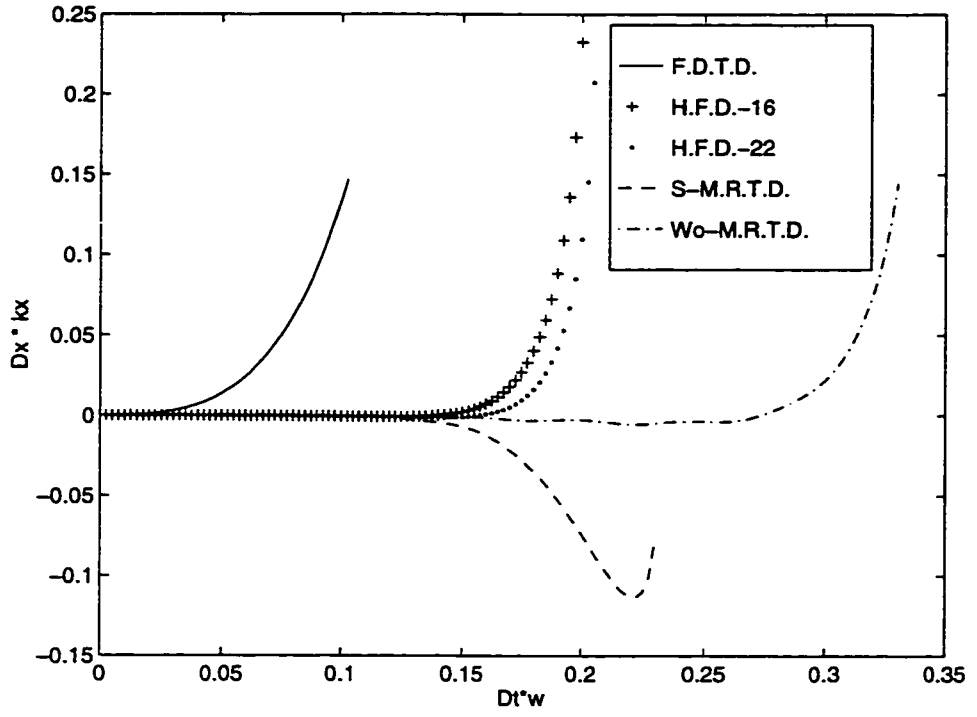

Figure 5.20: Comparison of the Dispersion Performance of S-MRTD and Wo-MRTD with Different Higher Order Yee's Schemes.

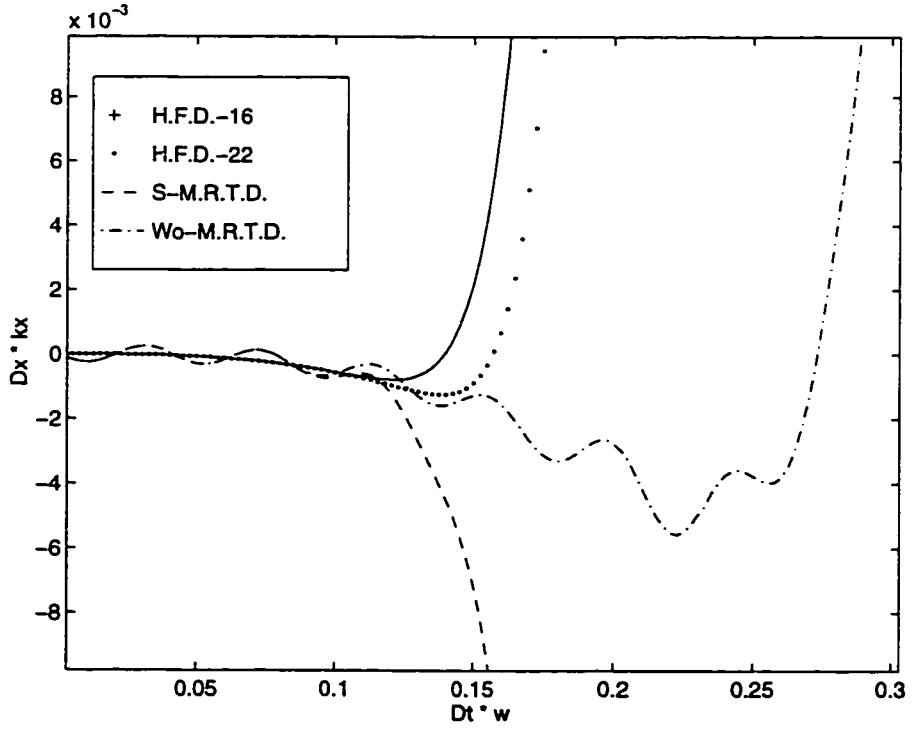

Figure 5.21: Details of Fig.(5.20).

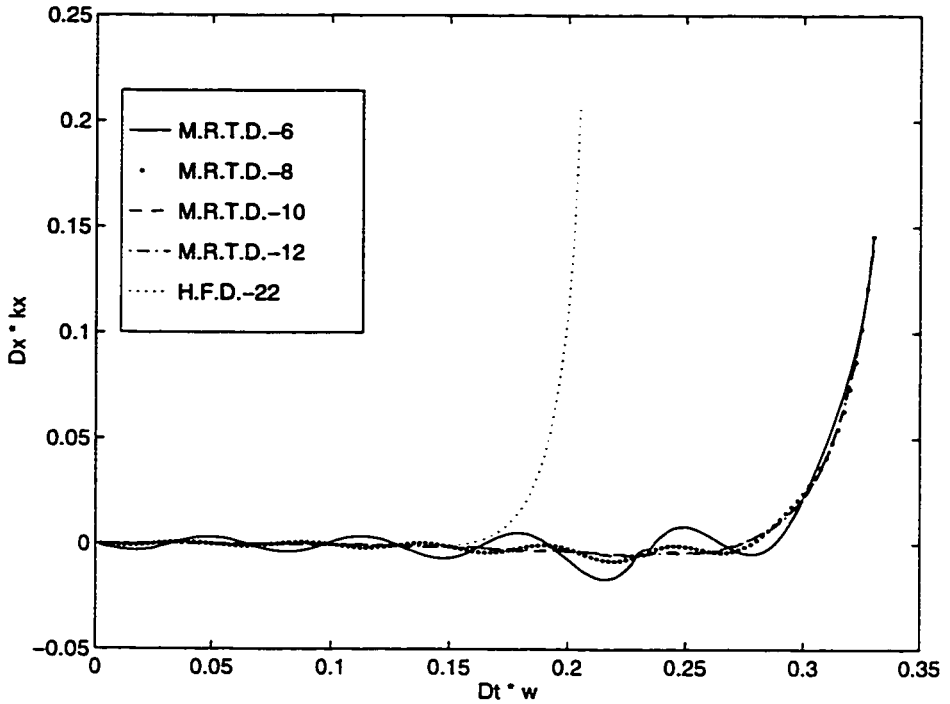

Figure 5.22: Comparison of the Oscillations of Wo-MRTD Scheme for Different Stencil Size.

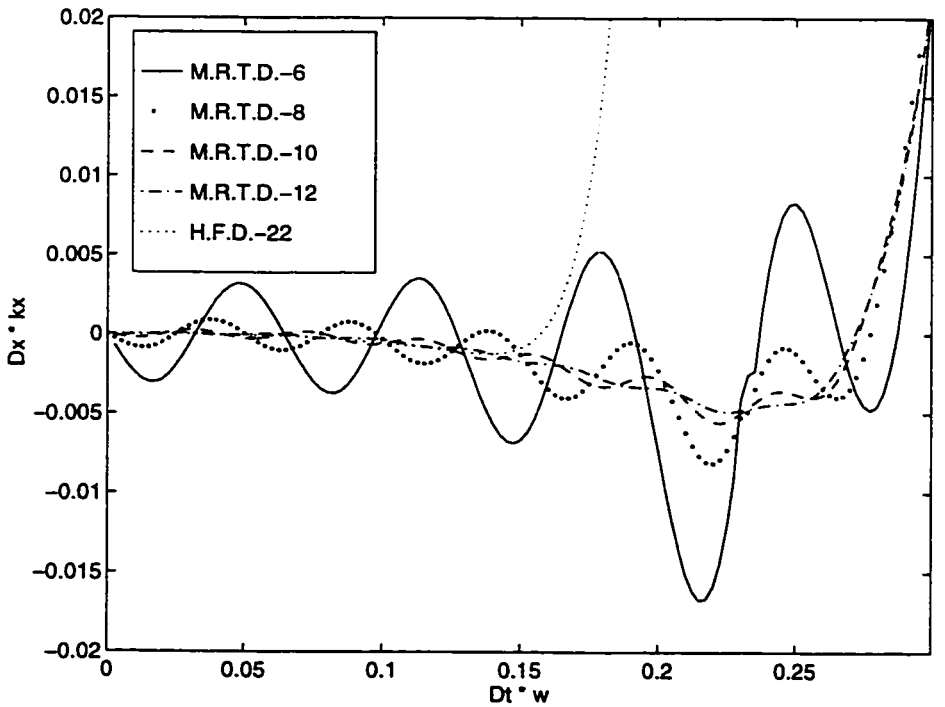

Figure 5.23: Details of Fig.(5.22).

CHAPTER 6

Development of a Space- and Time-Adaptive MRTD Gridding Algorithm for the Analysis of 2D Microwave Dielectric Geometries

6.1 Introduction

In CH.4, the MRTD Technique has been applied to a variety of homogeneous microwave problems and has exhibited significant savings in memory and execution time. Nevertheless the most important advantage of this new technique is its capability to provide space and time adaptive gridding without the problems that the conventional FDTD is encountering. This is due to the use of two separate sets of basis functions, the scaling and wavelets and the capability to threshold the field coefficients due to the excellent conditioning of the formulated mathematical problem. In this Chapter, a space/time adaptive gridding algorithm based on the MRTD scheme is proposed and applied to nonhomogeneous waveguide problems. As an example, the propagation of a Gabor pulse in a partially-filled parallel-plate waveguide is simulated and the S-parameters are evaluated. Wavelets are placed only at locations where the EM fields have significant values, creating a space- and time- adaptive

dense mesh in regions of strong field variations, while maintaining a much coarser mesh elsewhere. The modification of the 2D MRTD algorithm to include dielectric variation is presented and wavelet thresholding approaches are compared and evaluated.

6.2 The 2D-MRTD Nonhomogeneous scheme

6.2.1 The 2D-MRTD scaling and wavelets scheme

For simplicity the 2D-MRTD scheme for the TM_z modes will be used herein. To derive the 2D-MRTD scheme, the field components are represented by a series of cubic spline Battle-Lemarie [30] scaling and wavelet functions up to the r_{max}-resolution to the longitudinal direction in space and pulse functions in time in a similar way to CH3. Due to the entire domain basis functions, D of one cell is related to E values all over the neighboring cells. To circumvent this problem, the CurlD equations have to replace the CurlE equations and then the E-coefficients have to be calculated from the D-coefficients in a mathematically correct way. After inserting the field expansions in Maxwell's equations, we sample them using pulse functions in time and scaling/wavelet functions in space domain.

As an example, sampling $\partial D_x/\partial t, = -\partial H_y/\partial z$ in space and time, the following equations are obtained

$$\frac{1}{\Delta t}({}_{k+1}D^{\phi x}_{l+1/2,m} - {}_{k}D^{\phi x}_{l+1/2,m}) = -\frac{1}{\Delta y}\Big(\sum_{i=-m^{\phi}_{\phi}}^{m^{\phi}_{\phi}} a^{\phi}_{\phi}(i)_{k+1/2}\, H^{\phi y}_{l+1/2,m+i+1/2} + \sum_{r=0}^{r_{max}}\sum_{p=0}^{2^r-1}\sum_{i=-m^{\phi}_{\psi_{r,p}}}^{m^{\phi}_{\psi_{r,p}}} a^{\phi}_{\psi_{r,p}}(i)_{k+1/2}\, H^{\psi_{r,p}y}_{l+1/2,m+i+(2p+1)/2^{r+1}}\Big) \quad , \tag{6.1}$$

$$\frac{1}{\Delta t}\Big({}_{k+1}D^{\psi_{r',p'}x}_{l+1/2,m+(2p'+1)/2^{r'+1}} - {}_{k}D^{\psi_{r',p'}x}_{l+1/2,m+(2p'+1)/2^{r'+1}}\Big) = -\frac{1}{\Delta y}\Big(\sum_{i=-m^{\psi_{r',p'}}_{\phi}}^{m^{\psi_{r',p'}}_{\phi}} a^{\psi_{r',p'}}_{\phi}(i)_{k+1/2}\, H^{\phi y}_{l+1/2,m+i+1/2}$$

$$+ \sum_{r=0}^{r_{max}} \sum_{p=0}^{2^r-1} \sum_{i=-m_{\psi_{r,p}}}^{m_{\psi_{r,p}}^{\psi_{r',p'}}} a_{\psi_{r,p}}^{\psi_{r',p'}}(i)_{k+1/2}\, H_{l+1/2,m+i+(2p+1)/2^{r+1}}^{\psi_{r,p}y} \quad , \qquad (6.2)$$

where ${}_kD_{l,m}^{\xi x}$ and ${}_kH_{l,m}^{\xi y}$ with ξ=ϕ (scaling),$\psi_{r,p}$ (wavelets of r-resolution at the p-position of the cell) are the coefficients for the electric and magnetic field expansions . The indices l, m and k are the discrete space and time indices, which are related to the space and time coordinates via $x = l\Delta x$,$z = m\Delta z$ and $t = k\Delta t$, where Δx,Δz are the space discretization intervals in x- and z-direction and Δt is the time discretization interval. The coefficients $a_{\phi}^{\phi}(i), a_{\phi}^{\psi_{0,0}}(i), a_{\psi_{0,0}}^{\phi}(i), a_{\psi_{0,0}}^{\psi_{0,0}}(i)$ are derived in a similar way to CH.3. For an accuracy of 0.1% the values $m_{\phi}^{\phi} = 10 - 12$ and $m_{\phi}^{\psi_{0,0}} = m_{\psi_{0,0}}^{\phi} = m_{\psi_{0,0}}^{\psi_{0,0}} = 8 - 12$ have been used when only the 0-resolution of the wavelets was applied.

6.2.2 The PML numerical absorber

For open structures, the perfectly matched layer (PML) technique can be applied by assuming that the conductivity is given in terms of scaling and wavelet functions instead of pulse functions with respect to space [66]. The PML is characterized by artificial electric and magnetic conductivities σ^E and σ^H, which satisfy the relationship

$$\frac{\sigma_H}{\mu_o} = \frac{\sigma_E}{\epsilon} = \frac{\sigma_D}{\epsilon_o} \qquad (6.3)$$

for each cell with constitutive parameters (ϵ,μ_o). The spatial distribution of the magnetic conductivity for the absorbing layers is modeled by assuming that the amplitudes of the scaling and the wavelet functions have a polynomial distribution (linear, parabolic, ...) and by sampling this distribution with scaling and wavelet functions (Eq.(3.79)). It has been observed that the parabolic distribution is the most computationally efficient. For multidielectric non-magnetic structures, the electric conductivity is given from the above relationship assigning the appropriate ϵ. The MRTD mesh is terminated by a perfect electric

conductor (PEC) at the end of the PML region. Following a procedure similar to (3.4.3) the equations for the D_x scaling components in the PML region are given by

$$_{k+1}D^{x,\phi\phi}_{i-1/2,j} = e^{-\sigma^j_D \Delta t/\epsilon_o}\, {}_kD^{x\phi\phi}_{i-1/2,j} - e^{-0.5\sigma^j_D \Delta t/\epsilon_o}\frac{\Delta t}{\epsilon_o \Delta y}\Big(\sum_{j'=-n_a}^{n_a-1} a(j')_{k+1/2}\, H^{y,\phi\phi}_{i-1/2,j+j'+1/2}$$

$$+\sum_{r=0}^{r_{max}}\sum_{p=0}^{2^r-1}\sum_{j'=-m^{\phi}_{\psi_{r,p}}}^{m^{\phi}_{\psi_{r,p}}} a^{\phi}_{\psi_{r,p}}(i)_{k+1/2}\, H^{y,\phi\psi_{r,p}}_{i-1/2,j+j'+(2p+1)/2^{r+1}}\Big) \qquad ,(6.4)$$

Similar equations can be obtained for the wavelet equations. For the simulations presented in this paper, there are used 24 cells of PML medium with σ_H for designated R_{max}=1.e-6 for MRTD (coarser mesh) and for R_{max}=1.e-7 for FDTD (4 times/dimension finer mesh) which provide reflection coefficients in the region of -80 to -90 dB.

6.2.3 The Excitation Implementation

In order to implement an excitation $E_F(t)$ at $z = m\Delta z$ and to obtain an excitation identical to an FDTD excitation (pulse excitation with respect to space), the space pulse is decomposed in terms of scaling and wavelet functions.

$$_kE^{exc}_m \approx E_F(k\Delta t)\Big(\sum_{i=-\zeta_\phi}^{\zeta_\phi} c_\phi(i)\phi_{m+i} + \sum_{r=0}^{r_{max}}\sum_{p=0}^{2^r-1}\sum_{i=-\zeta_{\psi_{r,p}}}^{\zeta_{\psi_{r,p}}} c_{\psi_{r,p}}(i)\psi^{r,p}_{m+i}\Big) \qquad (6.5)$$

where the coefficients $c_\phi(i), c_{\psi_{0,1}}(i), c_{\psi_{1,1}}(i), c_{\psi_{1,2}}(i)$ (wavelets of 0- and 1-resolutions) are given in Chapter 3. For $i < 0$ it is $c_\phi(-i) = c_\phi(i)$, $c_{\psi_{0,1}}(i) = c_{\psi_{0,1}}(-1-i)$, $c_{\psi_{1,1}}(i) = c_{\psi_{1,2}}(-1-i)$ and $c_{\psi_{1,2}}(i) = c_{\psi_{1,1}}(-1-i)$. The above excitation components are superimposed to the field values obtained by the MRTD algorithm for the same time step. For example, the total $_kE^{\phi}_{m+i}$ will be given by

$$_kE^{\phi}_{m+i}\Big|_{total} = E_F(k\Delta t)\, c_\phi(i) + E^{\phi}_{k,m+i} \qquad . \qquad (6.6)$$

It has been observed that the minimum limits of the summations for an accuracy of 0.1% are $\zeta_\phi = \zeta_{\psi_{0,0}}$=4 and $\zeta_{\psi_{1,0}} = \zeta_{\psi_{1,1}}$=3 for the first 2 resolutions of the wavelets (r_{max}=1).

Similar accuracy can be observed when the scaling function at the excitation cell is set equal to the value of the excitation function $E_F(t)$. No superposition is used and the field scaling and wavelet values elsewhere are given by the MRTD equations. The wavelet coefficients are excited through the coupling of the discretized MRTD equations. In the following numerical simulations the latter excitation technique was employed since it adds significantly smaller computational overhead.

6.2.4 The Modelling of Dielectrics

Starting from the constitutive relationship $D = \epsilon E$ for the total electric field at one mesh point and sampling the scaling and wavelet components with a similar way to (A) we reach the following equations for D_x

$$ {}_kD^{\phi}_{i,j} = \sum_{j'=-l_\phi}^{l_\phi} c^{\phi}_{\phi d}(j')_k E^{\phi}_{i,j+j'} + \sum_{r=0}^{r_{max}} \sum_{p=0}^{2^r-1} \sum_{j'=-l_{\psi_{r,p}}}^{l_{\psi_{r,p}}} c^{\phi}_{\psi_{r,p}d}(j')_k E^{\psi_{r,p}}_{i,j+j'} \tag{6.7} $$

and

$$ {}_kD^{\psi_{r',p'}}_{i,j} = \sum_{j'=-\xi_\phi}^{\xi_\phi} c^{\psi_{r',p'}}_{\phi d}(j')_k E^{\phi}_{i,j+j'} + \sum_{r=0}^{r_{max}} \sum_{p=0}^{2^r-1} \sum_{j'=-\xi_{\psi_{r,p}}}^{\xi_{\psi_{r,p}}} c^{\psi_{r',p'}}_{\psi_{r,p}d}(j')_k E^{\psi_{r,p}}_{i,j+j'} \tag{6.8} $$

where

$$ c^{\phi}_{\phi d}(j') = \int_{-\infty}^{\infty} \epsilon \phi_k(z) \phi_{k+j'}(z) dz \tag{6.9} $$

$$ c^{\psi_{r,p}}_{\phi d}(j') = \int_{-\infty}^{\infty} \epsilon \phi_k(z) \psi^{r,p}_{k+j'}(z) dz \tag{6.10} $$

$$ c^{\phi}_{\psi_{r',p'}d}(j') = \int_{-\infty}^{\infty} \epsilon \psi^{r',p'}_{k}(z) \phi_{k+j'}(z) dz \tag{6.11} $$

$$ c^{\psi_{r,p}}_{\psi_{r',p'}d}(j') = \int_{-\infty}^{\infty} \epsilon \psi^{r',p'}_{k}(z) \psi^{r,p}_{k+j'}(z) dz \tag{6.12} $$

Equations (6.7) and (6.8) can be written in a compact form

$$ [\bar{D}] = [\bar{\bar{\epsilon}}][\bar{E}] \tag{6.13} $$

For geometries with dielectrics varying from air (ϵ_r=1) to Si (ϵ_r=2.56), it was observed that the above summations can be truncated for $l_\phi = l_{\psi_{0,0}} = \xi_\phi = \xi_{\psi_{0,0}} = 6$ when only one resolution of wavelets (r_{max}=0) was used. Also, the integrals can be approximated by finite summations of 10 cells on each side of the central cell (k-cell).

Due to the orthogonality relationship between the scaling and the wavelet functions, for uniform dielectrics (constant ϵ throughout the integration domain) these integrals are simplified to $c^{\phi}_{\phi d} = \epsilon\,\delta_{i,0}$, $c^{\psi_{r,p}}_{\phi d} = c^{\phi}_{\psi_{r',p'}} = 0$ and $c^{\psi_{r,p}}_{\psi_{r',p'}d}(i) = \epsilon\,\delta_{r',r}\,\delta_{p',p}\,\delta_{i,0}$ and $[\bar{\bar{\epsilon}}]$ becomes a diagonal matrix. For structures containing dielectric discontinuities, none of these integrals have a zero value. In this case, the whole geometry has to be preprocessed before the initialization of the time loop and coefficients $c^{\phi}_{\phi d}, c^{\psi_{r,p}}_{\phi d}, c^{\phi}_{\psi_{r',p'}}, c^{\psi_{r,p}}_{\psi_{r',p'}d}$ have to be assigned to any cell (m,n) and included in the matrix $[\bar{\bar{\epsilon}}]$. For each cell the amplitude of these coefficients is compared to the amplitude of the self-term $c^{\phi}_{\phi d}(i)$. If all coefficients are below a threshold (usually $\leq 0.1\%$), they are set to zero and this cell is exempted from the following inversion, otherwise it is included in a new submatrix. This submatrix has significantly smaller dimensions than $[\bar{\bar{\epsilon}}]$ (usually $\leq 10\%$) and contains only cells close to dielectric discontinuities. The inverse of this matrix is used for the calculation of the E from the D values for each time step. The inversion takes place only once, thus it adds only negligible computational overhead to the algorithm.

6.2.5 Total Field Calculation

Due to the nature of the Battle-Lemarie expansion functions, the total field is a summation of the contributions from the non-localized scaling and wavelet functions. For example, the total electric field $E_x(x_o, z_o, t_o)$ with $(i-1)\,\Delta x < x_o < i\,\Delta x$, $(j-1/2)\,\Delta z < z_o < (j+1/2)\,\Delta z$ and $(k-1/2)\,\Delta t < t_o < (k+1/2)\,\Delta t$ is calculated in the same way with

[31, 58] by

$$E_x(x_o, z_o, t_o) = \sum_{i'=-l_x}^{l_x} \phi_{i+i'-1/2}(x_o) \left(\sum_{j'=-l_{z\phi}}^{l_{z\phi}} {}_kE^{\phi x}_{i+i'-1/2,j+j'} \phi_{j+j'}(z_o) + \sum_{r=0}^{r_{max}} \sum_{p=0}^{2^r-1} \sum_{j'=-l_{z\psi(r,p)}}^{l_{z\psi(r,p)}} {}_kE^{\psi_{r,p}x}_{i+i'-1/2,j+j'+(2p+1)/2^{r+1}} \psi^{r,p}_{j+j'+(2p+1)/2^{r+1}}(z_o) \right) \tag{6.14}$$

where $\phi_i(x) = \phi(\frac{x}{\Delta x} - i)$ and $\psi_i^{r,p}(x) = \psi_i^r(\frac{x}{\Delta x} - p) = 2^{r/2}\, \psi_i^0(2^r \frac{x}{\Delta x} - p)$ represent the Battle-Lemarie scaling and r-resolution wavelet function respectively. For an accuracy of 0.1% the values $l_x = l_{z\phi} = l_{z\psi(0,0)} = 4$ have been used.

6.2.6 Time-Adaptive Gridding

The Multiresolution Analysis is based on the fact that the wavelets increase the local resolution of the expansion. Each added wavelet resolution virtually is equivalent to the use of a denser grid with half cell size. In addition, wavelets have significant values close to discontinuities or near regions of fast field variation, since they contain only high frequency spatial components. There are many different ways to take advantage of these wavelet characteristics in order to create a space and time adaptive gridding algorithm. In Digital Signal Processing, thresholding of the wavelet coefficients over a specific time- and space-window (5-10 points) contribute significant memory economy (factor between 4-8 in comparison to scaling-only expansions), but increase the implementation complexity and the execution time. Sometimes the added computational overhead is greater than the previous execution time.

The simplest way to create a dynamically changing grid is to threshold the wavelet components to a fraction (usually $\leq 0.1\%$) of the scaling function at the same cell (space adaptiveness) and/or to an absolute threshold (usually 0.0001 or a number smaller than

1/10000 of the peak of the excitation time-domain function). This comparison is repeated for each time-step (time adaptiveness). All components below this threshold are eliminated from the subsequent calculations. Th is is the simplest thresholding algorithm. It doesn't add any significant overhead in execution time (usually $\leq 10\%$), but it offers only a moderate (pessimistic) economy in memory (factor close to 2). Also, this algorithm allows for the dynamic memory allocation in its programming implementation by using the appropriate programming languages (e.g. C).

The principles of the dynamically changing time- and space-adaptive grid are demonstrated in (Fig.6.1). A pulse is propagating from the left to the right in a partially filled parallel plate waveguide. For t=0, the wavelets are localized at the excitation area. They follow the propagating pulse (t before the incidence to the dielectric interface) creating a moving dense subgrid. After the pulse has been split in reflected and transmitted pulses, the wavelets increase the grid resolution only around these pulses. Elsewhere the wavelet components have negligible values and are ignored.

6.3 Applications of 2D-MRTD

6.3.1 Air-Filled Parallel Plate Waveguide

The 2D-MRTD scheme is applied to the analysis of an air-filled parallel-plate waveguide with width 4.8 mm. The front and back open planes are terminated with a PML region of 22 cells and σ_E^{max} calculated for designated R_{max}=1.e-7. The waveguide is excited with a Gabor function 0-30GHz along a vertical line next to the PML region. A Gabor excitation is propagating for a distance of 2,000 mm. For the analysis based on Yee's FDTD scheme, a 4 $\times$ 1120 mesh is used resulting in a total number of 4480 grid points. When the structure is analyzed with the 2D-MRTD scheme, a mesh 2 $\times$ 160 (320 grid points) is

chosen ($dx = 0.24\lambda_o$, $dz = 0.42\lambda_o$ for $f = 30GHz$). This size is based on the number of the scaling functions, since the wavelets are used only when and where necessary. The time discretization interval is selected to be identical for both schemes and equal to the 1/4 of the 2D-MRTD maximum Δt. For the analysis we use 3,000 time-steps. The longitudinal distance is chosen such that no reflections would appear before the Gabor function is complete and the schemes dispersion performance can be evaluated. The normal electric field E_x is probed at three different locations and the results are plotted in (Fig.6.2) showing only minimal dispersion.

The capability of the MRTD technique to provide space and time adaptive gridding is verified by thresholding the wavelet components to the maximum of the 0.01% of the value of the scaling function at the same cell for each time-step and the absolute threshold of 10^{-5}. The use of the absolute threshold enhances the efficiency of the algorithm for very small field values. It has been observed that the accuracy by using only a small number of wavelets is equal to what would be achieved if wavelets were used everywhere. Though this number is varying in time , its maximum value is 122 out of a total of 320 to the z-direction (economy in memory by a factor of 5.1 to the z-direction) as it can be observed from (Fig.6.3). In addition, execution time is reduced by a factor 3-4. The principle of the space-adaptive grid is exhibited at (Fig.6.4) which represents the E_x field distribution at t=1000 time steps. The wavelets have a significant value only at the region of the propagating pulse, thus creating a locally dense grid.

6.3.2 Parallel-Plate Partially Filled Waveguide

The second structure analyzed with the MRTD algorithm was the geometry of (Fig.6.5). A Gabor pulse 0-30 GHz is propagating from the left (air region) to the right (region

with $\epsilon_r = 2.56$). PML regions of 16 cells with σ_E^{max} calculated for designated R_{max}=1.e-7 terminate the grid and wavelets of 0-resolution are used in the longitudinal direction. The reflection coefficient S_{11} is calculated by separating the incident and the reflected part of the probed field and taking the Fourier transform of their ratio (Fig.6.6). Similar accuracy can be obtained for a 4x640 FDTD grid and a 2x80 MRTD grid with relative threshold 0.01% and absolute threshold 10^{-3}. The maximum number of wavelets used is 36 (Fig.6.7) offering an economy in memory by a factor of 6.53 in comparison to the FDTD simulations for the longitudinal (z) direction. The results for 5 GHz (TEM propagation) are validated by comparison to the theoretical value obtained applying ideal transmission line theory [67] and are plotted at Table (6.1).

The time- and space-adaptive character of the gridding is exploited in (Fig.6.8) which show that the wavelets follow the reflected and the transmitted pulses after the incidence to the dielectric interface and have negligible values elsewhere. The location and the number of the wavelet coefficients with significant values are different for each time-step, something that creates a dense mesh in regions of strong field variations, while maintaining a much coarser mesh for the other cells.

6.3.3 Parallel-Plate Five-Stage Filter

The last structure analyzed with the variable grid is the 5-stage filter of (Fig.6.9). A Gabor function 0-4GHz is propagating from the left to the right. The input and output stages have $\epsilon_r = 12.5$ and the intermediate stages have $\epsilon_r = 50.5$ (stages with $d_1 = d_5 = 0.5mm$ and $d_3 = 2mm$) and $\epsilon_r = 1.$ (stages with $d_2 = d_4 = 14.mm$). The total length to the longitudinal direction is 600 mm and to the vertical 4.8 mm. PML regions of 16 cells with σ_E^{max} calculated for designated $R_{max} = 1.e-7$ terminate the grid and wavelets

of 0-resolution are used to the longitudinal direction. The structure is analyzed by using an FDTD grid of 8x1600 cells, a scaling only MRTD grid of 2x400 cells and an adaptive (scaling+wavelets) MRTD grid of 2x200 cells. The relative threshold has the value of 0.01% and the absolute threshold equals to 10^{-4}. The maximum number of wavelets required during the 3,000 time steps of the simulation is 102 (Fig.6.10) , offering an economy by 37.25% in comparison to the scaling only grid and by a factor of 6.37 in comparison to the FDTD scheme for the direction of wavelet expansion (z-direction). The accuracy in the calculation of the S-parameters is similar for all three schemes as it can be observed from (Fig.6.11). Again, the time- and space- adaptive character of the proposed gridding is demonstrated in (Fig.6.12) with the E_x field space distribution for t=1000 time steps.

6.4 Conclusion

A dynamically changing space- and time- adaptive meshing algorithm based on a multiresolution time-domain scheme in two dimensions and on absolute and relative thresholding of the wavelet values has been proposed and has been applied to the numerical analysis of various nonohomogeneous waveguide geometries. A mathematically correct way of dielectric modeling has been presented and evaluated. The field distributions and the S parameters have been calculated and verified by comparison to reference data. In comparison to Yee's conventional FDTD scheme, the proposed scheme offers memory savings by a factor of 5-6 per dimension maintaining a similar accuracy. The above algorithm can be effectively extended to three-dimension problems.

	S_{11} (Ω)	Relative error
Analyt. Value [67]	0.4298	0.0%
4x640 FDTD	0.4283	-0.3%
2x80 MRTD	0.4360	+1.4%

Table 6.1: S_{11} calculated by 2D-MRTD

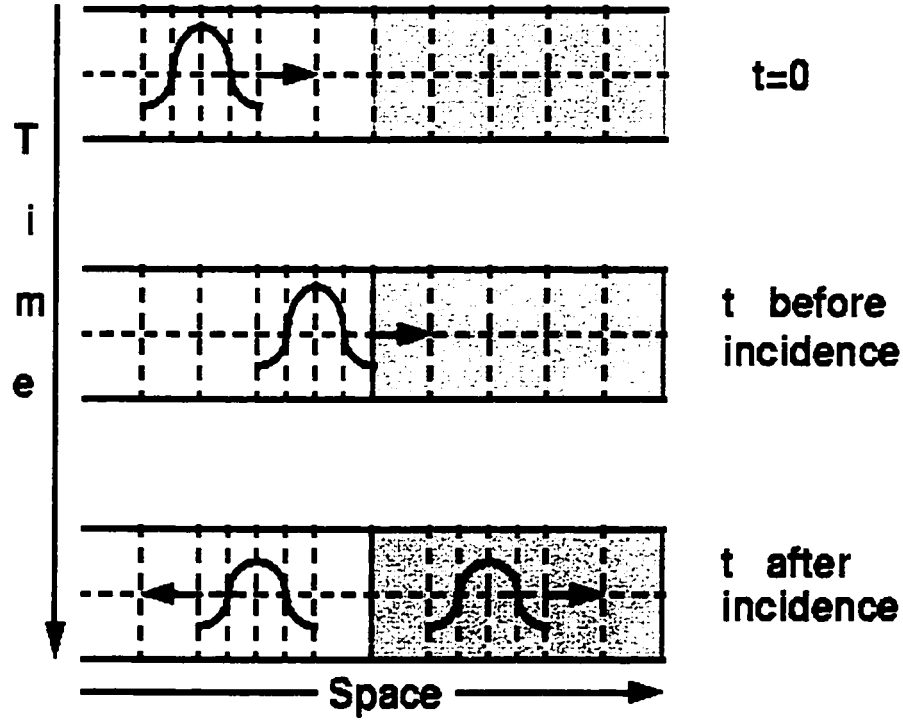

Figure 6.1: Time- and Space- adaptive grid.

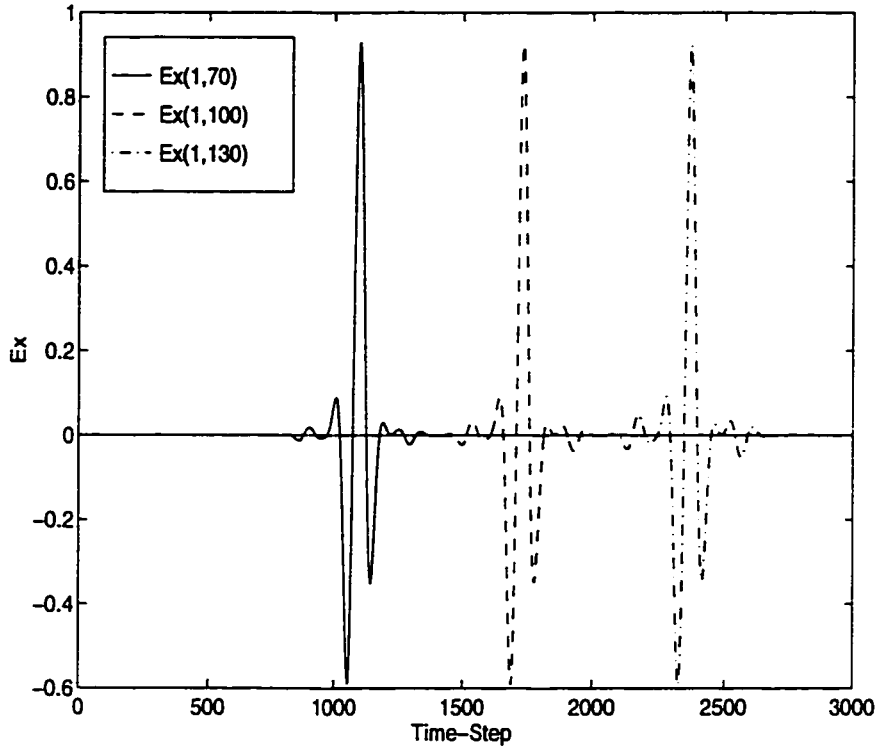

Figure 6.2: Normal E-field (Time-Domain).

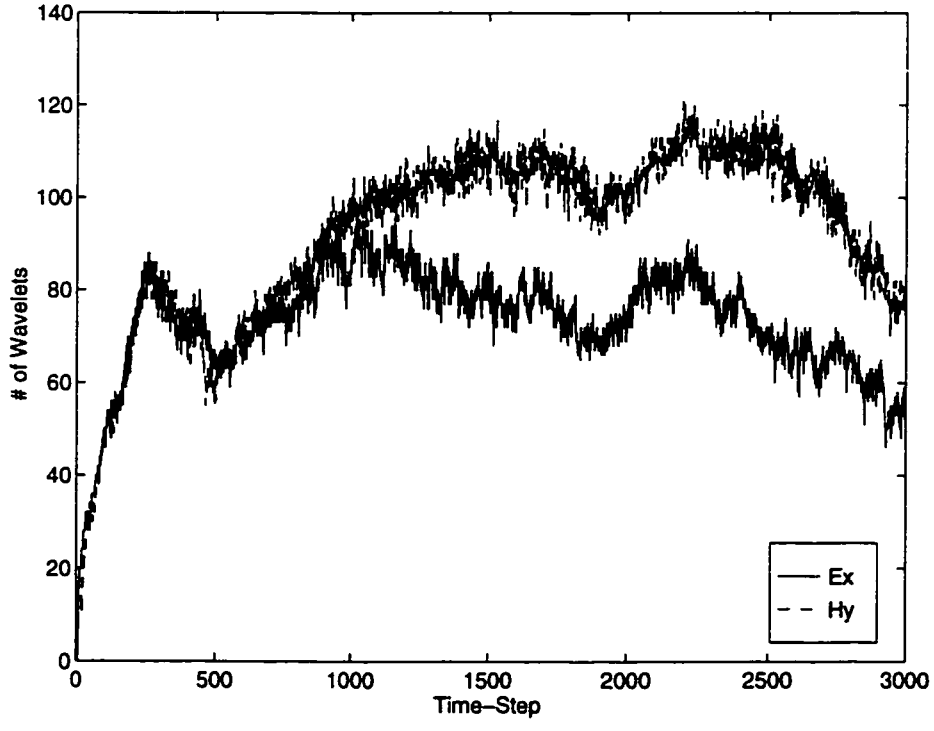

Figure 6.3: Non-zero Wavelets' Number

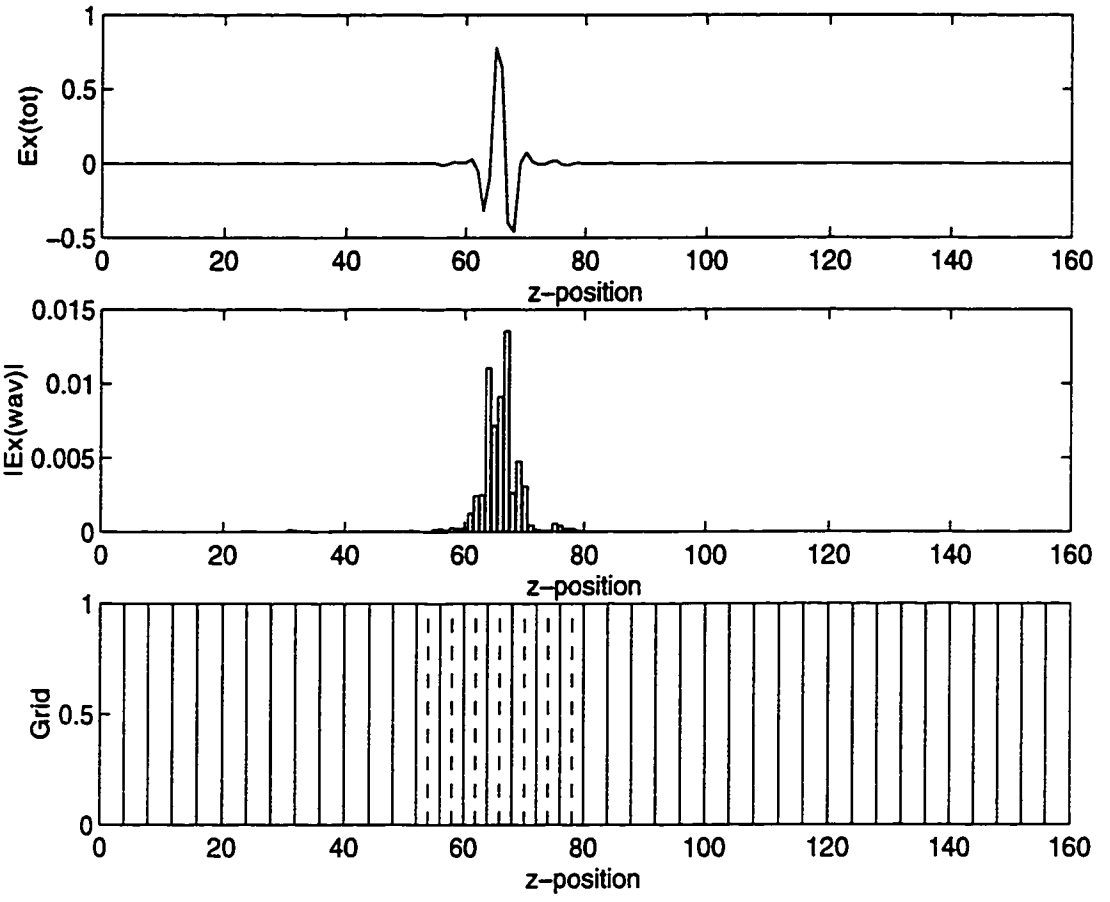

Figure 6.4: Adaptive Grid Demonstration (t=1000 steps).

Figure 6.5: Parallel-Plate Partially Filled Waveguide.

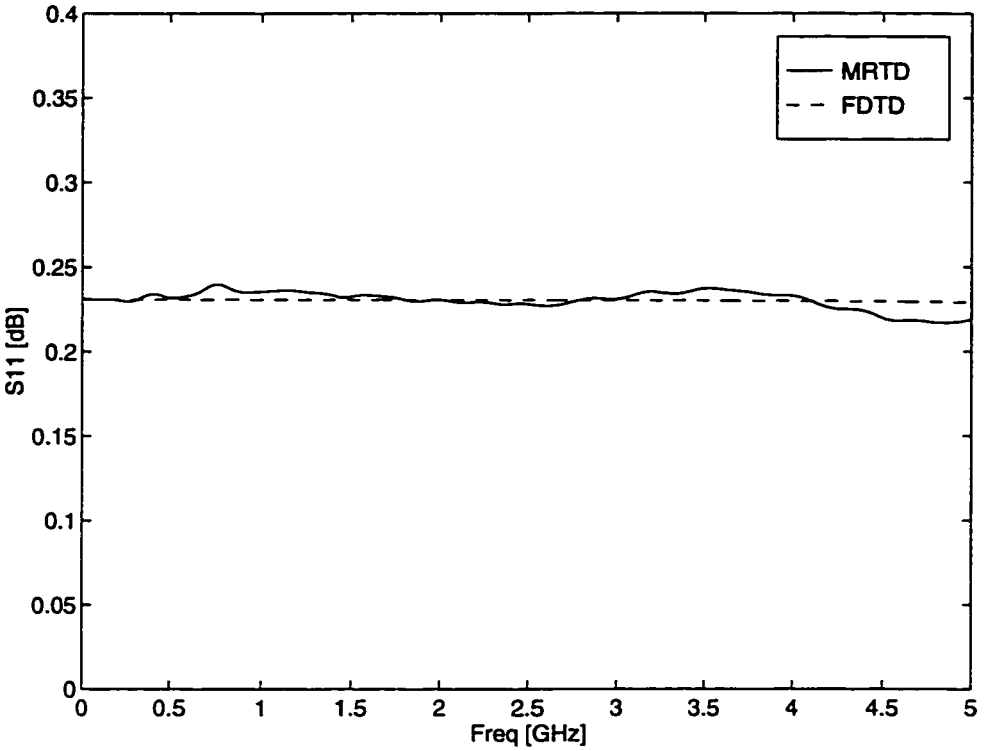

Figure 6.6: S-Parameters of the Waveguide.

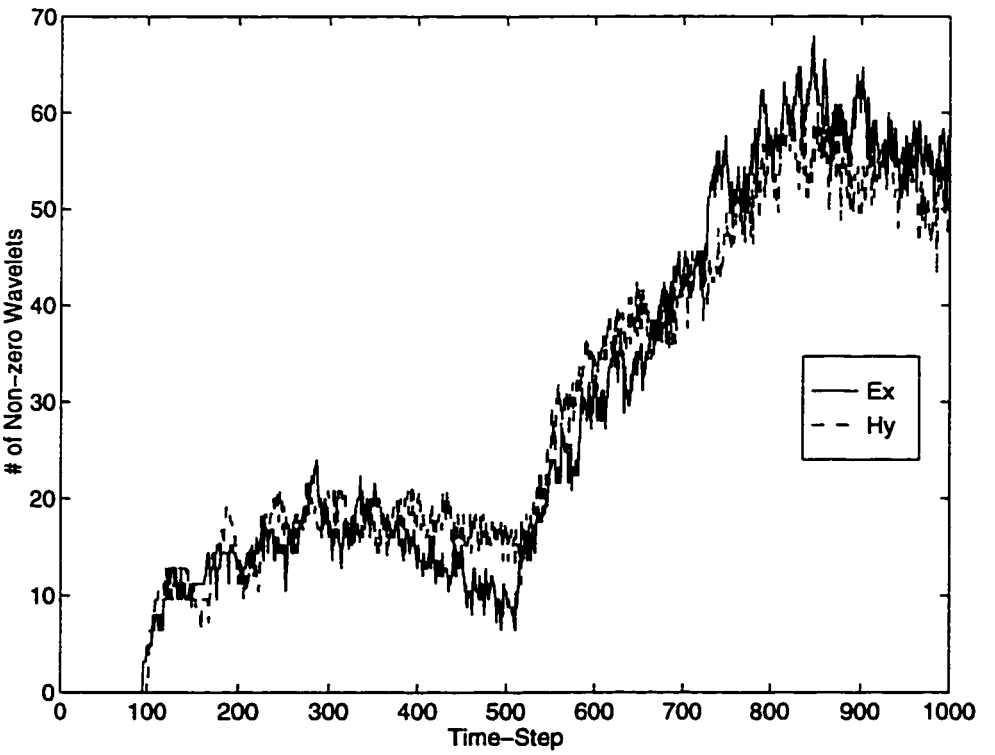

Figure 6.7: Non-zero Wavelets' Number.

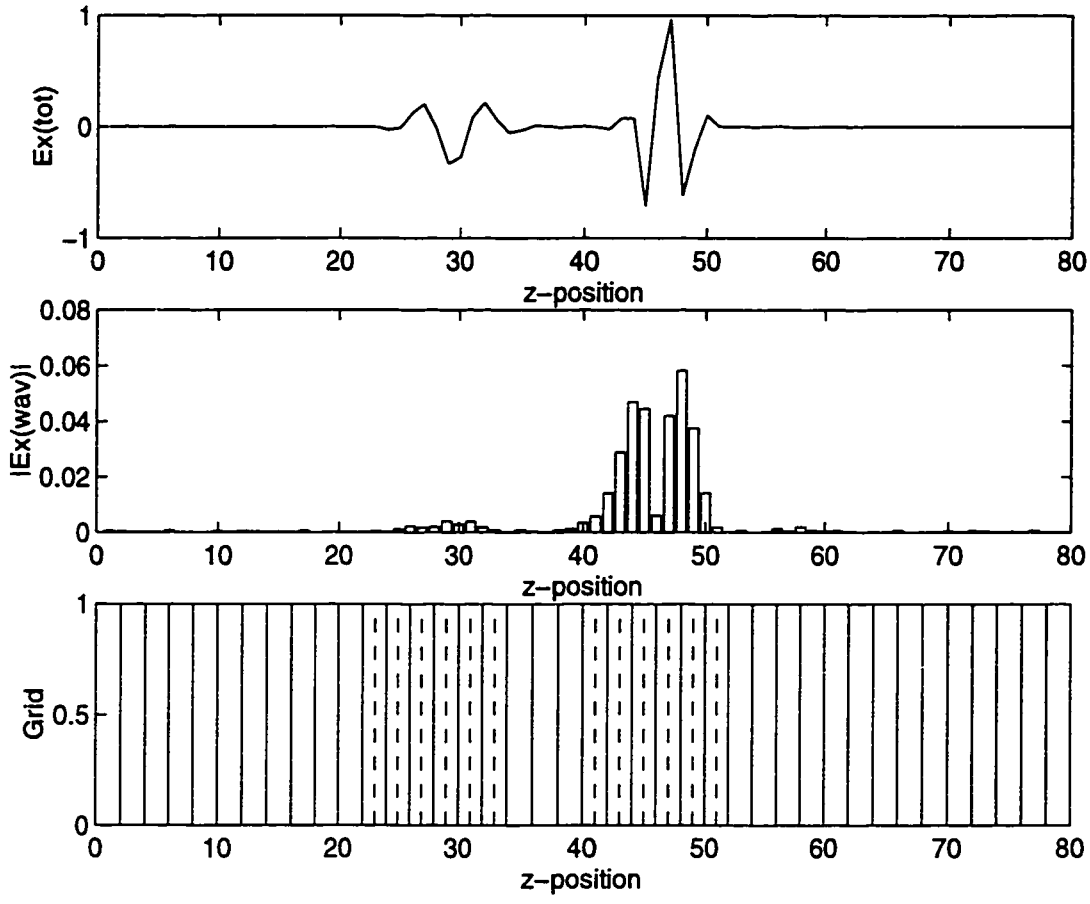

Figure 6.8: Adaptive Grid Demonstration (t=1000 steps).

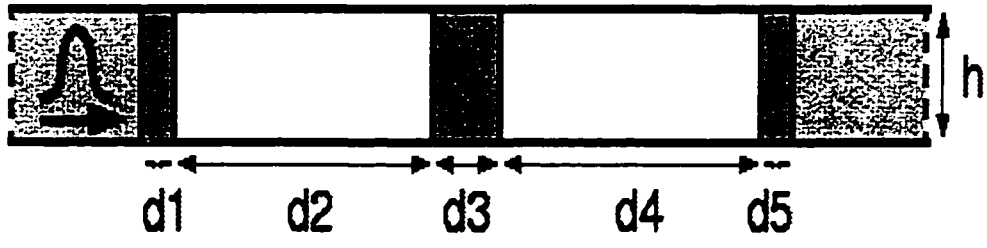

Figure 6.9: Parallel-Plate Five-Stage Filter.

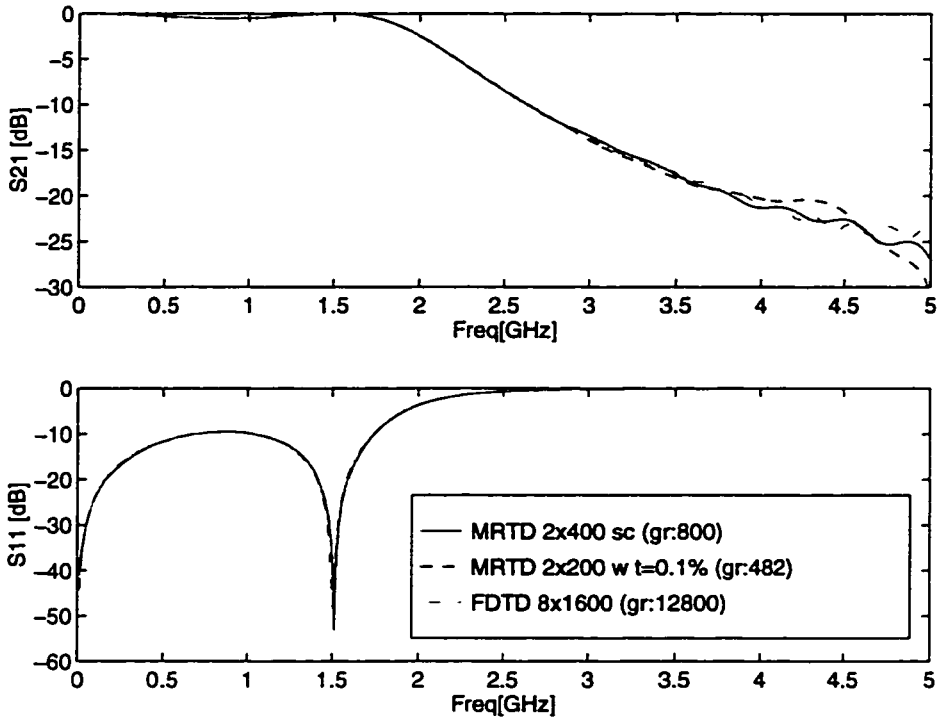

Figure 6.10: S-Parameters of the Filter.

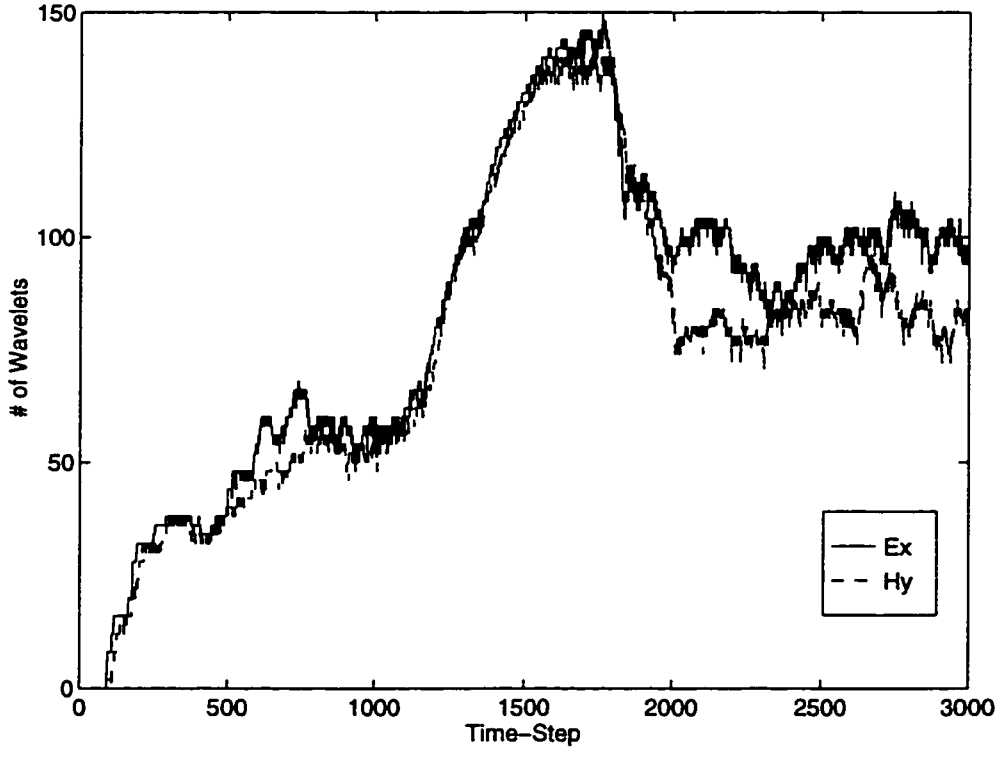

Figure 6.11: Non-zero Wavelets' Number.

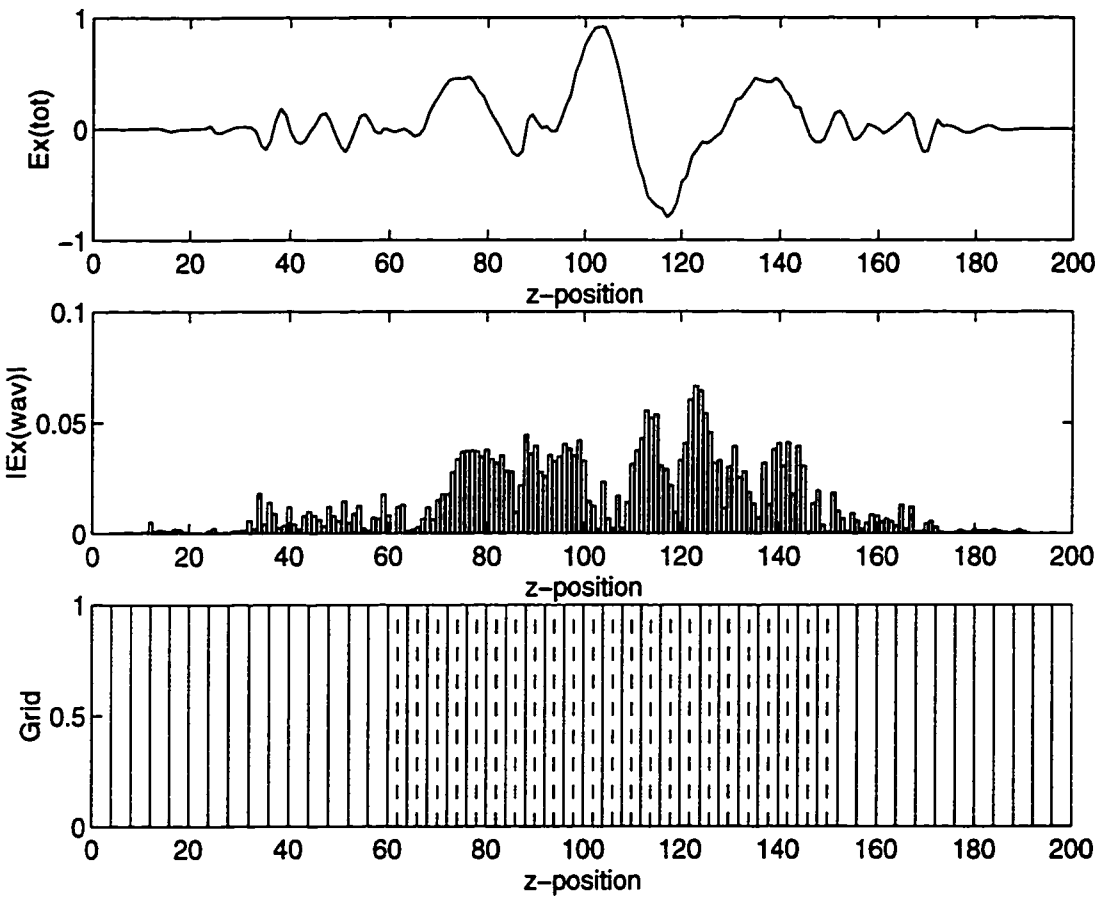

Figure 6.12: Adaptive Grid Demonstration (t=1000 steps).

CHAPTER 7

Time Adaptive Time-Domain Techniques for the Design of Microwave Circuits

7.1 Introduction

In the previous Chapters, MRTD schemes based on cubic spline Battle-Lemarie scaling and wavelet functions have been successfully applied to the simulation of 2D and 3D open and shielded problems [31, 58, 70, 66]. The functions of this family do not have compact support, thus the MRTD schemes have to be truncated with respect to space. Localized boundary conditions (PEC's, PMC's etc.) and material properties are modelled by use of the image principle and of matrix equations respectively. However, this disadvantage is offset by the low-pass (scaling) and band-pass (wavelets) characteristics in spectral domain, allowing for an a priori estimate of the number of resolution levels necessary for a correct field modelling. In addition, the evaluation of the moment method integrals during the discretization of Maxwell's PDEs is simplified due to the existence of closed form expressions in spectral domain and simple representations in space domain. Dispersion analysis of this MRTD scheme shows the capability of excellent accuracy with up to 2 points/wavelength (Nyquist Limit). However, specific circuit problems may require the use of functions with

compact support. Especially in the approximation of time derivatives, the use of entire domain expansion basis would require very high memory resources for the storage of the field values everywhere on the grid for the whole or a large fraction of the simulation time. This problem does not exist in the approximation of the spatial derivatives since the field values on the neighboring spatial grid points have to calculated and stored no matter what expansion basis are used. For that reason, Haar basis functions have been utilized and have led to [71]. As an extension to this approach, intervalic wavelets (Fig.7.1) may be incorporated into the solution of SPICE-type circuits , especially those containing active elements (PN Diodes, ...). Results from this new finite-domain expansion basis will be presented in this Chapter .

7.2 Time Adaptive MRTD Scheme

The major advantage of the use of Mutiresolution analysis to time domain is the capability to develop time and space adaptive schemes. This is due to the property of the wavelet expansion functions to interact weakly and allow for a spatial sparsity that may vary with time through a thresholding process. The adaptive character of this technique is extremely important for the accurate modelling of sharp field variations of the type encountered in beam focusing in nonlinear optics, etc. The use of the principles of the multiresolution analysis for adaptive grid computations for PDEs has been suggested by Perrier and Basdevant [72]. To understand the fundamental steps of such an adaptive scheme for Maxwell's hyperbolic system, let's consider Maxwell's equations in 2D (1 for space and 1 for time):

$$\frac{\partial \hat{u}}{\partial t} = A\hat{u} = \begin{bmatrix} 0 & -\epsilon(z)^{-1}\frac{\partial}{\partial z} \\ -\mu(z)^{-1}\frac{\partial}{\partial z} & 0 \end{bmatrix} \hat{u}, \quad \hat{u} = (E(z,t), H(z,t))^T \quad , \qquad (7.1)$$

After manipulation, the above equation can be written as

$$\mathbf{M}\hat{u} = \begin{bmatrix} \epsilon T_h^{\dagger} D_t & T_h^{\dagger} D_z \\ Z_h^{\dagger} D_z & \mu Z_h^{\dagger} D_t \end{bmatrix} \hat{u} = 0$$

where Z_h, T_h are half shift operators for space and time coordinates z,t and $Z_h^{\dagger}, T_h^{\dagger}$ are their Hermitian conjugates. D_t, D_z are difference operators given by:

$$D_t = \frac{1}{\Delta t}\left(\sum_{i=-9}^{8} a_{\phi t}(i) T^{-i} + \sum_{i=-9}^{9} a_{\psi t}(i) T^{-i}\right), \quad D_z = \frac{1}{\Delta z}\left(\sum_{i=-9}^{8} a_{\phi z}(i) Z^{-i} + \sum_{i=-9}^{9} a_{\psi z}(i) Z^{-i}\right) \quad , \tag{7.2}$$

where a_{ϕ}, a_{ψ} are the coefficients associated with the scalar and the wavelet functions respectively. At each time step we keep both the wavelet field values that are larger than a given threshold as well as the adjacent values. An adjacent wavelet field value is defined on the basis of the wavelet resolution level(s) incorporated in the solution. Recently, an efficient space/time adaptive meshing procedure was proposed [73] for Battle-Lemarie expansion functions. In this chapter, intervalic 0-order wavelets are used for the expansion of the fields and a simple thresholding procedure is employed. The adaptive mesh is applied to a variety of circuit problems and results are discussed in the next section.

7.3 Applications in SPICE problems

For simplicity, the 1D MRTD scheme will be derived. It can be extended to 2D and 3D in a straightforward way. In addition, only the 0-resolution of wavelets is enhanced. The Voltage and the Current are displaced by half step in both time- and space-domains (Yee cell formulation) and are expanded in a summation of scaling functions in space and scaling (ϕ) and wavelet (ψ_0) components in time

$$\begin{aligned} V(z,t) &= \sum_{m=-\infty}^{\infty} \sum_{i=-\infty}^{\infty} \left({}_iV_m^{\phi}\phi_i(t) + {}_iV_m^{\psi_0}\psi_{0,i}(t)\right)\ \phi_m(z) \\ I(z,t) &= \sum_{m=-\infty}^{\infty} \sum_{i=-\infty}^{\infty} \left({}_{i-0.5}I_{m-0.5}^{\phi}\phi_{i-0.5}(t) + {}_{i-0.5}I_{m-0.5}^{\psi_0}\psi_{0,i-0.5}(t)\right)\ \phi_{m-0.5}(z) \end{aligned} \tag{7.3}$$

where $\phi_i(t) = \phi(t/\Delta t - i)$ and $\psi_{0,i}(t) = \psi_0(t/\Delta t - i)$ represent the 0-order intervalic scaling and 0-resolution wavelet functions. The conventional notation ${}_kV_m$ is used for the voltage component at time $t = k\Delta t$ and $z = m\Delta z$, where Δt and Δz are the time-step and the spatial cell size respectively. The notation for the current I is similar.

Due to the finite-domain nature of the expansion basis, the Hard Boundary conditions (Open/Short Circuit) can be easily modeled. If a Short Circuit exists at the $z = m\Delta z$, then both scaling and wavelet voltage coefficients for the $m - cell$ must be set to zero for each time-step k.

$$ {}_kV_m^{\phi} = {}_kV_m^{\psi_0} = 0, \quad k = 0, 1, 2, ... \tag{7.4} $$

Similarly, an Open Circuit at $z = (m - 0.5)\Delta z$ can be modeled by applying the conditions

$$ {}_{k-0.5}I_{m-0.5}^{\phi} = {}_{k-0.5}I_{m-0.5}^{\psi_0} = 0, \quad , k = 0, 1, 2, ... \tag{7.5} $$

The alternating nature of the 0-resolution wavelet function guarantees the double time-domain resolution of the MRTD scheme. Assuming that the voltage scaling and wavelet coefficients at $m = \Delta z$ for a specific time-step k, two values can be defined for the time span $[(k - 0.5)\Delta t,\ (k + 0.5)\Delta t]$ of this time-step

$$ {}_kV_m^{total,1} = {}_kV_m^{\phi} + {}_kV_m^{\psi_0}, \quad t \in [(k - 0.5)\Delta t,\ k\Delta t] \tag{7.6} $$

$$ {}_kV_m^{total,2} = {}_kV_m^{\phi} - {}_kV_m^{\psi_0}, \quad t \in [k\Delta t,\ (k + 0.5)\Delta t] \quad . \tag{7.7} $$

7.3.1 Distributed Elements

Lossless Line

The ideal transmission line (Fig.7.2) equations are given by

$$ \begin{aligned} \frac{dV}{dz} &= -L_{dis}\frac{dI}{dt} \\ \frac{dI}{dz} &= -C_{dis}\frac{dV}{dt} \quad , \end{aligned} \tag{7.8} $$

where L_{dis}, C_{dis} are the distributed inductance and capacitance of the line. Inserting the expansions of Eq.(7.3) and applying the Method of Moments, the following MRTD equations are derived

$$\frac{C_{dis}}{\Delta t}\left({}_{k+1}V_m^{\phi} - {}_{k}V_m^{\phi}\right) = -\frac{1}{\Delta z}\left({}_{k+0.5}I_{m+0.5}^{\phi} - {}_{k+0.5}I_{m-0.5}^{\phi}\right) \quad (7.9)$$

$$\frac{C_{dis}}{\Delta t}\left({}_{k+1}V_m^{\psi_0} - {}_{k}V_m^{\psi_0}\right) = -\frac{1}{\Delta z}\left({}_{k+0.5}I_{m+0.5}^{\psi_0} - {}_{k+0.5}I_{m-0.5}^{\psi_0}\right) \quad (7.10)$$

$$\frac{L_{dis}}{\Delta t}\left({}_{k+0.5}I_{m-0.5}^{\phi} - {}_{k-0.5}I_{m-0.5}^{\phi}\right) = -\frac{1}{\Delta z}\left({}_{k}V_m^{\phi} - {}_{k}V_{m-1}^{\phi}\right) \quad (7.11)$$

$$\frac{L_{dis}}{\Delta t}\left({}_{k+0.5}I_{m-0.5}^{\psi_0} - {}_{k-0.5}I_{m-0.5}^{\psi_0}\right) = -\frac{1}{\Delta z}\left({}_{k}V_m^{\psi_0} - {}_{k}V_{m-1}^{\psi_0}\right) \quad (7.12)$$

It can be observed that Eqs.(7.9) and (7.11) updating the scaling coefficients only are independent of the Eqs.(7.10) and (7.12) updating the wavelet coefficients. To create an efficient time adaptive algorithm, all four equations must be coupled. An efficient way is to apply the excitation in a physically correct manner. If the excitation has the time-dependence $g(t)$ at the location $z = m_e\Delta z$, then the scaling and wavelet coefficients for this cell have to take the values

$$\begin{aligned} {}_{k}V_{m_e}^{\phi} &= \int_{(k-0.5)\Delta t}^{(k+0.5)\Delta t} g(t)\,\phi_k(t)\,dt \\ {}_{k}V_{m_e}^{\psi_0} &= \int_{(k-0.5)\Delta t}^{(k+0.5)\Delta t} g(t)\,\psi_{0,k}(t)\,dt \quad . \end{aligned} \quad (7.13)$$

To validate this approach, the MRTD algorithm was applied to the simulation of a lossless transmission line with $(L_{dis}, C_{dis}) = (20nH/m, 3nF/m)$ for a Gabor excitation and time-step $dt = dt_{max}/1.01$. (Fig.7.3) which displays the Voltage Scaling and Wavelet Coefficients evolution at $z = 200\Delta z$ for the first 800 time-steps of the simulation, shows that the wavelet coefficients have the correct shape (significant values only at areas with significant scaling function values) and are close to the 12% of the respective scaling functions. (Fig.7.4) which compares the total voltage value at $z = 200\Delta z$ calculated by FDTD (Sc.ONLY) and MRTD (Sc.+Wav.) for the time-steps 357–362 demonstrates the ability of this MRTD

scheme to double the conventional FDTD resolution in the time-domain by providing two values for each time-step. The fact that the wavelet coefficients take significant values only for a small number of time-steps allows for their thresholding by comparing them to a combination of relative to the respective value of the scaling coefficient (5.e-4) and absolute (1.e-6) thresholds. (Fig.7.5) proves that up to 60% of the maximum number of wavelet coefficients are necessary for an accurate simulation, offering an extra economy in memory by a factor of 20%.

Lossy Line

The lossy transmission line (Fig.7.6) equations are derived by the ideal transmission line equations (Eq.(7.8)) adding the Conductor Loss R_{dis} and the Dielectric Loss G_{dis}

$$\begin{aligned} \frac{dV}{dz} &= -R_{dis} I - L_{dis} \frac{dI}{dt} \\ \frac{dI}{dz} &= -G_{dis} V - C_{dis} \frac{dV}{dt} \quad . \end{aligned} \tag{7.14}$$

Following a procedure similar to the previous section, the following MRTD equations are derived

$$\begin{aligned} {}_{k+1}V_m^{\phi} = & - \frac{(C_1 - C_2)}{C_1^2} \Delta t \, ({}_{k+0.5}I_{m+0.5}^{\phi} - {}_{k-0.5}I_{m-0.5}^{\phi}) + \frac{C_2}{C_1^2} \Delta t \, ({}_{k+0.5}I_{m+0.5}^{\psi_0} - {}_{k-0.5}I_{m-0.5}^{\psi_0}) \\ & + \frac{(C_1 - C_2)^2 + C_2^2}{C_1^2} \, {}_kV_m^{\phi} - 2 \, \frac{C_2^2}{C_1^2} \, {}_kV_m^{\psi_0} \end{aligned} \tag{7.15}$$

$$\begin{aligned} {}_{k+1}V_m^{\psi_0} = & - \frac{C_2}{C_1^2} \Delta t \, ({}_{k+0.5}I_{m+0.5}^{\phi} - {}_{k-0.5}I_{m-0.5}^{\phi}) - \frac{(C_1 + C_2)}{C_1^2} \Delta t \, ({}_{k+0.5}I_{m+0.5}^{\psi_0} - {}_{k-0.5}I_{m-0.5}^{\psi_0}) \\ & - 2 \, \frac{C_2^2}{C_1^2} \, {}_kV_m^{\phi} + \frac{(C_1 - C_2)^2 + C_2^2}{C_1^2} \, {}_kV_m^{\psi_0} \end{aligned} \tag{7.16}$$

$$\begin{aligned} {}_{k+0.5}I_{m-0.5}^{\phi} = & - \frac{(C_3 - C_4)}{C_3^2} \Delta t \, ({}_kV_m^{\phi} - {}_kV_{m-1}^{\phi}) + \frac{C_4}{C_3^2} \Delta t \, ({}_kV_m^{\psi_0} - {}_kV_{m-1}^{\psi_0}) \\ & + \frac{(C_3 - C_4)^2 + C_4^2}{C_3^2} \, {}_{k-0.5}I_{m-0.5}^{\phi} - 2 \, \frac{C_4^2}{C_3^2} \, {}_{k-0.5}I_{m-0.5}^{\psi_0} \end{aligned} \tag{7.17}$$

$$\begin{aligned} {}_{k+0.5}I_{m-0.5}^{\psi_0} = & - \frac{C_4}{C_3^2} \Delta t \, ({}_kV_m^{\phi} - {}_kV_{m-1}^{\phi}) - \frac{(C_3 + C_4)}{C_3^2} \Delta t \, ({}_kV_m^{\psi_0} - {}_kV_{m-1}^{\psi_0}) \\ & - 2 \, \frac{C_4^2}{C_3^2} \, {}_{k-0.5}I_{m-0.5}^{\phi} + \frac{(C_3 - C_4)^2 + C_4^2}{C_3^2} \, {}_{k-0.5}I_{m-0.5}^{\psi_0} \quad , \end{aligned} \tag{7.18}$$

with

$$C_1 = C_{dis}\Delta z \quad , \quad C_2 = 0.5\, G_{dis}\Delta z\, \Delta t,$$

$$C_3 = L_{dis}\Delta z \quad , \quad C_4 = 0.5\, R_{dis}\Delta z\, \Delta t, \qquad .$$

For this type of transmission line, the equations giving the scaling and wavelet coefficients for voltage and current are coupled. Nevertheless, the condition (7.13) has to be applied in order to satisfy the physical boundary condition at the excitation cell(s). It has to be noted, that Eqs.(7.15)–(7.18) can be used only for lossy lines with low to medium Loss Coefficients. The threshold $C_2 \leq 4C_1$ for G_{dis} ($C_4 \leq 4C_3$ for R_{dis}) gave satisfactory results for all simulations. For higher loss coefficients, the Loss can be modeled in an exponential way similar to [66]. For example, for large values of R_{dis} ($C_4 > C_3$), Eqs.(7.17)–(7.18) have to be replaced by the following uncoupled expressions

$$ {}_{k+0.5}I^{\phi}_{m-0.5} = e^{\frac{-R_{dis}\Delta t}{L_{dis}}}\, {}_{k-0.5}I^{\phi}_{m-0.5} - e^{\frac{-0.5R_{dis}\Delta t}{L_{dis}}}\, \frac{\Delta t}{C_3}\, ({}_kV^{\phi}_m - {}_kV^{\phi}_{m-1}) \qquad (7.19)$$

$$ {}_{k+0.5}I^{\psi_0}_{m-0.5} = e^{\frac{-R_{dis}\Delta t}{L_{dis}}}\, {}_{k-0.5}I^{\psi_0}_{m-0.5} - e^{\frac{-0.5R_{dis}\Delta t}{L_{dis}}}\, \frac{\Delta t}{C_3}\, ({}_kV^{\psi_0}_m - {}_kV^{\psi_0}_{m-1}) \qquad (7.20)$$

Using this procedure, a termination layer similar to the FDTD widely used PML layer can be easily modeled. The R_{dis}, G_{dis} should have a spatial parabolic distribution with very high maximum value and they should satisfy the condition $G_{dis} = R_{dis}L_{dis}/C_{dis}$ for each cell of the layer. In this way, one matched transmission line can be simulated by choosing the appropriate R_{dis}, G_{dis} that satisfy the specified numerical reflection coefficient (usually smaller than -80dB).

For validation purposes, the MRTD algorithm was applied to the simulation of a lossy transmission line with $(L_{dis}, C_{dis}) = (20nH/m, 3nF/m)$ and $(R_{dis}, G_{dis}) = (0.1\Omega/m, 1.e-5\Omega^{-1}/m)$ for a Gabor excitation [50 MHz, 100 MHz], 5,000 time-steps with size $\Delta t = 0.79\Delta t_{max}$ and 4,000 cells with $\Delta z = 15cm$. (Fig.7.7(a)) which displays the Voltage Scaling

and Wavelet Coefficients evolution at $z = 1500\Delta z$ for the first 1400 time-steps of the simulation, shows that the wavelet coefficients have the correct shape (significant values only at areas with significant scaling function values and approximately equal to the values of the first derivative of the voltage spatial distribution) and are close to the 11% of the respective scaling functions. Figs.(7.7(b))–(7.7(c)) which compare the total voltage value at the same probe position calculated by FDTD (Scal.) and MRTD (Scal.+Wav0) for the time-steps 1000–1400 and 1103–1107 respectively, demonstrate the ability of this MRTD scheme to double the conventional FDTD resolution in the time-domain by providing two values for each time-step.

7.3.2 Lumped Elements

Passive Elements

Lumped Passive Elements such as Capacitors, Inductors and Resistors can be modeled in a similar way with the Distributed ones by numerically distributing them along one cell. For example, if one lumped Capacitor C_{lum} is located at $z = m\Delta z$ along a lossy line with $(R_{dis}, G_{dis}, L_{dis}, C_{dis})$, the voltage coefficients ${}_{k+1}V_m^{\phi}$, ${}_{k+1}V_m^{\psi_0}$ will still be given by Eqs.(7.15)–(7.16). The only difference is that the constant C_1 will have the new value $C_1 = C_{tot}\Delta z$ with

$$C_{tot} = C_{dist} + \frac{C_{lum}}{\Delta z} \quad . \tag{7.21}$$

PN-Diode

To model lumped active elements such as a PN-diode, their nonlinear equation has to be discretized after inserting the voltage and current expansions. The MRTD equations are not linear and require the use of numerical solvers for nonlinear systems. The combined

Newton-Raphson/Bisection solver has provided stable solutions for PN-diode simulations with $I_0 \leq 1.e-10A$,though sometimes diverges for larger values. The voltage scaling and wavelet coefficients for the diode cell are updated by inserting the voltage and current expansion in the equation

$$I_{DIODE}(V) = I_0\ (e^{qV/kT} - 1) \tag{7.22}$$

adding the diode capacitance C_j to the C_{dis} and applying the moments method, thus giving the nonlinear system for a diode positioned in parallel

$$\begin{aligned}(C_5 + C_{dis})\ {}_kV_m^{\phi} \;&+\; C_5\ {}_kV_m^{\psi_0} + (C_5 - C_{dis})\ {}_{k-1}V_m^{\phi} \\ &-\; C_5\ {}_{k-1}V_m^{\psi_0} + \frac{\Delta t}{\Delta z}({}_{k-0.5}I_{m+0.5}^{\phi} - {}_{k-0.5}I_{m-0.5}^{\phi}) \\ &+\; 0.5\ \Delta t\ C_j(e^{kT/q\ I_0\ ({}_{k-1}V_m^{\phi} - {}_{k-1}V_m^{\psi_0})} + e^{kT/q\ I_0\ ({}_kV_m^{\phi} + {}_kV_m^{\psi_0})}) = 0\end{aligned} \tag{7.23}$$

$$\begin{aligned}-C_5\ {}_kV_m^{\phi} \;&-\; (C_5 - C_{dis})\ {}_kV_m^{\psi_0} + C_5\ {}_{k-1}V_m^{\phi} \\ &-\; (C_5 + C_{lum})\ {}_{k-1}V_m^{\psi_0} + \frac{\Delta t}{\Delta z}({}_{k-0.5}I_{m+0.5}^{\psi_0} - {}_{k-0.5}I_{m-0.5}^{\psi_0}) \\ &+\; 0.5\ \Delta t\ C_j(e^{kT/q\ I_0\ ({}_{k-1}V_m^{phi} - {}_{k-1}V_m^{\psi_0})} - e^{kT/q\ I_0\ ({}_kV_m^{\phi} + {}_kV_m^{\psi_0})}) = 0\end{aligned} \tag{7.24}$$

with

$$C_5 = 0.5\ \Delta t\ G_{lum} \quad . \tag{7.25}$$

To validate the algorithm, the rectifier topology of (Fig.7.8) is analyzed using FDTD (Scaling Only) with $\Delta t = \Delta t_{max}/4.4$ and MRTD (Scaling+wavelets) with double time-step $\Delta t = \Delta t_{max}/2.2$. A lossless line with $(L_{dis}, C_{dis}) = (20nH/m, 3nF/m)$ and a PN-Diode with $I_0 = 3pA$ are used in the simulation. The probed total voltage is plotted in (Fig.7.9) and the agreement is very good. The use of an absolute threshold of 10^{-6} and a relative threshold of $5e-4$ offers an extra economy of 35% for the MRTD algorithm.

7.4 Discussion on the Values of the Absolute and Relative Thresholds

The fact that the wavelet coefficients take significant values only for a small number of time-steps allows for the development of a time adaptive gridding algorithm. One thresholding technique based on absolute and relative thresholds offers very significant economy in memory while maintaining the double resolution in time where needed. For each time-step the maximum value of the voltage scaling coefficient over the whole grid is identified. All wavelet components with values below a specific fraction (Relative Threshold) of the above number are eliminated. To take into consideration the time-steps that the voltage scaling components have a very small value (close to numerical accuracy of the algorithm), an absolute threshold is introduced. Similar approach is used for the current wavelet coefficients. It has to be noted that the absolute threshold for the current components is a scaled version of the absolute threshold for the voltage components in order to account for their time-lag by half time-step as well as for their relationship through the wave impedance of the respective medium(s). Different values of the relative and absolute thresholds are investigated in Figs.(7.11)–(7.12) in terms of

$$\begin{aligned} Memory\ Compression(\%) &= \#\ Wavelets(\%) \\ &= \frac{Number\ of\ Wavelets\ above\ Thresholds}{Total\ Number\ of\ Wavelets} \times 100\% \end{aligned} \tag{7.26}$$

and

$$Relative\ Error(\%) = \frac{||Voltage_{(Th)} - Voltage_{(NTh)}||_2}{||Voltage_{(Nth)}||_2} \quad , \tag{7.27}$$

where $Voltage_{(Th)}$ and $Voltage_{(NTh)}$ are the total voltage values at the probe position at $z = 1500\Delta z$ with and without the use of the thresholding algorithm and $||x||_2 = \sqrt{\sum_{t=0}^{N_t} |x_t|^2}$

is the norm-2 defined over the total number N_t of the simulation time-steps. For the simulations, it is used a lossy transmission line with $(L_{dis}, C_{dis}) = (20nH/m, 3nF/m)$ and $(R_{dis}, G_{dis}) = (0.1\Omega/m, 1.e-5\Omega^{-1}/m)$ for a Gabor excitation [50 MHz, 100 MHz], 5,000 time-steps with size $\Delta t = 0.79\Delta t_{max}$ and 4,000 cells with $\Delta z = 15cm$. Fig.(7.11) displays the performance for relative thresholds between 10^{-7} and 3×10^{-2} and absolute threshold of 10^{-7}. For values below 3×10^{-6} the Memory Compression is stabilized to 20% and accuracy close to 0.01%, though for values above 10^{-2} almost no wavelets are used and the additional accuracy offered by the wavelets is lost (accuracy $\approx$ 11%). It can be observed that in order to achieve accuracy below 1% a relative threshold below 5×10^{-4} has to be used. The best compromise between compression and accuracy can be achieved for Relative Threshold between 10^{-4} and 5×10^{-4} (Compression $\approx$ 10% and Relative Error $\in$ [0.1%, 1%]. In Fig.(7.12) the effect of the addition of the Absolute threshold is investigated for three different values of Relative Thresholds. Absolute Thresholds with values between 10^{-6} and 10^{-5} for a Relative Threshold of 5×10^{-4} increase the memory compression to $6\% - 7\%$ while maintaining a relative error below 1%. Thus, the values *Relative Threshold* $= 5 \times 10^{-4}$ and *Absolute Threshold* $= 5 \times 10^{-6}$ have been found to have the optimum performance. They offer a double resolution in time-domain in comparison to the conventional FDTD scheme, while increasing the memory requirements only by $6\% - 7\%$.

7.5 Conclusion

A Time Adaptive Time-Domain Technique based on intervalic wavelets has been proposed and applied to various types of circuits problems with active and passive lumped and distributed elements. This scheme, based on a combination of absolute and relative thresholding, exhibits significant savings in memory requirements while maintaining a similar accuracy with the conventional FDTD technique.

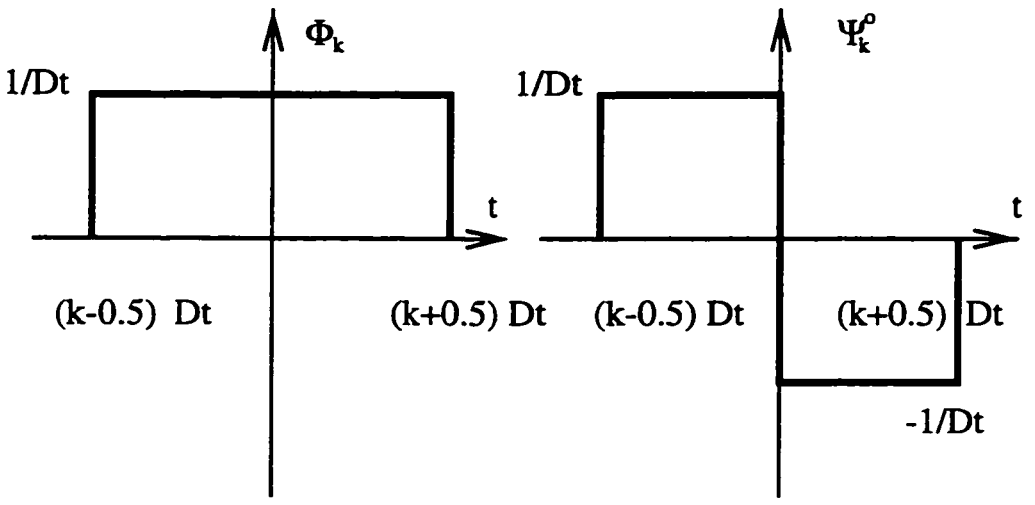

Figure 7.1: 0-Order Intervalic Function Basis.

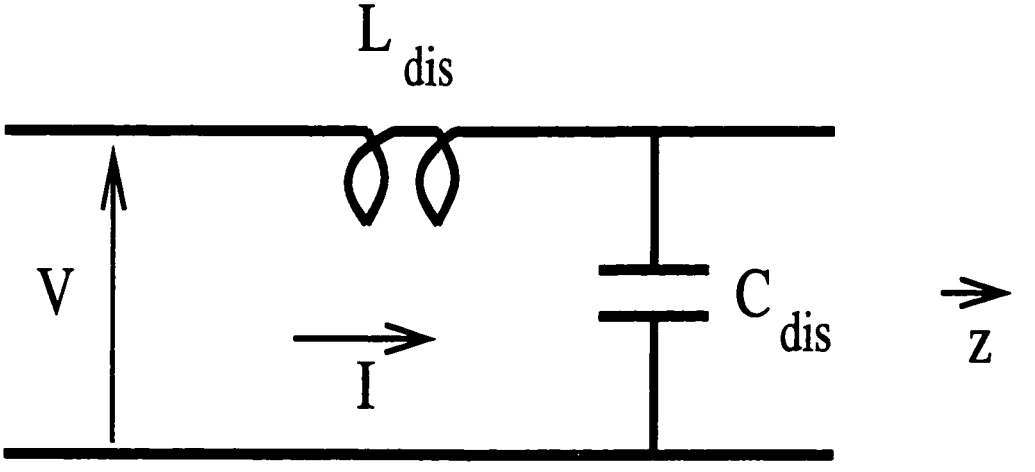

Figure 7.2: Ideal (Lossless) Transmission Line.

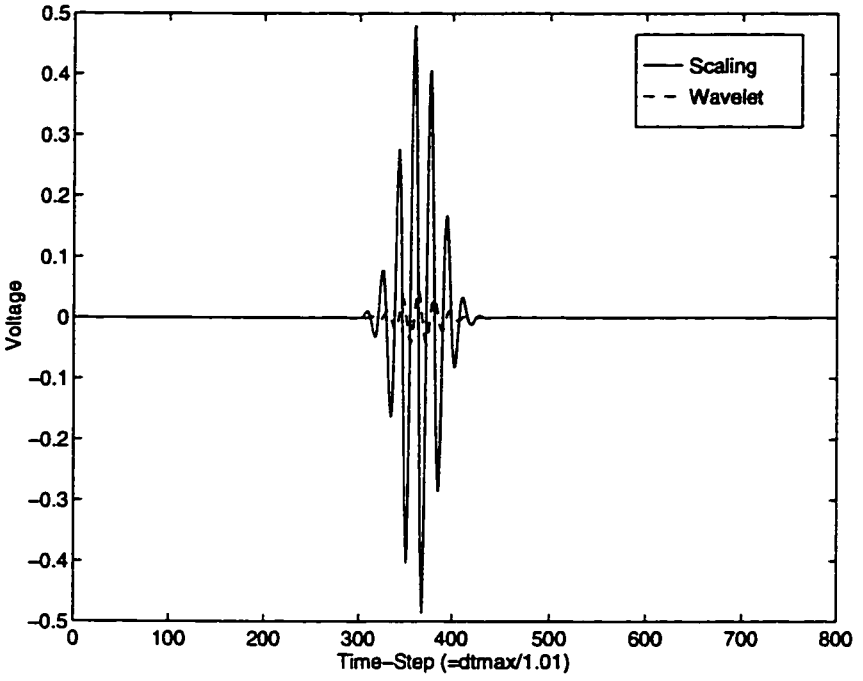

Figure 7.3: Voltage Coefficients.

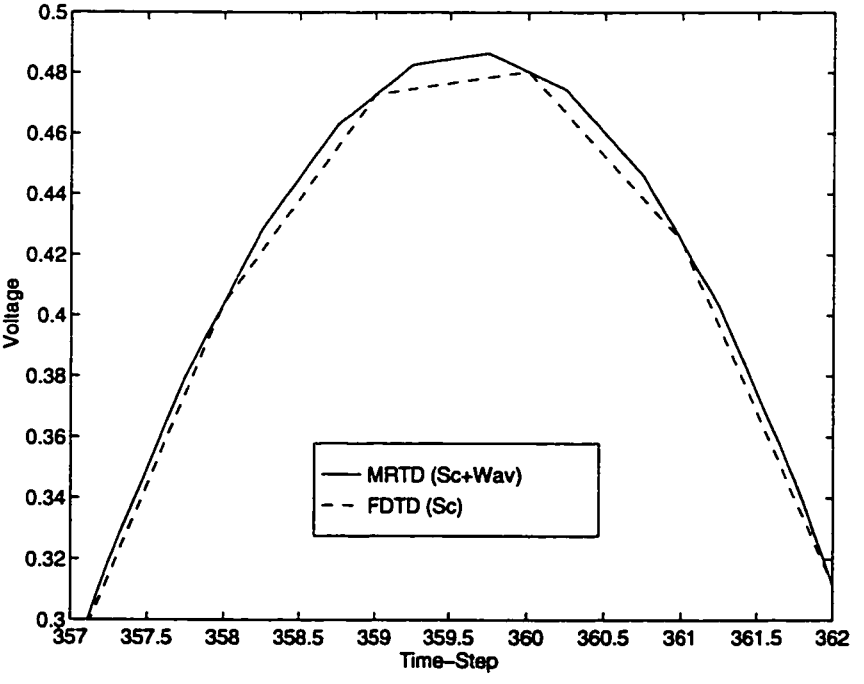

Figure 7.4: Comparison MRTD-FDTD.

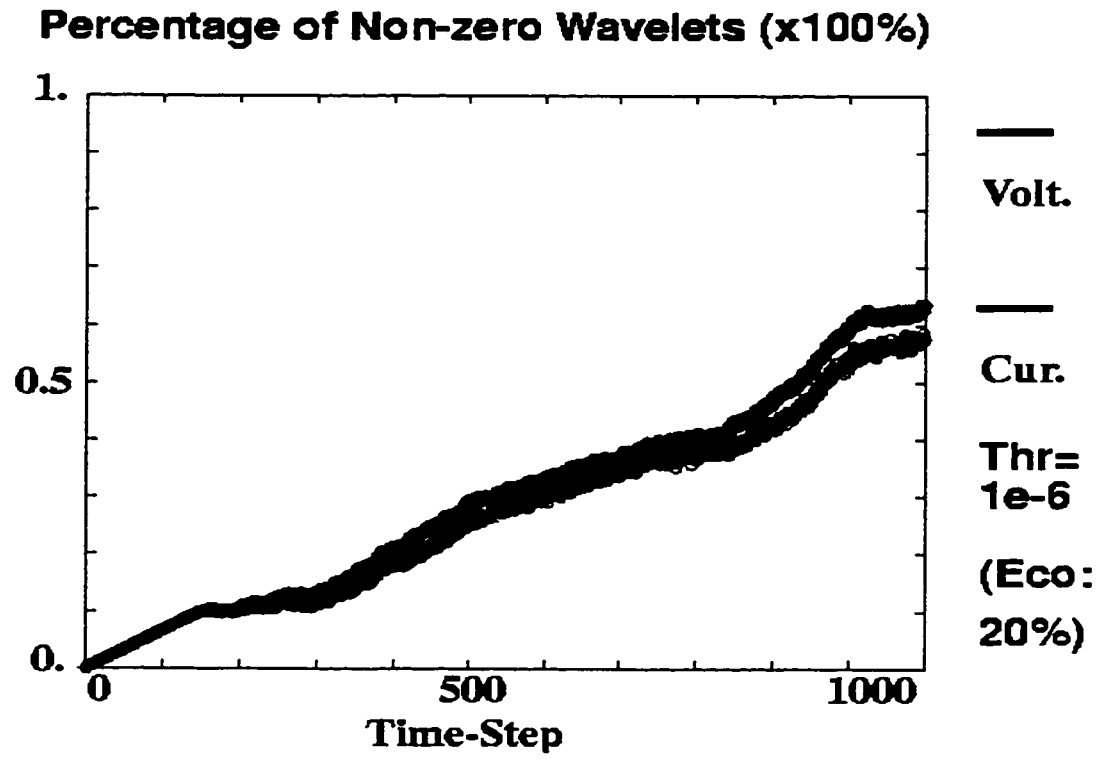

Figure 7.5: Fraction of Wavelets above Threshold.

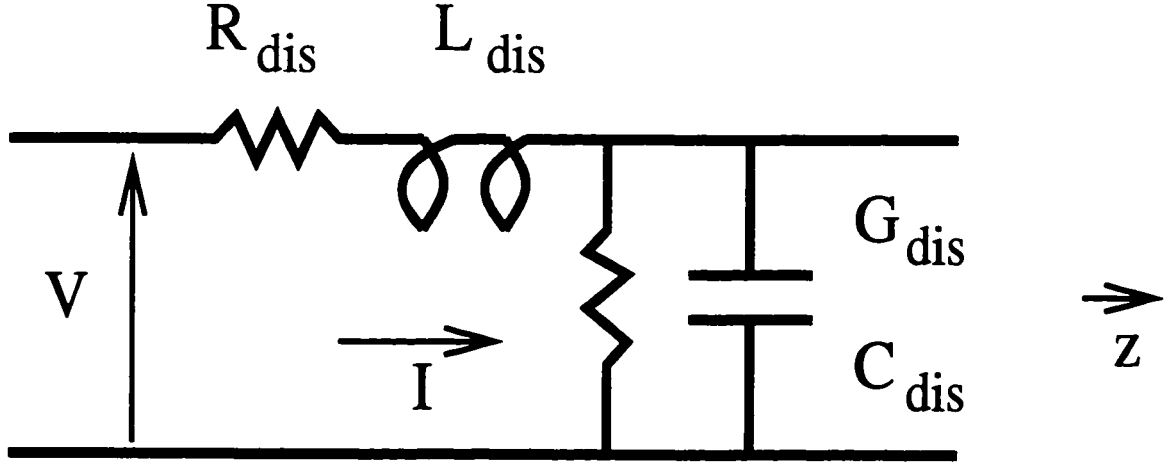

Figure 7.6: Lossy Transmission Line.

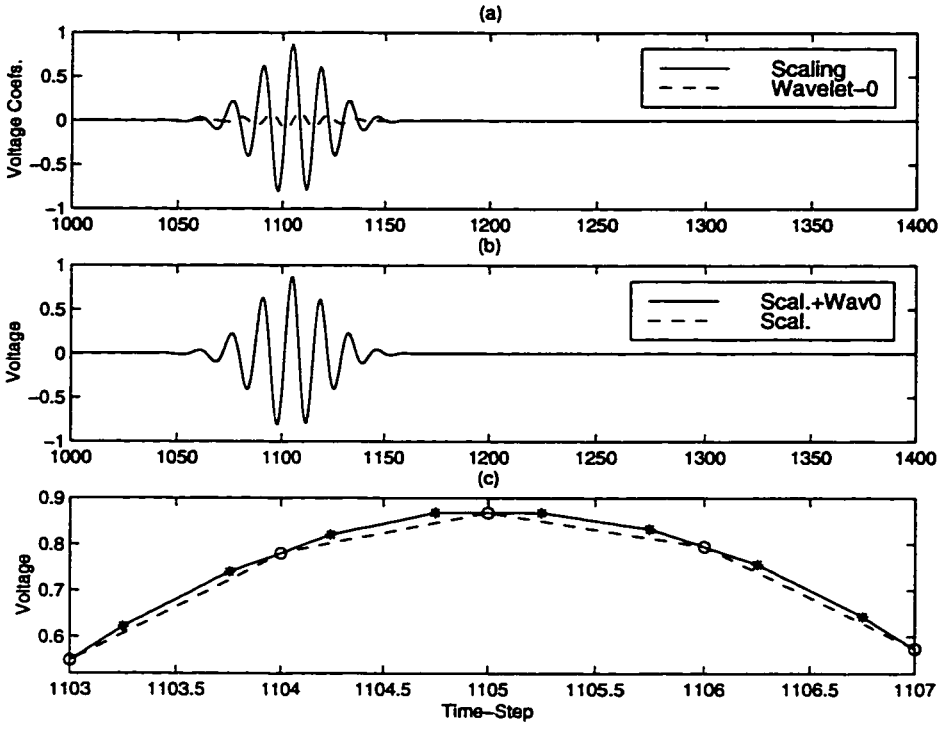

Figure 7.7: Voltage Coefficients - Demonstration of the Double Resolution in Time-Domain.

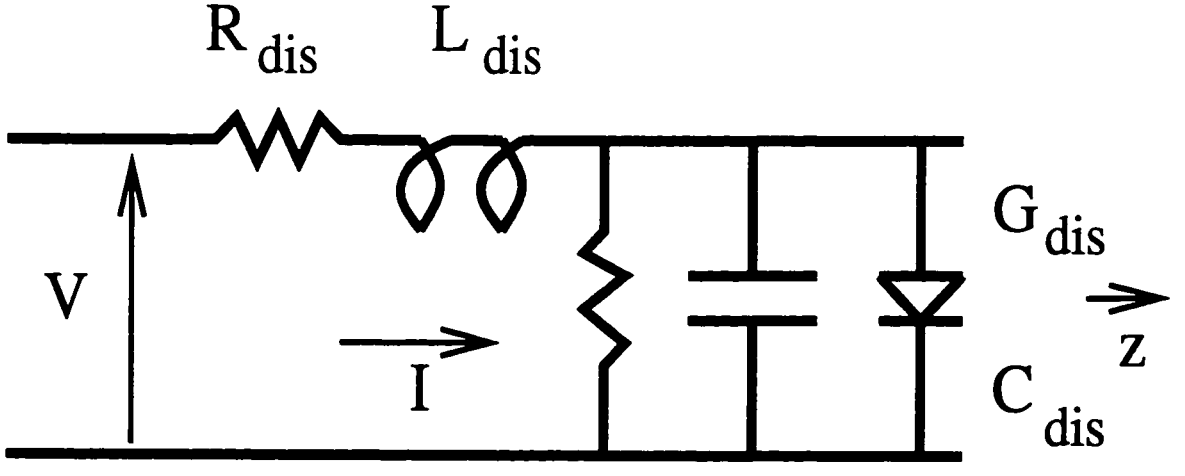

Figure 7.8: Rectifier Geometry.

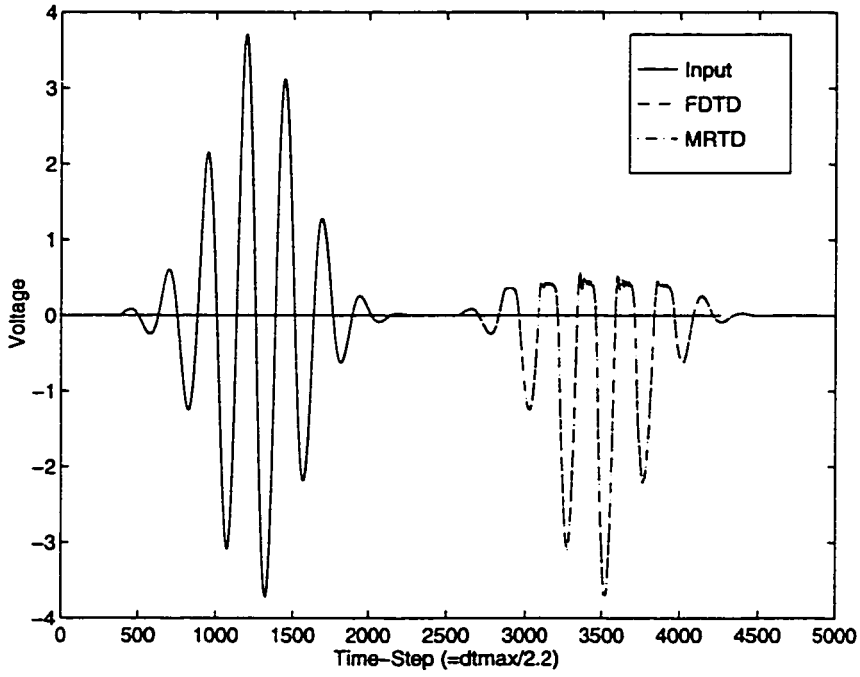

Figure 7.9: Comparison MRTD-FDTD.

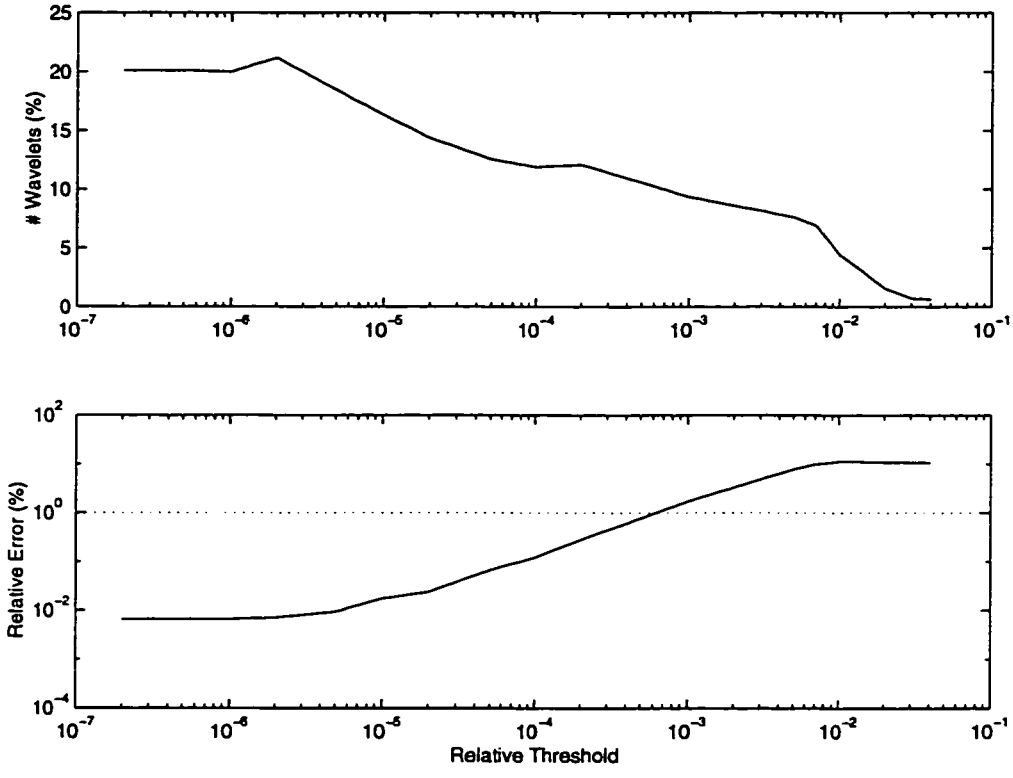

Figure 7.10: Parametric Investigation of Relative Threshold values (Absolute Threshold = 10^{-7}).

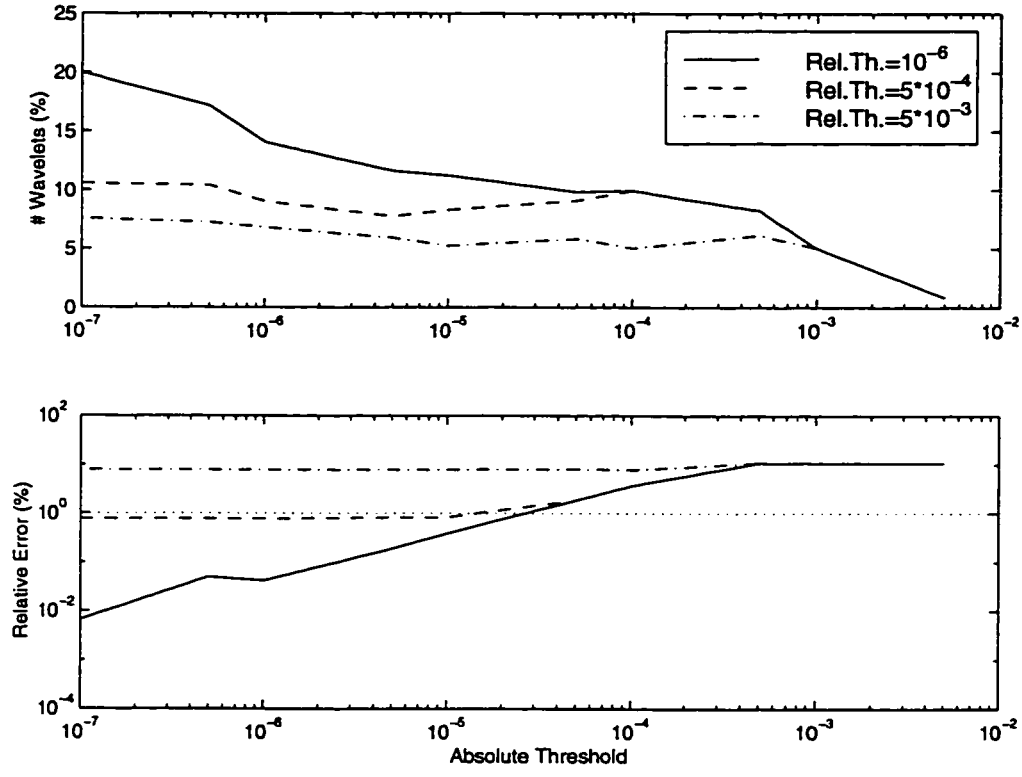

Figure 7.11: Parametric Investigation of Absolute Threshold values.

CHAPTER 8

Conclusions

8.1 Summary of Achievements

The goal of this dissertation was to develop efficient time-domain numerical techniques for the analysis and design of microwave circuits. The widely used FDTD Technique has been used as the starting point. Various planar circuits and waveguide geometries have been simulated and a memory-efficient waveguide absorber based on analytic Green's functions has been derived. This absorber has a similar performance to the PML absorber in terms of numerical reflection, but requires significantly less memory resources. The S-parameters of a specific waveguide probe structure have been calculated for a variety of critical geometrical parameters and its performance has been optimized by use of the above absorber.

The most fundamental contribution of this Thesis is that the principles of Multiresolution Analysis have been employed for the first time in Time-Domain numerical techniques and novel time-domain schemes based on field expansions in scaling and wavelet functions have been derived (MRTD). FDTD implementation schemes (excitation, hard/open boundaries) have been extended to Multiresolution schemes maintaining similar performance characteristics. Battle-Lemarie basis has been used for the expansion of field components in

Space-Domain throughout the Dissertation due to their special properties.

The MRTD schemes have been applied to the simulation of 2.5D shielded and open striplines and microstrips. In comparison to FDTD, they offer memory savings by a factor of 4-5 per dimension for macroscopic parameters (dispersion, characteristic impedance) and a factor of 2-3 per dimension for microscopic parameters (field distributions). In addition, the execution time requirements are decreased by a factor of 4-5 for 2.5D and the accuracy is comparable to FDTD. For geometries, where the edge effect is prominent, wavelets have to be introduced in order to improve the accuracy of the local field representation. A non-split formulation for the PML absorber for open structures has been derived and its performance is similar to the FDTD split PML (numerical reflection smaller than -100db). It has to be noted that due to the entire-domain character of the used basis, MRTD offer the opportunity of a multi-point field representation per cell.

Stability analysis has provided analytical expressions for the maximum stable time-step of the MRTD schemes. As far as it concerns dispersion, it has been proven that larger summation stencils decrease the numerical phase error making it significantly lower than FDTD for low and medium discretizations (up to 40 cells $/\lambda$ for stencil size of 10). The addition of wavelets further reduces this phase error for discretizations close to the Nyquist limit to values comparable to those of much denser grids, although it decreases the value of the maximum stable time-step.

Analysis of various nonhomogeneous geometries with MRTD schemes based on Battle-Lemarie expansion basis in Space-Domain have proven that wavelets can contribute to the development of a space- and time-adaptive meshing. This is the most important and unique feature of the Multiresolution Techniques!! Localized use of wavelets provides a zoom-in and zoom-out capability as well as computational efficiency without introducing errors due

to spurious numerical phase velocity mismatches. A combination of relative and absolute thresholds for the wavelet values offers memory savings by a factor of 5-6 per dimension without loss of accuracy in comparison to FDTD for 2D cases. The field distributions and the S-parameters have been calculated and verified by comparison to reference data. Arbitrary spatial distributions of the dielectric constant have been modelled in terms of scaling and wavelet functions in a mathematically correct way. The algorithm can be easily extended to 3D.

MRTD schemes based on expansion in Haar basis in the Time-Domain have been applied to various SPICE-type geometries. Simulations of numerous circuit problems with active and passive lumped and distributed elements have demonstrated the capability of these schemes to provide a real-time time-adaptive time-domain gridding algorithm for circuit analysis. Increased resolution in time-domain is achieved with significant savings in memory while the accuracy is similar to that obtained with the conventional FDTD Technique.

8.2 Future Work

Considering the above list of achievements, future work on the MRTD schemes should include the study of the effects of the enhancement of arbitrary wavelet resolutions for schemes based on entire-domain and finite-domain expansion basis. In addition, different functions should be tested and their performance for different geometries should be evaluated. It has been shown that the dielectric interfaces can be modeled by use of entire-domain basis by discretizing the constitutive relationship and inverting the matrix involved in the resulting tensor equation. Different techniques for this procedure could be compared in terms of efficiency in execution time as well as in terms of minimization of the dimension of these matrices.

As it was displayed in Chapters 6–7 dynamic gridding is achieved by a simple thresholding algorithm. It might be useful to perform a systematic study on the relationship between different thresholding schemes and the error of calculations in order to guarantee a predefined accuracy and justify an a-priori choice of a relative and an absolute threshold. The space- and time- adaptive grid could be a very promising tool for the analysis and optimization of geometries used in High Frequency VLSI and in Wireless Communication Systems. These geometries are characterized by large volumes and fine details, something that makes almost impossible their simulation with uniform and conventional non-uniform grids. On the contrary, MRTD schemes could employ coarse grids and use wavelets only where a larger resolution is needed.

BIBLIOGRAPHY

BIBLIOGRAPHY

[1] J.B.Keller, "Geometrical Theory of Diffraction", J.Optical Society of America, vol.52, 1962, pp.116-130.

[2] R.G.Kouyoumjian and P.H.Pathak, "A Uniform Geometrical Theory of Diffraction for an Edge in a Perfectly Conducting Surface", Proc.IEEE, vol.62, 1974, pp.1448-1461.

[3] R.F.Harrington, "Field Computation by Moment Methods", New York, Macmillan, 1968.

[4] K.R.Umashankar, "Numerical Analysis of Electromagnetic Wave Scattering and Interaction Based on Frequency-Domain Integral Equation and Method of Moments Techniques", Wave Motion, vol.10, 1988, pp.493-525.

[5] J.H.Richmond, "Digital Computer Solutions of the Rigorous Equations for Scattering Problems", Proc. IEEE, vol.53, Aug.1965, pp. 796-804.

[6] R.F.Harrington, "Matrix Methods for Field Problems", Proc. IEEE, vol.55, no.2, Feb.1967, pp. 136-149.

[7] L.D.Kovach, "Boundary-value Problems", Reading, MA: Addison-Wesley, 1984, pp.355-379.

[8] A.Thom and C.J.Apelt, "Field Computations in Engineering and Physics", London: D.Van Nostrand, 1961.

[9] M.N.O.Sadiku, "A Simple Introduction to Finite Element Analysis of Electromagnetic Problems", IEEE Trans. Educ., vol.32, no.2, May 1989, pp.85-93.

[10] K.S.Yee, "Numerical Solution of Initial Boundary Value Problems Involving Maxwell's Equations in Isotropic Media", IEEE Trans. Antennas and Propagation, vol.14, 1966, pp.302-307.

[11] A.Taflove and M.E.Brodwin, "Numerical Solution of Steady-State Electromagnetic Scattering Problems Using the Time-Dependent Maxwell's Equations", IEEE Trans. Microwave Theory and Techniques, vol.23, 1975, pp.623-630.

[12] G.Mur, "Absorbing Boundary Conditions for the Finite-Difference Approximation of the Time-Domain Electromagnetic Field Equations", IEEE Trans. Electromagnetic Compatibility, vol.23, 1981, pp.377-382.

[13] J.-P.Berenger, "A Perfectly Matched Layer for the Absorption of Electromagnetic Waves", Computational Physics, vol.114, 1994, pp.185-200.

[14] D.S.Katz, E.T.Thiele and A.Taflove, "Validation and Extension to Three Dimensions of the Berenger PML Absorbing Boundary Condition for FDTD Meshes", IEEE Microwave and Guided Wave Letters, vol.4, 1994, pp.344-346.

[15] A.Taflove and K.R.Umashankar, "Radar Cross Section of General Three-dimensional Scatterers", IEEE Trans. Electromagnetic Compatibility, vol.25, 1983, pp.433-440.

[16] K.R.Umashankar and A.Taflove, "A Novel Method to Analyze Electromagnetic Scattering of Complex Objects", IEEE Trans. Electromagnetic Compatibility, vol.24, 1982, pp.397-405.

[17] D.H.Choi and W.J.Hoefer, "The Finite-difference Time-domain Method and its Application to Eigenvalue Problems", IEEE Trans. Microwave Theory and Techniques, vol.34, 1986, pp.1464-1470.

[18] X.Zhang, J.Fang, K.K.Mei and Y.Liu, "Calculation of the Dispersive Characteristics of Microstrips by the Time-domain Finite-difference Method", IEEE Trans. Microwave Theory and Techniques, vol.36, 1988, pp.263-267.

[19] J.G.Maloney, G.S.Smith and W.R.Scott, Jr., "Accurate Computation of the Radiation from Simple Antennas using the Finite-difference Time-domain Method", IEEE Trans. Antennas and Propagation, vol.38, 1990, pp.1059-1065.

[20] S.M.El-Ghazaly, R.P.Joshi and R.O.Grondin, "Electromagnetic and Transport Considerations in Subpicosecond Photoconductive Switch Modeling", IEEE Trans. Microwave Theory and Techniques, vol.38,1990, pp.629-637.

[21] B.Toland, B.Housmand and T.Itoh, "Modeling of Nonlinear Active Regions with the FDTD Method", IEEE Microwave and Guided Wave Letters, vol.3, 1993, pp.333-335.

[22] W.Sui, D.A.Christensen and C.H.Durney, "Extending the two-dimensional FDTD Method to Hybrid Electromagnetic Systems with Active and Passive Lumped Elements", IEEE Trans. Microwave Theory and Techniques, vol.40, 1992, pp.724-730.

[23] S.Mallat, "Multiresolution Representation and Wavelets", Ph.D. Thesis, University of Pennsylvania, Philadelphia, 1988.

[24] Y.Meyer, "Ondelettes et Fonctions Splines", Seminaire EDP, Ecole Polytechnique, Paris, December 1986.

[25] L.L.Schumaker, "Spline Functions: Basic Theory", Wiley-Interscience, New York, 1981.

[26] H.C.Schweinler and E.P.Wigner, "Orthogonalization Methods", J.Math.Phys., 11 (1970), pp.1693-1694.

[27] G.Battle, "A Block Spin Construction of Ondelettes, Part I:Lemarie functions", Comm. Math. Phys., 110 (1987), pp.601-615.

[28] P.G.Lemarie, "Ondelettes a Localization Exponentielles", J.Math. Pures Appl., 67 (1988), pp.227-236.

[29] , A.Haar, "Zur Theorie der Orthogonalen Funktionsysteme", Math.Ann., 69 (1910), pp.331-371.

[30] I.Daubechies, "Orthonormal Bases of Compactly Supported Wavelets", Comm. Pure Appl. Math., 41 (1988), pp.909-996.

[31] M.Krumpholz, L.P.B.Katehi, "MRTD: New Time Domain Schemes Based on Multiresolution Analysis", IEEE Trans. Microwave Theory and Techniques, vol. 44, no. 4, pp. 555-561, April 1996.

[32] R. Holland, "Finite-difference time-domain (FDTD) analysis of magnetic diffusion", IEEE Transactions on Electromagnetic Compatibility, vol. 36, pp. 32-39, Feb.1994.

[33] A.Bayliss and E.Turkel, "Radiation Boundary Conditions for wave-like equations", Comm. Pure Appl. Math., vol. 23, pp. 707-725, 1980.

[34] B.Engquist and A.Majda, "Absorbing Boundary Conditions for the numerical simulation of waves", Mathematics of Computation, vol. 31, pp. 629-651, 1977.

[35] R.L.Higdon, "Absorbing Boundary Conditions for difference approximations to the multidimensional wave equation", Mathematics of Computation, vol. 47, pp. 437-459, 1986.

[36] Z.P.Liao et al., "A transmitting boundary for transient wave analyses", Scientia Sinica (Series A), vol. XXVII, pp. 1063-1076, 1984.

[37] K.K.Mei and J.Fang, "Superabsorption-a method to improve absorbing boundary conditions", IEEE Trans. Antennas Propagation, vol. 40, pp.1001-1010, Sept.1992.

[38] A.Taflove, "Computation of the Electromagnetic Fields and Induced Temperatures within a Model of the Microwave-Irradiated Human Eye", Ph.D. Dissertation, Department of Electrical Engineering, Northwestern University, Evanston, IL, June 1975.

[39] S.M.Kay, "Modern Spectral Estimation", Englewood Cliffs, NJ: Prentice-Hall, 1988.

[40] L.Marple, "A new autoregressive spectrum analysis algorithm", IEEE Trans. Acoustics, Speech and Signal Processing, vol. 28, pp. 441-454, 1980.

[41] J.M.Rollins and J.M.Jarem, "The input impedance of a hollow-probe-fed, semi-infinite rectangular waveguide", IEEE Transactions on Microwave Theory and Techniques, vol. 37, pp. 1144-1146, Jul.1989.

[42] A.G.Williamson, "Coaxially fed hollow probe in a rectangular waveguide", Proc. Inst. Elec. Eng., vol. 132, part H, pp. 273-285, 1985.

[43] W.W.S. Lee and E.K.N. Yung, "The Input Impedance of a Coaxial Line Fed Probe in a Cylindrical Waveguide", IEEE Transactions on Microwave Theory and Techniques, vol. 42, pp. 1468-1473, Aug.1994.

[44] E.Tentzeris,N.Dib,L.Katehi,J.Oswald and P.Siegel, "Time-Domain Characterization of Diode-Mounting structures", Nasa Terahertz Symposium Digest, March 1994.

[45] P.B.Johns, K.Aktharzad "The Use of Time Domain Diakoptics in Time Discrete Models of Fields", Int.J.Num.Methods Eng., vol. 17, pp. 1-14, 1981.

[46] W.J.R.Hoefer "The Discrete Time Domain Green's Function or Johns' Matrix - A new powerful Concept in Transmission Line Modelling (TLM)", Int.Journal of Num.Modeling, vol. 2, pp. 215-225, 1989.

[47] T.W.Huang, B.Housmand, T.Itoh "The Implementation of Time-Domain Diakoptics in the FDTD Method", IEEE Transactions on Microwave Theory and Techniques, vol. 42, pp. 2149-2155, Nov.1994.

[48] C.Eswarappa, W.J.R.Hoefer "Diakoptics and Wideband Dispersive Absorbing Boundaries in the 3-D TLM Method with Symmetrical Condensed Node", IECE Transactions, vol. E74, no. 5, pp.1242-1250, May 1991.

[49] M.Righi, W.J.R.Hoefer "Efficient 3D-SCN-TLM Diakoptics for Waveguide Components", IEEE Transactions on Microwave Theory and Techniques, vol. 42, pp. 2381-2385, Dec.1994.

[50] M.Righi, W.J.R.Hoefer, M.Mongiardo and R.Sorrentino "Efficient TLM Diakoptics for Separable Structures", IEEE Transactions on Microwave Theory and Techniques, vol. 43, pp. 854-859, Apr.1995.

[51] M.Werthen, M.Rittweger, I.Wolff " FDTD-Simulation of Waveguide Junctions using a new Boundary Condition for Rectangular Waveguides", Proc. 24th European Microwave Conference, pp.1715-1719, 1994.

[52] F.Moglie, T.Rozzi, P.Marcozzi and A.Schiavoni "A New Termination Condition for the Application of FDTD Techniques to Discontinuity Problems in Close Homogeneous Waveguide", IEEE Microwave and Guided Wave Letters, vol. 2, no. 12, pp. 475-477, Dec.1992.

[53] M.Krumpholz, B.Bader and P.Russer "On the theory of Discrete TLM Green's functions in Three-dimensional TLM", IEEE Transactions on Microwave Theory and Techniques, vol. 43, pp. 1472-1483, Jul.1995.

[54] M.Werthen, M.Rittweger and I.Wolff "Multi-mode Simulation of Homogeneous Waveguide Components Using a Combination of the FDTD and FD^2 Method", Proc. 25th European Microwave Conference, pp.234-237, 1995.

[55] M.Schwarz "Information, Transmission, Modulation and Noise", McGraw-Hill International Editions, pp. 72-76, 7th Ed., 1987.

[56] M.Krumpholz, C.Huber and P.Russer "A field theoretical comparison of FDTD and TLM", IEEE Transactions on Microwave Theory and Techniques, vol. 43, pp. 1935-1950, Aug.1995.

[57] C-Y.Chi, G.M.Rebeiz, "Planar Microwave and Millimeter-Wave Lumped Elements and Couple-line Filters Using Micro-Machining Techniques",IEEE Trans. Microwave Theory and Techniques, pp. 730-738, April 1995.

[58] E.M.Tentzeris, R.L.Robertson, M.Krumpholz, L.P.B.Katehi, "Application of MRTD to Printed Transmission Lines", Proc. MTT-S 1996, pp. 573-576.

[59] M.Krumpholz, L.P.B.Katehi, "MRTD Modeling of Nonlinear Pulse Propagation", to be published at the IEEE Trans. Microwave Theory and Techniques.

[60] S.Xiao, R.Vahldieck, "An Improved 2D-FDTD Algorithm for Hybrid Mode Analysis of Quasi-planar Transmission Lines", MWSYM 93, vol. 1, pp.421-424.

[61] B.C.Wadell, "Transmission Line Design Handbook", pp. 136-137, Artech House, 1991.

[62] A.Taflove, "Computational Electrodynamics", Artech House, 1995.

[63] K.L.Shlager and J.B.Schneider, "Analysis of the Dispersion Properties of the Multiresolution Time-Domain Method", IEEE AP-S 1997 Proceedings, vol. 4, pp. 2144-2147, 1997.

[64] W.Y.Tam, "Comments on "New Prospects for Time Domain Analysis"", IEEE Microwave and Guided Wave Letters, vol. 6, pp. 422-423, 1996.

[65] M.Krumpholz, L.P.B.Katehi, "New Prospects for Time Domain Analysis", IEEE Microwave and Guided Wave Letters, pp. 382-384, November 1995.

[66] E.Tentzeris, R.Robertson, M.Krumpholz and L.P.B. Katehi, "Application of the PML Absorber to the MRTD Technique", Proc. AP-S 1996, pp. 634-637.

[67] D.M.Pozar, "Microwave Engineering", pp. 94-96, Addison-Wesley, 1990.

[68] M.Krumpholz, P.Russer, "Two-Dimensional FDTD and TLM", Int.Journal of Num. Modelling, vol. 7, no. 2, pp. 141-153, February 1993.

[69] P.Russer, M.Krumpholz, "The Hilbert Space Formulation of the TLM Method", International Journal of Numerical Modelling: Electronic Networks, Devices and Fields, vol. 6, no. 1, pp. 29-45, February 1993.

[70] R. Robertson, E. Tentzeris, M. Krumpholz, L.P.B. Katehi, "Application of MRTD Analysis to Dielectric Cavity Structures", Proc. MTT-S 1996, pp. 1861-1864.

[71] K.Goverdhanam, E.Tentzeris, M.Krumpholz and L.P.B. Katehi, "An FDTD Multigrid based on Multiresolution Analysis", Proc. AP-S 1996, pp.352-355.

[72] V.Perrier and C.Basdevant, "La decomposition en ondelettes periodiques: un outil pour l'analyse des champs inhomogenes. Theorie et algorithmes", La Recherche Aerospatiale, no.3, pp.53-67, 1989.

[73] E.Tentzeris, R.Robertson, A.Cangellaris and L.P.B. Katehi, "Space- and Time- Adaptive Gridding Using MRTD", Proc. MTT-S 1997, pp. 337-340.

IMAGE EVALUATION
TEST TARGET (QA-3)

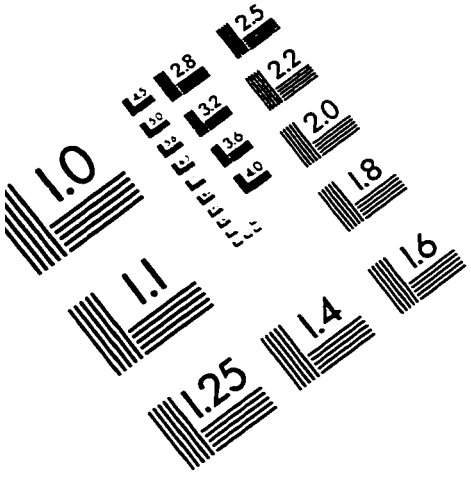

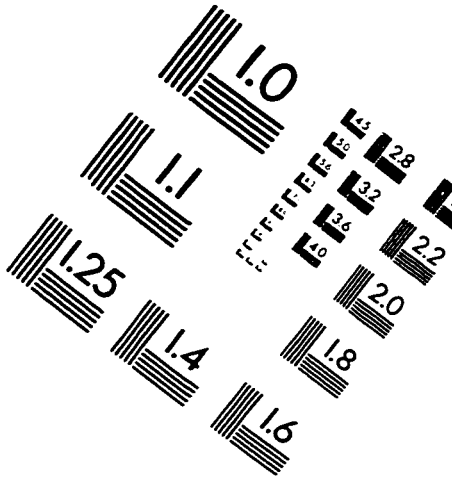

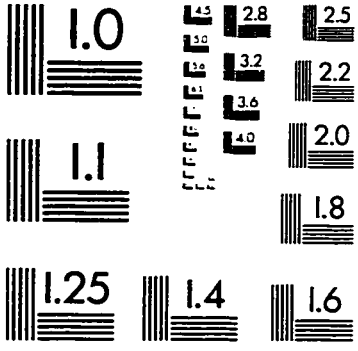

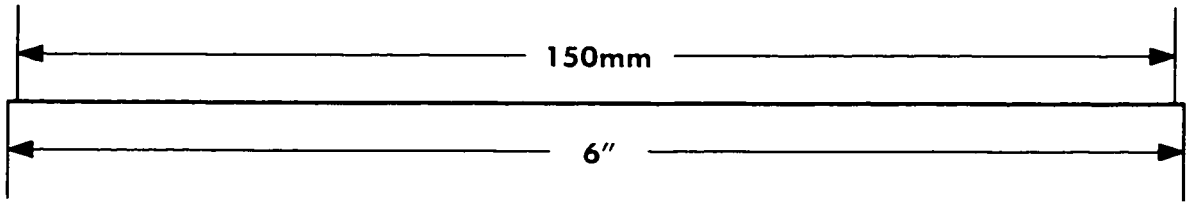

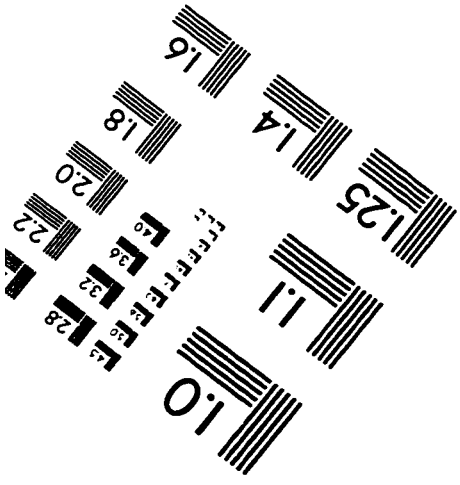

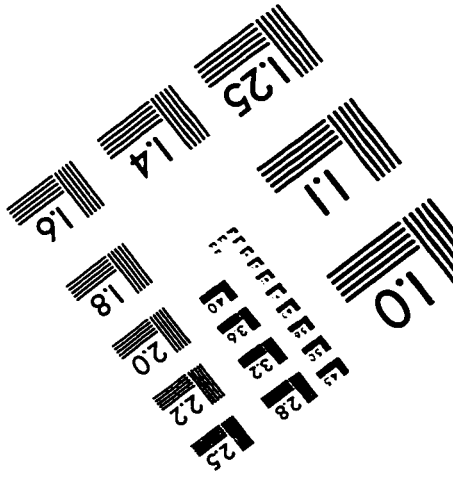

APPLIED IMAGE, Inc
1653 East Main Street
Rochester, NY 14609 USA
Phone: 716/482-0300
Fax: 716/288-5989